LOW-BACKGROUND BALLOON-BORNE DIRECT SEARCH FOR IONIZING MASSIVE PARTICLES AS A COMPONENT OF THE DARK GALACTIC HALO MATTER

by

Patrick Charles McGuire

A Dissertation Submitted to the Faculty of the

DEPARTMENT OF PHYSICS

In Partial Fulfillment of the Requirements
For the Degree of

Doctor of Philosophy

In the Graduate College

THE UNIVERSITY OF ARIZONA

1 9 9 4

STATEMENT BY AUTHOR

This dissertation has been submitted in partial fulfillment of requirements for an advanced degree at The University of Arizona and is deposited in the University Library to be made available to borrowers under rules of the library.

Brief quotations from this dissertation are allowable without special permission, provided that accurate acknowledgment of source is made. Requests for permission for extended quotation from or reproduction of this manuscript in whole or in part may be granted by the head of the major department or the Dean of the Graduate College when in his or her judgment the proposed use of the material is in the interests of scholarship. In all other instances, however, permission must be obtained from the author.

SIGNED: _____

ACKNOWLEDGEMENTS

I need to thank foremost those people associated with the University of Arizona who had the most to do with our dark matter project, many of whom were volunteer or underpaid: Burt Pifer, Delmar Barker, Ken Kendall, Deborah Nassif, Jesus Pando, Lou Russo, Ronald Norton, Travis Metcalfe, Hau Nguyen, Brad Guss, Abe Young, Carol Tang, and Peter Halverson (UC-Irvine). Eric James, Dave Fein, and Andy Milder all volunteered a day of their time to help install the last of four detectors at our mountain lab. I cannot give enough thanks to my dissertation advisor, Theodore Bowen — I could not ask for a more patient, intelligent, interesting, and hard-working advisor than he is. I cannot thank Ted enough for providing the environment in which we could dream of such an interesting/novel dissertation experiment (who would have ever dreamed of searching for dark matter at balloon-altitude, of all places?).

The NASA Space Grant and Pima Community College Grant supported most of our undergraduate employees. A NSF/U.S. Dept. of Education/State of Arizona Fellowship supported myself for my first three years at Arizona. The NSF SGIR program (grant 91-21427) supported much of my summer employment and my post-fellowship academic years, along with much of the cost of doing the balloon-borne and mountain-top experiments.

We will forever be indebted to Bob Streitmatter and our other IMAX collaborators for allowing us to participate in their balloon experiment and for all the support and criticism that they have offered us in our collaborative dark matter search. The IMAX experiment was supported by NASA/GSFC RTOP 353-87-2 and NASA grant NAG-1418. The institutions which participated in the IMAX experiment include: GSFC Laboratory for High Energy Astrophysics, NMSU Particle Astrophysics Lab, University of Siegen (Germany), Caltech Space Radiation Lab, University of Arizona, and the National Scientific Ballooning Facility. Our IMAX collaborators include: Louis Barbier, Eric Christian, Bob Golden, Barb Kimbell, Steve Stochaj, Roy Park, Bob Hall, Don Righter, John Ormes, Allan Labrador, Bob Streitmatter, John Mitchell, Steve Schindler, Manfred Simon, Wolfgang Menn, Olaf Reimer, Bill Webber, Dick Mewaldt, Glenn Albritton, Andy Davis, Steve Holder, and Max.

I also thank the following people or institutions from the University of Arizona for their help on or conversations about our dark matter project during my tenure here at the U. of A.: Mike Eklund, Leif Shaver, John Rutherfoord, Mike Shupe, the University of Arizona Experimental Elementary Particle Physics VAX/SGI cluster, the UA Physics Department Sun workstation cluster, the UA Physics/Atmospheric Sciences High Altitude Observatory on Mt. Lemmon, Steward Observatory, Kirk McLaughlin, Fulvio Melia, Adam Burrows, Henry Hill, Johann Rafelski, Christoph Best, David Harley, Mikolai Sawicki, J.D. Garcia, Kwan Lai, Doug Toussaint, John Leavitt, Larry McIntyre, Don Ashbaugh, Eva Ramirez, Iris Wright, Mitzi Demartino, Soraya Torabi, Nancy Kern, Jacki Fahey, Evelyn Burros, Sigurd Kohler, Bruce Barrett, Robert Parmenter, Dave Arnett, Peter Carruthers, Ina Sarcevic, Dandan Guo, and Bob Thews.

I have learned a great deal from the conversations on dark matter at conferences, during/after colloquiua, and through email with David Caldwell, Fred Reines, Kim Griest, Buford Price, Michael Turner, Steve Barwick, Dave Schramm, Anibal Gattone, Rita Bernabei, Sheldon Glashow, Barry Barish, Neil Spooner, Gary Liu, Daniel Snowden-Ifft, Ed Diehl, and Glenn Starkman.

I appreciate the respect, friendship and good times that I shared with my parents Joan and Charles McGuire, my brothers Chad, Michael, and David, and all my relatives and friends. These people have helped me to stay healthy and happy during my long and arduous, but interesting, years in school.

TABLE OF CONTENTS

LIST OF FIGURES

LIST OF TABLES

ABSTRACT

A dark matter (DM) search experiment was flown on the IMAX balloon payload, which tested the hypothesis that a minor component of the dark matter in the Galactic halo is composed of ionizing ($dE/dx > 1$ MeV/g/cm^2 or $\sigma > 2 \times 10^{-20}$ cm^2) supermassive particles ($m_x \in [10^4, 10^{12}]$ GeV/c^2) that cannot penetrate the atmosphere due to their low-velocities ($\beta \in [0.0003, 0.0025]$). The DM search experiment consisted of a delayed coincidence between four ~ 2400 cm^2 plastic scintillation detectors, with a total acceptance of ~ 100 cm^2 sr. In order to search for ultra-slow particles which do not slow down in the IMAX telescope, the experiment contained TDCs which measured the time-delays $T_{i,i+1} \in [0.3, 14.0]$ μs between hits in successive counters to $\sim 1\%$ precision. Using the first 5 hours of data at float altitude (5 g/cm^2 residual atmosphere), we observed ~ 5 candidate non-slowing dark matter events, consistent with the background expected from accidental coincidences of 4 events. This implies that the DM flux is less than 6.5×10^{-6} cm^{-2}s^{-1}sr^{-1} (95% C.L.). Similar results were also obtained for particles which slow down in the counter telescope. This experiment effectively closes much of a previously unconstrained 'window' in the mass/cross-section joint parameter space for massive particles as the dominant halo DM, and implies that for certain regions of this parameter space massive particles cannot be more than one part in 10^5 by mass of all the DM. These results can also directly constrain 'light' magnetic monopoles and neutraCHAMPs in a previously unconstrained mass region $m_x \in [10^6, 10^9]$ GeV.

CHAPTER 1

INTRODUCTION

Two of the biggest mysteries in modern astrophysics may soon be solved. The first mystery is the exact value of the average density of the universe. With the recent repair of the near-sighted Hubble Space Telescope (HST), astronomers will be able to observe the redshift and brightness of distant galaxies to precisely determine the Hubble constant. From the value of the Hubble constant, they can determine the mean density of the universe to decide whether additional ('dark') matter is needed to account for the observed mean density of the Universe. The second mystery is the composition of the non-luminous ('dark') matter that surrounds our galaxy with a murky gravitational halo. For many years, there has been striking evidence that spiral galaxies, including our own galaxy, have 'flat' rotation curves, with rotational velocities independent of r [1][2]. From the observed distribution of luminous matter in a galaxy (stars and hydrogen gas), models of the gravitational potential in that galaxy predict that the rotational velocity of a star as a function of radius, r, from the center of that galaxy will decrease as $r^{-1/2}$, for large r[3][4]. In order to explain this discrepancy between the observed flat rotation curves and the predicted decreasing rotation curves, several predictive models have been formulated, such as the existence of non-Newtonian gravity active on long distances[5][6] or the existence of a cloud of dark matter (DM) around each of the galaxies[4],[7]-[14]. The dark matter model for the flat rotation curves of galaxies has been the more popular hypothesis of the two, probably because the predictions of the dark matter model make predictions which can be more easily tested here on the earth. For example, for our own galaxy, one dark matter model[9][15] predicts that if the dark matter halo is spherically

symmetric, then the density of dark matter halo in the solar neighborhood is:

$$\rho \in [4 \times 10^{-3}, 10^{-2}]\ M_{\odot}/\mathrm{pc}^3 \equiv [2.4, 7.4] \times 10^{-25}\ \mathrm{g/cm}^3 \equiv [0.17, 0.42]\ \mathrm{GeV/cm}^3, \quad (1.1)$$

which is equivalent[16] to a flux of

$$\Phi \in [1.0, 2.5] \times \frac{10^6\ \mathrm{GeV}}{m_x}\ \mathrm{cm}^{-2}\mathrm{s}^{-1}\mathrm{sr}^{-1}, \quad (1.2)$$

where m_x is the mass of the dark matter object in GeV, and the mean speed of the galactic dark matter objects, $\bar{v} \approx 240$ km/s $= 8.0 \times 10^{-4}c$, has been used[18][19]. The flux of the dark matter objects as a function of velocity will follow a 'cut-off' Maxwellian distribution [16][17][18]:

$$\begin{aligned} \frac{d\Phi}{du} &= 3.6 f_d\ \mathrm{cm}^{-2}\mathrm{s}^{-1}\mathrm{sr}^{-1}\Theta\left(\tfrac{v_{\max}}{\tilde{v}} - u\right) u^3 \exp\left(-u^2\right) \\ &\quad \times \left(\tfrac{\rho}{0.3\ \mathrm{GeV/cm}^3}\right)\left(\tfrac{\tilde{v}}{213\ \mathrm{km/s}}\right)\left(\tfrac{10^6\ \mathrm{GeV}}{m_x}\right) \end{aligned} \quad (1.3)$$

, where we have used a mid-range value for the dark matter density, $\rho = 0.3$ GeVcm^{-3}, f_d is the fraction of the dark matter halo which the object represents, and

$$u \equiv v/\tilde{v}. \quad (1.4)$$

We will assume a velocity dispersion of $\tilde{v} = \bar{v}\sqrt{\pi}/2 = 213$ km/s and a galactic escape cutoff velocity of $v_{\max} = 640$ km/s[18][19]. If $f_d \sim 1$, then for masses $m_x < 10^6$ GeV the galactic halo dark matter flux in equations 1.2 and 1.3 larger than the cosmic ray flux, which has the order of magnitude (~ 1 cm^{-2}s^{-1}sr^{-1}).

The halo dark matter density and flux in Equations 1.1 and 1.2 is enhanced by gravitational clustering by a factor of $\sim 10^5$ over the mean density of an $\Omega = 1$ universe[20]. This dark matter density may also be enhanced even more by trapping in the gravitational field of the sun or earth[21][22][23], but significant trapping at these low velocities[1] has been found to be unlikely[24][25]. Additionally, the halo DM density also may be enhanced over the density in Equation 1.1 by a factor of perhaps 50% if

[1] The escape velocity from the sun at a distance 1 A.U. from the sun is $\sim 1.40 \times 10^{-4}c = 42$ km/s, and the escape velocity from the earth at the earth's surface is $\sim 1.23 \times 10^{-5}c = 3.69$ km/s. Our dark matter search is *not* sensitive to these velocities.

the dark matter halo is not spherical but slightly flattened[26][27]. The motion of the sun in the galaxy and of the earth around the sun will cause a slight annual modulation ($\sim 1\%$) of the dark matter flux as seen by earth-bound detectors[28][29]. Additionally, since the earth is not perfectly transparent to some dark matter objects[2], the rotation of the earth about its axis will cause a shadowing effect, causing a diurnal modulation of the dark matter flux[30] (see Appendix C). If by some means one can show that a particular dark object[3] exists *and* has sufficient mass density to account for the density in equation 1.1, then they will have solved the Galactic halo dark matter problem.

The dominant approach that astronomers are taking to solve the first mystery (the density of the universe) consists of finding a better method to measure distance in the universe and then measuring the brightness and recessional velocity of the most distant, and hence the dimmest, galaxies. There are many different approaches being taken to solve the second mystery (the composition of the dark matter in our galactic halo). These approaches include using the planned (1997) NICMOS infra-red camera upgrade to the HST and also ground based optical/infrared observatories to search for undisputed infra-red signature of brown dwarfs, which could be the dark galactic halo matter. Advancing technology has allowed dedicated ground-based observational programs such as MACHO and EROS to report detections [31][32] of several gravitational microlensing candidate events while observing 10^6 stars in the Large Magellenic Cloud. The observation of these microlensing events might imply that our dark Galactic Halo is largely made of sub-stellar mass objects such as brown dwarfs. Maybe some astrophysical objects which are totally unpredicted will be discovered by the Hubble ST or the advancing ground-based optical/infrared observing technology; and just maybe, one of these 'nearby' discoveries will be able to account for the Galactic halo dark matter. Yet the Hubble Space Telescope and ground-based optical/infrared observers cannot detect all possible candidates for the dark matter problem – radio/microwave telescopes might be necessary to observe cold, dark hydrogen clouds

[2] e.g., supermassive particles with a small energy, E, compared to their rate of energy loss, dE/dx.
[3] e.g., planets, brown dwarfs, black holes, comets, neutrinos, supermassive particles.

[33][34]; very large underground neutrino detectors would be required to detect neutrino oscillations of low-energy solar or atmospheric neutrinos and hence measure the tiny mass of neutrinos[4] [35]. A whole host of different 'elementary' particles have been hypothesized as solutions to the dark matter problem (e.g. a small rest mass for ordinary neutrinos[36][37][38], WIMPs[39], cosmions[40], monopoles[41], CHAMPs[42], very massive neutrinos[39][43][44], SIMPs[45][46][47], strange quark nuggets[48], the lightest supersymmetric partner (LSPs, e.g. photinos, neutralinos)[49], axions[50]); and novel particle detectors are required to detect each different dark matter candidate.

Weakly Interacting Massive Particles (WIMPs) (which include cosmions, massive neutrinos, LSPs) are considered by many scientists to be a likely dark matter particle candidate, especially since their ultra-low cross-section ($\sigma \sim 10^{-36}$ cm^2) would have made them very difficult to detect. However many different experimenters are actively searching for WIMPs, e.g. Caldwell and collaborators [51] use ultra-pure solid-state detectors at very low temperature and very far underground (to avoid cosmic-ray background) to attempt to detect the neutralino. By attaching thermistors to single crystals of silicon or germanium at low temperature, the WIMP hunters hope to detect the phonons from the collisions of WIMPs with nuclei in the detector. In the early universe, the low WIMP cross-section would make it quite likely that enough WIMPs could survive annihilation from anti-WIMPs, so as to be abundant enough to solve the missing matter problem today [43]. However, particles which have a much higher annihilation cross-section than WIMPs would not survive annihilation in the early universe, and would therefore not be abundant enough to be a likely dark matter candidate.

Despite the popular prejudice that dark matter particles must interact weakly (e.g., WIMPs [43][51], light neutrinos [36]-[38]), so as to go unobserved and to survive primordial annihilation [43], ionizing massive particles (IMPs) might be abundant enough and yet be unobservable enough to be the dominant dark halo matter (DDHM) in the galactic halo [42][46][58][47]. Examples of IMPs include: CHAMPs (electrically

[4] due to the large number density of relic neutrinos, the small neutrino masses could add up to account for the missing matter

CHArged Massive Particles), SIMPs (Strongly Interacting Massive Particles), monopoles and "strange" quark nuggets. IMPs *can* have a relic abundance that is large enough to constitute all the dark matter in the universe[42]. If IMPs annihilate with anti-IMPs (of equal initial density) in the early universe and if the universe is to be IMP-dominated ($\rho \sim \rho_c \approx 2 \times 10^{-29} h^2$ g/cm^{-3}, where the Hubble-constant, h, is between $h \sim \frac{1}{2}$ and $h \sim 1$), then the annihilation cross-section (times relative velocity) must be [43]

$$\sigma\beta = 3 \times 10^{-38} h^{-2} \text{ cm}^2. \tag{1.5}$$

If IMPs annihilate weakly, then their annihilation cross-section in the early universe is [42]:

$$\sigma\beta = (m_p/m_x)^2 \, 1.2 \times 10^{-31} \text{ cm}^2, \tag{1.6}$$

where m_p is the proton mass, and m_x is the IMP mass. Therefore, in order for weakly-annihilating IMPs to dominate the universe, from Equations 1.5 and 1.6, we obtain:

$$m_x \sim 2 \times 10^3 h \sqrt{\frac{\rho}{\rho_c}} \text{ GeV}. \tag{1.7}$$

If IMPs annihilate strongly, then their annihilation cross-section in the early universe is [42]:

$$\sigma\beta = (m_p/m_x)^2 \, 3.5 \times 10^{-26} \text{ cm}^2. \tag{1.8}$$

Therefore, in order for strongly-annihilating IMPs to dominate the universe, we obtain from Equations 1.5 and 1.8:

$$m_x \sim 10^6 h \sqrt{\frac{\rho}{\rho_c}} \text{ GeV}. \tag{1.9}$$

If IMPs are to dominate not the universe, but the galactic halos, then the required IMP density is reduced by a factor of ten; and the necessary IMP mass is reduced by a factor of the square root of ten, to $600h$ GeV and $3 \times 10^5 h$ GeV for the weakly- and strongly-annihilating IMPs, respectively. If there is an IMP/anti-IMP abundance asymmetry, these mass estimates will be only upper limits. If IMPs for some reason do not have antiparticles (e.g., strange quark nuggets), then we cannot use these bounds on the IMP mass. Nonetheless, IMPs in a wide mass range can be abundant enough to solve the

halo dark matter problem, and if IMPs have antiparticles, the range of interesting IMP masses includes $m_x \in [6 \times 10^2, 3 \times 10^5]h$ GeV.

Since the high interaction cross-section of IMPs would have easily observable consequences, one can readily reinterpret past experiments [17]-[64] or invent clever arguments [47][65]-[69] to rule out different hypothetical IMPs as the DDHM, within the theoretically most favored ranges of IMP mass, m_x, number density, n_x, and interaction cross-section with ordinary nuclei σ_{xN}. However, we have found, for a broad range of the joint mass and interaction cross-section parameter space, that generic IMPs have not been ruled out as the dominant halo dark matter, as previously thought (see Chapter 2).

Additionally, several ideas point to an IMP mass or number density outside their current theoretically favored ranges for IMPs as the DDHM. First, some models based upon the results of the COBE experiment suggest that cold dark matter (CDM) alone cannot explain the clumping of galaxies; hot dark matter (HDM) (e.g., light neutrinos) might be 30% of all dark matter[70]. Therefore, since IMPs would be considered as CDM[5] the IMP number density required to be the DDHM is lowered. Second, the theoretical estimates[42][43] of the mass range for IMPs-as-DDHM might be too low, and the density or flux range too high. Third, the simplest models have always assumed that there is a DDHM. However, the dark matter halo may be a 'cosmic garbage-dump' for many different supermassive relics (neutron stars, brown dwarfs, black holes, WIMPs, IMPs), which have a large mass compared to their energy-dissipation rate, preventing collapse into the galactic disk. Could none of these dark halo matter candidates dominate? Why not search for the less dominant forms? Fourth, even if IMPs existed as a very minor component of the dark halo matter, they might be most abundant in the galactic halo (especially if their mass is very high), with small velocities of order $\beta \sim 10^{-3}$, and with large cross-sections which make them much easier-to-detect than WIMPs. Even if WIMPs (with very small cross-sections) are eventually detected by the deep underground searches, it will still be very difficult to extract information about the

[5] with non-relativistic velocities at the time of the decoupling of the background radiation from matter

WIMPs' characteristics[26] (e.g., velocity – both magnitude and direction, and mass). If WIMPs are the DDHM, and IMPs are a very minor component of the halo dark matter, IMPs might still be much easier to detect and to characterize (velocity, mass, and interactions). Fifth, recent big bang nucleosynthesis calculations [71] have suggested that the Galactic halo dark matter (corresponding to $\Omega \sim 0.10$) cannot be accounted for by dark baryons, since these calculations suggest that $0.015 < \Omega_{\text{Baryon}} < 0.070$. Therefore $\Omega_{\text{Non-Baryon, Halo}} > 0.03$, and some effort must be made to determine its identity.

Recently, the MACHO and EROS collaborations have announced [31][32] several gravitational microlensing candidate events while observing 10^6 stars in the Large Magellenic Cloud (LMC). These results *might* imply [73][74] that much of the Galactic halo is composed of sub-stellar massive (baryonic) compact halo objects (MACHOs), such as jupiter-sized planets, neutron stars, brown-dwarfs, asteroids, black-holes, or even dark fractal-like hydrogen clouds[34]. Yet the MACHO/EROS results are still *very* consistent with MACHOs being only a minor component of the halo dark matter – the observers have only detected ~ 4 MACHOs, while they initially expected ~ 30 during their observing time[6]. Such compact baryonic dark matter (BDM) is not CDM, since the precursors of the MACHOs were presumably ordinary hydrogen clouds[7]. Primordial nucleosynthesis arguments are consistent with the halo matter being composed of primarily BDM [38][71]. However, even if MACHOs are the dominant halo DM, exotic non-BDM is still needed to explain the formation of galactic clusters. Considering that MACHOs are still consistent with being only a minor halo DM component, and that non-BDM is necessary for large-scale structure formation, we feel that it is still worthwhile to search for IMPs despite the possible discovery of MACHOs. Indeed, the possibility that MACHOs are the dominant halo matter increases the need to look for minor components of the halo matter.

Therefore, considering the motivations listed above, IMP search experiments

[6] Their events, which show amplification of a LMC star for a period of ~ 1 month seem to suggest MACHO masses of $\sim 0.1 M_{\odot}$.

[7] which had not decoupled from the background photon radiation at the time of the initial density perturbations which seeded structure formation [38]

need a sensitivity many orders-of-magnitude better than the previously expected flux above the atmosphere of $\Phi_{\rm IMP} \sim 1$ cm^{-2}s^{-1}sr^{-1} (for $m_x \sim 10^6$ GeV).[8] Due to the high interaction cross-section of IMPs, and the non-relativistic nature ($\beta_{\rm CDM} \sim 0.001$, $v_{\rm CDM} \sim 300$ km/s) of any CDM candidate, a balloon-altitude time-of-flight search for very slow IMPs is a plausible method to search for such low fluxes for the mass-range $m_x \in [10^4, 10^{10}]$ GeV. A balloon or satellite-borne search experiment is necessary to search for IMPs with a cross-section to mass ratio exceeding $\sigma/m_x \sim 10^{-27}$ cm^2/GeV.

We have found the time-of-flight technique using at least 4 scintillation detectors allows us to perform IMP searches that not only are sensitive to very low fluxes, but also allow us to detect IMPs with a relatively small energy loss[85]. The GSFC/Caltech/Siegen/NMSU IMAX collaboration was preparing a balloon-borne experiment[86] with a payload that included four widely separated 1-2 cm thick plastic scintillation detectors, when the Arizona group proposed adding electronics so that the flight could also search for slowly-moving IMP dark matter with only a 5 g/cm^2 overburden. The search, requiring a low-power, lightweight, low readout-rate electronics module, was agreed upon as an Arizona-IMAX collaboration. The details of the importance of this IMP search[87] and its implementation are the subject of this dissertation.

1.1 Historical Context for our IMP Search

When a hypothetical negatively-CHArged Massive Particle (negative CHAMP), X^-, combines with a proton, p, it forms an electrically neutral composite object, X^-p, called a 'neutraCHAMP' [42]. Due to the relatively large binding energy, $E_B = -25$ keV, of neutraCHAMPs, some particle physics theorists reasoned in 1989 [42][82] that if neutraCHAMPs existed in our Galaxy as 'dark' matter at velocities of $v \sim 10^{-3}c$, then neutraCHAMPs should easily be able to travel through the Earth's atmosphere without

[8] N.B. In this dissertation, all masses will be given in units where the speed of light is equal to one, $c = 1$, e.g. 10^6 GeV/c$^2 \equiv 10^6$ GeV.

losing much energy and without being absorbed by the atmosphere. Therefore, a significant flux of neutraCHAMPs might reach mountain altitude or even sea-level and have observable consequences, like neutral-particle cosmic ray event rates with a sidereal time-dependence[75]-[79], the unusually long pulse-trains seen in early neutrino detectors[80], and excess heat generation in cold-fusion experiments[81]-[84]. This possibility of neutraCHAMPs explaining previously unexplained terrestial phenomena and simultaneously solving a significant problem in astrophysics (dark matter) interested us keenly in 1989, so we began a mountain altitude search for neutraCHAMPs at that time.

By early 1990, the problem of explaining cold fusion largely disappeared; however the possibility of neutraCHAMPs existing as dark matter remained somewhat viable. NeutraCHAMPs are also much easier to detect than the standard dark matter particle candidate (e.g., WIMPs), but not many experimenters have searched for neutraCHAMPs or put useful limits on the abundance of neutraCHAMPs as dark matter. Therefore, since neutraCHAMPs could exist and also be the dominant dark matter in our Galactic halo, we continued our neutraCHAMP search at mountain altitude.

In the fall of 1990, after a summer of calculations to determine the energy loss of neutraCHAMPs in detectors and in the atmosphere (see Appendix A), we decided that neutraCHAMPs would not likely be able to remain neutral in their flight through the atmosphere and therefore would probably be stopped in the atmosphere above our detectors at mountain altitude. Therefore, we decided to move our neutraCHAMP search to balloon altitude. This decision forced us to find the rare balloon payload with at least four levels of scintillation detectors for our neutraCHAMP search, and also willing and flexible collaborators. Fortunately, the IMAX collaboration had a balloon flight planned for the summer of 1991 which had the requisite four scintillation detectors; the IMAX collaborators were also more than willing to add our dark matter particle search experiment to their cosmic ray astrophysics program for antiprotons and light nuclei[86].

With the then upcoming flight opportunity for our neutraCHAMP search on board IMAX, we soon realized that we would be able to perform an unprecedented

search for *any* supermassive dark matter particle candidate in an unexplored range of the joint parameter space of mass and energy loss (see Chapter 2). This work was unprecedented for several reasons. First and foremost, dark matter hunters have rarely searched for dark matter particles at balloon or satellite altitude. Second, when a search for dark matter particles at balloon or satellite altitude has usually been performed, the experimenters have been unable to reject the background with flux $\sim$ 1 $cm^{-2}s^{-1}sr^{-1}$ from ordinary cosmic rays, which deposit energies of $>$ 2 MeV/g/cm^2. Our search for Ionizing Massive Particles (IMPs) with a four-fold delayed coincidence between the four scintillation detectors stack[85] was the first dark matter particle search experiment flown at balloon altitude which could reject the cosmic ray background to a flux level of $\sim$ 10^{-5} $cm^{-2}s^{-1}sr^{-1}$ and have a relatively small energy-loss threshold ($\sim$ 3.5 MeV/g/cm^2) (see Chapter 3 for further discussion of the multiple detector time-of-flight background rejection technique).

We built a single electronic module to detect dark matter events with the existing IMAX scintillation detectors, and successfully tested the electronics with the IMAX detectors at the May 1991 integration in Las Cruces, New Mexico. In June 1991, after integration, the collaboration decided to postpone the flight planned for the summer of 1991, until the performance of the aerogel detectors could be improved. By January 1992, the IMAX flight was rescheduled for the summer of 1992. Our group in Arizona received further funding for our dark matter search on IMAX in February 1992. The IMAX collaboration had a successful detector integration at Las Cruces in March 1992. From April through June of 1992, the Arizona Group finalized the flight electronics to be flown on IMAX (see Chapter 4 for the circuit design), replacing the shift registers and the crystal oscillator with monostable univibrators[9]. In mid-June 1992, I transported our equipment (NIM and CAMAC crates, computer, etc.) by truck from Tucson, Arizona to Lynn Lake, Manitoba, Canada to the IMAX launch site.

We successfully tested prior to flight the IMAX detectors with our new dark

[9]This eliminated excess noise from the crystal oscillator seen in our electronics during integration, which prevented accurate measurement of the signal pulse-heights by our electronics.

matter electronic module, and at 21.36 hours CDST July 16, 1992, the IMAX payload was launched by NSBF[10] from Lynn Lake. The payload reached an altitude of about 120,000 feet (or equivalently, 5 g/cm^2) by 5.0 hours CDST July 17, 1992. We monitored the dark matter data from the IMAX flight (see Chapter 5) until the balloon was out of radio range of Lynn Lake at about 12.0 hours CDST July 17, 1992; we saw the unusual anomalous events in our dark matter data at that time, but did not have any immediate idea as to their nature. The winds in the upper atmosphere carried the IMAX balloon and its payload to the west, and the IMAX payload was 'cut-down'[11] above Peace River, Alberta, Canada at 23.5 hours CDST July 17, 1992.

The IMAX collaboration then recovered and dismantled the payload from Peace River, and the Arizona group recovered the dark matter electronic module from the payload, for post-flight calibration[12]. As discussed in Chapter 6, post-flight calibration of the module was completed by January 1993. A second calibration which quantified the temperature-dependence of the module was finished in October 1993. In the summer and fall of 1993 we performed a mountain altitude search for the anomalous events seen during the IMAX flight (see Chapter 8). In Chapters 7 and 9 of this dissertation, we present IMP search data analysis and the upper limits on the IMP flux which were derived from the IMAX flight data. As discussed in Chapter 9, these upper limits effectively 'close' much of a window in IMP parameter space which was described in Chapter 2. Unfortunately, we are still uncertain of the precise nature of the anomalous events, as described in Chapters 5, 6 and Appendix B; but the existence of the anomalous events does not negate our IMP flux upper limits.

[10] the National Scientific Ballooning Facility

[11] The helium in the balloon was partially released by radio command to lower the payload's altitude, then the payload was released from the balloon by radio command, and finally the payload parachuted into a swamp.

[12] so as to avoid possible loss or damage during handling/shipping after flight

CHAPTER 2

IMP PROPAGATION THROUGH MATTER AND PREVIOUS CONSTRAINTS UPON THE EXISTENCE OF IMPS

Without an accurate theory of IMP interactions with matter, we cannot estimate the detectable IMP flux beneath a given thickness of atmosphere with a given configuration of detectors. Each hypothetical form of an IMP will have different possible interactions in the atmosphere, the different interactions basically depending either upon possible IMP compositeness or upon the different possible IMP charges. Therefore, we enumerate the properties of different IMP candidates so that we can later use our experimental IMP search results to constrain the parameter space of each type of IMP. During our enumeration of IMP candidates and their properties, we will tabulate the previous constraints upon IMPs within a multidimensional parameter space. For later reference, we also include a section discussing the response of scintillation detectors to slow ($\beta \sim 10^{-3}$) particles.

2.1 SIMPs

A strongly-interacting massive particle (SIMP) [45][46] is a supermassive particle which is electrically neutral, but carries the (short-range) strong charge, and has no compositeness evident at halo velocities ($\beta \sim 10^{-3}$). A SIMP can be considered similar to a supermassive neutron. SIMPs form a sub-class of ionizing massive particles (IMPs). SIMP/nucleus interactions can be characterized by a single parameter, the elastic scattering cross-section; while IMP/nucleus interactions may be both elastic and inelastic (e.g. neutraCHAMPs).

Starkman, Gould, Esmailzadeh and Dimopoulos [47] have studied the mass and scattering cross-section parameter space for SIMPs. By tabulating the regions of sensitivity for various cosmic ray experiments and dark matter searches, they have found a few 'holes' in parameter space where no effective constraints can be placed on the hypothesis that SIMPs are the dominant cold dark matter (CDM). They parametrize the energy loss of a SIMP travelling through normal material as:

$$\frac{dE}{dx} = -\sum_A n_A \sigma_A \left(\frac{m_{red}(A)^2}{m_A} \right) v^2 , \tag{2.10}$$

where n_A is the isotope number density, σ_A is the SIMP/nucleus energy-transfer cross-section and m_A is the isotope mass. $m_{red}(A)$ is the reduced mass of the isotope-SIMP system, with relative velocity, v. The quantity $m_{red}(A)^2 v^2 / m_A$ is the average energy transfer per collision assuming isotropic scattering. From this energy loss in a given material, the SIMP energy degrades as:

$$E(x) = E(0) \exp\left(-\frac{2\sigma_p}{M_x} \mathcal{F} x \right) , \tag{2.11}$$

where σ_p is the SIMP energy-transfer cross-section on protons and

$$\mathcal{F} = \sum_A f_A \left(\frac{m_{red}}{m_A} \right)^2 \frac{\sigma_A}{\sigma_p} , \tag{2.12}$$

where f_A is the mass fraction in the material of a given isotope with atomic mass A.

2.1.1 Constraints upon SIMP Parameter Space

Starkman *et al.* consider experiments performed with the main cosmic ray telescope on Pioneer 11, a large area plastic-etch detector flown and retrieved from Skylab, deep underground germanium double-beta decay spectrometers, and balloon-borne silicon detectors. After making our own minor reinterpretion of these experiments in the same manner as Starkman *et al.*, we plot these results in Figure 2.1, where M_x is the SIMP mass, σ is the elastic energy transfer cross-section, and the gray-shading represents the maximum SIMP fraction of the halo matter allowed, f_d. Note the significant 'hole' in

parameter space, centered at $M \sim 10^8$ GeV and $\sigma \sim 10^{-20}$ cm^2, where SIMPs are unconstrained as the dominant cold dark matter component of the Galactic halo.

We will use the same basic assumptions as Starkman *et al.*, namely the energy degradation from Equations 2.11-2.12, a mid-range flux from Equation 1.2

$$\Phi = 1.8 \text{ cm}^{-2}\text{s}^{-1}\text{sr}^{-1} \left(\frac{10^6 \text{ GeV}}{m_x} \right), \tag{2.13}$$

and that the typical speed of the SIMPs is $v \sim 10^{-3}c$. The only differences between our interpretations of the SIMP parameter space and the Starkman *et al.* interpretation are:

- The Starkman interpretation of SIMP parameter space consists of determining those regions of the joint mass and elastic cross-section parameter space where SIMPs cannot be the dominant Galactic halo dark matter. We analyze the SIMP parameter space to include three parameters: mass, elastic cross-section, *and* halo dark matter fraction, f_d. For the regions of parameter space constrained by Starkman *et al.*, the parameter $f_d \leq 1$.

- The Starkman interpretation of the cosmic ray experiment aboard Pioneer 11 did not include the ~ 1 mil thick mylar shield above the top detector. This will prevent any SIMP with a sufficiently high cross-section-to-mass ratio from reaching the top detector.

- We have included the unpublished results of a similar cosmic ray experiment on board the IMP 7 satellite [97], which have less triggering requirements and are therefore easier to interpret than the Pioneer 11 results. These IMP 7 results better constrain SIMPs than the Pioneer 11 results.

- The graphs in the Starkman interpretation have an error in the Skylab Plastic Etch Experiment: excluding to the left rather than to the right of the diagonal line. We also fully trust this experiment, so we include the whole exposure. Also, light cosmic rays would not cause enough damage to the plastic etch detectors to be detectable, as suggested by Starkman *et al.*.

- We include search experiments by Barish *et al.*[90], Kajino *et al.*[91], Orito *et al.*[115], Bacci *et al.*[116], and new results from Caldwell *et al.*[37].
- We do not put as much weight in the mini-blackhole argument as do Starkman *et al.*, so we plot it (Figures 2.3 and 2.4) and discuss it separately.

As an example, we will discuss the constraints on SIMPs from the monopole search performed by Barish *et al.*[90]. The minumum detectable SIMP energy loss in their plastic scintillation detectors was:

$$\frac{dE}{dx}\left(\beta = 10^{-3}, \text{SIMP}\right) \sim \frac{0.03}{0.006}\, 0.33 \frac{dE}{dx}\left(\beta = 1, \mu\right) = 1.65 \frac{dE}{dx}\left(\beta = 1, \mu\right), \tag{2.14}$$

where we have used the relative efficiencies of ionization as determined in Section 2.6, and the ionization threshold of $I_{thr} = 0.33 I_{\beta=1,\mu}$, as determined by Barish *et al.*[90]. From this minimum detectable energy loss, we compute the minimum energy-transport cross-section for which their constraints are applicable:

$$\sigma \sim \frac{\epsilon}{\beta^2}\frac{dE}{dx} = \frac{1.78 \times 10^{-27}\ \text{g/MeV/c}^2}{(10^{-3})^2}\left(1.65 \times 2.0\ \text{MeV/g/cm}^2\right) = 5.9 \times 10^{-21}\ \text{cm}^2. \tag{2.15}$$

This lower bound on their detectable SIMP cross-section is visible as the lower edge of the 'Monopole Search' triangle in Figure 2.1. The diagonal upper edge of this triangle is computed from the constraint that SIMPs not lose significant velocity while traveling through the 1000 g/cm^2 of atmosphere en route to the detectors at sea-level. From Equation 2.11, we can follow Ref. [47] and compute:

$$\begin{aligned}\left(\frac{\sigma}{m_x}\right)_{\max} &= \frac{\epsilon}{\mathcal{F}x}\ln\frac{\beta_0}{\beta_{\min}} \sim \frac{1.78\times10^{-24}\ \text{g/GeV}}{1.0\times1000\ \text{g/cm}^2}\ln\left(\frac{10^{-3}}{2.7\times10^{-4}}\right) \\ &\sim 2.3\times10^{-27}\text{cm}^2/\text{GeV},\end{aligned} \tag{2.16}$$

where $\beta_{\min} = 2.7 \times 10^{-4}$ is from Ref. [90], and we have unrealistically assumed for simplicity that all nuclei in the atmosphere have the same cross-sections with SIMPs, or equivalently, $\mathcal{F} = 1$ (in Figure 9.46, we relax this assumption). Lastly, we compute the upper limit on the SIMP mass fraction of the halo as a function of SIMP mass (shown in gray-shades in Figure 2.1), assuming the flux in Equation 2.13:

$$f_d|_{\max} = \frac{\Phi_{\max}}{\Phi} = \frac{4.7 \times 10^{-12}\ \text{cm}^{-2}\text{s}^{-1}\text{sr}^{-1}}{1.8\ \text{cm}^{-2}\text{s}^{-1}\text{sr}^{-1}\frac{10^6 GeV}{m_x}} = \frac{m_x}{3.8 \times 10^{17}\ \text{GeV}}. \tag{2.17}$$

Note that when $m_x > 3.8 \times 10^{17}$ GeV, then the experiment by Barish *et al.* no longer constrains SIMPs as objects in the dark matter halo since $f_d > 1$. Also, the lines defined by Equations 2.15 and 2.16 intersect at $m_x = 2.6 \times 10^6$ GeV, where $f_d(\max) = 3.8 \times 10^{-7}$. This is a significant constraint upon the halo dark matter SIMP flux.

The right-triangular shape and the parallel, vertical stripes of gray-shading (for f_d) are common to many of the experimental constraints shown in Figure 2.1. However, any experiment which places different flux limits corresponding to varying energy thresholds will have a non-triangular shape, with non-vertical stripes. Also, when individual nuclear recoils are detectable, then the constrained region will have diagonal stripes of f_d gray-shading, as in the solid state detectors' results[51][61][116].

This behavior of the stripes of the f_d gray shading is easily derivable from the work by Starkman *et al.*[47]. For single nuclear recoil events, the expected event rate is $f_d \sigma n / m_x$, where f_d is the IMP halo dark matter mass fraction and n is the number of active nuclei in the detector. When we equate this expected dark matter event rate with the measured background in their detector (which is just a number), we find that f_d is inversely proportional to σ / m_x, which results in diagonal stripes in the f_d gray-shading. For IMP events with multiple recoils, the expected dark matter event rate is $f_d A \Delta\Omega(\sigma, m_x)/m_x$, where A is the area of the detector and $\Delta\Omega(\sigma, m_x)$ is the amount of solid-angle that contains IMPs which can penetrate the atmospheric/earth overburden and still maintain detectable velocities. If this solid-angle varies slowly with σ and m_x in the region of interest, then we can take it as a constant. Now, when we set the expected DM rate equal to the background, we find that f_d is proportional to m_x – the σ dependence has dropped out, and we have vertical stripes of f_d gray shading.

2.1.2 SIMP Constraints from Miniature Black Hole Formation and Subsequent Neutron Star Cannibalization

Starkman *et al.* elaborate upon arguments by Gould *et al.*[66] and Goldman & Nussinov [68] which show that for a wide-range of SIMP masses and cross-sections, SIMPs cannot

exist in any abundance because otherwise they would collect at the center of every neutron star, and then form a mini-blackhole (MBH) $M \sim 10^{-12} M_{\odot}$ (the order of an asteroid mass worth of SIMPs), which would subsequently cannibalize the neutron star. Since we know neutron stars exist and are long lived[88], then SIMPs cannot be very abundant within a very broad range of masses and cross-sections (see Figures 2.3 and 2.4). However, we believe that the SIMP/MBH argument is very model-dependent [68] since we can easily envision a SIMP model with SIMPs having enough pressure on the quantum scale to offset the gravitational pressure and prevent formation of the mini-blackhole. For example, if the SIMPs are not elementary particles, but composed of many elementary fermions, as might occur in strange quark nuggets, and if these elementary fermions have a mass much less than $\sim 10^8$ GeV[68], then the accreted mass of SIMPs necessary to form a black hole might be $\sim M_{\odot}$ (strange stars might exist with $\sim M_{\odot}$[101]), rather than $\sim 10^{-12} M_{\odot}$. This amount of accretion is impossible, so that this MBH argument fails to constrain *all* different types of SIMPs as dark matter.

Nonetheless, the MBH argument does constrain SIMPs if the SIMPs are elementary particles, especially if the SIMPs are fermions[68][47]. By an extension of the arguments given in References [68], [66] and [47], we compute the maximum SIMP fraction by mass of the Galactic halo, f_d, as a function of m_x and σ. We summarize our results in Figures 2.3 and 2.4, where there are two different regions, as discussed in the figure captions.

2.1.3 Other Astrophysical Constraints upon SIMPs

We will discuss here the constraints shown in Figures 2.1 and 2.2, as 'Galactic Halo Stability' and 'Interstellar Cloud Heating'. Chivukula *et al.*[67][47] investigated the effect of IMPs losing energy by collisions with atoms in hydrogen clouds in the Galaxy and consequently heating up the hydrogen clouds. These heated hydrogen clouds should

cool by emission of UV photons. By requiring that the cloud be in thermal equilibrium, the heating rate $\gamma_h \sim 10^6 f_d \sigma v^3 m_p/m_x$ should be less than or the same order of the observed cooling rate $\lambda = (8.1 \pm 4.8) \times 10^{-14}$ eV/s, and we derive that $f_d \leq 8 \times 10^{-24}$ cm^2/GeV(m_x/σ). Since this argument only applies for slowing rates σ/m_x *above* a certain threshold, 8×10^{-24} cm^2/GeV, the cloud-heating argument complements terrestial IMP detection experiments, where there inevitably is an overburden which demands that the slowing rate be *less* than a certain maximal value.

In a similar spirit, we take the stability of the galactic halo as an assumption in our model of dark matter. By requiring that the infall time of halo particles due to energy loss be much more than the Hubble time, Starkman *et al.*[47] find that $\sigma/m_x \leq 5 \times 10^{-24}$ cm^2/GeV, which applies for *arbitrarily small* f_d. Indeed, in the absurd case where the spherical dark matter halo consisted of only one particle, if that particle had a slowing rate in excess of this upper limit, then it would collapse into the Galactic disk during the Hubble time of 5 billion years, and there would be no more halo. Therefore, the halo-stability constrained region will only have only one gray-shade, which we will make black, here corresponding to no value of $f_d > 0$ allowed. Unfortunately, there are some caveats. First, if the IMPs have electrical or magnetic charge, then they may be able to be re-accelerated in the Galactic magnetic field, and if the rate of supernovae is high enough, then IMPs might be shock accelerated back into the halo. Second, the Galactic halo may be somewhat flattened already[27], possibly due to dissipation of energy by the dark matter objects. Therefore, due to these caveats, the maximum slowing rate determined by Starkman *et al.* might be too low, and our IMP parameter space not as well constrained. Therefore, due to these considerations, we also show the SIMP parameter space in Figure 2.2 without the constraints from the galactic halo stability argument; these constraints would apply without qualification to all SIMPs, regardless of their magnetic or electrical charge.

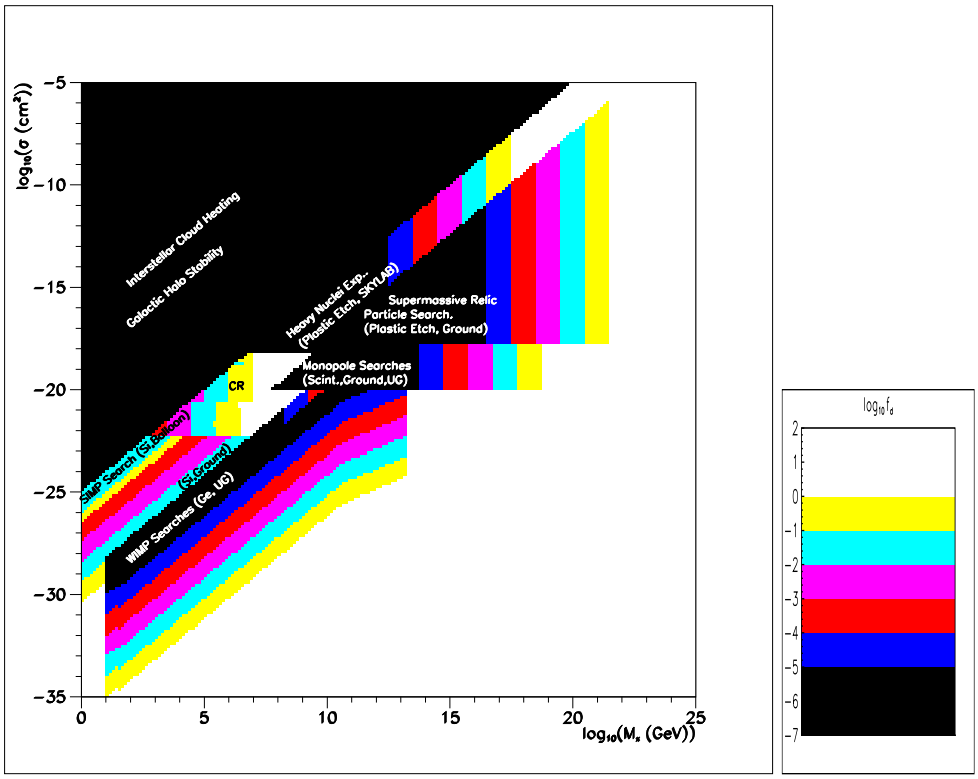

Figure 2.1: Pre-IMAX plot of neutral SIMP parameter space (mass, *elastic* cross-section, and maximum dark matter fraction). The maximum neutral SIMP halo matter fraction is shown in gray-shades as a function of SIMP mass and transport cross-section. The darkest gray regions (black) correspond to the maximum halo matter fraction being $f_{\rm dark} < 10^{-5}$, while the white region corresonds to $f_{\rm dark} > 1.0$ (unconstrained). The gray-scale increments logarithmically (see gray-scale chart). See Starkman *et al.*[47] or the following references for further details (**Interstellar Cloud Heating** [67], **Galactic Halo Stability** [47], **CR (Cosmic Ray Experiments)**[93][97], **SIMP Search (Si, Balloon, Ground)** [61], **Plastic Etch Experiments (Skylab, Ground)**[94][115], **Monopole Searches (Scint., Ground, UG (Underground))**[90][91][92][95][96], **WIMP Searches (Ge, UG (Underground))**[37][51][116][117]).

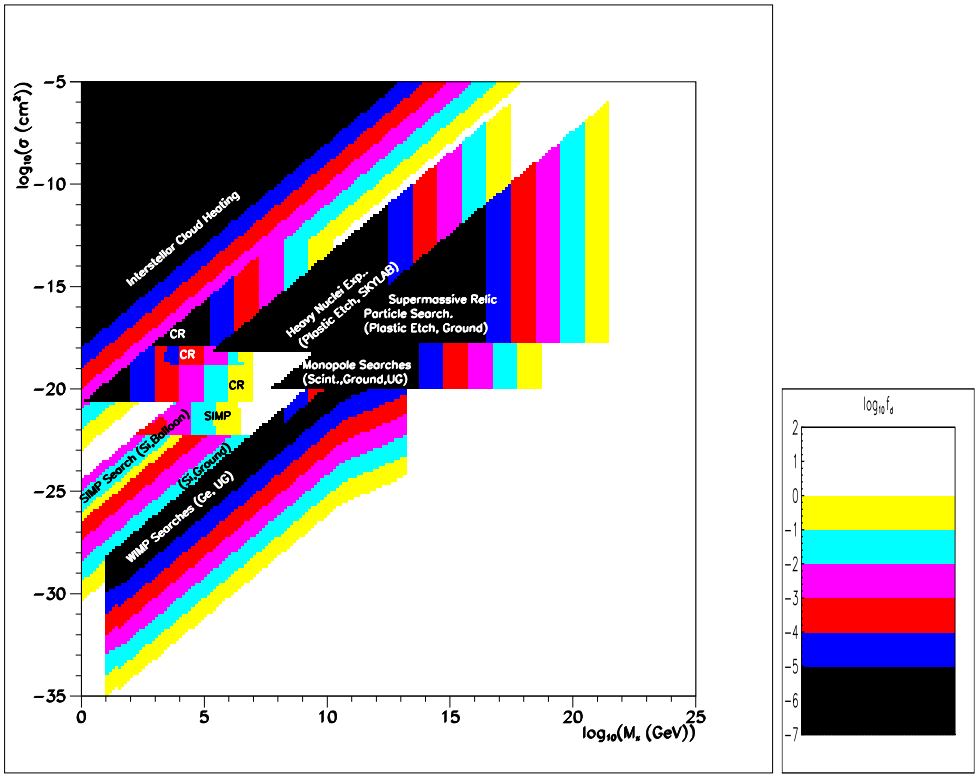

Figure 2.2: Pre-IMAX plot of charged IMP parameter space (mass, *elastic* cross-section, and maximum dark matter fraction). The upper limit on the charged IMP halo matter mass fraction is shown in gray-shades as a function of IMP mass and transport cross-section. The darkest gray regions (black) correspond to the maximum halo matter fraction being $f_{\rm dark} < 10^{-5}$, while the white region corresonds to $f_{\rm dark} > 1.0$ (unconstrained). The gray-scale increments logarithmically (see gray-scale chart). See Starkman *et al.*[47] or the following references for further details: (**Interstellar Cloud Heating** [67], **CR (Cosmic Ray Experiments)**[93][97], **SIMP Search (Si, Balloon, Ground)** [61], **Plastic Etch Experiments (Skylab, Ground)**[94][115], **Monopole Searches (Scint., Ground, UG (Underground))**[90][91][92][95][96], **WIMP Searches (Ge, UG (Underground))**[37][51][116][117]). We have not included galactic halo stability constraints due to the possible reacceleration of charged IMPs into the halo. We also do not include the constraints from chemical searches for charged IMPs or the constraints from various direct CHAMP searches.

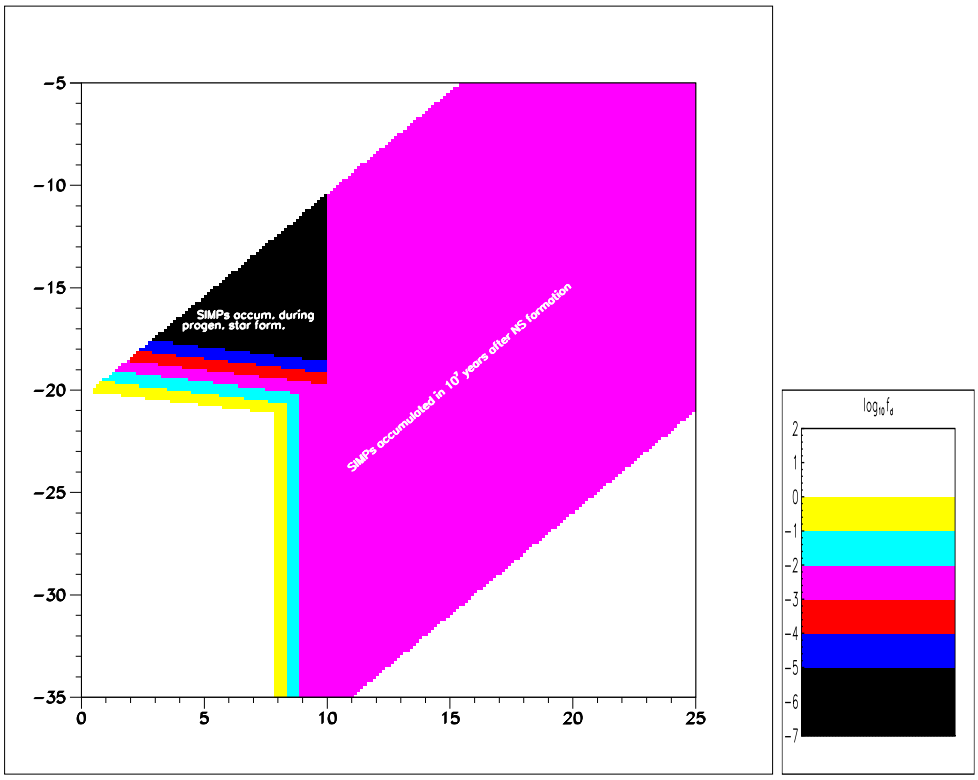

Figure 2.3: Model-dependent Neutron Star/Mini-Blackhole constraints on SIMP parameter space (mass, *elastic* cross-section, and maximum dark matter fraction). The maximum SIMP halo matter fraction is shown in grey-shades as a function of SIMP mass and elastic transport cross-section. For $M_x > 10^8$ GeV, for the constrained cross-sections, the neutron star collects enough SIMPs in $\sim 10^7$ years to spawn a mini-blackhole at its center. For the region which constrains $M_x < 10^{10}$ GeV, the SIMPs are accumulated during the collapse of the protostellar hydrogen cloud, and after the neutron star is born, the SIMPs form the mini-blackhole which devours the neutron star in about 10 years. The accumulation during collapse MBH argument and the accumulation after collapse argument both are affected by the requirement that the mini-blackhole be massive enough to accrete the neutron star, otherwise evaporating by Hawking radiation. See Figure 2.1 and Refs. [47], [68], and [66] for further details.

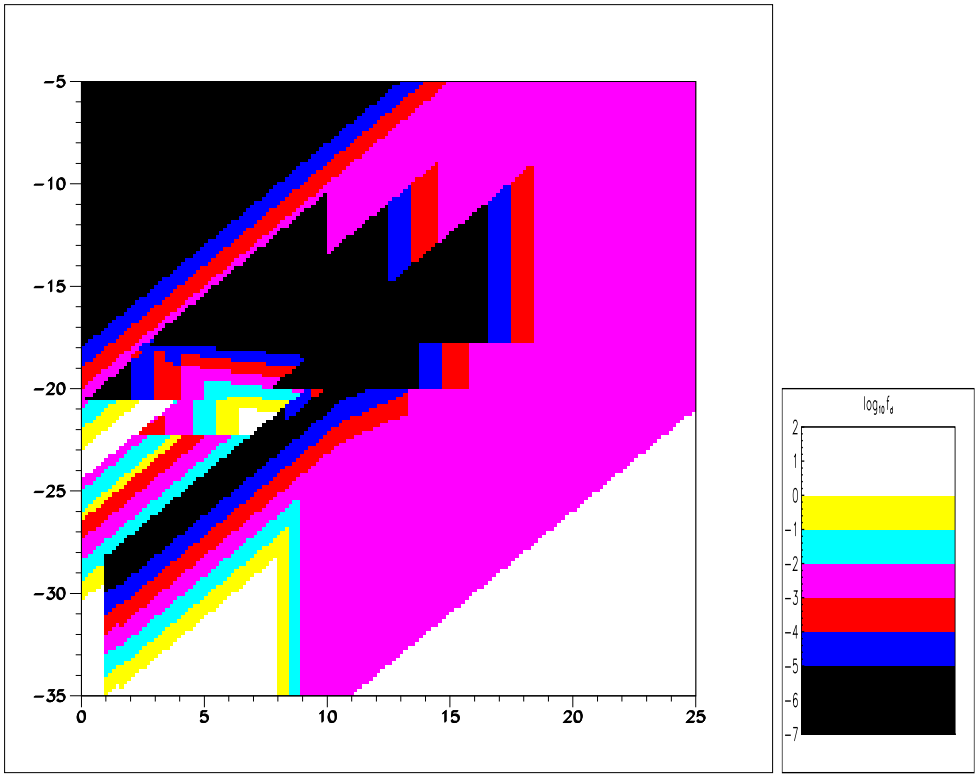

Figure 2.4: Pre-IMAX plot of SIMP parameter space (mass, *elastic* cross-section, and maximum dark matter fraction) also including the highly model-dependent limit from the possible accumulation of SIMPs and subsequent formation of mini-blackholes in neutron stars. The maximum SIMP halo matter fraction is shown in gray-shades as a function of SIMP mass and transport cross-section. See Figures 2.2 and 2.3 and Refs. [47], [68], and [66] for further details. We do not include the slightly model dependent galactic halo stability argument so that some of the other constraints will be more visible.

2.2 Un-neutralized CHAMPs

A charged-massive particle (CHAMP) is a hypothetical supermassive relic of the big-bang, which has unit electrical charge (± 1) and point-like properties at non-relativistic velocities[102]-[108]. DeRujula, Glashow, and Sarid (DGS)[42] popularized CHAMPs as a viable dark matter candidate. A CHAMP might additionally be strongly-charged, but otherwise CHAMPs can be regarded as a supermassive stable electron or as a supermassive stable proton, whose properties at $\beta \sim 10^{-3}$ depend primarily upon its electric charge and mass.

2.2.1 Positively-Charged CHAMPs

Since negatively-charged CHAMPs will quickly bind to a nucleus in the atmosphere or in a detector to become neutral or positively-charged, we only consider here the energy loss of positively-charged CHAMPs due to elastic Coulomb scattering. Lindhard *et al.*[109] have calculated the energy loss of slowly-moving ions in atomic collisions, which seems to agree with experiment down to ion velocities of $\beta \sim 10^{-3}$:

$$\frac{dE}{dx} \simeq \frac{(Z')^2}{A} P \left(\frac{8\beta}{\alpha} + \frac{\pi}{e} Z^{2/3} \right) , \tag{2.18}$$

where the coefficient $P = \pi(\hbar c)^2/\epsilon m_p m_e = 1433$ MeV/g/cm^2, the first term in the brackets is due to electronic collisions, the second term is due to nuclear collisions, Z and A are the charge and atomic mass of the target nucleus, $Z' = +1$ is the charge of the CHAMP, and $\epsilon \equiv 1.78 \times 10^{-27}$g/MeV is the conversion constant from mass to energy. At $\beta = 10^{-3}$, this gives an energy loss (primarily due to recoil nuclei) of ~ 500 MeV cm^2/g in nitrogen. More precise estimates[109] agree with the Born approximation, and give an energy loss of ~ 200 MeV cm^2/g. At this speed and with this energy loss, even CHAMPs of mass, $M_x \sim 1$ PeV $\equiv 10^6$ GeV, can only traverse ~ 2.5 g/cm^2 of material. Therefore, cosmic-ray searches for singly-charged CHAMPs (for $M_x < 2$ PeV) with $\beta \sim 10^{-3}$ must be relegated to satellite-borne experiments; balloon-borne experiments (at 5 g/cm^2) are only sensitive to $M_x > 2$ PeV. Ground-level cosmic ray searches would

only be sensitive to such CHAMPs if their mass is greater than $\sim$ 1000 PeV = 10^9 GeV. Ground-level sea water chemical searches for super-heavy H_2O (X^+HO) are now sensitive to $M_x < 10$ PeV[47][98][99][100].

2.2.2 Fractionally-Charged CHAMPs

Fractionally-charged CHAMPs of negative charge ($Z' = -q$, where $q < 1$) will hastily bind to a positively charged nucleus in the atmosphere, so we will only consider fractionally charged CHAMPs of positive charge. Charges of $+\frac{1}{3}$ and $+\frac{2}{3}$ are especially interesting because, if quarks can exist independently of other quarks, one might expect that they would have huge mass, much higher than the quark masses inferred from their bound states. If the free-quarks have masses which exceed $\sim$ 1 TeV, then the free-quarks could be the dark matter in the galactic halo if abundant enough, having velocities of $\sim 10^{-3}c$. Many searches have been performed for 'light' relativistic free-quarks in cosmic rays, but few have been made for heavy non-relativistic free-quarks[89][90][115].

The energy loss for fractionally-charged CHAMPs would be given by eq. 2.18, but reduced by a factor of $Z' \in (0, 1)$, giving $500(Z')^2$ MeV cm^2/g, or $200(Z')^2$ MeV cm^2/g in the more refined computation. For $Z' = 1/3$, a balloon-borne search for non-relativistic fractionally-charged particles might therefore be sensitive to masses $M_x > 0.2$ PeV.

2.2.3 Negative-CHAMP/Nucleus Conglomerates

Since a negatively-charged CHAMP combining with an ordinary positively-charged nucleus is energetically favored, and since the most abundant nucleus in the atmosphere is nitrogen, a typical CHAMP/nucleus conglomerate in air is $X^- - {}^{14}N$. This conglomerate is a tightly-bound ($Q = -3.5$ MeV) object, in which the binding energy is so large that the CHAMP is imprisoned within the confines of the nitrogen nucleus ($r_N = 2.9$ fm), harmonically oscillating in the uniform charge distribution of the nucleus. Therefore, the

CHAMP/nitrogen conglomerate appears as a supermassive carbon nucleus, with charge $Z' = +6$.

With large Z', the CHAMP/nucleus composite will have an energy loss of $\sim 18\,(Z'/6)^2$ GeV cm^2/g, where we have normalized the result to $Z' = 6$. Since these composites have MeV binding energies, at the non-relativistic velocities of interest these composites will not break apart. Therefore, the only important process is energy loss by elastic Coulomb scattering off other nuclei; the range for particles of 1 PeV mass and with a velocity of $v \sim 10^{-3}$ is approximately 0.07 g cm^{-2}. A balloon-borne search at 5 g cm^{-2} would only be sensitive to masses greater than ~ 72 PeV.

2.3 NeutraCHAMPs

A neutraCHAMP is a negatively-charged CHAMP bound to a proton, resulting in a *neutral* hydrogen-like atom with binding energy of $E_B = 25$ keV.[1] This structure is observable even at non-relativistic velocities, for example resulting in interactions in which the neutraCHAMP fragments into its components or in which the neutraCHAMP charge-exchanges its proton for another nucleus of higher mass or charge (wherein the neutraCHAMP possibly loses its neutrality). However, neutraCHAMPs may be able to propagate through the entire atmosphere without losing the neutralizing proton [42]. This possibility of detecting neutraCHAMPs at sea-level or even mountain-altitude was our original motivation for looking for IMPs as dark matter candidates. NeutraCHAMPs differ from SIMPs since they have a large inelastic scattering cross-section, $\sigma_{\rm inel}$.

The important neutraCHAMP interactions with matter (N represents an arbitrary nucleus) include:

[1] NeutraCHAMPs can be easily excited to the first excited state by an X-ray with energy 19 keV. This exotic Lyman-α absorption line and the deuterated Lyman-α line at 38 keV may be responsible for the pairs of absorption lines seen in X-ray bursts or other unexplained X-ray astrophysics phenomena[63][65][162]-[170].

$$
\begin{array}{rcccccl}
X^- p + N & \rightarrow & X^- p & + & N & & \text{(elastic)} \\
 & \rightarrow & X^- N & + & p & & \text{(exchange)} \\
 & \rightarrow & X^- & + & N & + \; p & \text{(dissociation)} \\
 & \rightarrow & (X^- p)^* & + & N & & \text{(excitation)} \\
 & \rightarrow & (X^- N)^* & + & p & & \text{(exchange-excitation)} \; .
\end{array}
$$

DGS have estimated the cross-sections for all these reactions except for the 'exchange-excitation' reaction. If this exchange-excitation reaction is large enough, then (as detailed below) neutraCHAMPs cannot be detected at ground or mountain altitudes.

2.3.1 Energy-loss by elastic scattering

By two different techniques, DGS find upper and lower bounds for the neutraCHAMP energy loss by elastic scattering in the r^{-4} polarization potential, due to the polarization induced by the nuclear Coulomb field in close encounters:

$$\frac{dE}{dx} \;\in\; [0.15, 32] \text{ MeV cm}^2 \text{ g}^{-1},$$

where an intermediate value is favored (maybe $\sim$2 MeV cm^2 g^{-1}). Since a CHAMP has an energy of:

$$E \;=\; 500 \text{ MeV} \left(\frac{M_x}{1 \text{ PeV}}\right) \left(\frac{v}{300 \text{ km s}^{-1}}\right)^2 ,$$

only those neutraCHAMPs with very large mass or relatively high velocity will not slow down and stop in the atmosphere before impinging on detectors at ground-level (1000 g cm^{-2}) or mountain altitude (700 g cm^{-2}). However, if inelastic processes are significant, then even these more massive neutraCHAMPs might not reach ground altitude. For a classical estimate of the stopping power, see Appendix A.

2.3.2 Dissociation of NeutraCHAMPs

DGS also calculate the cross-section for the neutraCHAMP 'dissociation' reaction, which is invariably followed by the rapid stopping of the remaining bare X^-. This reaction

is endothermic, requiring that $\beta > \alpha/\sqrt{A}$. For the velocities of interest, $\beta \sim 10^{-3}$, the atomic mass of the colliding nucleus needs to be ~ 40 for the dissociation reaction to proceed. Therefore, argon is the only element abundant (1%) in the atmosphere that has large enough A to strip a neutraCHAMP, and for velocities above the threshold velocity of 345 km/s, the cross-section for this reaction [42] amounts to ~ 20 kilobarns at velocities only 10% above the threshold velocity. Thus neutraCHAMPs which exceed this velocity break apart after traveling through only a few milligrams of the atmosphere, while neutraCHAMPs below 345 km/s are unaffected by dissociation.

2.3.3 Exchange Reactions

The neutraCHAMP 'exchange' reaction is exothermic, so no threshold velocity exists. Therefore, if this reaction has a low cross-section, then low-velocity neutraCHAMPs can 'survive' (remain neutral) after propagating through significant amounts of material. Otherwise, if the exchange cross-section is more than ~ 0.1 barn for velocities below 345 km/s, then together with the high cross-section for dissociation for velocities above 345 km/s, neutraCHAMPs (regardless of velocity or mass) *cannot* be detected at ground level or even mountain altitude. If the exchange cross-section exceeds ~ 10 barns, then the neutraCHAMPs cannot be detected as cosmic rays even at balloon altitude.

The difference of binding energies between a neutraCHAMP and a CHAMP-nucleus composite is large (e.g., for nitrogen, the CHAMP-nucleus composite has a binding energy of ~ 3.5 MeV, as compared to the neutraCHAMP binding energy of 0.025 MeV). Therefore, the exchange reaction is highly favored on energetic grounds alone. DGS calculate the cross-section for this reaction in the Born approximation, by computing the matrix element:

$$\mathcal{M} \approx \int\int d^3x\, d^3y\, \Psi_i^* \frac{Z\alpha}{y} \Psi_f \ ,$$

with $\Psi_i = e^{i\mathbf{k}\cdot\mathbf{x}}\phi_p(y)$, where $\phi_p(y)$ is a ground-state Coulomb wave function; and $\Psi_f = e^{i\mathbf{q}\cdot\mathbf{y}}\phi_N(x)$, where $\phi_N(x)$ is a ground-state harmonic oscillator wave function (for

nitrogen, the CHAMP-nucleus composite is so tightly bound, that the CHAMP is inside the nitrogen nucleus and sees a uniform nuclear charge distribution). With the matrix element as computed above, DGS estimate the exchange cross-section with nitrogen as:

$$\sigma_{\rm exchange} \sim 16 \text{ mb } \left(\frac{300 \text{ km/s}}{v}\right),$$

which is small enough to imply that low-velocity ($v < 345$ km/s) neutraCHAMPs can be detected at mountain altitude or even ground-level. The smallness of this exchange cross-section follows from the requirement that the exchange results in the ground-state of the CHAMP-nucleus composite.

We believe that the 'exchange-excitation' reaction, followed by a transition of the CHAMP-nucleus conglomerate to the ground state will make charge-exchange inevitable in a small amount of atmosphere:

$$X^- p + N \rightarrow (X^- N)^* + p \rightarrow X^- N + p + \gamma \quad \text{(indirect exchange)},$$

where the de-excitation photons are in the soft gamma-ray region, $E_\gamma \in [0.01, 3.5]\, MeV$ (for $N = {}^{14}N$). DGS do *not* compute the cross-section for the exchange-excitation reaction, but we believe that in analogy to the capture of negative mesons, there would be a high probability of capture into an $X^- N$ Bohr orbit with the same size as the $X^- p$ neutraCHAMP system, with a cross-section of $\sim \pi(30 \times 10^{-13} \text{ cm})^2 = 28$ barns (a much greater classical estimate might be derived from the critical impact parameter derived in Appendix A, $\pi(216 \text{ fm})^2 = 1500$ barns).

2.3.4 Summary

If the exchange-excitation cross-section is in the range, $\sigma_{ee} \in [0.1, 10]$ barns, then we should execute a balloon-borne experiment to search directly for unscathed neutraCHAMPs as cosmic rays with velocities below 345 km/s and an energy-loss of ~ 2 MeV cm^2/g. If the exchange-excitation cross-section is much lower than 0.1 barns, then a similar mountain- or ground-altitude search ought to be sufficient. If the exchange-excitation

cross-section is much higher than 10 barns, then a satellite- or rocket-borne experiment with thin detectors would be necessary to observe unscathed neutraCHAMPs.

2.4 Monopoles

Polyakov[52] and 't Hooft[53] showed in 1974 that should the forces of nature be 'unified' at high energies or temperatures, then magnetic monopoles should exist, with masses near the grand unified scale of $m_x \sim 10^{15}$ GeV. Such supermassive monopoles will catalyze proton decay through the Callan-Rubakov[54] mechanism, and will have the minimal Dirac magnetic charge of $g = 0.5e$, or multiples of this charge[55]. Due to their excessive mass, these $m_x = 10^{15}$ GeV monopoles would be able to penetrate the Earth and trigger proton decay detectors, despite their low velocity ($v \sim 10^{-3}c$) and high energy loss[56] ($dE/dx \sim 30(v/300 \text{ km/s})$ MeV/g/cm^2).

However, it is possible to construct grand unified theories with monopole masses as low as 10^4 GeV[57]. These light monopoles sometimes occur in non-SU(5) models and would not catalyze proton decay, and would have multiple magnetic charges[55]. Due to their multiple magnetic charges, such light monopoles might have ~ 100 MeV/g/cm^2 energy loss, and definitely would not be able to penetrate the atmosphere and would not be detectable at sea level. Such light monopoles warrant high altitude direct searches with solid state detectors or plastic scintillator detectors. However, due to a widely-accepted galactic magnetic field survival argument by Parker[20], such light monopoles ($m_x = 10^4$ GeV) are unlikely to contribute more than one part in 10^{17} of the galactic halo dark matter, and therefore the urgency of this search seems to fade.

2.5 Strange Quark Nuggets

Witten [58] has predicted that baryonic matter with roughly 1/3 each of up, down and strange quarks might be energetically more stable than normal baryonic matter. Such strange quark 'nuggets' (SQNs) are possible relics of the hypothetical quark-gluon plasma

phase of the early universe [48], and might also be produced and ejected in supernovae. These conglomerates of strangeness are likely to consist of many quarks, possibly ranging up to even sub-stellar masses ('strange' stars [101]), or down to the mass of an ordinary nucleus (e.g. the 'H'-particle, an object with 2 strange quarks, with a mass near 2 GeV [111]). Strange nuggets are also predicted to have a slight excess of up quarks (the quark fractions are $f_u \approx f_d \sim 1.2$ (by isospin symmetry), $f_s \sim 0.6$, $f_u + f_d + f_s \equiv 3$), which results in an object of high positive charge ($Q/A \sim 0.2$) when all the quark charges are added together [110]. For masses $M_x < 10^9$ PeV $= 1.5$ ng, the resulting cross-section (from the cloud of electrons surrounding the highly-charged strange nucleus) is:

$$\sigma \sim \pi(1\text{Å})^2 = 3.1 \times 10^{-16}\ \text{cm}^2\,,$$

which results in an energy loss of [48]:

$$\frac{dE}{dx} \sim 2 \times 10^5\ \text{MeV/g/cm}^2\,.$$

This tremendous energy-loss prohibits nuggets with masses smaller than $\sim$ 1000 PeV from reaching balloon altitude. Indeed, one might wonder if SQNs could have captured enough electrons during their formation and/or subsequent existence, so as to remain electrically neutral. The number of electrons required to neutralize a single SQN of mass $M = 10^7$ GeV is $\sim 2 \times 10^6$ [110]. If the SQN is *not* accompanied by a full cloud of electrons, then the cross-section for SQN interactions will be significantly reduced.

If stable strange quark nuggets exist, then they will likely populate the galactic halo at non-relativistic velocities ($\beta \sim 10^{-3}$). If the nuggets are not too massive (thereby rare) or too minor of a component of the dark halo matter, then they might be amenable to a direct particle search experiment [90][91][112].

2.5.1 Neutral Strange Quark Nuggets

If SQNs either have a mass $m_x > 10^{15}$ GeV or do not have a quark content asymmetry[2], then the interaction cross-section can be estimated geometrically as :

$$\sigma \sim \pi r^2 \sim \pi \left(\frac{3}{4\pi} \frac{m_x}{\rho} \right)^{\frac{2}{3}} = \left(\frac{m_x}{10^6 \text{ GeV}} \right)^{\frac{2}{3}} \times 10^{-22} \text{ cm}^2 ,$$

or equivalently:

$$\frac{dE}{dx} = 0.05 \left(\frac{m_x}{10^6 \text{ GeV}} \right)^{\frac{2}{3}} \text{ MeV/g/cm}^2 ,$$

where we have assumed a mean density for strange matter of $\rho \sim 1$ GeV/fm^3. By inspection of Figure 2.1, we find that for masses $M_x \in [10^6, 10^{11}]$ GeV, neutral strange quark nuggets (nSQNs) have not been well-constrained. The range-mass relation for nSQNs is:

$$R \sim 10^4 \text{ g/cm}^2 \left(\frac{m_x}{10^6 \text{ GeV}} \right)^{\frac{1}{3}} .$$

If the detectors are sensitive to very small signals, then ground-level searches for nSQNs are sensitive to $M_x > 1000$ GeV. Even the lightest neutral nSQNs ($M_x \sim 2$ GeV) can reach balloon altitude, but very sensitive detectors are needed [61].

If we use the density of ordinary matter ($\rho \sim 10^{23}$ GeV/cm$^3 = 10^{-16}$ GeV/fm^3), rather than the density of nuclear matter in Equation 2.5.1, we arrive at an estimate for the geometric cross-section of meteoroids which is $\sim 5 \times 10^{10}$ higher than the nSQN cross-section. We include this meteoroid result in Figure 2.5 for comparison purposes.

2.6 Response of Plastic Scintillation Detectors to Slow Particles

Ficenec *et al.*[118] measured the light yield L (in eV) of slow protons in plastic scintillator (NE-110) as a function of velocity, $\beta \in [2.5 \times 10^{-4}, 5 \times 10^{-3}]$. No previous measurements had been performed at these velocities[119][121]. We used the data from the experiment by Ficenec *et al.* to determine[3] the efficiency (dL/dE_p) for producing scintillation light

[2] so that the SQNs are electrically neutral

[3] by direct differentiation

with protons of energy E_p (produced by neutron recoil). We found that at velocities $\beta \in [6 \times 10^{-4}, 1.5 \times 10^{-3}]$, the efficiency is at a peak and is roughly constant:

$$\frac{dL}{dE_p} = 0.006 \pm 0.0015. \tag{2.19}$$

This recent result is roughly twice the efficiency (for $\beta \sim 10^{-3}$) that we obtained from the data from the experiment by Ahlen *et al.*[121]. At higher velocities, it has been shown that several different plastic scintillation materials give nearly the same light production efficiencies[122]. The scintillation plastics which we used in the IMAX experiment were Bicron BC-420, BC-400, BC-408, and BC-420, for detectors T1, S1, S2, and T2, respectively. These Bicron scintillators[123] all have approximately the same light production efficiency for relativistic particles (3%) as the Nuclear Enterprises NE-110 scintillator. We will also assume that the light production efficiency at low velocities is the same as determined from the experiment by Ficenec *et al.*, 0.6%.

From the $\sim 0.6\%$ efficiency of light production by proton recoils at low velocities, we can compute the the expected light production for IMPs in scintillator plastic, dL/dx:

$$\frac{dL}{dx} = \left(\frac{dL}{dE_C} + \frac{dL}{dE_p} + \frac{dL}{E_e} \right) \frac{dE}{dx} \approx \frac{dL}{dE_p} \frac{dE}{dx}, \tag{2.20}$$

where dE/dx is the energy loss by IMPs due to collisions with nuclei and electrons in the scintillation plastic. We conservatively assume (due to lack of measurements) that the light production is negligible for the recoils of carbon atoms[4] from IMP collisions, though these collisions might produce much more light than the proton collisions. At these velocities, $\beta \ll \alpha$, direct collisions between IMPs and electrons do not contribute much to the light production. We will often assume that the IMP energy transfer cross-section σ is independent of velocity for low velocities[47][48], or equivalently that the energy loss of IMPs is proportional to β^2:

$$\frac{dE}{dx}(\mathrm{MeV/g/cm^2}) = \frac{\sigma(\mathrm{cm^2})}{\epsilon} \beta^2, \tag{2.21}$$

where $\epsilon = 1.78 \times 10^{-27}$ g/MeV is the conversion factor from energy to mass. With this assumption and from the 0.6% light conversion efficiency, we can easily compute the

[4] in the scintillator hydrocarbons

light yield for slow-moving IMPs in plastic scintillators:

$$\frac{dL}{dx} = 0.006 \text{ MeV/g/cm}^2 \frac{\sigma}{1.78 \times 10^{-21} \text{cm}^2} \left(\frac{\beta}{10^{-3}} \right)^2 . \tag{2.22}$$

We can compare this to the light yield for minimum-ionizing ($\beta \sim 1$) particles of $dL/dx = 0.06$ MeV/g/cm^2, and we find that we only get signals larger than minimum-ionizing for IMPs with the highest velocities $\beta \sim 3.3 \times 10^{-3}$ and with $\sigma > 1.78 \times 10^{-20}$ cm^2. Fortunately, it is relatively easy to detect a long (100 ns) pulse of light from a low-velocity IMP passing through a 1-cm thick scintillation detector with total light yield a small fraction of the light yield from a minimum-ionizing particle. Therefore, plastic scintillators can be made sensitive to slow-moving IMPs with cross-sections ($\sigma \geq 10^{-20}$ cm^2), a region of parameter space which has not been fully constrained for IMPs as a dark matter candidate (e.g., the window in the parameter space of Figure 2.1 at $m_x \sim 10^7$ GeV and $\sigma \sim 10^{-20}$ cm^2). Therefore, since large-area ($A \geq 10^4$ cm^2) plastic scintillation detectors can by made without great expense, plastic scintillation detectors seem to be a logical choice to search for IMPs with fluxes less than 10^{-4} cm^{-2}s^{-1} and with cross-sections greater than 10^{-20} cm^2. Of course, for IMP masses near 10^7 GeV with these cross-sections, a balloon or satellite altitude experiment is required to detect slow-moving ($\beta \sim 10^{-3}$) IMPs since these IMPs significantly slow-down in the atmosphere.

2.7 Chapter Summary

In Figure 2.5, we summarize the different IMP candidates mentioned in this chapter. The IMPs that are least-constrained and amenable to our balloon-borne search are:

- SIMPs in a window of parameter space:

$$10^{-28} \text{ cm}^2/\text{GeV} < \sigma_{\text{el}}/M_x < 10^{-25} \text{ cm}^2/\text{GeV},$$

$$10^{-20} \text{ cm}^2 < \sigma_{\text{el}} < 10^{-18} \text{ cm}^2.$$

  Within this window, for masses $M > 10^6$ GeV, SIMPs are unconstrained by previous experiments as the dominant dark halo matter. However, for $M > 10^6$ GeV

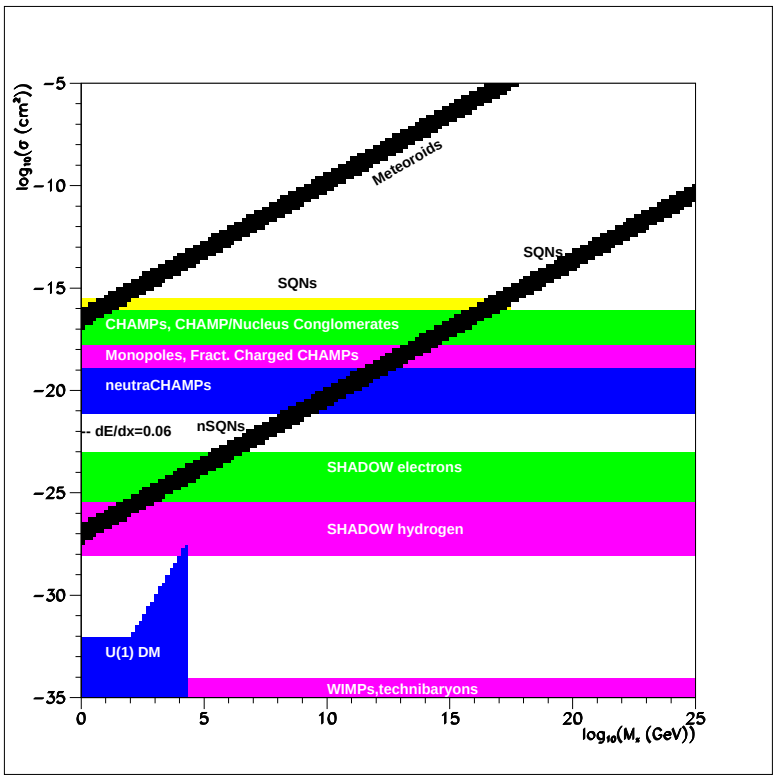

Figure 2.5: The joint mass and cross-section parameter space of different SIMP models. The different shades of gray represent a different model: SQN = strange quark nuggets; nSQN = neutral strange quark nuggets; monopoles; shadow matter[46]; WIMPs and technibaryons[113]; meteoroids; $U(1)'$ dark matter particles[114], CHAMPs, neutraCHAMPs, and CHAMP/Nucleus Conglomerates. The cross-sections referred to for all these particle dark matter candidates are the elastic energy-transport cross-section at $\beta \sim 10^{-3}$. We also indicate that $\sigma = 10^{-22}$ cm^2 corresponds to $dE/dx = 0.06$ MeV/g/cm^2.

SIMPs are constrained by the mini-blackhole argument to be only a minor component of the dark halo matter. Within the same window, for $M < 10^6$ GeV, the previous balloon-borne silicon detector experiment of Rich, Rocchia, and Spiro has a background which is low enough to constrain SIMPs to be a few percent of the dark halo matter.

- NeutraCHAMPs are not well constrained as halo matter, since their elastic scattering cross-section is small enough to lie in the same range as the window in SIMP parameter space mentioned above. NeutraCHAMPs also have an additional parameter to constrain, $\sigma_{\rm inel}$, the inelastic scattering cross-section (e.g. charge exchange), which makes neutraCHAMPs more difficult to constrain than the generic SIMP or the highly-ionizing bare CHAMP.

- Monopoles can also be better constrained by experiment in this same window. However the constraints from accepted astrophysical arguments are many orders-of-magnitude beyond the reach of an experimental search for monopole masses near 10^6 GeV.

- Neutral Strange Quark Nuggets of mass $M_x \sim 10^8$ GeV can be detected by our experiment, but have already been constrained by ground-based scintillation detector experiments [90][91]. A one day balloon flight can do little to further constrain neutral SQNs in this mass range. Also, the unconstrained region near $M_x \sim 10^6$ GeV should also be attainable from the ground, but detectors with a sensitivity to 2-3 nugget/nucleus collisions per g/cm^2 and with a background of less than ~ 0.1 cm^{-2}s^{-1}sr^{-1} would be necessary. The surface experiment of Rich, Rocchia, and Spiro had too high a background for this region[61][47]. The sea-level scintillation detector experiments[90][91] could not detect the expected signal, ~ 40 keV energy deposition per nugget per detector (their thresholds were ~ 6 MeV/g/cm^2[90] and ~ 1 MeV/g/cm^2[91]). The undergound WIMP detectors are too far underground to detect these nuggets, which would stop before reaching the detectors.

CHAPTER 3

T.O.F. TECHNIQUE TO DETECT ULTRA-SLOW IMPS

The time-of-flight method would easily detect slowly moving massive particles, as long as their collision cross-section is sufficient to produce scintillation signals, so we denote such particles as *ionizing* massive particles (IMPs). Accidental coincidences are the principal background to slow moving IMPs. No known particle is massive enough to simulate the passage of a slow IMP through a stack of several sufficiently thick scintillation counters.

With a stack of four ~ 1 cm thick scintillation detectors (Fig. 3.6), by measuring the time delay between hits in successive counters (see Figure 3.7), $T_{i,i+1}$, we can compute the velocity, $v_i = d_{i,i+1}/T_{i,i+1}$ between each successive pair of counters. If the velocity change, $\Delta v_{i,i+1} = v_{i+1} - v_i$, while traversing each interior counter is nearly zero, then a particle must have passed through the counter and deposited more than the minimal detectable energy, $\Delta E_{\rm thr}$, with very small change in momentum. Therefore, for small rates of slowing down[1],

$$\Delta v_{12} = \Delta v_{23} = \Delta v_{34} \approx 0 \tag{3.23}$$

is the obvious signature for an IMP passing through all four counters. For a particle of mass, $M \sim 1$ PeV, and velocity, $\beta \sim 0.001$, the kinetic energy is $T \sim 0.5$ GeV, and the momentum is $p \sim 1$ TeV/c. Therefore, for an energy loss of

$$\Delta E \sim \frac{dE}{dx}\,(\mathrm{THR}) \sim 3.5\ \mathrm{MeV/g/cm^2}\ \times\ 1.8\ \mathrm{g/cm^2} = 6.3\ \mathrm{MeV}, \tag{3.24}$$

the change in velocity is:

$$\frac{\Delta v}{v}\ \approx\ \frac{\Delta E}{2E}\ \sim\ 6 \times 10^{-3}. \tag{3.25}$$

[1]The IMPs must have a small energy loss (or energy-transport cross-section) compared to their mass

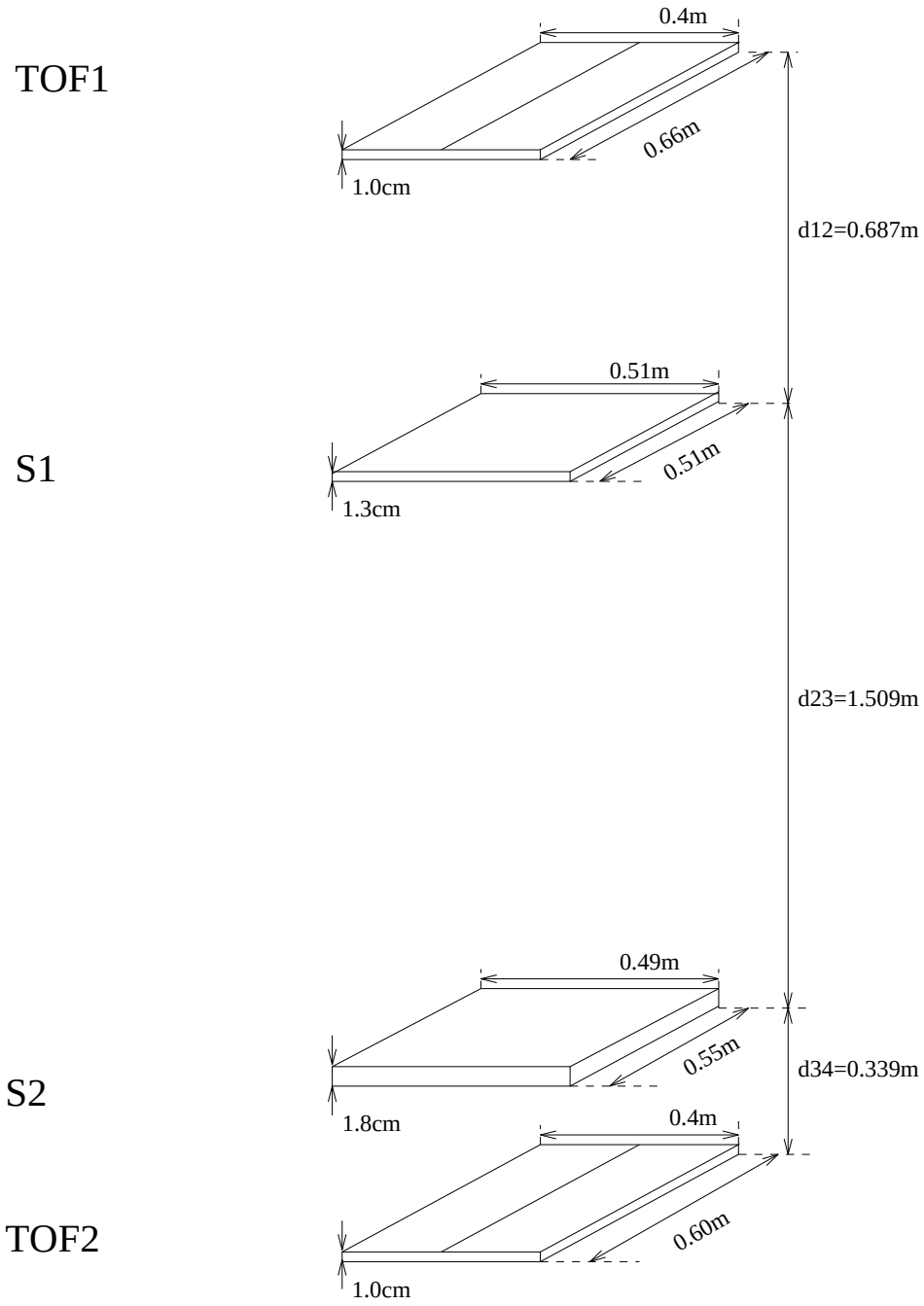

Figure 3.6: Diagram of IMAX Telescope, showing the positions and dimensions of the 4 scintillation detectors.

For lower masses or higher energy losses, the change in velocity would be larger. If the particle time-of-flight between a pair of counters is 5μs, then in order to have a measurable change in velocity, we need to be able to resolve time-of-flight differences smaller than 30 ns.

3.1 Delayed Coincidence Logic

A time-of-flight experiment requires a sequence of delayed coincidence logic gates. Each successive pair of counters needs to be able to sample the same range of velocity. For the unevenly spaced IMAX counters (see Figure 3.6), we show in Figure 3.7 the delayed gate arrangement designed to measure a velocity range of $v \in [100, 750]$ km/s, using the counter spacings from Figure 3.6. We expect a Maxwellian distribution of IMP velocities (with $\tilde{v} \sim 213$ km/s, cut-off by the galactic escape velocity $v_{\max} \sim 640$ km/s)[17][18]. Due to the small counter spacing between counters 3 & 4, and the anti-coincidence gate time for prompt pulses of 200 ns, we chose 750 km/s as the upper limit of the range for velocity measurement. We only include 3 counters in the coincidence, but we do measure the time delay T_{34}.

3.2 Estimate of Measurable Mass Range

The D-module registers overload pulses for $\Delta E > \Delta E_{\max}$ (see Table 6.8), where typically $\Delta E_{\max} \sim 40$ MeV. Since the velocity resolution, $f_v \equiv \sigma_v / v$, is of the order of 2% (see Section 6.2.2) and the minimum velocity measured is $v_{\min} \sim 100$ km/s, the D-module can measure a maximum mass of:

$$\begin{aligned} m_{x,\max} &\sim \frac{2\,(\Delta E_{2,\max} + \Delta E_{3,max})}{(v_1 - v_3)(v_1 + v_3)} \sim \frac{(\Delta E_{2,\max} + \Delta E_{3,\max})}{\sqrt{2} f_v \left(\frac{v_{\min}}{c}\right)^2} \\ &\sim 1.3 \times 10^8 \text{ GeV}, \end{aligned} \tag{3.26}$$

where $\Delta E_{2,\max} = 30.0 \times 1.3 = 39.0$ MeV and $\Delta E_{3,\max} = 57.4 \times 1.8 = 103$ MeV, and we have assumed that $(v_1 + v_3)_{\min} \approx 2 v_{\min}$ and $(v_1 - v_3)_{\min} \approx \sqrt{2}\sigma_v$. The D-module can

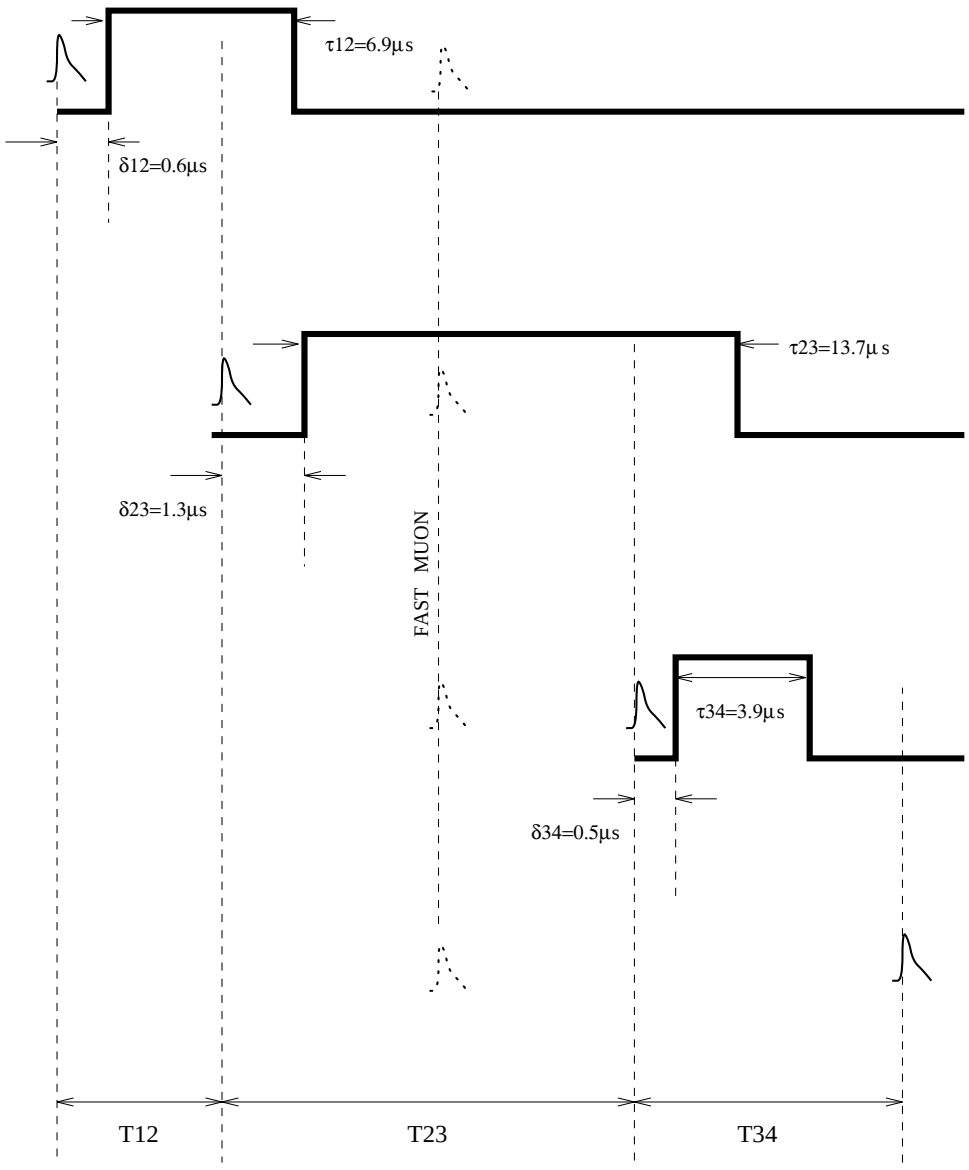

Figure 3.7: Delayed-coincidence timing diagram for 3 counters. For each successive gate, we indicate the gate-delay, $\delta_{i,i+1}$, and the gate-width, $\tau_{i,i+1}$. We also indicate the time delays, $T_{i,i+1}$, between intercounter pulses. The fourth counter is not included in the coincidence, but as long as there is a hit in the fourth counter during the τ_{34} gate, T_{34} is measured. If more than one counter has a hit within an anticoincidence gate of 200 ns, then all the participating counter pulses are vetoed, e.g., the indicated fast muon which went through all four detectors has been vetoed.

detect particles with masses above 1.3×10^8 GeV, but it cannot resolve their masses. Disregarding propagation through the atmosphere and requiring a 4-counter coincidence, the D-module can detect a particle with mass no less than:

$$\begin{aligned} m_{x,\min} &\sim \frac{2\left(\Delta E_{\mathrm{thr},2} + \Delta E_{\mathrm{thr},3}\right)}{\left(v_{12,\max}\right)^2 - \left(v_{34,\min}\right)^2} \\ &\sim 1200 \text{ GeV}, \end{aligned} \tag{3.27}$$

where we used the velocity limits $v_{12,\max} = 1150$ km/s and $v_{34,\min} = 76$ km/s, and the energy deposition thresholds $\Delta E_{\mathrm{thr},2} = 2.7$MeV and $\Delta E_{\mathrm{thr},3} = 6.3$MeV. Hence, the D-module's measurable mass range is $m_x \in [1200, 1.3 \times 10^8]$ GeV. We accounted for scintillation light saturation effects in the above calculation (see Sections 2.6 and 6.3). Also, if the IMP interacts in additional material between the scintillation detectors, amounting to ~ 8.5 g/cm^2 (see Table 6.1), the actual minimum detectable mass would be increased to ~ 3300 GeV, and the maximum measurable mass might also be enhanced.

3.3 TOF Background: Low-Mass Particles

Slow non-supermassive particles are not a background in our search. In a single 1 cm scintillator, slow non-supermassive charged particles with $\beta \sim 10^{-3}$ will lose enough energy to stop. With discriminator thresholds set at approximately one-fifth the minimum-ionizing signal for a 1 cm scintillator, the nuclear recoils from slow neutrons deposit too little energy (for $\beta_n = 0.003$, $\Delta E \leq 20$ keV) to be detected. If a slow neutron does not interact elastically, but gets absorbed in one counter[2], then the neutron will not be able to satisfy a 4-counter coincidence. Hence, with sufficiently thick counters and sufficiently high discriminator thresholds, neither charged nor neutral non-supermassive particles can be an IMP background.

[2] which could give a signal above the discriminator threshold

3.4 TOF Background: Electronic Noise

If each counter has the same separation from its neighbors, electronic noise might be a background in a time-of-flight search. A stray radiofrequency signal might give a signal at the same time delay for all three time delay measurements. Fortunately, in our search, each nearest-neighbor counter separation differs greatly from the others, ensuring different time delays between successive counters for a particle moving at uniform velocity, so that electronic noise probably does not cause false signals that satisfy our time-of-flight requirement.

3.5 TOF Background: Accidental Coincidences

Accidental coincidences are the main background that will consistently diminish the sensitivity of a time-of-flight search for slow supermassive particles in cosmic rays. The time-ordered accidental coincidence rate $A(n)$ for n counters is proportional to each counter's singles rate, R_i, and to the gate width, $\tau_{j-1,j}$, for each of the delayed coincidence gates:

$$\begin{aligned} A(n) &= \prod_{i=1}^{n} R_i \prod_{j=2}^{n} \tau_{j-1,j} \ , \qquad\qquad \text{for } n \geq 2 \\ &= R(R\tau)^{n-1} \qquad \text{if } \forall i,j : R_i = R \text{ and } \tau_{j-1,j} = \tau, \end{aligned}$$

where the customary factor of n has been suppressed due to the time-ordering requirement. Near the top of the atmosphere, the total particle vertical flux at solar minimum at Lynn Lake[3] is [126] ~ 0.25 cm^{-2}s^{-1}sr^{-1}. For a single scintillator size of 2500 cm^2, this corresponds to a count rate of nearly 2000 Hz. Since the discriminator thresholds are low, the singles rates at float might be $R \sim 4000$ Hz, due to additional PMT noise. If $R = 4000$ Hz and $\tau = 10\,\mu$s, for all counters, then $R\tau \approx 0.04$ and the accidental delayed

[3]These measurements were performed at Saskatoon, Saskatchewan, Canada, which is about 1000 km further south than Lynn Lake, Manitoba, Canada. The IMAX flight occured at solar minimum as did Komori *et al.*'s 1962 flight from Saskatoon. 'Solar minimum' is when the minimum in the solar magnetic activity occurs, so that the cosmic ray flux at the earth is at its maximum, due to a solar-magnetic cutoff occurring at a lower rigidity.

coincidence rate is

$$A(n) \approx 4000 \times (0.04)^{n-1} \text{ Hz},$$

which gives $A(4) \sim 0.26$ Hz. With a total 4-counter solid angle of $\Delta\Omega \sim 100$ cm^{2}sr, a 4-counter delayed-coincidence experiment would therefore be sensitive to fluxes greater than:

$$\Phi_{\text{IMP}} \sim \frac{A(4)}{\Delta\Omega} \sim 10^{-3} \text{ cm}^{-2}\text{s}^{-1}\text{sr}^{-1}.$$

If TDCs measure the actual time-delays between hits in successive counters with a timing resolution of ~ 50 ns, then the velocity resolution is typically:

$$f_v \equiv \sigma_v / v \sim 50 \text{ ns}/5\,\mu\text{s} = 0.01,$$

where we have assumed that the fractional error of the detector spacing is negligible, and have taken a typical time delay of 5 μs. Then the accidental rate of IMP-like events that satisfy the time-of-flight requirement for n detectors will be:

$$A_{\text{TOF}}(n) \sim nA(n) \times (f_v)^{n-1},$$

where we have assumed that the velocity resolution is the same for each of the $n-1$ detector pairs, and the factor of n is the customary prefactor for an accidental rate calculation for n measurements. For 4 detectors, and with a velocity resolution of 1%, as determined above, we compute from Eq. 3.5 that $A_{\text{TOF}}(4) \sim 10^{-4}$ Hz, which corresponds to ~ 4 accidental events in a 10 hour balloon flight. Thus, the time-of-flight method has a minimum detectable flux of

$$\Phi_{\text{IMP,min}} \sim 3 \times 10^{-6} \text{ cm}^{-2}\text{s}^{-1}\text{sr}^{-1} \tag{3.28}$$

($\Phi_{\text{IMP,min}}$ corresponds to detecting about 10 events in a 10 hour flight).

The TOF method does not need x-y spatial information to reject accidentals, so we do not need to analyze the volumes of data that might result from multi-wire proportional chambers (MWPCs) or drift chambers[4]. Not only can the 4 scintillation

[4]N.B. assuming MWPCs can operate on the $\sim 5\mu$s time scale necessary to detect slow particles.

counter time-of-flight method detect highly ionizing slow supermassive particles with high flux sensitivity, but the TOF method can also detect such particles that deposit energy at the minimum-ionizing level or lower, with a sensitivity that rivals other methods. In fact, for a detector with an energy loss threshold of $dE/dx \sim 1$ MeV/(g/cm^2), the background from relativistic cosmic rays is so high (~ 1 cm^{-2}s^{-1}sr^{-1}), that in order to make useful constraints on IMPs as minor components of the halo dark matter[5], we *must* use a delayed coincidence between *multiple* detectors to reject this background. We are unaware of any other technique that has sufficient capability to reject the background from relativistic cosmic rays in this parameter range (see Figures 2.1 and 2.2).

3.6 Expected Time-Delay Distributions from Accidental Coincidences

If we have two detectors (numbered 1 and 2) of uncorrelated pulses, and measure the time-delay $t_{12} = t_2 - t_1$ between a pulse which occured in detector 1 at time t_1 and in detector 2 at time $t_2 > t_1$, then the probability distribution $P(t_{12})$ will depend exponentially on the waiting-time t_{12}:

$$P(t_{12})\, dt_{12} = \frac{1}{\tau}\, e^{-t_{12}/\tau}\, dt_{12}, \tag{3.29}$$

where τ is the mean time-interval between pulses in detector 2, $\tau \equiv 1/R_2$, where R_2 is the single counting rate of source 2. For $t_{12} << \tau$, then $P(t_{12})$ is approximately a constant, independent of t_{12}. Therefore, a histogram of t_{12} (see Figure 5.11) should be uniform or 'flat' for time-delays t_{12} within a gate (see Figure 3.7) of width $\tau_{12} << \tau$. Any deviation from flatness is a signature of pulses that are correlated with each other, and should be reconciled. We should not regard a non-flat time-delay distribution as a positive signal for the existence of IMPs – the precise time-of-flight signature of a non-slowing down IMP will always be the primary IMP trigger. Nonetheless, correlated pulses will always baffle us, so I will discuss in Appendix B possible sources of correlated pulses between different detectors in our time-of-flight scheme to detect IMPs.

[5]for masses of order 10^6 GeV, and elastic cross-sections of order 10^{-20} cm^2

CHAPTER 4

EXPERIMENTAL SETUP

The GSFC/Caltech/Siegen/NMSU IMAX collaboration was preparing a balloon-borne experiment [86] with a payload that included four widely separated 1-2 cm thick $\sim$ 2400 cm^2 plastic scintillation detectors, when the Arizona group proposed adding electronics so that the flight could also search for slowly-moving IMP dark matter particles with only a 5 g/cm^2 overburden. The search, requiring a low-power, lightweight, low readout-rate electronics module, was agreed upon as an Arizona-IMAX collaboration. To accommodate these constraints, the Arizona group designed and constructed a special-purpose detector module (D-module) to discriminate the PMT pulses, to provide delayed coincidences, and to measure the time delays between hits in successive counters and the pulse heights in each counter. An Ortec ADC811 CAMAC module transferred the analog time delay and pulse height outputs of the D-Module to an onboard VAX for processing and telemetry. From each scintillation detector's[1] group of PMTs[2], IMAX provided a charge of $\sim$ 10 pC per minimum ionizing particle to the D-module. In order to avoid possible interchannel crosstalk in our D-module, we chose to set our discriminator thresholds at $\sim$ 2 pC. Therefore, for the 1 cm thick counters, the D-module's light detection threshold was $\Delta L_{\rm thr} \sim 0.4$ MeV. The resolution of the input charge measurements was better than 1 pC. The resolution of the time delay measurements for each channel was between 5 ns-80 ns, over a $0.4\,\mu{\rm s} - 15\,\mu{\rm s}$ range.

[1] TOF1=two BC-420 scint. paddles, S1=light integration box with BC-400 scint., S2=light integration box with BC-408 scint., TOF2=two BC-420 scint. paddles

[2] TOF1=four Hamamatsu R2803 PMTs, S1=four Hamamatsu R1307 PMTs, S2=twelve Hamamatsu R2490 PMTs, TOF2=four Hamamatsu R2803 PMTs

4.1 The IMAX Apparatus

The IMAX main experiment [86] included a superconducting magnet to bend the trajectories of relativistic cosmic rays, with hopes of accurately measuring the low-energy antiproton spectrum. Multi-wire proportional counters, drift chambers, aerogel and Teflon Čerenkov detectors, and scintillation detectors all helped to distinguish different types of particles (see Figure 4.8). An aluminum gondola of 1.08 g/cm^2 thickness, 3.67 m height and 1.52 m diameter enclosed the detectors and onboard VAX.

4.2 IMAX Flight Parameters

At 2.6 hours UT on July 17, 1992[3], the IMAX payload was launched on an NSBF[4] balloon from Lynn Lake, Manitoba, Canada (56.5° LAT, 101° LON). The balloon ascended slowly, reaching float $\sim$ 7.5 hours after launch (Fig. 4.9). Fortunately for the IMP search, the slow ascent gives us much valuable information as to a possible altitude dependence of a hypothetical IMP signal. For example, if we can measure the IMP velocity spectrum at each altitude, we might be able to estimate the velocity spectrum of IMPs (see Equation 1.3) before encountering the atmosphere, and perhaps even the IMP mass.

Soon after dawn ($\sim$ 10 hours UT), the IMAX payload finally reached float altitude, 5 g/cm^2, and remained at float for $\sim$ 15 hours. At 15.1 hours UT, there was a sudden onset of subtle electrical noise in the D-module in the IMAX payload, as evidenced by more RMS scatter and a slight upward shift in the D-module's time-delay pedestals. The internal payload temperature increased significantly during the flight, heating the electronics to above 50°C. At $\sim$ 2.5 hours UT, 7/18/92, the bending magnet was turned off, and the balloon operators commanded a partial release of helium from the balloon, which caused the payload to gradually descend to $\sim$ 8 g/cm^2, over a

[3]or equivalently 21.6 hours CDST (Central Daylight Savings Time) on July 16, 1992
[4]National Scientific Ballooning Facility

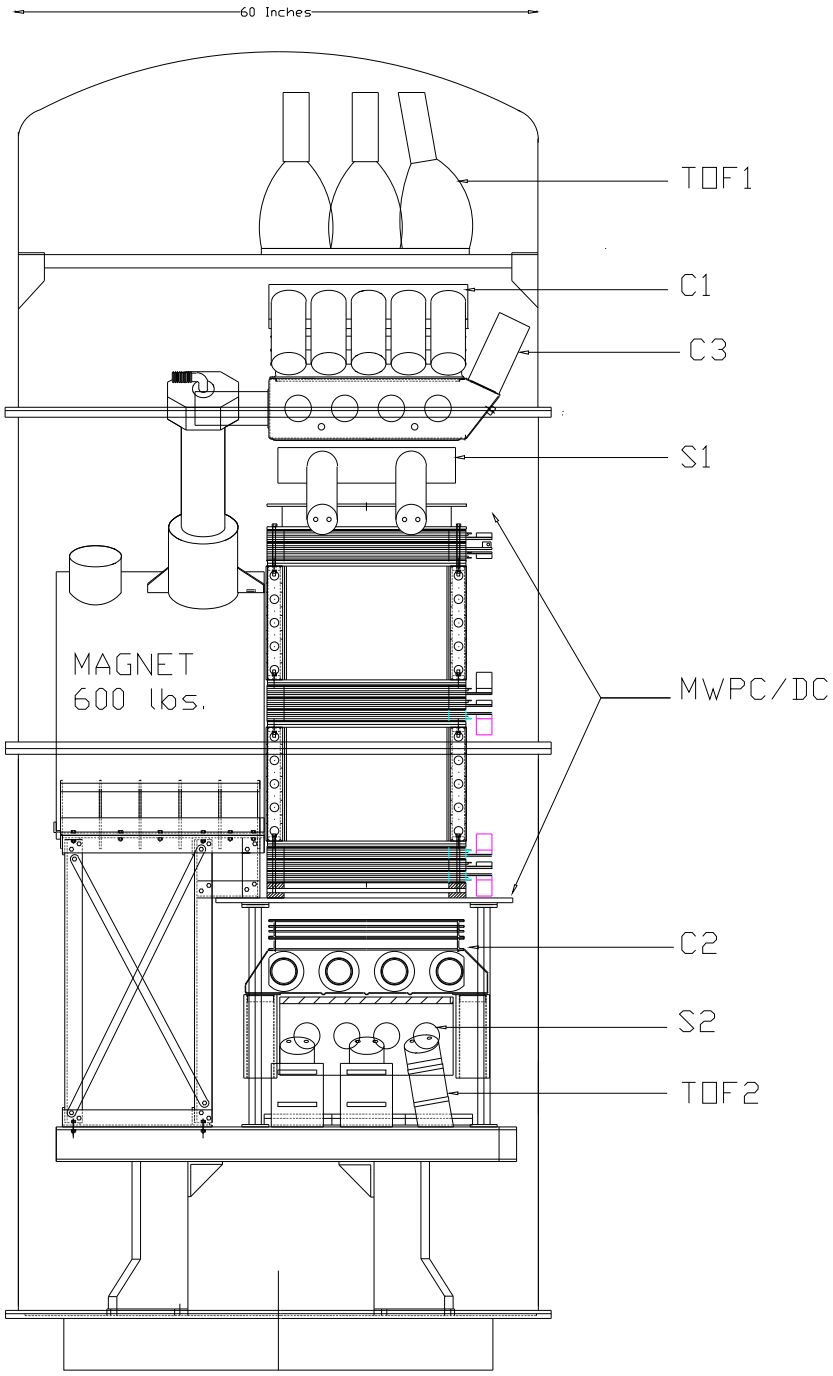

Figure 4.8: Diagram of IMAX payload, showing the positions of the 4 scintillation detectors, along with the Čerenkov detectors, multi-wire proportional chambers, drift chambers, and superconducting magnet.

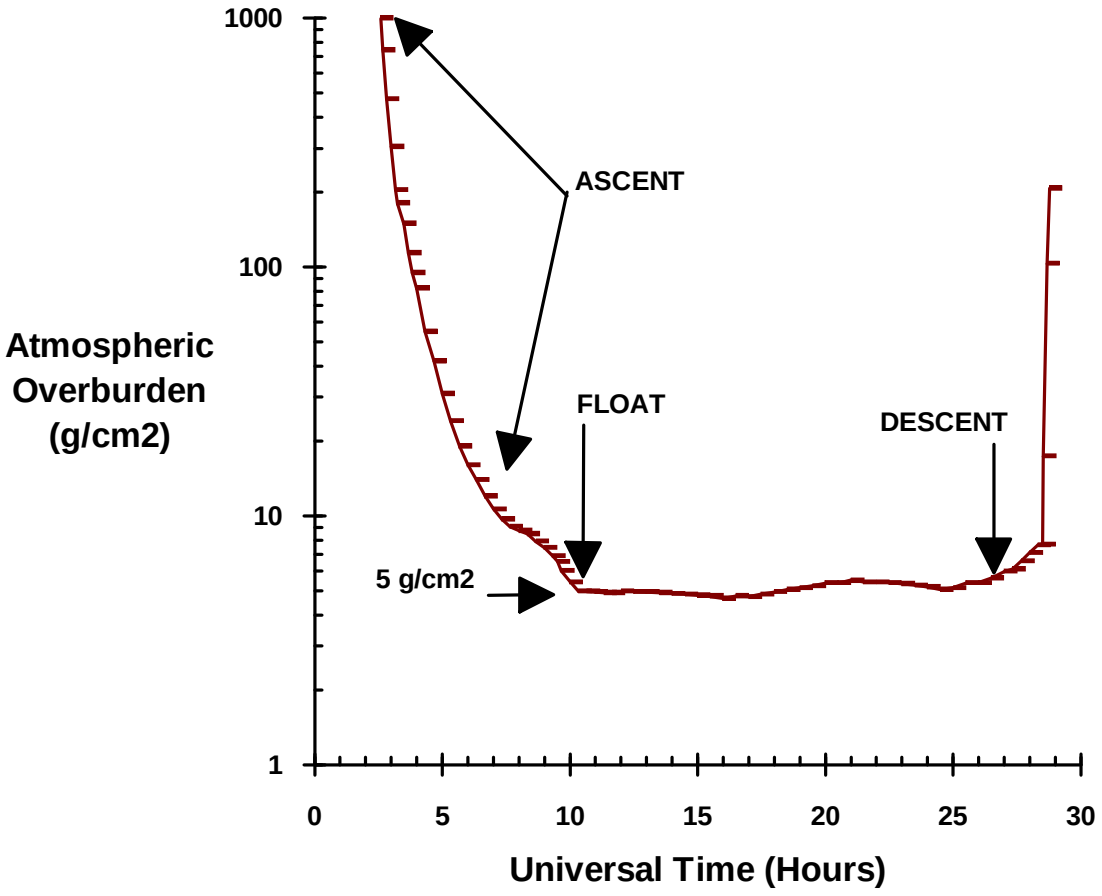

Figure 4.9: Atmospheric overburden versus universal time during the IMAX flight, July 17-18,1992 (0.0 hours UT = Midnight on 7/16/92). Arrows indicate the times when the payload reached float altitude, and when the payload began to descend. Note the rather long ascent.

2 hour period. At 4.5 hours UT, the balloon payload was cut-down, over Peace River, Alberta (56.6° LAT, 118° LON), and the payload parachuted to the ground.

4.3 D-Module Design/Implementation

We constructed the Slow Pulse Sequence Detector Module ('D-module', see Figure 4.10) as a CAMAC module on a perfboard with 'Speedwire' technology[5]. The D-module contained analog components and 44 integrated circuits (ICs) and consumed a moderate 7.4 Watts of power. The D-module included 4 separate charge-sensitive amplifiers (integration time $\sim$ 100 ns) and discriminators, each sensitive to $\sim$ 2 pC. The discriminators each had 300 ns wide pulses and also had a prompt 'anticoincidence' (or 'veto') with the other discriminators via a 100 ns strobe delayed by 100 ns from the rising edge of each counter's discriminator pulse. In the following discussion, by 'anticoincidenced discriminator pulse', we mean the 100 ns pulse which results when a single discriminator fires and none of the other discriminators fire within 200 ns afterwards (this is a four-fold exclusive-OR veto with a 200 ns gate width).

The first detector's anticoincidenced discriminator pulse triggers a delayed gate via two successive edge-triggered univibrators ('one-shots'), as in the top trace in Figure 3.2. This delayed gate was put in coincidence with the anticoincidenced discriminator signal from the second detector – such a 'two-fold' coincidence then triggers a second delayed gate, as in the middle trace in Figure 3.2. Likewise, a coincidence between the third detector's anticoincidenced discriminator pulse and the second delayed gate, is called a 'three-fold' coincidence, and triggers a third (prompt) gate. This 'three-fold' delayed coincidence also triggers the readout of the D-module by strobing the Ortec ADC, which samples the voltage levels of the D-module's Time-to-Analog Converters (TACs) for time-delay measurement and the D-module's Sample/Holds for pulse height

[5]Speedwire is an an advancement over the 'wire-wrap' technology and is manufactured by BICC-VERO Electronics, Hamden, Connecticut.

measurement. If an anticoincidenced discriminator pulse from the fourth detector occurs during the third gate, then the time delay T_{34} is measured – however a 'four-fold' coincidence is not required for readout of the D-module.

For readout of each event, we isolate capacitors with high-speed analog switches (sampling time $<$ 100 ns from trigger) to sample and store the pulse height of each detector's amplified pulse. These stored pulse heights (SH1, SH2, SH3, SH4) are later read by the Ortec ADC. The successive anticoincidenced discriminator pulses also trigger the separate starts and stops of 3 TACs (TAC12, TAC23, TAC34), which are implemented by switching charge-integrating operational-amplifiers ("OP-amps") with high speed analog switches. The sample and holds and the TACs have been calibrated on the ground as discussed in Chapter 6. The IMAX flight distributions of the time-delays measured by the TACs and the pulse heights measured by the sample and holds are shown in Chapter 5. There are separate scaler outputs (ECL) for the 4 anti-coincidenced discriminator rates and for the two-fold and three-fold delayed coincidence rates, which are measured and cleared once each second. These scaler rates are shown as a function of time during the flight in Appendix C.

The time-constant of each of the 5 univibrators is controlled by the values of a resistor and capacitor. The capacitor is slightly temperature dependent, giving different gate widths at different temperatures. Through the IMAX flight, this was less than a $\sim 1\%$ effect. Likewise, the time-delay measurement depended on the $\sim 1\%$ temperature stability of the integration capacitors, and therefore, the calibration of the temperature dependence of the D-module was necessary, as detailed in Section 6.2.1. All voltages were internally regulated, so the stability of the current sources for the TACs and Sample/Holds should not be a factor.

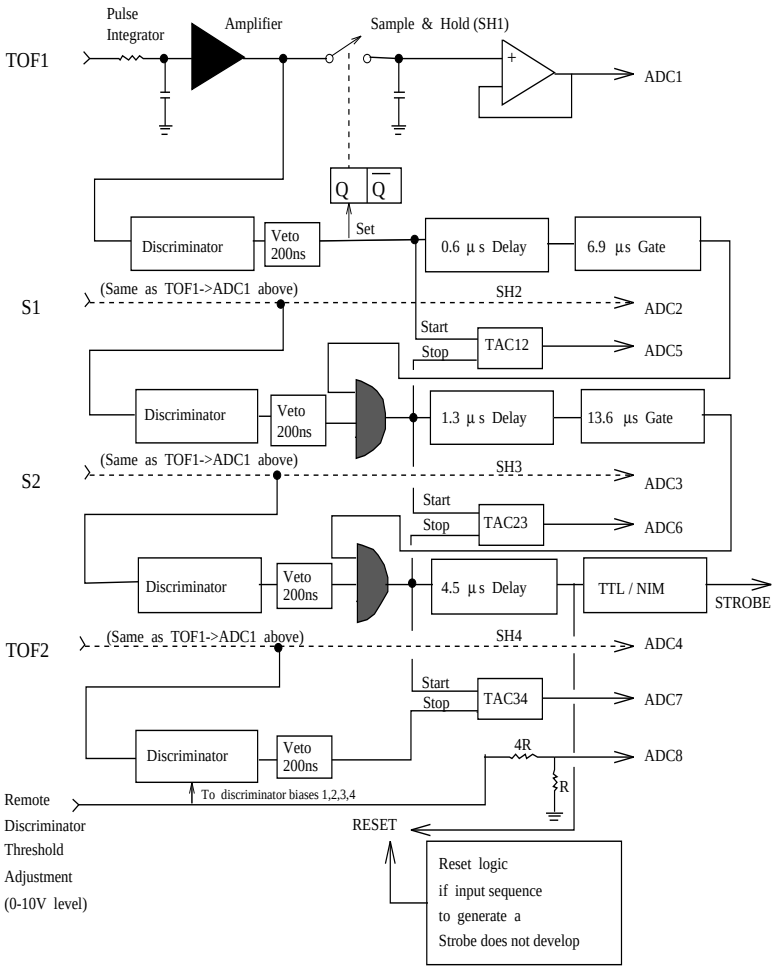

Figure 4.10: Logic Diagram of Slow Pulse Sequence Detector Module (D-Module), see text for details.

4.4 Flight Data Acquisition and Offline Analysis Software

The D-module triggered the Ortec ADC completely asynchronous from the IMAX main trigger at a rate of $\sim$ 4 Hz at float altitude (see Appendix C). Prior to flight we had arranged with the BBMF[6] to have the onboard VAX real-time operating system and the CAMAC crate controller card check the Ortec ADC every 0.25 seconds for a 'data-ready' signal. If the Ortec ADC has data ready, then the VAX/CAMAC system reads the eight 12-bit words from the Ortec ADC and stores these eight words along with a time stamp in a 48 word 'Dark Matter' frame. The Dark Matter frame is then placed in a short buffer with the 'Science' and 'Engineering' frames for FIFO radio telemetry to the ground-based receiving station[7]. A scalar module also measured the six D-module counting rates (4 singles rates, the double coincidence rate, and the triple coincidence rate), and recorded these rates in one of the Engineering data frames which was also telemetered to the ground receiving station. The NSBF telemetry system sent the IMAX data to the receiving stations at $\sim$ 130,000 bps, and the data was stored on analog tapes at the receiving stations. These analog tapes were transcribed after the flight to digital 8mm video tapes for use with VAX Exabyte tape drives by the different members of the IMAX collaboration. During the IMAX flight, we monitored the flight dark matter data in the 'wrap' data files. These wrap files contained a sample of the flight data and were recorded typically every hour for 15 or 30 minutes. The real-time and post-flight dark matter analysis software used the GDS[8] library to extract the dark matter science frame from the wrap files[9], and then to plot the D-module and scaler readings in histograms on the computer screen. For further understanding of the data, we could re-run (within minutes during the flight) the histogram binning with different cuts.

Until October 1992, we used the wrap data files from the flight for our data

[6] the Balloon-Borne Magnet Facility, based at NMSU

[7] The receiving station was at the launch site at the Lynn Lake airport before the payload went out of radio range at about noon CDST on 7/18/92, after which time, the down range station at Fort Macmurray, Alberta, received the data and controlled the payload.

[8] Golden Data System

[9] the dark matter data represented about 1% of all the IMAX data during the flight

analysis. After October 1992, we began to receive the full Exabyte data tapes and we also gained access to the full IMAX flight data over the computer network from the BBMF/NMSU database[10].

A few months after the flight, we decided to complement the GDS library with the standard CERN data analysis libraries, which include PAW[11] as an interactive front end analysis tool. PAW has allowed us great flexibility in studying the data, as PAW directly produced all the data plots shown in this dissertation (as encapsulated Postscript files). The CERN libraries and PAW also allow us to create a very large and flexible array called an 'N-tuple', which contains the raw data words and many new analyzed data words for each event. We could later apply very sophisticated cuts on each event in the N-tuple, using either batch processing or the very intuitive interactive PAW interface to the CERN libraries.

[10] To speed up the process of acquiring the IMAX data after the flight, we extracted most of the dark matter events from the IMAX data remotely on the NMSU computers, and then transferred these much smaller data files over the computer network to the Arizona computers

[11] Physics Analysis Workstation

CHAPTER 5

DATA FROM THE IMAX FLIGHT

The data from the IMAX flight shown in this chapter (unless otherwise noted) are for the first five hours after the balloon payload reached float altitude of 5 g/cm^2, between 10.0 and 15.0 hours UT. After 15.0 hours UT, the temperature of the IMAX payload exceeded $\sim$ 35 degrees Celsius, the D-module time-delay measurements were not as accurate as prior to 15.0 hours UT, so we choose not to use this data (as discussed in Chapters 4 and 6). The time delay distributions (Figure 5.11) from the IMAX flight appear very peculiar – with a very large peak at $\sim$ 2.0 μs in the T_{23} distribution, and an $\tau \sim 0.5$ μs exponential decay distribution for T_{12} (both of these unusual distributions ride on top of the dominant flat distributions from the accidental coincidences). Furthermore, we find that the unusual events in T_{23} are correlated with the unusual events in T_{12} (Figure 5.13). If we select only those events with small pulse-height amplitudes in the 3$^{\rm rd}$ scintillation detector *and* with T_{23} within the unusual peak at 2.0 μs, then the background from accidentals is minimized, leaving an enriched sample of 'anomalous events' (Figures 5.14 and 5.15). If the events do *not* satisfy the previous anomalous event cut, then the resulting distributions (Figures 5.16, 5.17, and 5.18) are quite 'clean', consisting of primarily accidental coincidences. Note that the time delay distribution for T_{34} (both for the original data, and for the anomalous event-enriched data) is relatively featureless compared to the unusual distributions for T_{12} and T_{34}.

We show raw pulse-height histograms from flight in Figure 5.12. The effect of the non-linearities found during the post-flight calibration is quite evident at $\sim$ 1500 mV. Channel X_1 (i.e., the signal for channel X_1 comes from the top detector, channel X_4 from the bottom detector) has a sub-zero or near-zero pedestal, so there is a prominent

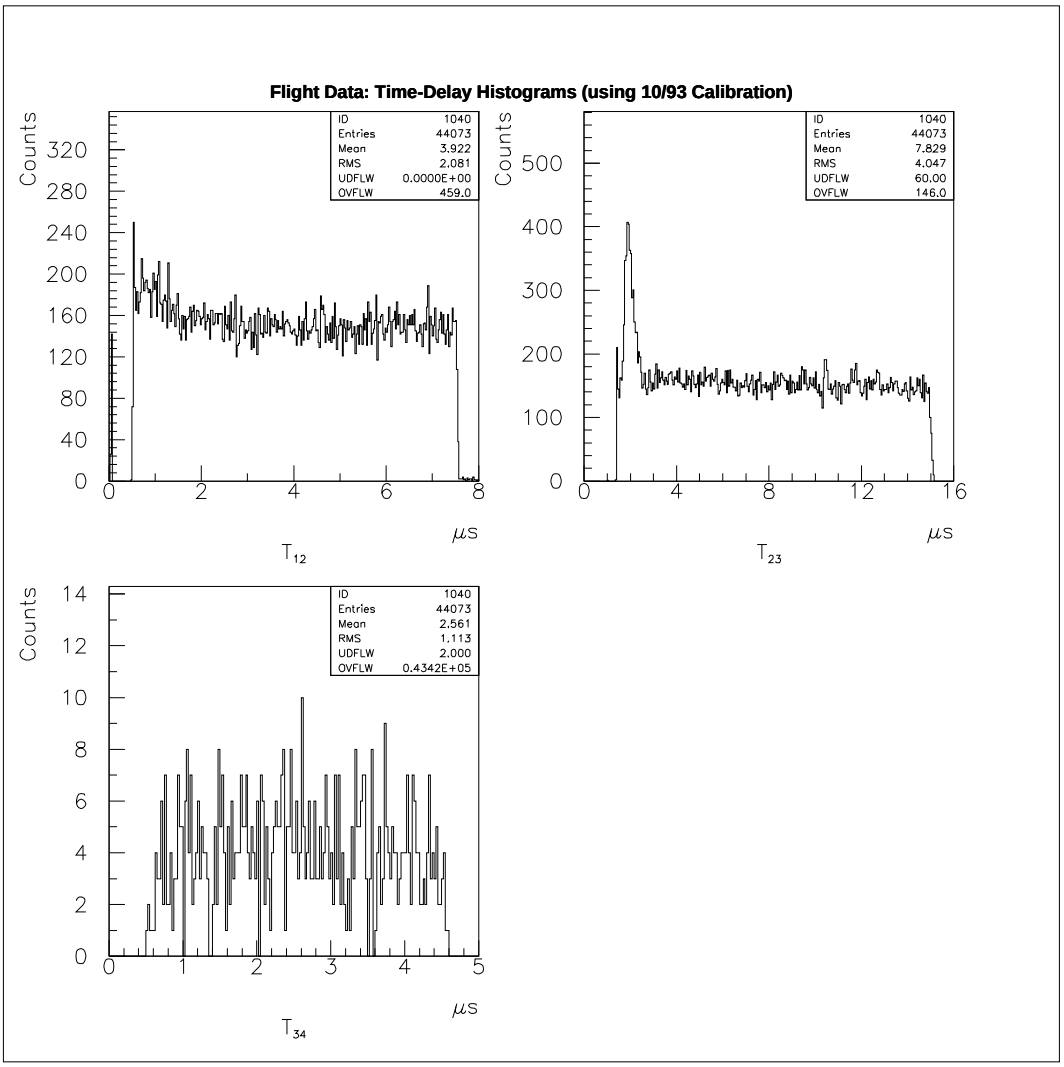

Figure 5.11: The IMAX flight time-delay histograms for the three time-delay channels using the 10/93 calibration (see chapter 6) show the expected flat distributions for accidental coincidences *plus* unusual structure for T_{12} and T_{23} near the beginning of the timing gates. This data consists of the float data (5 g/cm^2) which had CAMAC temperatures lower than 34.0° C, or equivalently UT $\in [10.0, 15.0]$ hours.

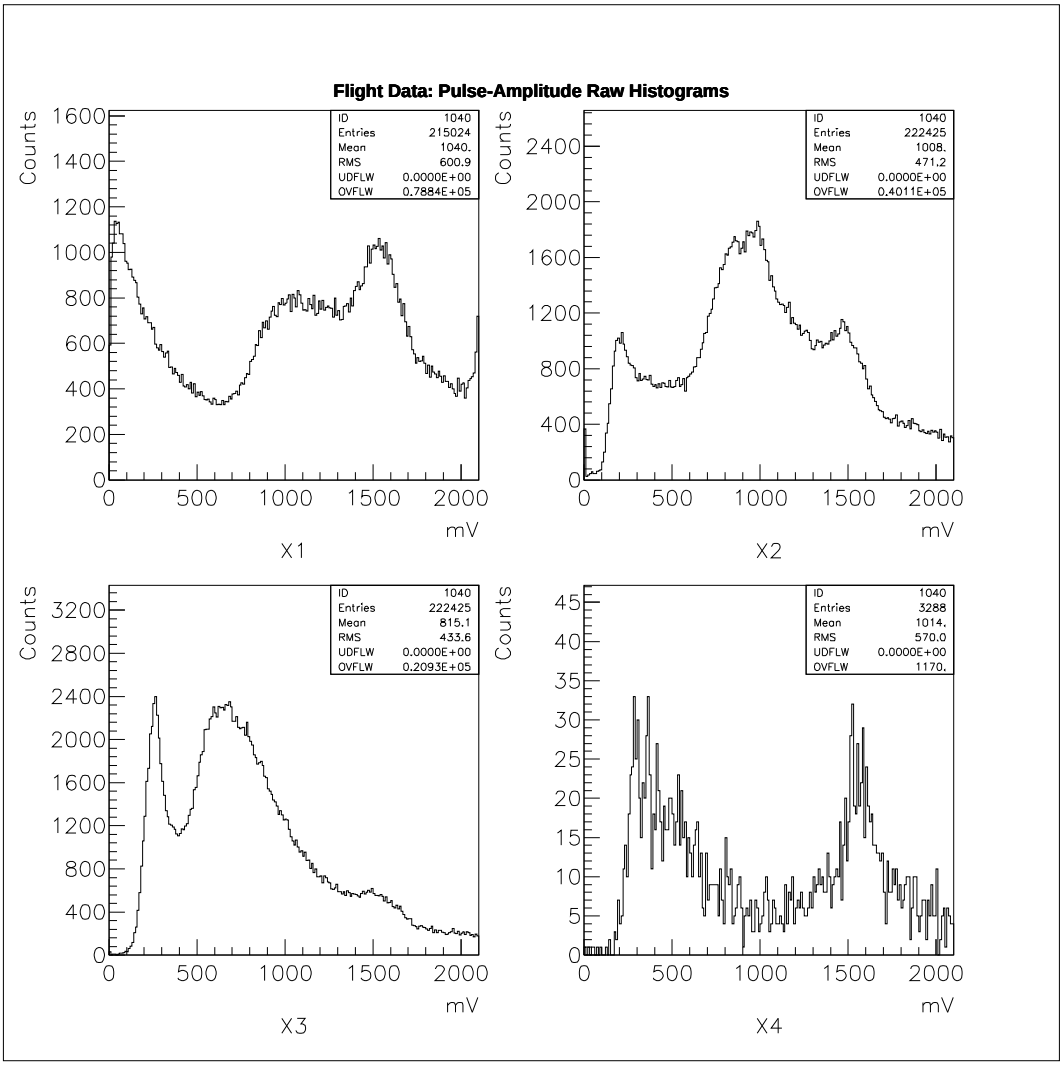

Figure 5.12: The raw pulse-height histograms for the four channels from IMAX flight show the expected Landau distributions from minimum-ionizing particles, plus PMT dark-current pulses, *plus* some artificial peaks. The PMT noise peaks are typically smaller than 500 mV; the Landau peaks are typically between 500 mV and 1000 mV; and the artificial peaks due to strong lorentzian non-linearities in the ADC response (see Chapter 6) are usually $\sim$ 1500 mV. Note the overflow bin contents in the sub-key for each histogram. Also 7401 counts are in the X_1 underflow bin, which is not shown or indicated in the sub-key.

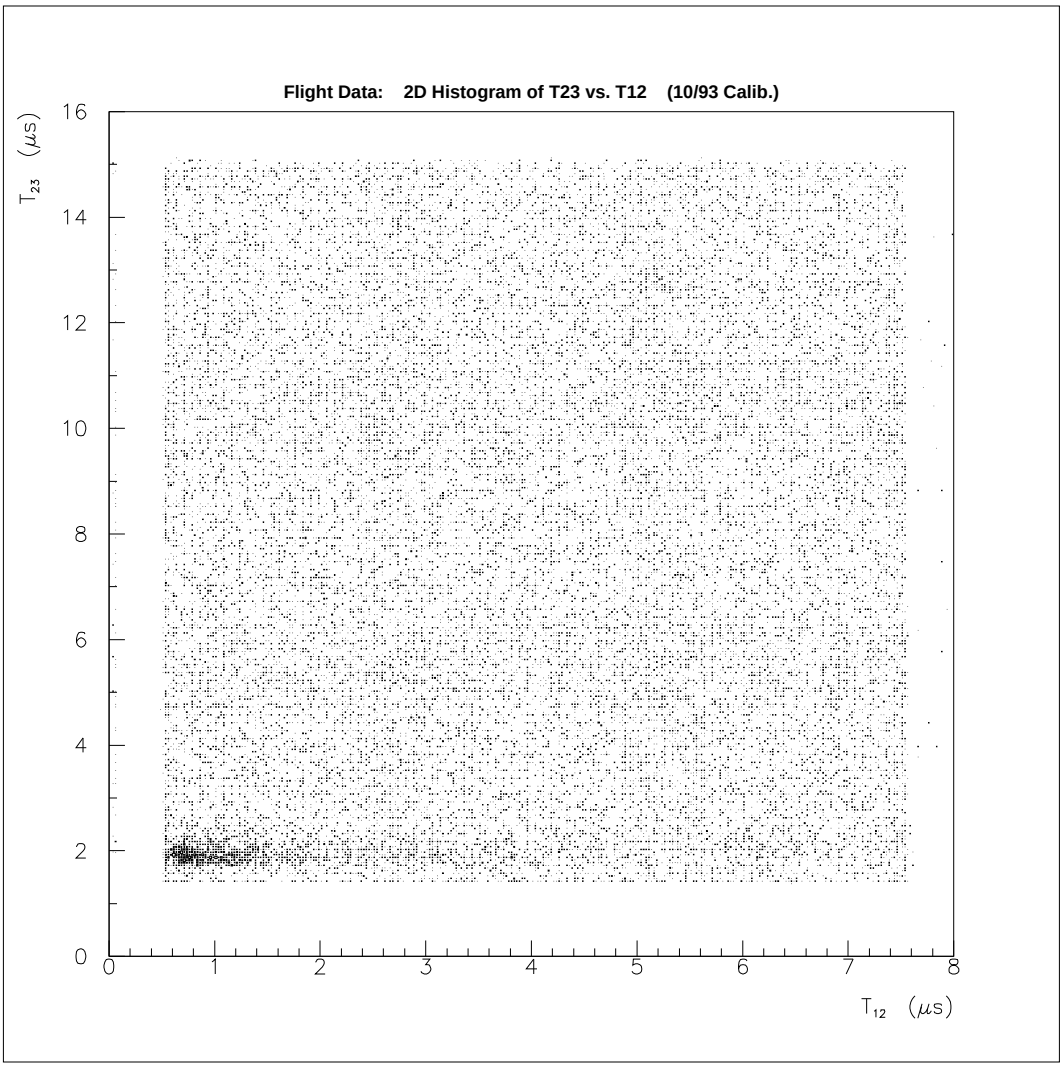

Figure 5.13: The IMAX flight two-dimensional histogram of T_{23} vs. T_{12} using the 10/93 calibration (see chapter 6) show the expected uniformity due to accidental coincidences *plus* unusual structure for T_{12} and T_{23} both near the lower edge of the gate. The number of counts in each bin is proportional to the area of the square centered on the bin – each bin is ($\Delta T_{12} = 0.025\mu$s, $\Delta T_{23} = 0.05\mu$s) in dimensions. This data consists of the float data (5 g/cm^2) which had CAMAC temperatures lower than 34.0° C, or equivalently UT $\in [10.0, 15.0]$ hours.

underflow bin for this channel. Channel X_1 also has indications of a sharp rise just before the overflow bin at ~ 2000 mV. We do not understand this rise, but it may either be due to an unnoticed effect in the amplitude calibration in the lab, or the sec(θ) effect discussed below, or possibly due to highly-ionizing slow protons that stop in the top detector.

There is no clear Landau peak in channel X_4. This is somewhat surprising, since we observed a good Landau peak in the ground muon runs at about 1000 mV in channel X_4. However, due to the delayed coincidence (see Figure 3.7) required during flight (but not during the ground muon runs, see Figure 6.29) and due to the vetoing of 2, 3, and 4-fold prompt anticoincidences (see Section 4.3), the muons that trigger the accidental delayed coincidences during flight must come at predominantly wide-angles into each detector. The wide-angles would demand a longer path-length as the muon obliquely traverses a 1 cm scintillation detector, due to sec(θ) being larger. Therefore, the Landau peaks should shift upwards during the flight, as compared to the ground muon runs. This effect would be especially severe for channel X_4, due to the close proximity of detector 3 to detector 4, and also due to the large amount of charge observed from detector 4 during the ground muon runs. Perhaps the Landau peak in channel X_4 is buried in the non-linearity peak at 1550 mV, or more likely the Landau peak is in the overflow bin. We calculate that the enhancement of the Landau peak positions from the ground muon tests to the flight distributions will exceed a factor of two for all four detectors, so that in particular, the X_4 Landau peak should be at $X_4 > 2000$mV.

In Appendix B, we discuss some possible sources of pulses with correlated time-delays, including an explanation that would imply new particle physics. However, after a detailed calibration and study of the D-module, we will conclude in the next chapter that these peculiarities in the timing and pulse-height distributions are not due to new particle physics, but are man-made. Therefore, the clean distributions (Figure 5.16) (after eliminating the anomalous events) contain the non-man-made events of interest to our IMP search.

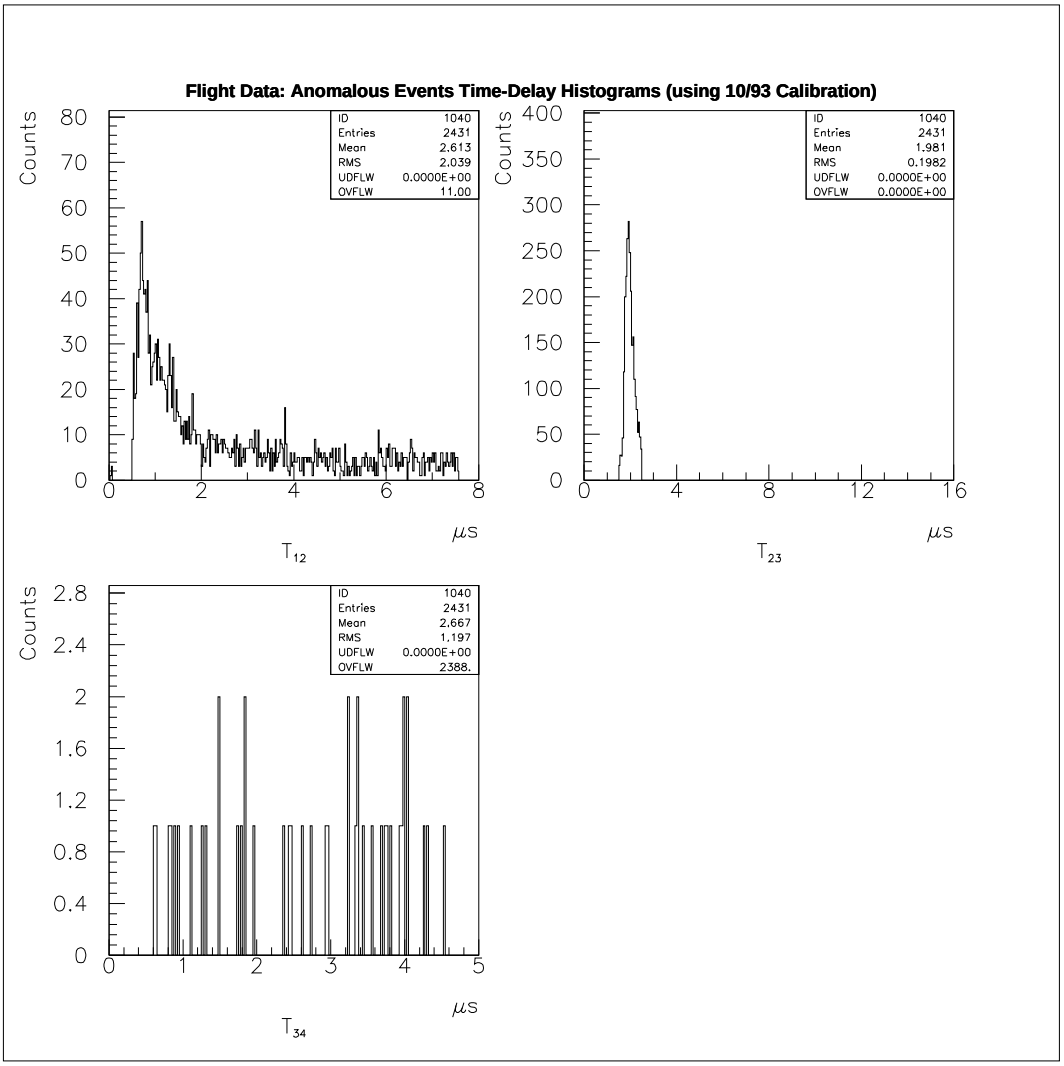

Figure 5.14: The IMAX flight time-delay histograms for the three time-delay channels using the 10/93 calibration (see chapter 6) show unusual structure for T_{12} and T_{23} near the beginning of the timing gates with a minimum of uniformly-distributed accidental coincidences. This data consists of the float data (5 g/cm^2) which had CAMAC temperatures lower than 34.0° C, or equivalently UT $\in [10.0, 15.0]$ hours. The event cuts required that $X_3 < 400$ mV and $T_{23} \in [1.5, 2.5]\mu$s occur simultaneously.

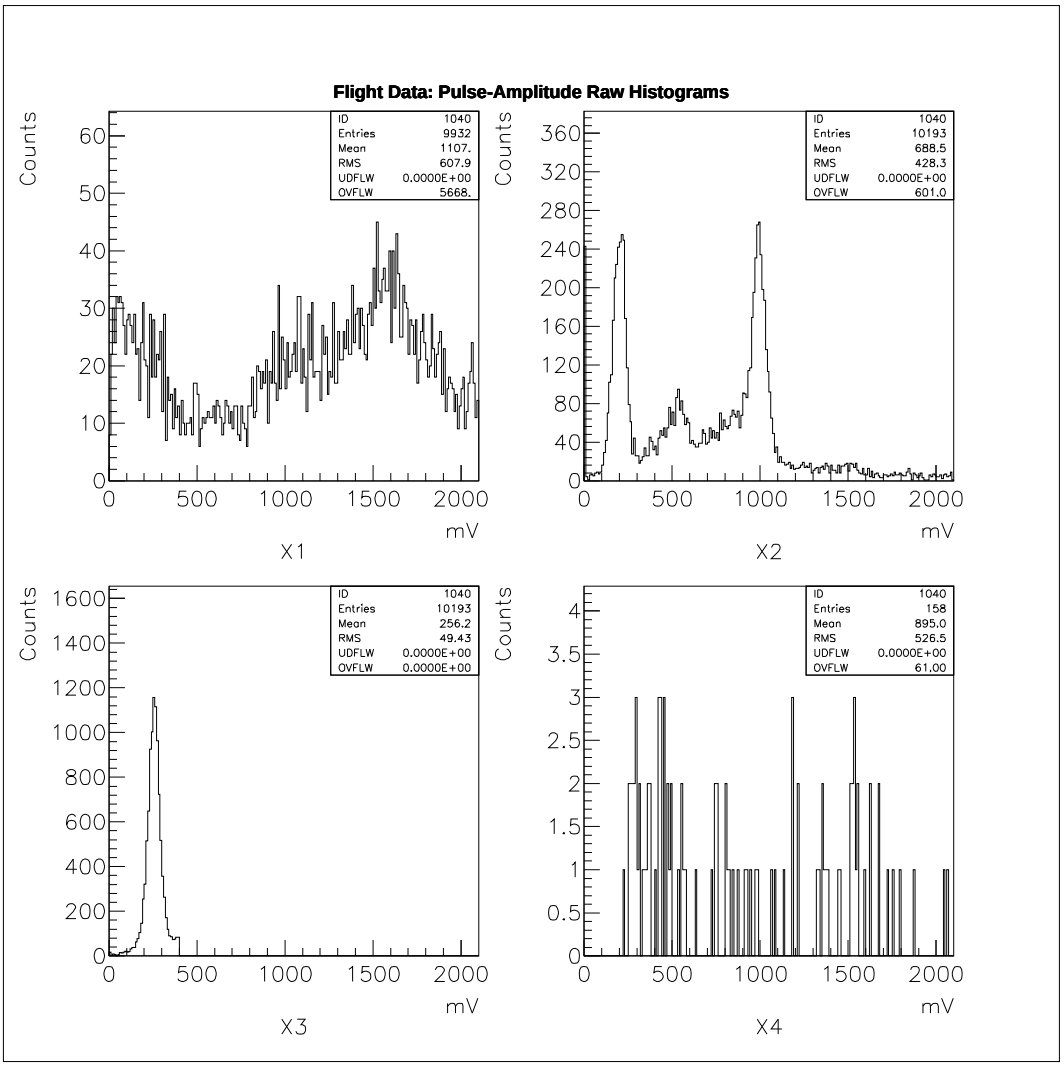

Figure 5.15: The raw pulse-height histograms are shown for the four channels for the anomalous events during the IMAX flight. Note the overflow bin contents in the sub-key for each histogram. Also 261 counts are in the X_1 underflow bin, which is not shown or indicated in the sub-key. We use the same event cuts on X_3 and T_{23} as in Figure 5.14. The data set consists of IMAX flight data during the time interval $[2.787, 25.281]$ hours UT, so as to enhance the statistics on anomalous events.

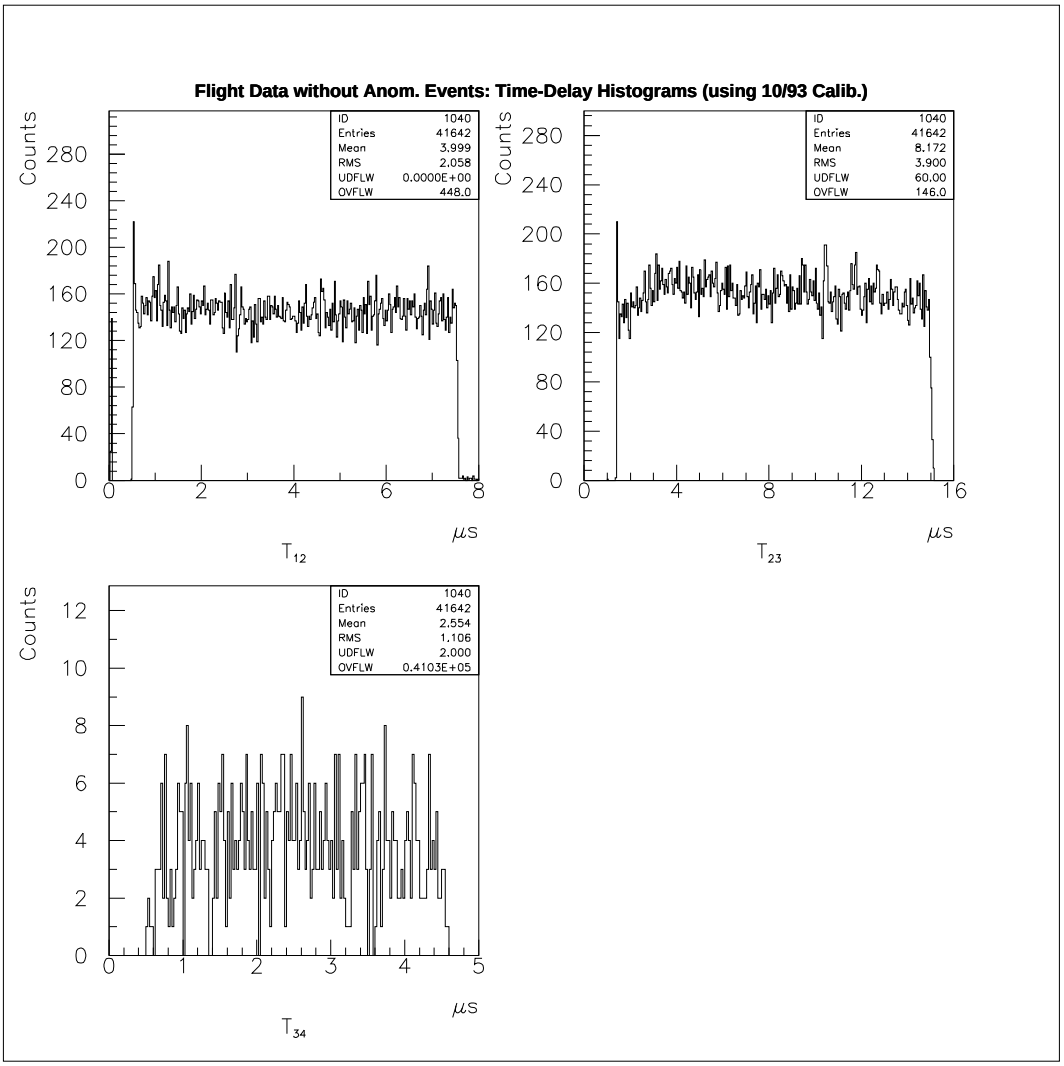

Figure 5.16: The IMAX flight time-delay histograms for the three time-delay channels using the 10/93 calibration (see chapter 6) show the expected flat distributions for accidental coincidences without the unusual structure for T_{12} and T_{23} near the beginning of the timing gates. This data consists of the float data (5 g/cm^2) which had CAMAC temperatures lower than 34.0° C, or equivalently UT $\in [10.0, 15.0]$ hours. The event cuts required that $X_3 \in [50, 150]$ mV and $T_{23} \in [1.5, 2.5]\mu$s *not* both occur in the same event.

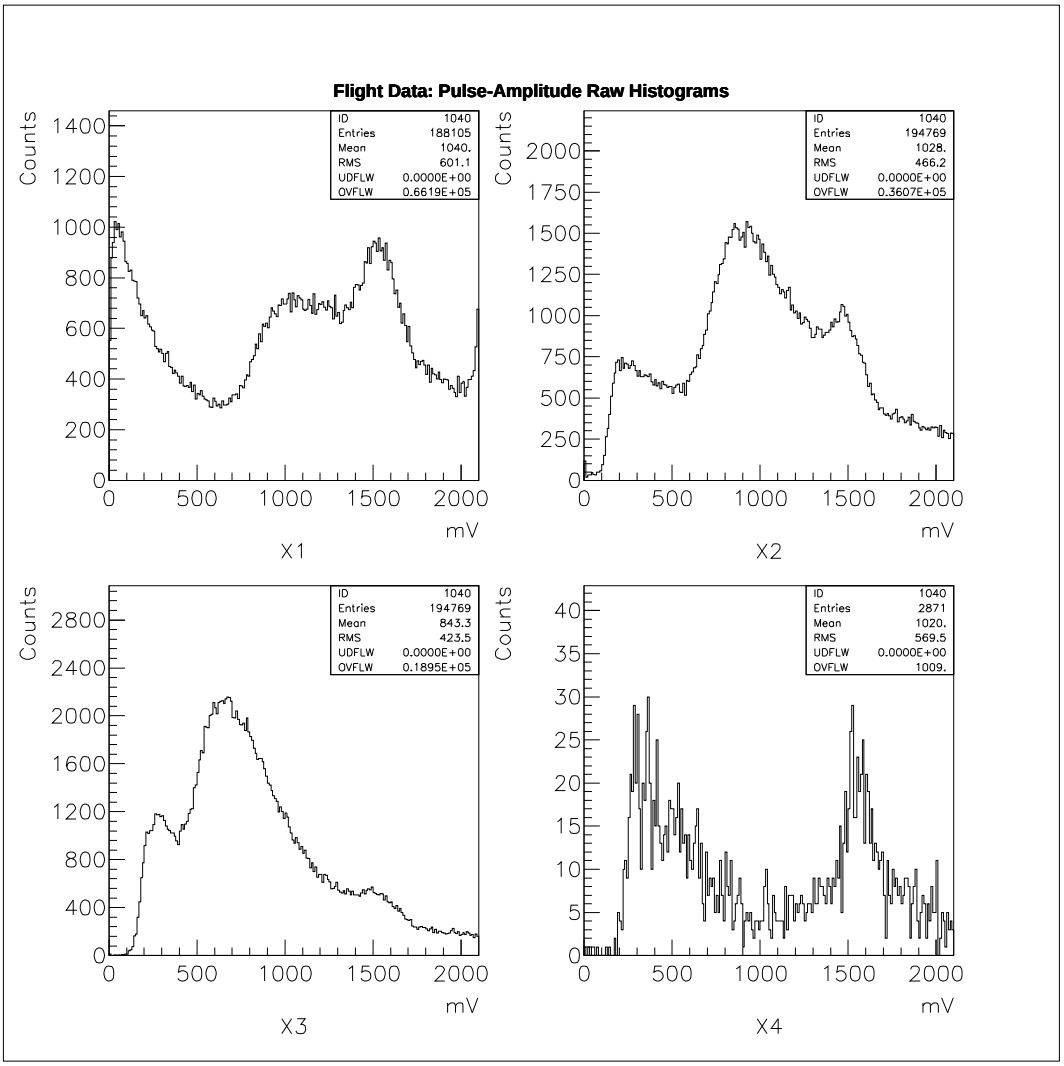

Figure 5.17: The raw pulse-height histograms are shown for the four channels for the non-anomalous events the during IMAX flight. Note the overflow bin contents in the sub-key for each histogram. Also 6664 counts are in the X_1 underflow bin, which is not shown or indicated in the sub-key. We use the same event cuts on X_3 and T_{23} as in Figure 5.16. The data set consists of IMAX flight data during the time interval $[2.787, 25.281]$ hours UT.

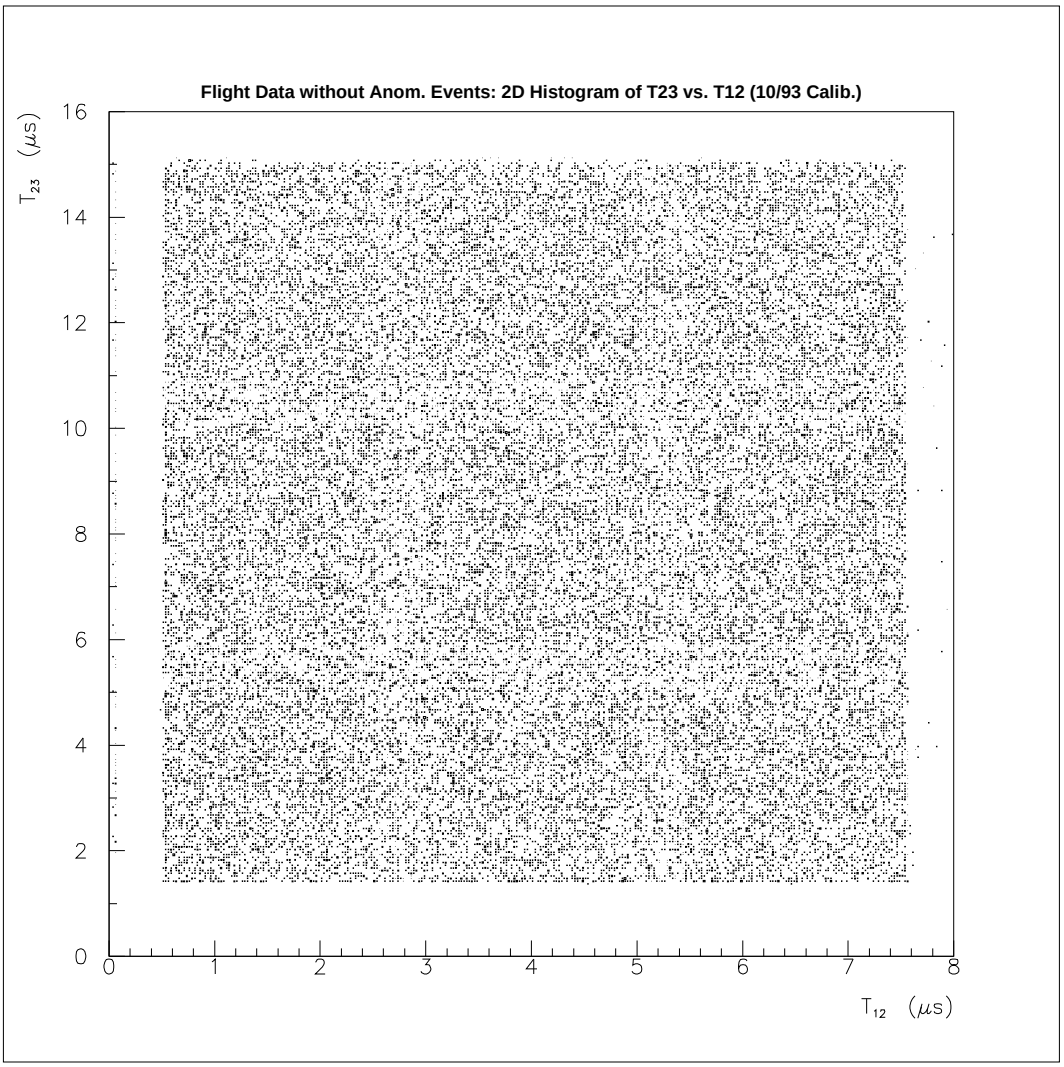

Figure 5.18: The IMAX flight two-dimensional histogram of T_{23} vs. T_{12} using the 10/93 calibration (see chapter 6) shows primarily accidental coincidences when we eliminate the anomalous events. The number of counts in each bin is proportional to the area of the square centered on the bin – each bin is ($\Delta T_{12} = 0.025\mu$s, $\Delta T_{23} = 0.05\mu$s) in dimensions. This data consists of the float data (5 g/cm^2) which had CAMAC temperatures lower than 34.0° C, or equivalently UT $\in [10.0, 15.0]$ hours. The event cuts required that $X_3 \in [50, 150]$ mV and $T_{23} \in [1.5, 2.5]\mu$s *not* both occur in the same event.

CHAPTER 6

EQUIPMENT CALIBRATION

Our time-of-flight search for ultra-slow ultra-massive particles is simple in concept and implementation. A well-executed IMP search requires several precise measurements of ultra-slow velocities, consequently requiring good pre-flight measurements of counter separations and excellent flight measurements of time-delays between hits in successive scintillation detectors. Additionally, if we are to search for IMPs that actually slow down within the IMAX telescope, we will need good estimates of the total overburden of material above each of the active scintillation detectors. If we can can estimate (to some precision) the light output for each particle passing through a detector, $\Delta L = \epsilon\, \Delta E$ (ϵ is the combined light production and collection efficiencies), we can perhaps clarify ambiguities in possible IMP slowing-down events, and also reject more background than possible without pulse-height measurements. *A posteriori*, we find that the D-module's performance moderately depends on the air temperature near the module. Since the data we used from the IMAX flight sampled an 8° C range of temperatures, a post-flight temperature calibration of the D-module is vital to accurate time-delay measurements during the flight, as discussed in Section 6.2.1.

6.1 Detector and Absorber Thickness and Separation Measurements

The IMAX cosmic ray telescope consists of 4 levels of scintillation detectors (see Figure 3.6) from which the D-Module received signals, and several other detectors interspersed between these scintillation detectors (see Figure 4.8). These other detectors include: 2 separate aerogel Čerenkov detectors, each composed of three layers of aerogel; 1 Teflon

Čerenkov detector, composed of 2 layers of Teflon; multi-wire proportional chambers (MWPCs), and drift chambers. Besides the scintillation detectors, only the Čerenkov detectors contributed significantly to the path length of material within the telescope.

Since the various detectors were installed on a complex scaffolding in the IMAX gondola and since the detectors were of different horizontal dimensions (sometimes prohibiting direct distance measurements), the distance measurements ($d_{i,i+1}$) required much care. IMAX researchers measured the counter separations from two different reference points to sub-millimeter accuracy, and performed consistency checks, finally deciding that their measurements were consistent to better than 0.5 cm. This is a rather large uncertainty, but we will be conservative and use this upper limit on the uncertainty of the distance measurements as the actual distance uncertainty. The dominant uncertainties for the grammage estimates (x_i) are:

- a manufacturer's stated fractional uncertainty of 5% on the thicknesses of the scintillators[124].
- an assumed fractional uncertainty of 5% on the thicknesses of the Teflon radiators.
- a manufacturer's stated fractional uncertainty of 5% on the specific gravity of Teflon (2.2 ± 0.1 g/cm^3)[125].
- typical measured aerogel refractive indices of $n - 1 \sim 0.049 \pm 0.006$, implying a 10-15% fractional uncertainty in the aerogel densities [156].

In Tables 6.1 and 6.2, we compile the inferred values of the counter thicknesses and distances, along with our computed uncertainties. In Table 6.2, we also include the total thickness of material above each of the scintillation detectors used in our IMP search.

Detector	**Type**	i	$d_{i,i+1}$ **(cm)**	x_i **g/cm^2)**
Atmo.	Air			5.0
Gondola	Aluminum			1.08
T1	BC420 Scint.	1	11.9 ± 0.7	1.032 ± 0.05
C1a	Teflon cher.	2	10.6 ± 0.7	2.2 ± 0.14
C1b	Teflon cher.	3	6.3 ± 0.7	2.2 ± 0.14
C3a	aerogel cher.	4	4.1 ± 0.7	0.66 ± 0.10
C3b	aerogel cher.	5	4.1 ± 0.7	0.75 ± 0.11
C3c	aerogel cher.	6	31.7 ± 0.7	0.68 ± 0.10
S1	BC400 Scint.	7	125.6 ± 0.7	1.31 ± 0.07
C2a	aerogel cher.	8	4.1 ± 0.7	0.69 ± 0.08
C2b	aerogel cher.	9	4.1 ± 0.7	0.69 ± 0.09
C2c	aerogel cher.	10	17.1 ± 0.7	0.68 ± 0.07
S2	BC408 Scint.	11	33.9 ± 0.7	1.83 ± 0.09
T2	BC420 Scint.	12		1.03 ± 0.05

Table 6.1: Thicknesses (x_i) and separations ($d_{i,i+1}$) of the various IMAX detectors. The 0.7 cm uncertainty for each of the separations comes from adding in quadrature the grossly conservative errors for each of the positions of two neighboring detectors (~ 0.5 cm).

Detectors	i, j	$d_{i,j}$ **(cm)**	x_{j-1} **(g/cm^2)**
T1, S1	$1, 7$	68.6 ± 0.7	13.61 ± 0.27
S1, S2	$7, 11$	150.9 ± 0.7	16.98 ± 0.31
S2, T2	$11, 12$	33.9 ± 0.7	18.82 ± 0.33

Table 6.2: Separations ($d_{i,j}$) of detectors used by the D-Module and the total amount of material above detector j, x_{j-1}. We include the gondola shell and the atmosphere at float altitude in the grammage estimates.

6.2 Time-Delay Measurements

Prior to the IMAX flight, during pre-flight integration in Lynn Lake, we calibrated the D-module with an Arizona/Irvine-constructed prototype computer-controlled Pulse-Generator module (G-module). This prototype had computer-control of the time-delay of the 4 output pulses, but lacked computer-control of the pulse-heights of the 4 output pulses. The prototype G-module had low output-time-delay resolution, ranging from < 20 ns at time delays of 500 ns, to > 400 ns at time delays of 10μs. With the prototype G-module, we found that the time-delay measurement capabilities of the D-module were linear enough for our pre-flight satisfaction and definitely monotonic, with a maximum differential deviation from linearity of $\sim 10\%$.

From the pre-flight muon-calibration (see the Amplitude Measurement section below), we also determined that the (relativistic particle) PMT signals from detectors S1 and S2 are delayed by 80 ns and 17 ns, respectively from the signals from detectors T1 and T2. We do not fully understand these delays, but they might have been partially caused by the the inherent delay caused by the white light-collection boxes used only by S1 and S2, and not by T1 and T2, and the 3-inch diameter PMTs of detector S1 would be expected to introduce greater delays than the 2-inch PMTs of dector S2.

After the IMAX flight, we personally recovered the D-module from the payload in Peace River, Alberta, Canada, so as to avoid possible damage during handling/shipment after the flight. We had completed the upgrade to the G-module during our 1 month stay at Lynn Lake. Therefore, after returning to Tucson, we calibrated the D-module again, but with the greater precision offered by the new G-module. Since the new G-module uses a linear univibrator design, the output-time-delay resolution is nearly independent of time delay, with $\sigma_{G,T_{ij}} \sim 5$ ns, for $T_{ij} \in [300, 15000]$ ns (as determined from a calibration with an HP5328A universal counter). This upgrade in G-module precision allowed us to quantify slight channel-dependent non-linearities in the D-module time-delay measurements. In Table 6.3, we give the parameters for a polynomial fit of the

G-module output time-delays vs. the D-module measured time-delays (January 1993). The functional form of the polynomial we used to fit the time-delay calibration is:

$$T_{i,i+1} = \sum_{j=0}^{n} a_j (X_{i,i+1} - X_{i,i+1}^{\rm ref})^j, \tag{6.30}$$

where $T_{i,i+1}$ is the G-module output measured in μs, $X_{i,i+1}$ is the D-module output measured in Volts[1], n is the degree of polynomial used in the fit, a_j are the coefficients[2], and $X_{i,i+1}^{\rm ref}$ is the 'reference' level for this time-delay channel. The 'reference' level for channels X_{12} and X_{23} is the smallest time-delay measured for each of these channels and refers to the lower edge of the time-delay histogram, which does not vary much between the hours 10.0 and 15.0 UT (see Figures 6.22 and 6.23). For channel X_{34}, the reference level is the position of the overflow bin.

Coeff.	T_{12}	T_{23}	T_{34}
$a_0(\mu{\rm s})$	$0.615 - 0.080$	$1.347 + 0.063$	$6.651 + 0.017$
$a_1(\mu{\rm s/V})$	5.6645	11.54	5.878
$a_2(\mu{\rm s/V}^2)$	9.8175×10^{-2}	0.4350	3.377
$a_3(\mu{\rm s/V}^3)$	-3.551×10^{-2}	-0.2634	1.960
$a_4(\mu{\rm s/V}^4)$			0.4090

Table 6.3: Calibration of D-module time delays: coefficients to a polynomial fit (1/93). The terms added or subtracted to the a_0 terms are due to the 80 ns and 17 ns delays mentioned in the text.

During post-flight data-analysis, we discovered a strong systematic (diurnal) time dependence of the D-module's time-delay measurements, which was correlated with the temperature changes of the CAMAC crate which contained the D-module. We also found in this analysis that the D-module would occasionally strobe the Ortec ADC (indicating that an event occurred, and that the event data needs to be sampled and stored in the ADC for future read-out to the on-board VAX), but no data would be present for the ADC to read-out, hence the pedestal of the ADC would be stored in the ADC's memory. These pedestal events are evident in the X_{12} and X_{23} distributions shown in Figure 6.23 as the events with TDC readings of less than 40 mV. We had not planned

[1]However, we will often use the units of milliVolts for $X_{i,i+1}$, especially when we display distributions of $X_{i,i+1}$.

[2]in microsecond and Volt units to eliminate excessive scientific notation

this fortunate accidental measurement of the pedestals. In retrospect, these recurring in-flight accidental pedestal measurements were very useful in establishing the reference levels discussed above. The knowledge of the pedestals or reference levels allowed us to track with good-precision the systematic change of the time-delay measurements with time, correcting the time-delay measurements for a secular change in the pedestals during the flight.

In addition to the secular change of the pedestals during the flight, we also observed a large upward shift of the time-delay pedestals at 15.1 hours UT, accompanied by the onset of a large amount of RMS noise ($\sim$ 5-10 mV) on the time-delay pedestals, where the noise had previously been less than 1 mV. We will discuss this noise-onset further in Section 6.2.1.

The large temperature-dependence of the D-module's time-delay measurements and time-delay 'pedestals' also prompted us to perform a second post-flight calibration of the D-module with the G-module. This second calibration (October 1993) determined the temperature-dependence of the time-delay calibration coefficients. Also, we steadily monitored the G-module's calibration during the D-module's temperature-calibration, so we have quite a bit more confidence in the second calibration than we have in the first calibration (see Section 6.2.1).

With the second calibration data, we first show the residual discrepancy between the data and a linear fit (see Figure 6.19) so that the effect of non-linearities can be emphasized. Note the slight change in character for $T_{12} < 1\mu$s. This is probably due to the non-zero width of the discriminator pulse which triggers the TDC. Channel T_{23} has a kink at $10.5 \pm 0.4\mu$s. This kink is currently unexplained, but is apparent in the flight T_{23} histograms (see Figure 5.16). Channel T_{34} has a 30 mV (peak-to-peak) lorentzian-like resonance between 3.0 and 4.5μs.

Channels T_{12} and T_{23} have a slight quadratic term which is accounted for by a global quadratic fit, and channel T_{34} has a lorentzian resonance which is accounted for by a piecewise quadratic fit. We chose the boundary time-delay between the two different

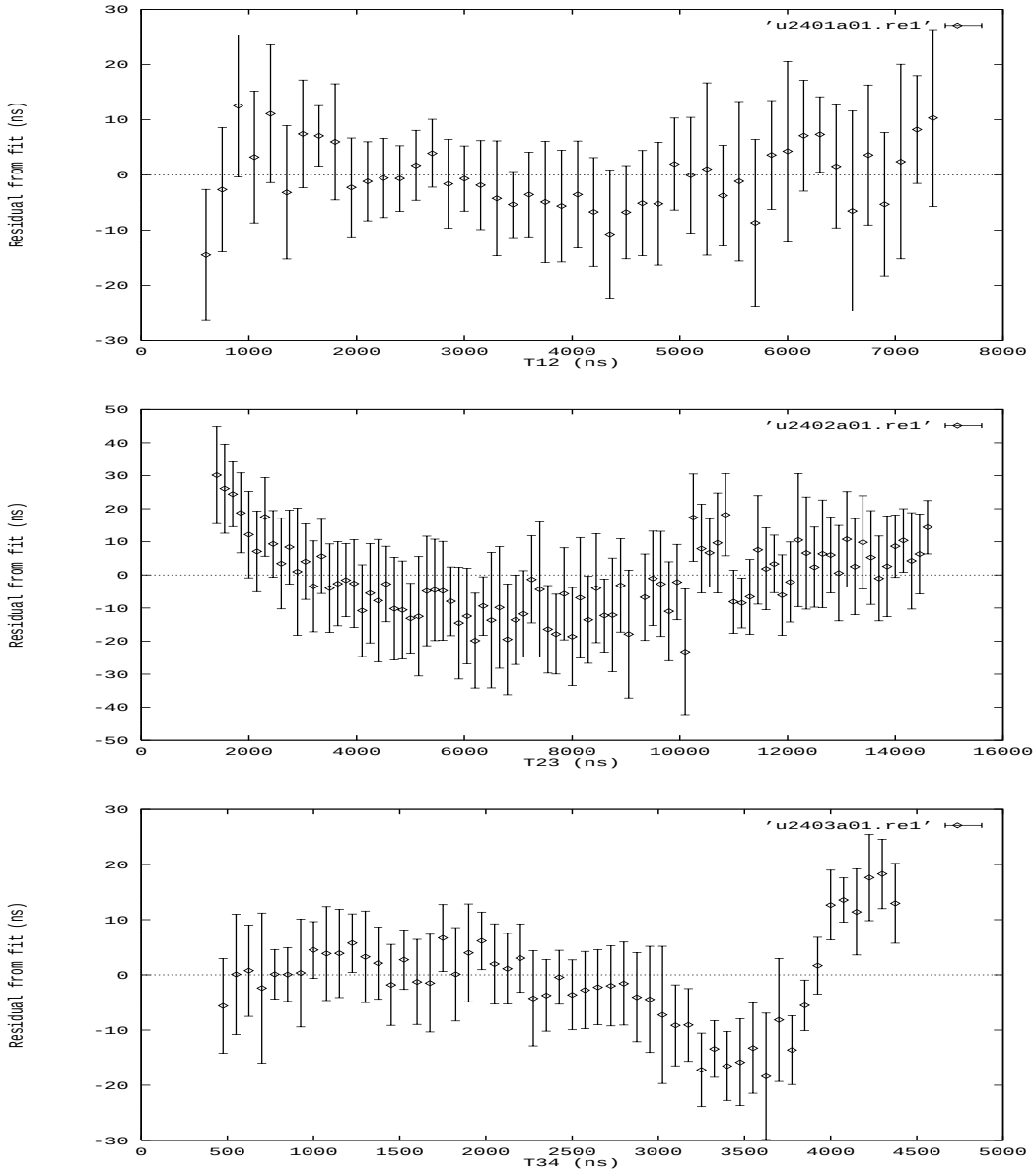

Figure 6.19: At an air temperature of $T = 24.0 \pm 0.1$ degrees C, the residuals for all channels T_{ij} from a linear fit show good evidence for a systematic quadratic discrepancy from zero. The error bars are single measurement errors, determined from the RMS of 20 measurements. The residuals for channel T_{34} from a linear fit also show a lorentzian resonance for $T_{34} \in [3.0, 4.5]\mu$s.

Coeff.	T_{12}	T_{23}	T_{34}
$a_0(\mu s)$	0.581 ± 0.0031	1.3539 ± 0.0031	4.5659 ± 0.0022
$a_1(\mu s/V)$	5.861 ± 0.005	11.772 ± 0.004	3.426 ± 0.003

Table 6.4: Calibration of D-module time delays: coefficients to a linear fit (10/93) at 24.0 ± 0.1 degrees C. The muon calibration delays of 80 ns and 17 ns should be added to the a_0 terms, as in Table 6.3.

Coeff.	T_{12}	T_{23}	$T_{34} <= 3.5\mu$**s**	$T_{34} > 3.5\mu$**s**
$a_0(\mu s)$	0.631 ± 0.026	1.337 ± 0.023	4.364 ± 0.052	4.424 ± 0.0027
$a_1(\mu s/V)$	5.829 ± 0.004	11.677 ± 0.039	3.331 ± 0.0254	3.496 ± 0.101
$a_2(\mu s/V^2)$	0.028 ± 0.015	0.083 ± 0.014	0.063 ± 0.018	0.48 ± 0.42

Table 6.5: Calibration of D-module time delays: coefficients to a quadratic fit (10/93) at 24.0 ± 0.1 degrees C. The T_{34} fit has been split into two parts, as indicated. The muon calibration delays of 80 ns and 17 ns should be added to the a_0 terms, as in Table 6.3.

pieces of the T_{34} fit to be 3.500μs. The residuals from these quadratic fits are shown in Figure 6.20.

6.2.1 Temperature Dependence

Prior to the IMAX flight, the IMAX collaboration made arrangements with the NSBF to launch the payload at dusk, so that high daytime temperatures could be avoided. Therefore, with the lower night-time temperatures, the Čerenkov PMT noise would not be severe enough to limit the range of relativistic particle velocity determination. Unfortunately, the IMAX payload ascended at a remarkably slow rate, not reaching float altitude until dawn (see Figure 4.9). Since a night flight had been planned, much insulation had been wrapped around the IMAX gondola to prevent heat-loss during the cold night. The extra insulation probably caused the internal temperature of the gondola (which contained the detectors and electronics) to rise considerably (up to $55°C$) during the daytime hours. Most of the electronics had only been tested up to $40°C$, so it is remarkable that the payload operated reasonably well despite these high temperatures. However, the changing temperature (see Figure 6.21) did directly affect the performance of the D-module, causing:

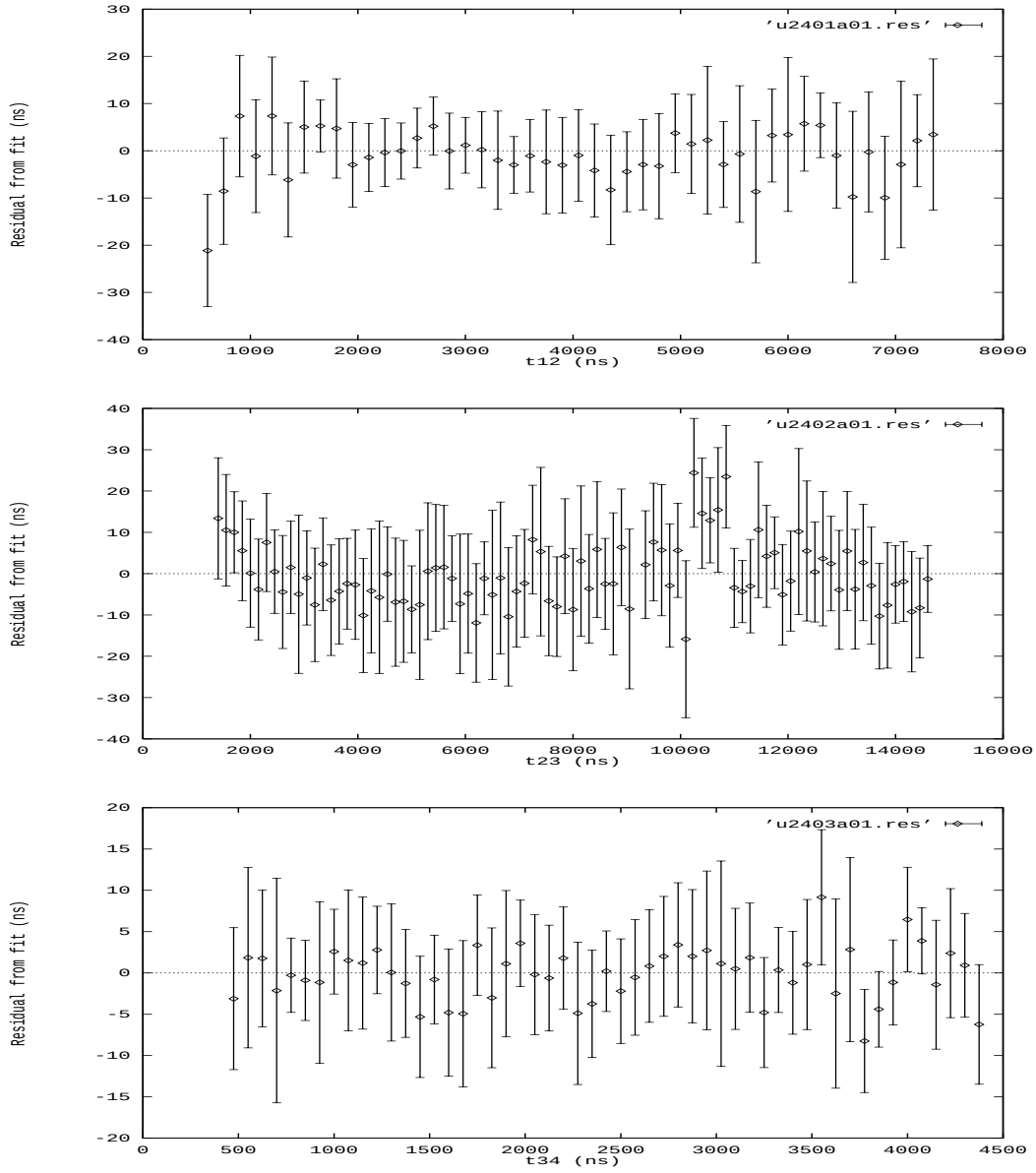

Figure 6.20: At an air temperature of $T = 24.0 \pm 0.1$ degrees C, the residuals for channel T_{ij} from quadratic fits show little evidence for a systematic discrepancy from zero. The discrepancy for $T_{12} < 1.0\mu$s is probably caused by the non-zero width of the stopping TDC discriminator pulse. The error bars are single measurement errors, determined from the RMS of 20 measurements. The glitch observed at $T_{23} = 10.5 \pm 0.4\mu$s is currently unexplained. The piecewise fit used exclusively for channel T_{34} has removed the lorentzian resonance observed in the linear fit residuals at $T_{34} \in [3.0, 4.5]\mu$s. The boundary time-delay between the two pieces of the piecewise quadratic fit is $T_{34} = 3.500\mu$s.

- the capacitance in the charge-integrating TACs to change slightly, thus changing the calibration conversion factors;
- at 15.1 hours UT, the onset of a small parasitic oscillation (5 - 10 mV) that affected all channels of the D-module, as evidenced by the superposition of this amplitude noise term on all the outputs;
- (possibly) at 26 hours UT, the slight upward shift of the S2 discriminator threshold, thus completely eliminating the anomalous events.

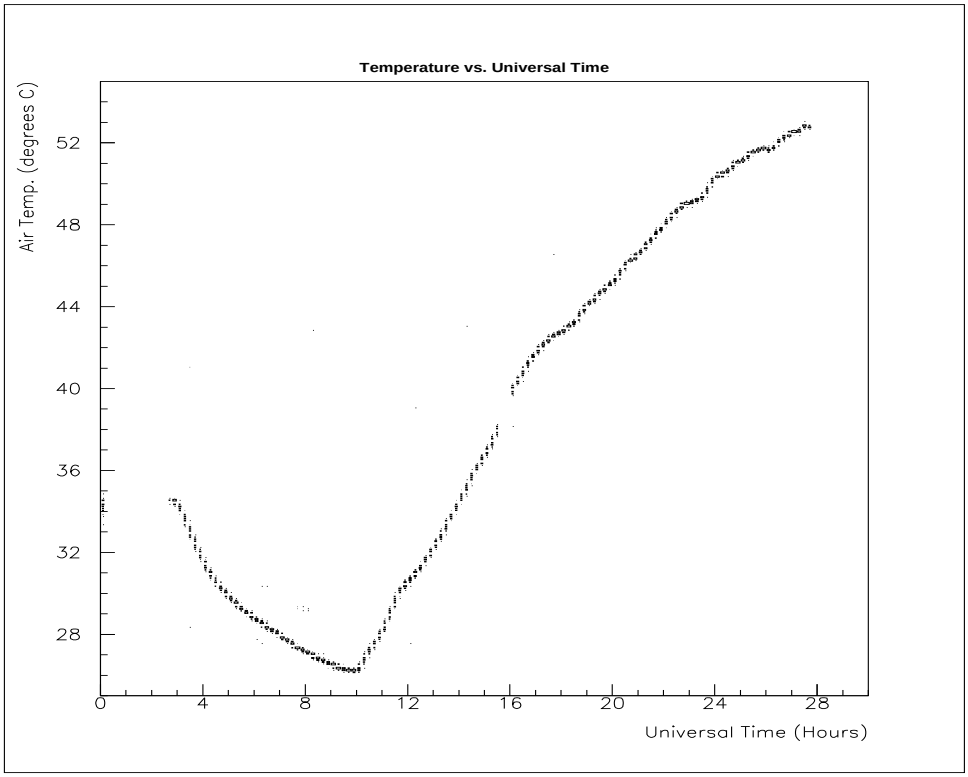

Figure 6.21: During the IMAX flight, the temperature of the gondola first dropped to $\sim$ 28 degrees Celsius and then rose substantially, reaching 55 degrees C at the end of the flight. NSBF launched IMAX at $\sim$ 2.6 hours UT on 7/17/92.

Hereafter, 'reference' levels will refer to the lower edge of the time-delay histograms for T_{12} and T_{23}, and the overflow value for T_{34}. In Figure 6.22, we show the flight temperature-dependence of the T_{ij} mean reference levels. These mean reference

levels are taken from the position of the edge of the T_{ij} distributions shown in Figure 6.23, which shows the noise-free evolution of the reference levels up to 15.1 UT ($\sim$ 35 degrees C) and the noisy timing shift at 15.1 UT. Since a lack of precision in the time-delay reference levels corresponds to a lack of precision in the time-delay conversion, we do not use the data from the flight after the onset of noise at 15.1 hours UT. The shift of the T_{ij} mean reference levels (Figure 6.22) is partly due to a shift in the pedestal due to a combination of the change in temperature and the change in voltage of the D-module/Ortec ADC811 combination. The temperature (Figure 6.21) starts at $\sim 35°$ C, goes down to $\sim 28°$ C, and back up again, reaching $\sim 53°$ C – yet there is little hysteresis in the reference levels in Figure 6.22 in the region $< 35°$ C; larger amounts of hysteresis with temperature might be expected if the reference levels did not depend on temperature alone. Therefore, the reference level closely follows temperature, so we account for the reference level shift by subtracting the temperature-dependent reference level prior to converting the TDC milliVolt reading into a time-delay in microseconds (see Equation 6.30).

At Lynn Lake, prior to installation into the IMAX gondola before the July 1992 flight, we performed a temperature-test of the D-module (with the prototype G-module) within a temperature range of $T \in [5, 40]$ degrees Celsius. No obvious malfunctions were apparent from the 7/92 temperature tests, as apparent from the histograms and scatterplots from the temperature tests that we studied at that time. One year after the IMAX flight, we conducted a careful temperature calibration of the D-module (with the new G-module), by controlling the air temperature near the insulation-isolated D-module with a hot-air blower within the temperature range of $T \in [24.0, 36.7]$ degrees Celsius. To our surprise, we found that the small parasitic oscillation observed during the flight (possibly due to non-D-module equipment) above 36 degrees Celsius (see Figure 6.23), probably was caused by the D-module itself, as we observed 5 to 10 mV (Peak-to-Peak) sawtooth oscillations of $\approx 2\mu s$ period (492 ± 17 kHz) emanating from the D-module outputs as measured with an oscilloscope at D-module temperatures above $34°C$. These oscillations grew in amplitude as the temperature increased and were clearly evident in

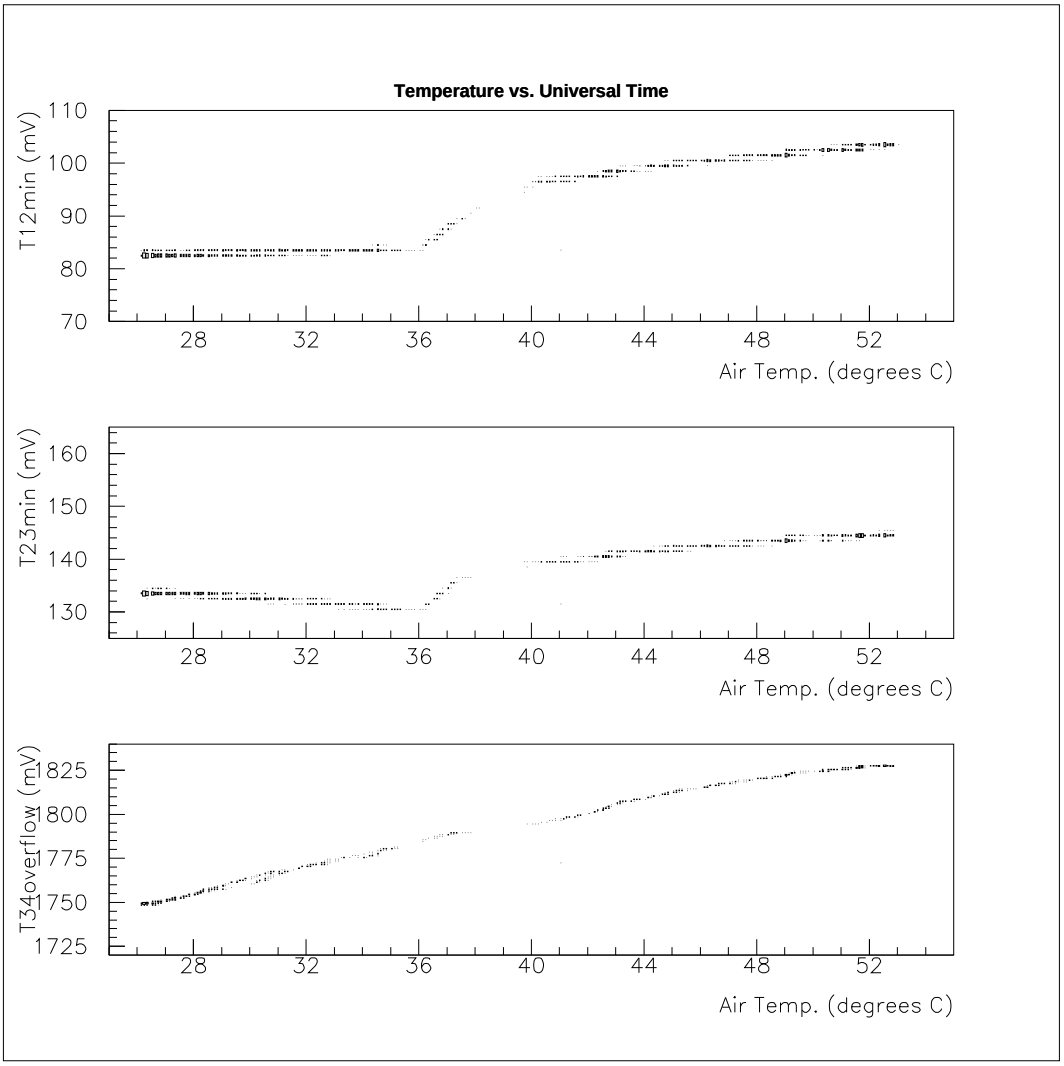

Figure 6.22: The time-delay mean reference levels vary with temperature during the IMAX flight, with a remarkable change in behavior at $T \sim 36°$ C (15.1 hours UT). This change in mean reference levels is also accompanied by an unusually large amplitude oscillation of the reference levels from their mean values (see Figure 6.23).

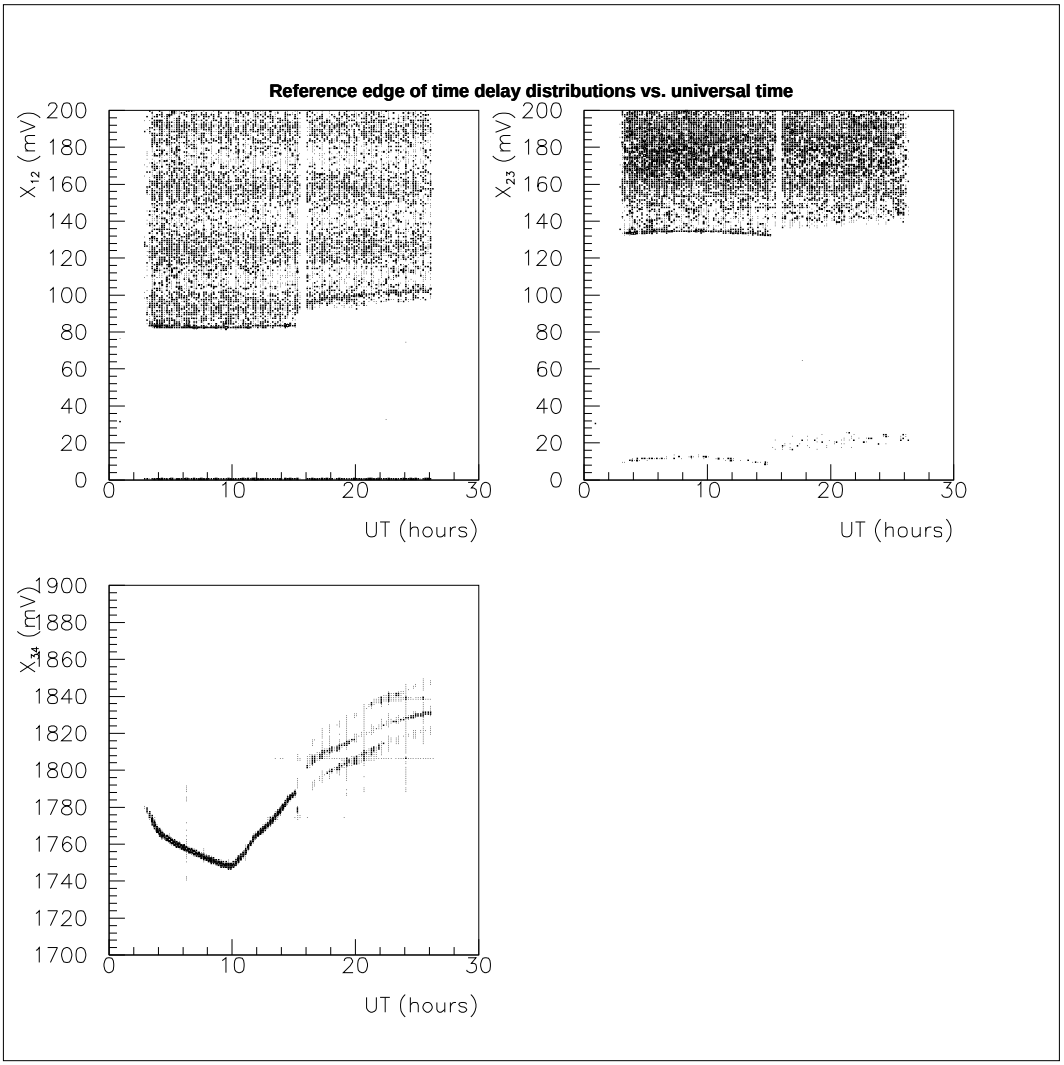

Figure 6.23: The time-delay reference levels vary with universal time during the IMAX flight, with a remarkable oscillatory behavior at 15.1 hours UT ($T \sim 36°$ C). See Figure 6.22 for the mean value of the reference levels as a function of temperature. We do not use the data from the flight after the onset of the large oscillations in the reference levels.

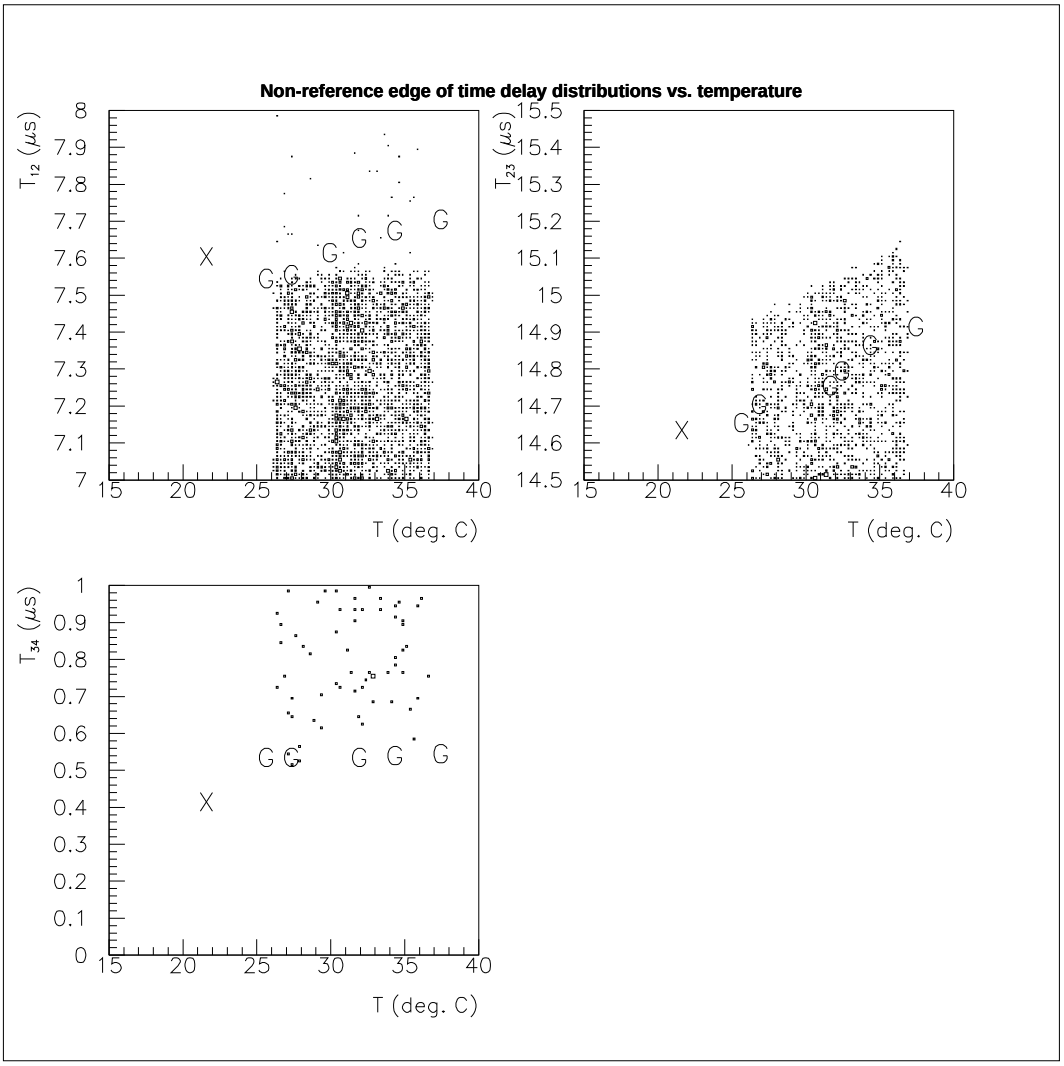

Figure 6.24: The time-delay non-reference levels vary with temperature during the IMAX flight. The G symbols correspond to the temperature dependence of the non-reference levels during the ground temperature calibration (10/93), while the X symbol is the non-reference level during the ground calibration (1/93).

the histograms and scatterplots (tabulated from our Tucson data (7/92)) as somewhat larger error bars on the measured X_{ij} values from the Ortec ADC.

During the 10/93 ground calibration, we also measured the temperature dependence of the positions of the two edges of the TDC gate, the previously-discussed reference edge and the 'non-reference' edge. The position of the reference edge (measured in mV) for each TDC mostly depends on the position of that TDC's pedestal. After we subtract the pedestals from the TDC measurements and compute the time-delay as in Equation 6.30, we can plot the $T_{i,i+1}$ distributions as a function of temperature or time to see if there are any systematic trends. The position of the other 'non-reference' edge of the $T_{i,i+1}$ histograms will be the maximum measured time-delay for T_{12} and T_{23} and the minimum measured time-delay for T_{34}. The non-reference edge position as a function of temperature does show similar systematic trends as a function of temperature for both the flight data and for the ground calibration data (see Figure 6.24), but there are slight discrepancies (which we will take to be systematic errors in Section 6.2.2). Since the temperature-dependence of the $T_{ij,\mathrm{max}}$ levels measured in the lab closely mimics the temperature-dependence of the non-reference levels during the flight, we can use the post-flight temperature-calibration coefficients and knowledge of the flight temperature changes to correct for the temperature behavior of the module. The time-delay calibration coefficients depend slightly upon temperature, as summarized in Table 6.6. Channel T_{12} is the most temperature sensitive channel of the three TDC channels.

We show the differences between the new and the old calibrations, new(T_{ij}) − old(T_{ij}), for two different temperatures in Figures 6.25 and 6.26. The new D-Module calibration coefficients differ from the 1/93 calibration coefficients by a significant amount, which is probably due to the careful monitoring and updating of the G-module calibration with the HP5328A universal counter during the 10/93 tests. Note the $\approx$ 100 ns discrepancies for large T_{12} and large T_{23} and *all* T_{34}. We found in 10/93 that the G-module's calibration can easily change from day-to-day or due to ambient temperature/voltage changes by 40 to 100 ns, especially for the longer time delays. Prior to the

Chan.	Coeff.	Temp. Dependence
T_{12}	a_0 (μs)	$0.5654 + 0.0012T - 0.080 + (0.1207 \pm 0.0196)$ $-((0.00350 \pm 0.00071)T)$
	a_1 (μs/V)	$(6.0376 \pm 0.078) - ((0.0099 \pm 0.0028)T)$
	a_2 (μs/V^2)	0.0460 ± 0.0061
T_{23}	a_0 (μs)	$1.2795 + 0.00136T + 0.063 + (0.0406 \pm 0.0174)$ $-((0.00065 \pm 0.00063)T)$
	a_1 (μs/V)	$(11.6899 \pm 0.0693) - ((0.000745 \pm 0.0025)T)$
	a_2 (μs/V^2)	$(0.0320 \pm 0.0578) + ((0.00215 \pm 0.00209)T)$
$T_{34} \leq 3.5\mu$s	a_0 (μs)	$4.1780 + 0.0105T + 0.017 - (0.100 \pm 0.039)$ $+((0.00116 \pm 0.00142)T)$
	a_1 (μs/V)	$(3.416 \pm 0.118) - ((0.00364 \pm 0.00427)T)$
	a_2 (μs/V^2)	-0.0644 ± 0.0083
$T_{34} > 3.5\mu$s	a_0 (μs)	$4.1780 + 0.0105T + 0.017 - (0.0063 \pm 0.0027)$
	a_1 (μs/V)	$(3.83 \pm 0.45) - ((0.0132 \pm 0.0158)T)$
	a_2 (μs/V^2)	-0.498 ± 0.177

Table 6.6: We show the dependence of time-delay calibration coefficients upon temperature $T \in [24, 34]^\circ$ C (10/93). The coefficients are defined in Equation 6.30.

1/93 D-module calibration, we had last calibrated the G-module in 11/92, so the observed discrepancies between the two D-module calibrations are quite reasonable. Also, the CAMAC air-temperature during the 1/93 calibration was probably about 20 degrees Celsius, which would significantly shift the D-module response for larger T_{12} time-delays, compared to the $T > 24$ degrees Celsius 10/93 calibration temperatures.

6.2.2 Slowness Uncertainties

We found in our second calibration (11/93) that the widths of the time delay gates on the ground differ systematically from these widths during the flight, by about 1.8%, 1.7%, and 4%, for T_{12}, T_{23}, and T_{34}, respectively (see Figure 6.24). For T_{12} and T_{23}, this systematic uncertainty causes the longest time-delays to be uncertain by 145 ns and 238 ns, respectively. Since our reference level for T_{34} is not the minimum measured time-delay (as for T_{12} and T_{23}), but rather the maximum measured time-delay, the shortest measured time-delays will be the most uncertain for T_{34}, by 180 ns.

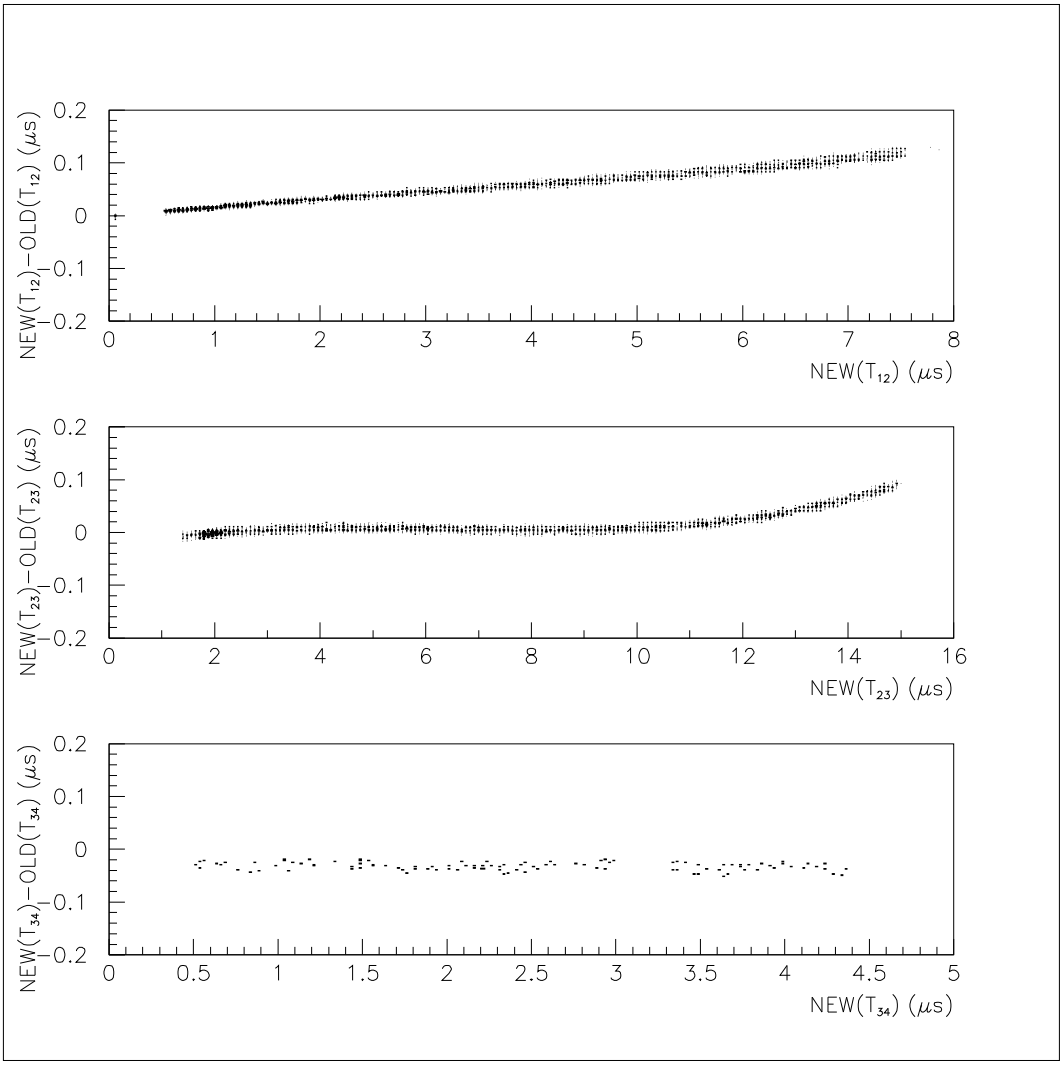

Figure 6.25: IMAX flight data is used to show the differences between the new (10/93) and old (1/93) D-module calibrations. The difference between the new and old time-delay calibrations is plotted as a function of the time-delay computed from the new calibration for $T \in [26.5, 28.0]$ degrees Celsius. The differences between the calibrations does not change very much over this range of temperatures.

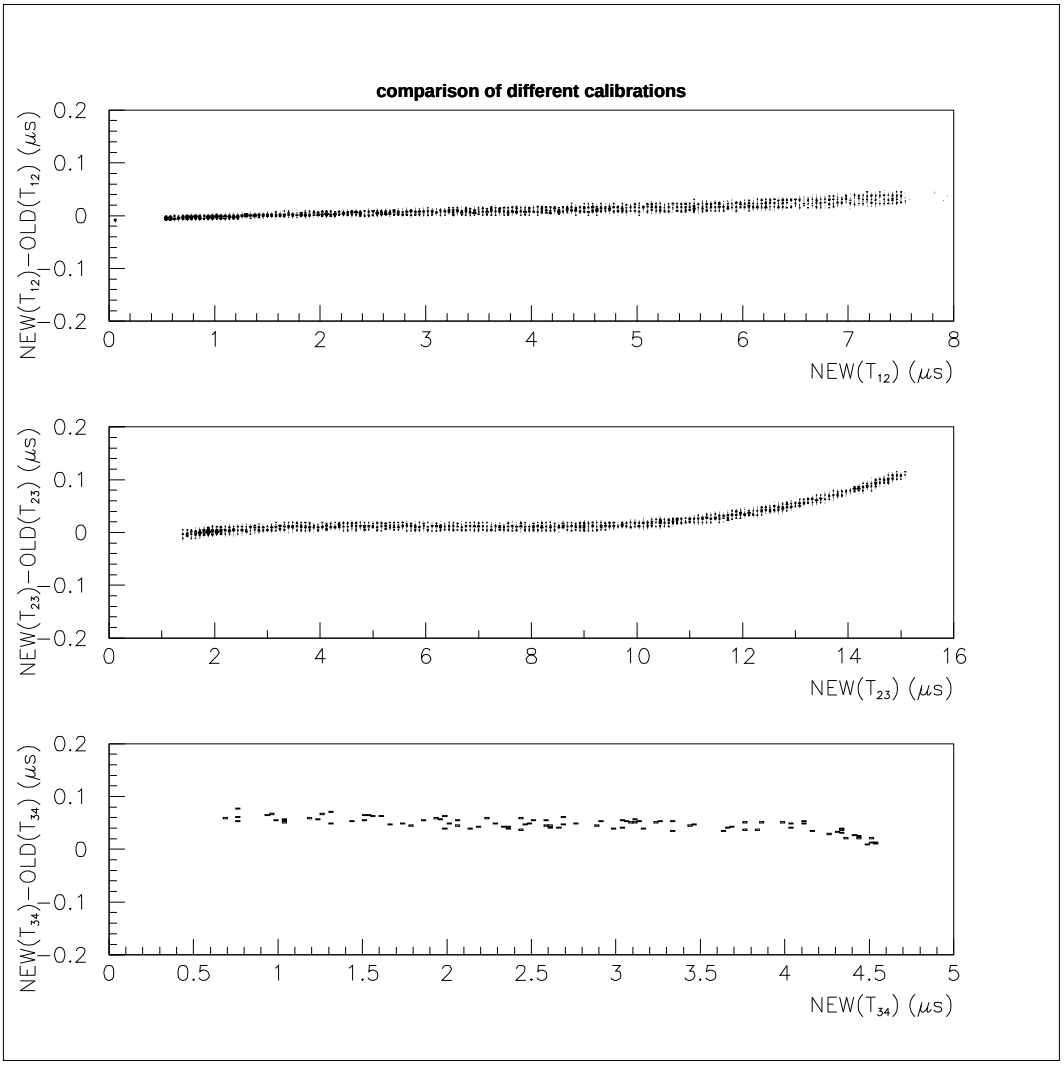

Figure 6.26: IMAX flight data is used to show the differences between the new (10/93) and old (1/93) D-module calibrations. The difference between the new and old time-delay calibrations is plotted as a function of the time-delay computed from the new calibration for $T \in [32.5, 34.0]$ degrees Celsius. The differences between the calibrations does not change very much over this range of temperatures.

By our conservative estimates, the detector positions are known to 5 mm, which corresponds to detector separations which are known to an uncertainty of 1.2%, 0.7% and 3.0%, for the d_{12}, d_{23}, and d_{34}, respectively (see Table 6.2).

In Chapter 7, we will introduce the notion of slowness, which is equal to the reciprocal of velocity. Slowness will supersede velocity as our primary variable that characterizes the hypothetical slow-moving IMP. From the previous considerations of the time-delay and detector separation uncertainties, we compute the slowness uncertainty for flight data, and summarize the results in Figure 6.27. Slowness S_{34} differs in character from the other two slownesses due to the difference in position of the reference level.

6.3 Amplitude Measurements

Before the IMAX flight in Lynn Lake, we roughly hand-calibrated the D-module's pulse-charge measuring devices (ADCs) using the fixed pulse-charge outputs of the prototype G-module, and a multitude of attenuators. This pre-flight calibration convinced us that the ADCs were monotonic, linear to within 25%, had little inter-channel crosstalk with thresholds set above ~ 2 pC, and had an active range roughly between $[2, 30]$ pC. The IMAX collaboration had agreed to apportion us roughly 20 pC of charge per mininum-ionizing-particle (MIP) per detector, putting MIPs right in the middle of each ADCs' active range.

Just before gondola-closing in Lynn Lake, we performed a muon-calibration, by sequentially plugging each scintillation detector's PMT signal into channel 1 of the D-module (now in the IMAX gondola), leaving the other 3 channels of the D-module without signals, and using the IMAX master trigger, delayed by 3.5μs, to strobe the ADC to read the D-module's outputs. This configuration avoided the relativistic particle anti-coincidence which we had wired into the D-module (see section 4.3), and allowed measurement of each detector's relativistic particle Landau distribution of energy loss. Pre-flight analysis of the resulting muon-calibration histograms (see Figure 6.29)

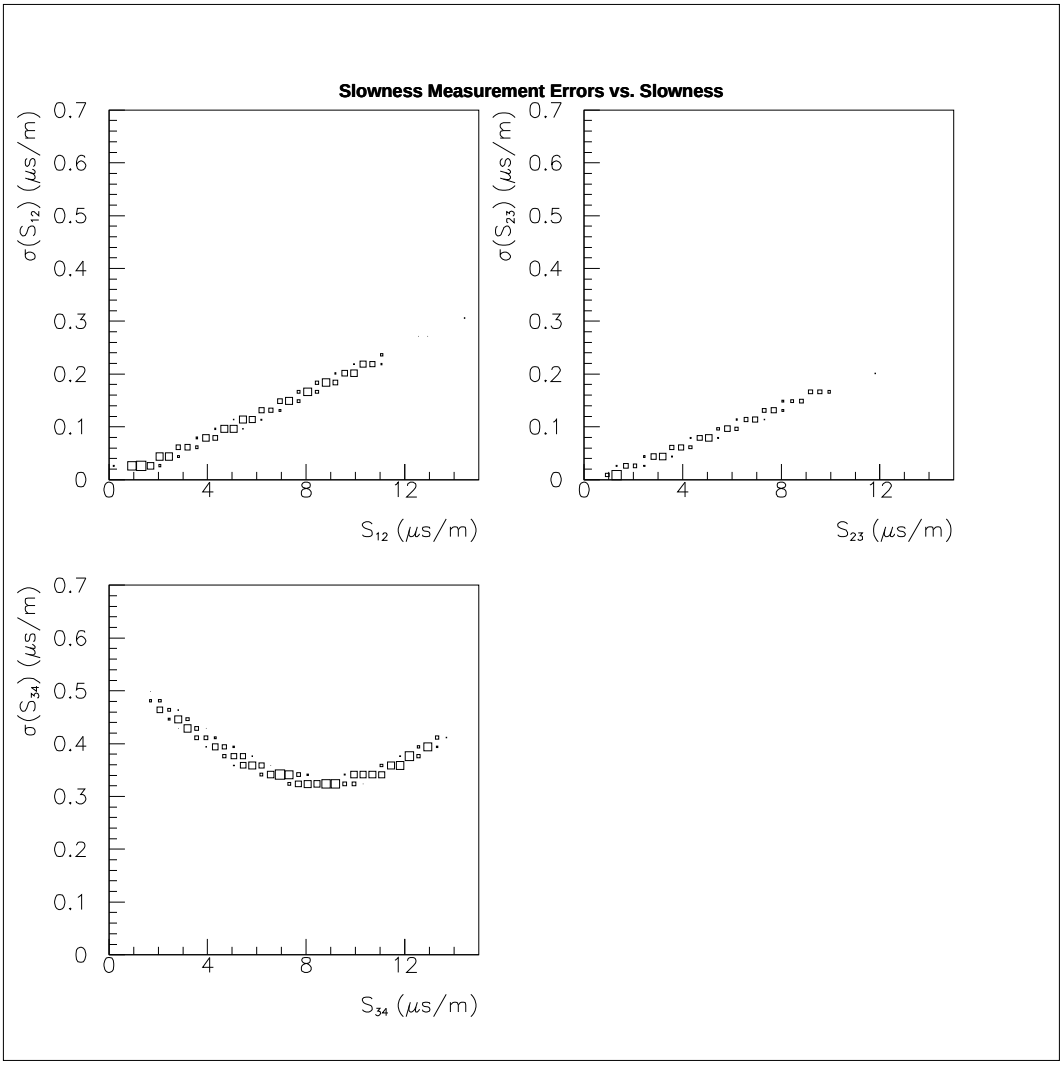

Figure 6.27: The slowness uncertainties vary with slowness during the IMAX flight. See text for discussion.

prompted us to ask the IMAX collaboration for more charge from the S1 scintillation detector, which was provided by turning up the voltage of the S1 PMTs just prior to flight. During the muon-calibration, we also measured the pedestals for the pulse-amplitude measurements by triggering the Ortec ADC with a pulse-generator that made NIM pulses asynchronously from the muon events. All of the detectors' signals were plugged into their respective flight configuration D-module inputs during this pedestal measurement, and the resulting histograms are shown in Figure 6.28.

Additional pre-flight analysis of the muon-calibration histograms showed unusual features in the S1 and S2 distributions, which prompted us to observe the raw PMT signals prior to the D-module with a storage oscilloscope. The oscilloscope showed a strong correlation between the IMAX master trigger and unusual artificial after-pulsing in the S1 and S2 PMT signals, with a small pulse $\sim$ 300 ns after the main muon pulse. The exact cause of this afterpulsing was unknown, but in the pre-flight discussions, the IMAX collaboration decided that the after-pulsing was inconsequential to the ultra-slow IMP search, since 300 ns is a much shorter time than the time-delay for an IMP to travel between two-detectors and be accepted by the D-module.

In our Tucson lab, after D-module recovery from Peace River, we calibrated the pulse-charge response of the D-module with the upgraded G-module. The new G-module has computer-controlled pulse-height outputs, which enabled very precise characterization of the non-linearities of the ADCs. We found the standard very slight ($\sim 5\%$) non-linearities for ADC values $X_i < 500$ mV. We also found an unusually strong ($\sim 25\%$) non-linearity for each ADC channel at a D-module reading of $\sim$ 1500 mV. This unfortunate non-linearity probably results from either a resonance between different D-module components, or an unusually strong charge-injection at 1500 mV. We fit the ADC calibration curves (Figure 6.30) to the sum of a polynomial and a lorentzian:

$$A_i \;=\; a_0 + a_1 x_i + a_2 x_i^2 + a_3 L(x_i, a_4, a_5) \;, \tag{6.31}$$

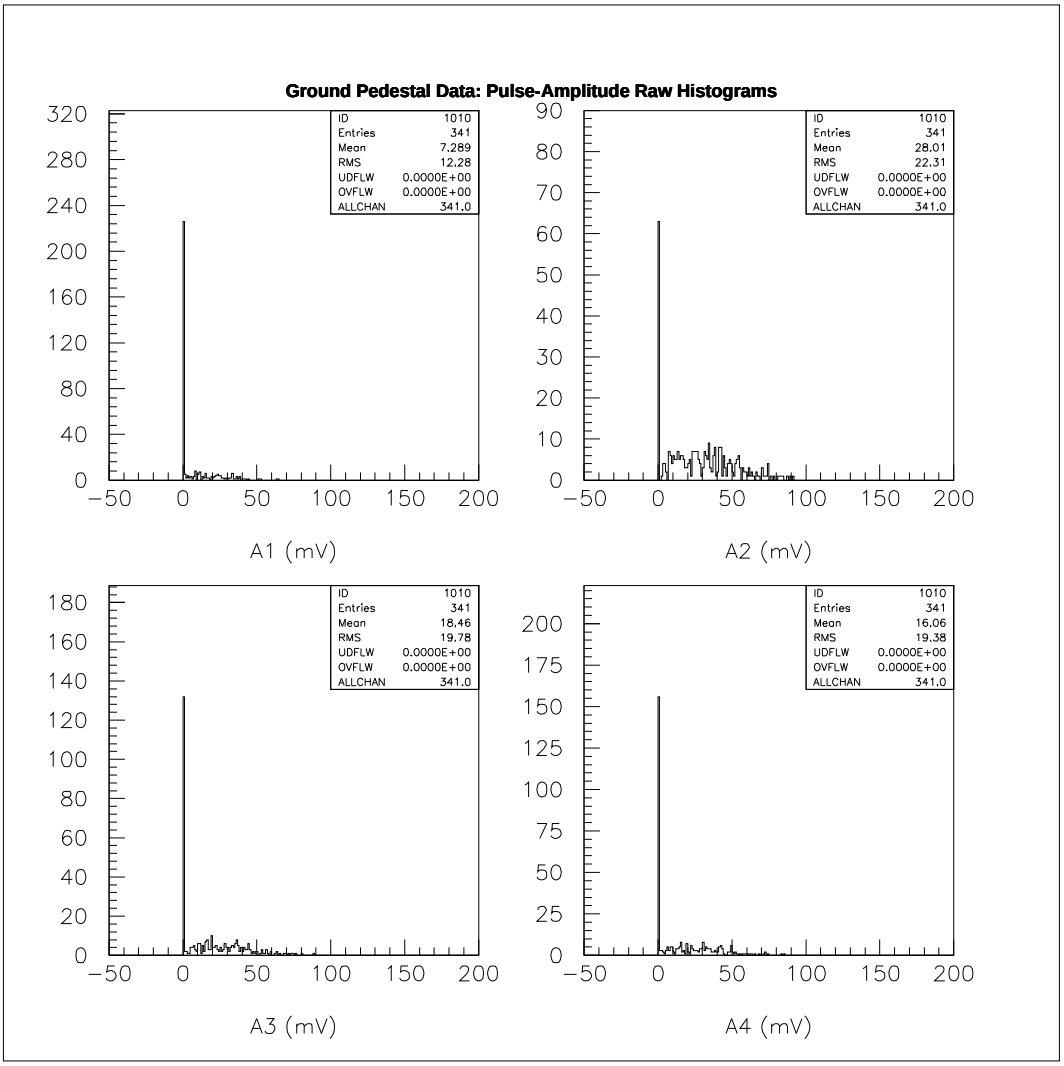

Figure 6.28: Raw pulse-height histograms from ground pedestal measurement run at Lynn Lake. We show the raw pulse-height histograms for the four channels from the ground pedestal measurement runs at Lynn Lake.

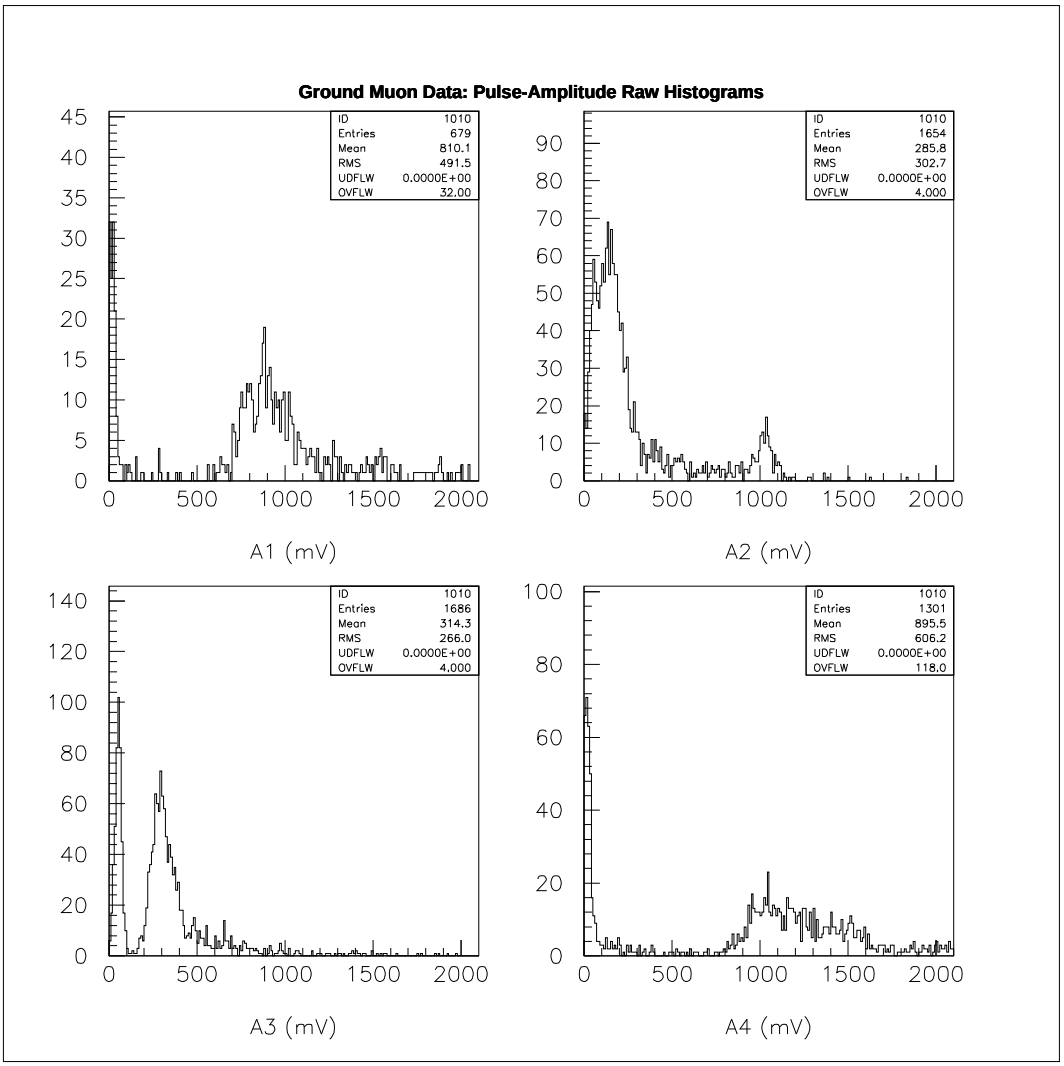

Figure 6.29: The raw pulse-height histograms for the four channels from the ground muon calibration runs at Lynn Lake show the expected Landau distributions from minimum-ionizing particles. The Landau peaks are typically between 500 mV and 1000 mV, but channel A_2 (IMAX detector S1) has a Landau peak at $\sim$ 200 mV, and an artificial peak at $\sim$ 1000 mV, possibly caused by the IMAX electronics-caused afterpulsing at $\sim$ 300 ns after the time-of-flight trigger.

where the lorentzian is given by:

$$L(x_i, a_4, a_5) \quad = \quad \frac{(x_i - a_4)}{1 + \frac{(x_i - a_4)^2}{a_5^2}} \ . \tag{6.32}$$

The coefficients to these fits are tabulated in Table 6.7. These non-linear fits may be useful if we should find that the flight data contains some interesting structure in the amplitude histograms, or if we are interested in searching for IMPs with exclusively large pulse-heights (we would want to use the energy-loss scale determined from these fits). But currently, we only compare the threshold of the ADC in raw milliVolt units to the position of the Landau peak during ground tests, thus allowing us to compute an approximate energy-loss threshold of our IMP search experiment (see Section 6.3.1). Due to the larger uncertainties in the amplitude measurements than in the time-delay measurements, we did not calibrate the amplitude measurements as a function of temperature.

Coeff.	A_1	A_2	A_3	A_4
a_0 (pC)	0.8247	0.7737	0.609	0.374
a_1 (pC/V)	7.7377	7.389	5.924	0.3634
a_2 (pC/V^2)	1.8428	0.7733	2.865	3.601
a_3 (pC/V)	0	34.531	43.53	27.58
a_4 (V)	0	1.5213	1.5648	1.5363
a_5 (V)	0	0.10594	0.0982	0.0970
G(THR) (mV)	29	72	138	211
G'(THR) (pC)	1.0	1.4	1.5	1.4
G(OVER) (mV)	2101	2086	2038	2089
G'(OVER) (pC)	24.0	20.0	24.6	22.6
G'(OVER)/G'(THR)	24.0	14.3	16.4	16.1

Table 6.7: We present the amplitude calibration coefficients as defined in Equations 6.31 and 6.32. These coefficients were used for the fits to the calibration data shown in Figure 6.30. We also interpret the thresholds and overflows, in milliVolts and picoCoulombs, from the ground calibration data shown in Figure 6.30.

6.3.1 Calculation of Energy Loss Threshold

From the ground tests at Lynn Lake, the flight pulse height distributions, and the measurements by Ficenec *et al.*[118] of the light production efficiency of slow protons (Section

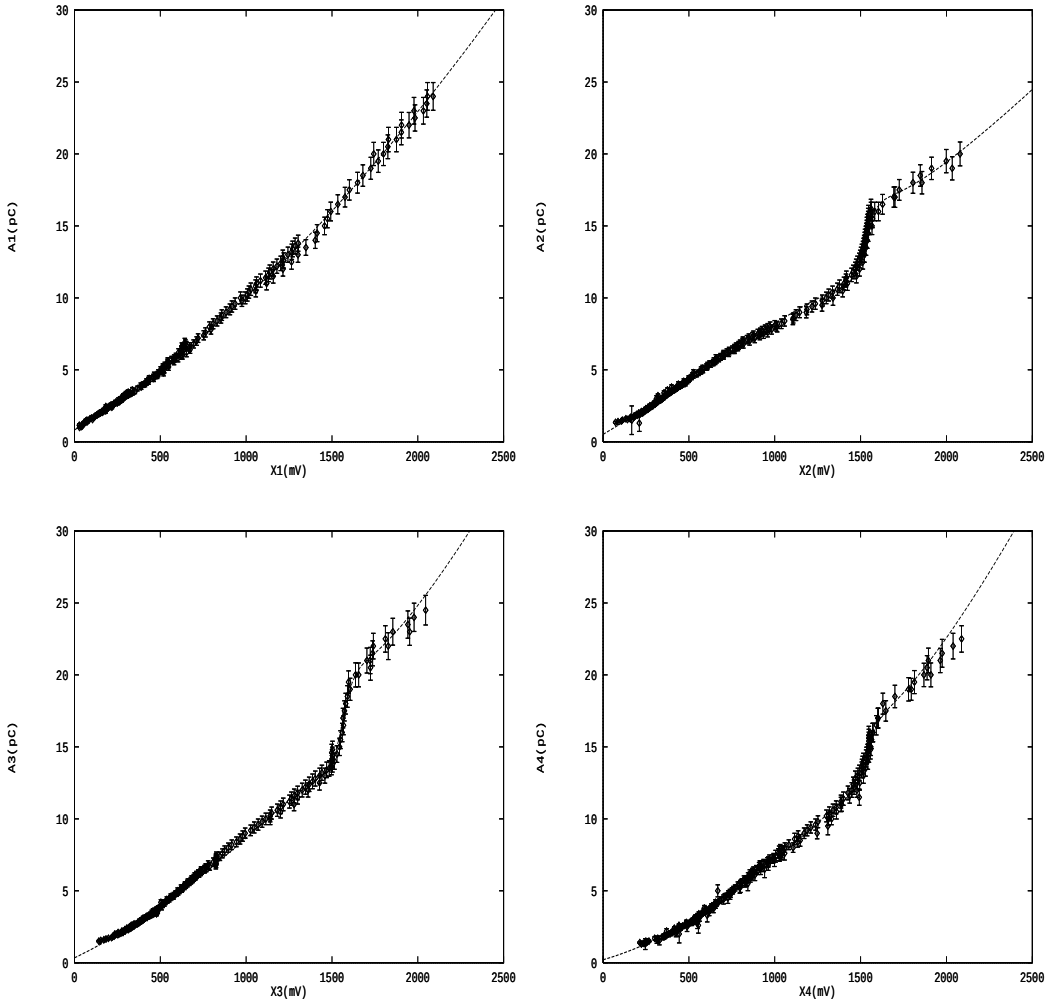

Figure 6.30: We fit the amplitude calibration data (January 1993) to non-linear curves using a Marquardt-Levenberg fitting procedure. Channel 1 has a quadratic polynomial dependence, while channels 2-4 have an additional lorentzian resonance at X_i near 1500 mV

2.6) we can estimate the smallest energy loss that each scintillation detector can measure. From Figure 6.29, we estimate the positions of the peaks of the minimum-ionizing particle Landau distributions for the four pulse-amplitude channels during the ground muon calibration runs, tabulated as G(MIP) in Table 6.8. From Figure 6.28, we compute the position of the pedestals of the four pulse-amplitude channels of the D-module during the ground pedestal-measurement run. For the pedestal computation, we assume that the pedestals have a gaussian distribution with standard deviation $\sigma = 25$ mV. We compute the ratio of the number of pedestal counts which have $A_i \leq 0$ mV to the total number of pedestal events (341), and use the error function to estimate the mean-value of the gaussian-distributed pedestal events, as tabulated as G(PED) in Table 6.8. Lastly, from the flight distributions of the pulse-amplitudes for each detector (see Figure 5.12), we estimate the position of the discriminator settings and list these settings as F(THR) in Table 6.8. We compute the energy loss threshold, dE/dx(THR), during the flight for slow ($\beta \sim 10^{-3}$) particles with the following equation:

$$\frac{dE}{dx}(THR) = \left(\frac{\frac{dL}{dE}(\beta = 1)}{\frac{dL}{dE}(\beta = 10^{-3})} \right) \frac{(\text{F(THR)} - \text{G(PED)})}{(\text{G(MIP)} - \text{G(A1,P)})} \frac{2 \text{ MeV}}{\text{g/cm}^2}, \tag{6.33}$$

where $dL/dE(\beta = 1) \approx 0.03$ is the ionization efficiency for fast particles, $dL/dE(\beta = 10^{-3}) \approx 0.006$ is the ionization efficiency for slow particles (see Section 2.6), and G(A1,P) is the position of the pedestal from the ground pedestal run for channel A_1. The computed values of dE/dx are accurate to $\sim 30\%$, with uncertainty dominated by three factors: our neglect of the non-linear pulse-height conversion curves (Figure 6.30), the uncertainty in the pedestal positions (which were sometimes negative), and the assumption that the change of PMT-gain for Channel 2 just prior to the IMAX flight resulted in a factor of two increase in the A_2 signal. The first detector probably had the lowest dE/dx threshold because it not only had a large signal from the detector, but also had (by chance) been the channel with the most debugging prior to flight. The values for dE/dx(THR) shown in Table 6.8 were computed from a more sophisticated method than presented here (and differ from the thresholds calculated from Equation 6.33 by less than 60%). The more sophisticated method properly takes into account the effect of the nonlinearity and the shifts in the thresholds and pedestals between the flight and

the ground calibration.

CHAN	G(MIP)	G(PED)	F(MIP)	F(THR)	$\frac{dE}{dx}$(THR)	$\frac{dE}{dx}$(OVER)
A_1	850 ± 50	-10	1030 ± 20	50 ± 10	0.9	21.6
A_2	350 ± 40	23	900 ± 50	200 ± 20	2.1	30.0
A_3	300 ± 20	7	630 ± 30	230 ± 20	3.5	57.4
A_4	1020 ± 50	2	> 2100	280 ± 20	1.4	22.5

Table 6.8: Computation of Energy-Loss Thresholds for IMAX flight. See text for definitions of some of the variables. F(MIP) is the position of the minimum-ionizing particle peak during flight. The units of G(MIP), G(PED), F(MIP), and F(THR) are milli-Volts. The dE/dx(THR) and dE/dx(OVER) values shown in this table have the units of MeV/g/cm^2 and have an accuracy of $\sim 30\%$. The dE/dx(OVER) values are computed from the product of dE/dx(THR) shown here and G'(OVER)/G'(THR) shown in Table 6.7.

6.4 Interchannel Crosstalk Analysis

In October 1992, we performed our first post-flight interchannel crosstalk analysis of the D-module. At that time, the flight data suggested to us that the 'anomalous' flight events were associated with a large pulse from the top Time-of-Flight detector (T1). Therefore, we put very large pulses (-5 V $\times 200$ ns $/50\Omega = -20{,}000$ pC) into channel 1 of the D-module, and no signals into the other 3 channels, hoping to trigger the D-module by the hypothetical crosstalk between channel 1 and the other channels. We observed no such crosstalk triggers. When we plugged the same large signal into channel 1 and three different regular-sized (~ 20 pC) scintillation detector signals into channels 2 - 4, we saw no anomalous events in the resulting T_{12} and T_{23} time-delay histograms. We also performed the same experiment but this time, with the large pulses in channel 2, and the normal-sized scintillation detector pulses in channels 1, 3, and 4, but saw no anomalous events in the T_{12} and T_{23} time-delay histograms. Therefore, we concluded that the anomalous events were probably not due to the crosstalk of a large pulse in one channel causing spurios pulses in the other channels.

In October 1993, we studied the cross-talk properties of the D-module for the second time since the IMAX flight. This time, we plugged the large ($-20{,}000$ pC)

pulse into channel 1, and checked with an oscilloscope probe to see if this caused any of the other channels' discriminators to fire simultaneously. The threshold charge for any discriminator to fire is ~ -2 pC, so this means that there is no crosstalk between channel 1 and the other three channels over a dynamic range of at least 4.0 orders of magnitude. Likewise, when we sequentially plugged the large pulse into channels 2, 3, and 4, we observed no discriminator pulses in the three channels with no input signal to occur simultaneously with the input pulse. *However*, when the large pulse stimulated the 4^{th} discriminator, we noticed a discriminator pulse in channel 3 about 2.06μs *after* the discriminator pulse in channel 4. This unusual crosstalk afterpulsing in channel 3 requires a pulse in channel 4 with a charge greater than $X_4 \sim 60$ pC, which is in the overflow bin of the fourth ADC (A_4(overflow) ~ 40 pC).

This unusual crosstalk involving channel 4 perplexed us at first, since channel 4 does not seem to participate in the production of anomalous events. Anomalous events consist of an exponential time-delay distribution in channel T_{12} (with time constant $\tau_{12} \sim 0.5\mu$s), a nearly delta-function distribution of time-delay in channel T_{23} (at $T_{23} \sim 2.0\mu$s), and small pulses in channel 3 ($A_3 \sim 100$ mV). Channel 4 does not seem to be involved in the anomalous events. In Appendix B, we discuss the possibility that decaying muons can take advantage of this interchannel cross-talk in our module to produce anomalous events, and find a couple of flaws with this hypothesis.

6.5 Inter-module Crosstalk

In November 1993, we finally produced in our Mt. Lemmon Lab events which are remarkably reminiscent of the anomalous events seen during flight. The cause of these unusual Mt. Lemmon events do not seem to be interchannel crosstalk, as hypothesized above.

We observed a very big peak in channel T_{23} at $X_{23} \approx 178$ mV. This effect seems to dominate at 6 PM MST, and seems to disappear at 6 AM MST. The anomalous events

seen on Mt. Lemmon were slightly correlated with long T_{12} time delays, $X_{12} \sim 1100$ mV. All the pulse-heights were relatively small $X_i < 300$ mV. We found that by switching the $3^{\rm rd}$ detector signal with the $2^{\rm nd}$ detector signal eliminated the anomaly. We also found that by exchanging the $3^{\rm rd}$ detector signal with the $4^{\rm th}$ detector signal *increased* the time-delay from 178 mV to 203 mV, the shift being nearly in proportion with the change in counter spacing, as one might expect if these events are caused by slow moving particles. However, this effect was not reproducible. We moved counter 4 down by 29 cm, expecting to see the time-delay T_{24} increase proportionately. We saw no change – the X_{23} peak (with channel 4 plugged into channel 3) remained at 203 mV. Hence, slow-particles are not likely the cause of the anomalous-like events observed on Mt. Lemmon.

We were using a redundant trigger module for delayed coincidences (DCD module) with separate discriminator modules and separate amplifier modules. We found that when we unplugged the DCD module or deactivated one of the 2 different inputs into the DCD-module from counter 2, the anomalous events seen in the D-module readout *disappeared*. We also found that afterpulsing in the amplifiers due to double-overshoot with time-delays $T_{\rm afterpulse} \approx 1.4\,\mu$s might have contributed to causing the anomalous events. Hence, the anomalous events observed at our Mt. Lemmon lab were not due to new particle physics, but due to inter-module cross-talk, possibly through a bad Lemo cable ground, or maybe through the ECL scaler cable. Therefore, it is quite possible that a similar phenomenom, crosstalk between the IMAX electronics and the D-module, occurred during the IMAX balloon flight causing the anomalous events (e.g. the CAMAC 2415 High Voltage supplies used for the drift chambers on the IMAX experiment may have been arc-ing at ~ 500 kHz).

CHAPTER 7

SEARCH FOR PRIMARY IMPS

Our definition of a primary IMP is one that appears to be a *single* supermassive particle that travels through all 4 scintillation detectors, producing signals above threshold in each of the detectors. The primary IMP can either impinge upon the atmosphere and propagate through the remaining overburden to and through the IMAX gondola, or it can be produced by an impinging cosmic ray in the atmosphere or in the gondola shell above the first scintillation detector T1.

7.1 Negligible Velocity-Change Search

From the distance measurements and the time-delay measurements of the last chapter, we compute the 3 velocities for each event, along with the associated uncertainties. From each velocity, we compute the 'slowness' between detector i and detector $i+1$ as $s_i \equiv 1/v_i$, where v_i is the velocity measured between these these detectors; slowness is measured in the units of μs/m. We use slowness as our primary variable rather than velocity because the background distributions for slowness are uniform (flat) as opposed to the background distributions for velocity which are proportional to v^{-2}.

From these 3 slownesses, we compute the weighted mean slowness, $\bar{s}$, and the weighted chi-squared deviation from the mean , χ^2:

$$\begin{aligned} \bar{s} &= \frac{1}{\Omega}\sum_{i=1}^{3}\frac{s_i}{\sigma_{s_i}^2} \\ \chi^2 &= \sum_{i=1}^{3}\frac{(s_i-\bar{s})^2}{\sigma_{s_i}^2} \quad , \end{aligned} \tag{7.34}$$

where Ω is given by:

$$\Omega = \sum_{i=1}^{3}\frac{1}{\sigma_{s_i}^2} \quad . \tag{7.35}$$

If $\chi^2 < 2.5$ (as detailed in Section 7.1.1), then the event is consistent with an IMP that passes through all four detectors without gaining any slowness, or equivalently, without slowing down.

For N degrees-of-freedom, we should study distributions of $(\chi^2)^{N/2}$, whose distribution is slowly-varying (or flat) for background events and is a decaying exponential for hypothetical signal events. For $u \equiv (\chi^2)^{N/2}$, the probability distribution of u for signal events is :

$$P(u)\,du = \frac{C_N}{2}\exp -u^{2/N}\,du, \tag{7.36}$$

where C_N depends only on the number of degrees of freedom N. These qualities of the distribution only hold true for the $N/2$ power of χ^2.

Since we begin with 3 slownesses and use 1 degree of freedom to determine the weighted mean, we are left with a χ^2-distribution with 2 degrees-of freedom. Therefore, $N/2$ is 1, which implies that by looking at the distribution of χ^2, we can determine whether or not there is an IMP signal above the background from accidental coincidences.

7.1.1 Optimal χ^2-histogram Bin Width

Since the signal events would exponentially decay in χ^2 for one degree of freedom and the background events were found to be uniformly distributed in χ^2 (for $\chi^2 < 100$), the signal and noise are best computed by defining the signal as the total number of events found with chi-squared smaller than u, $S(u) = N_s(\chi^2 < u)$, and the background in a

similar manner, $B(u) = N_b(\chi^2 < u)$. Therefore,

$$\begin{aligned} S(u) &= n_s(1 - e^{-u/2}) \\ B(u) &= n_b u \ , \end{aligned} \tag{7.37}$$

where n_s is the total number of signal events and n_b is the total number of background events per unit of χ^2. Hence the signal-to-noise ratio, $E(u)$, is given by:

$$\begin{aligned} E(u) &= \frac{S(u)}{\sqrt{S(u) + B(u)}} \\ &= \frac{n_s(1 - e^{-u/2})}{\sqrt{n_s(1 - e^{-u/2}) + n_b u}} \ . \end{aligned} \tag{7.38}$$

The signal-to-noise ratio can be maximized by choosing chi-squared bins of optimal width, $\Delta\chi^2_m$, and looking for an enhancement above a uniform background in the first χ^2 bin. The optimal width is given by setting the derivative of the logarithm of the signal-to-noise, with-respect-to bin-width, equal to zero:

$$\begin{aligned} \frac{d}{du}(\ln E(u)) &= \frac{d}{du}\left(\ln S - \tfrac{1}{2}\ln(S+B)\right) = 0 \\ &= \frac{\frac{1}{2}e^{-u/2}}{1 - e^{-u/2}} - \frac{1}{2}\frac{\frac{n_s}{2}e^{-u/2} + n_b}{n_s(1 - e^{-u/2}) + n_b u/2} = 0 \end{aligned} \ . \tag{7.39}$$

If $n_b/n_s > 1$, then individual IMP events cannot be distinguished from individual accidental background events, and the above equation reduces to:

$$\frac{e^{-u/2}}{1 - e^{-u/2}} = \frac{1}{u} \ , \tag{7.40}$$

which is a transcendental equation with solution $u \equiv \Delta\chi^2_m = 2.514$. If $n_b/n_s > 1$, then $E(\Delta\chi^2_m) \approx 0.29\sqrt{n_s/n_b}$, which becomes quite small for large n_b/n_s. In a similar spirit, we can derive that if $n_s/n_b \gg 1$, then $E(u = 2.514) \approx 0.78\sqrt{n_s}$, independent of n_b. Therefore, for $n_s/n_b \gg 1$, the signal-to-noise ratio will be $E(2.514) \approx 10$ when $n_s \approx 164$. For any value of n_s/n_b, the total number of signal events, n_s, is computed by Equation 7.37 from the measured number of events in the first bin of the χ^2 histogram, to be:

$$n_s = \frac{S(\Delta\chi^2_m)}{1 - \exp\left(-\Delta\chi^2_m/2\right)} \approx 1.3S(\Delta\chi^2_m). \tag{7.41}$$

7.1.2 Results of $\Delta v \approx 0$ Search

We show the IMAX flight and Monte Carlo distributions of χ^2 and of $\bar{s}$ (see Eq. 7.34) for the negligible-Δv search in Figures 7.31-7.34. From the IMAX flight distribution of χ^2 in Figure 7.31 (where we use the optimal bin width of $\Delta\chi^2_m = 2.5$), we determine the number of background events, $B(\Delta\chi^2_m) \equiv n_b \Delta\chi^2_m$, by averaging over all bins for $\chi^2 < 100$:

$$B(\Delta\chi^2_m) \quad = \quad 4.0 \pm 0.3 \quad . \tag{7.42}$$

The actual number of events observed with $\chi^2 < \Delta\chi^2_m$, is:

$$N(\Delta\chi^2_m) \quad = \quad 5 \quad , \tag{7.43}$$

which corresponds[127] to a 95% C.L. upper limit $S(\Delta\chi^2_m) < 7$. Correcting this result for the number of IMP events which would be expected outside the first χ^2 bin (Equation 7.41), we obtain $n_s < 9.1$.

In Figures 7.32-7.34, we plot the flight and Monte Carlo distributions of $\bar{s}$ with different cuts, $\chi^2 < \infty$, $\chi^2 < 60$, and $\chi^2 < 2.5$. For the flight distribution with the $\chi^2 < \infty$ cut (Figure 7.32), the anomalous events are clearly visible, at $\bar{s} \in [1.5, 2.0]\mu$s/m, which is not at the same position as the peak in the IMP Monte Carlo distribution. When we require that $\chi^2 < 60$ (Figure 7.33), most of the anomalous events disappear, but a small bump above the minimal accidental coincidence background remains; otherwise the flight data mirrors the accidental coincidence Monte Carlo. For $\chi^2 < 2.5$ (Figure 7.34), the anomalous events in the flight data disappear altogether, as do the $a_1 = 0.04$ cm^2/g IMP Monte Carlo events, and only 5 flight data events remain. The fitted slownesses of these 5 events are quite consistent with the distribution expected from accidental coincidences. The error bars for S_{12} and S_{23} shown in Figure 6.27 are the prime determinants in the shape of the restricted-χ^2 slowness distributions shown here.

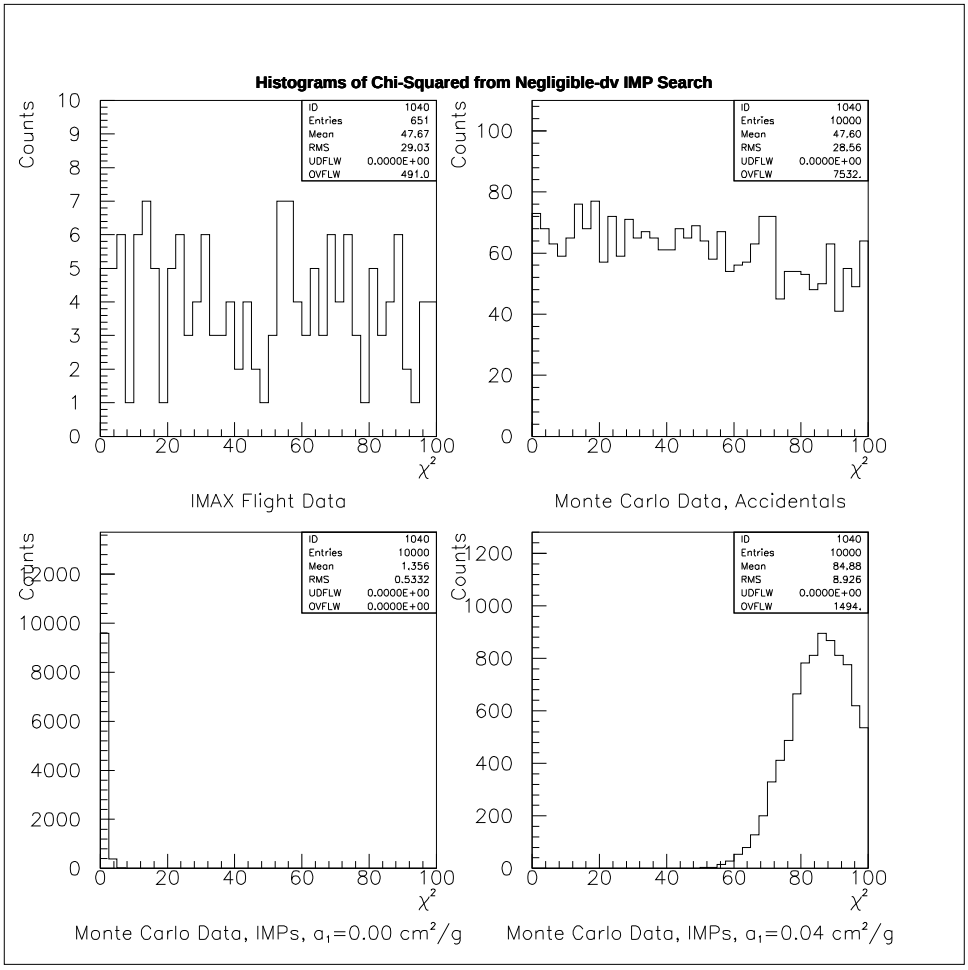

Figure 7.31: IMAX flight and Monte Carlo χ^2-distributions for fitting each four-fold coincident event to a constant velocity. For UT $\in [10.0, 15.0]$ hours, we checked each four-fold coincidence for consistency with a single particle that has travelled through all 4 scintillation detectors. We show the data from the IMAX flight, and from three separate Monte Carlos, one for purely accidental coincidences, and two for IMP-like events with different values of a_1 (see Section 7.4). If an event has $\chi^2 < 2.5$, then it is consistent with a constant velocity IMP. Note the flatness of the background for the $\Delta v = 0$ distribution up to $\chi^2 = 100$ in both the IMAX flight data and the simulated accidental coincidences.

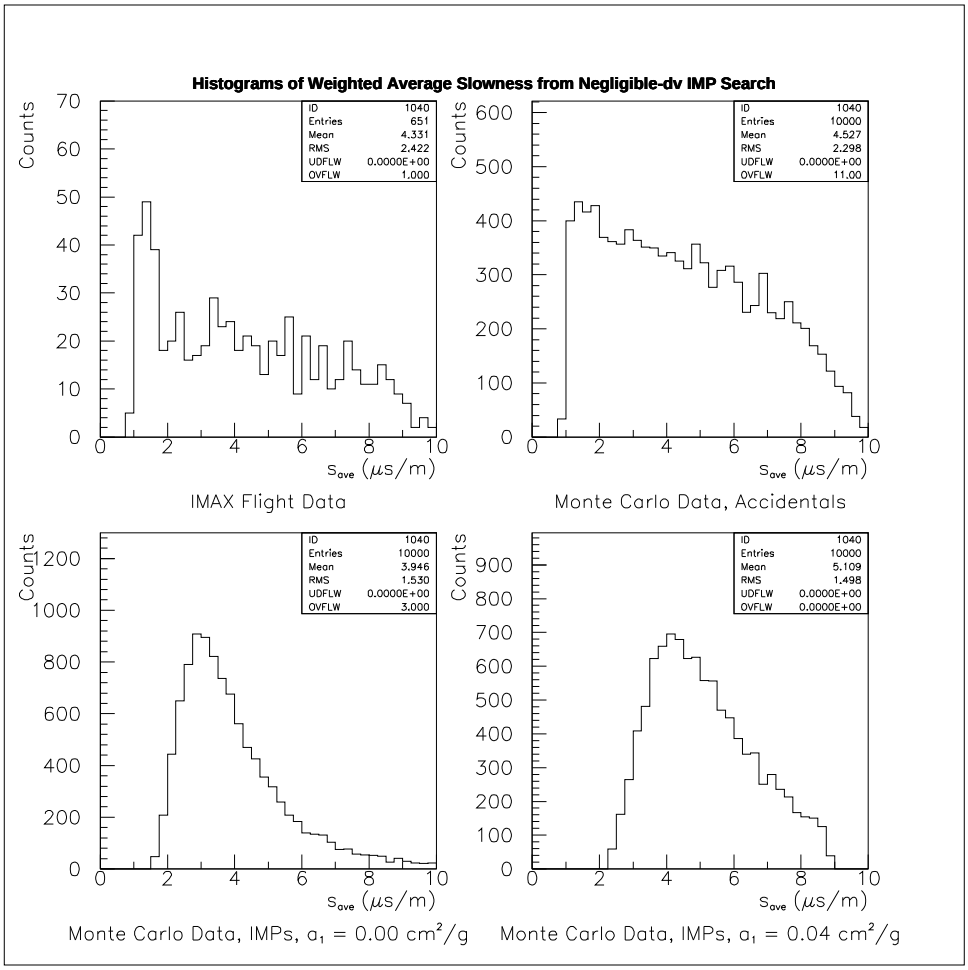

Figure 7.32: **Negligible-Δv $\bar{s}$-distributions without χ^2 cut.** We show the IMAX flight and Monte Carlo $\bar{s}$-distributions for fitting each four-fold coincident event to a constant slowness. For UT $\in [10.0, 15.0]$ hours, we checked each four-fold coincidence for consistency with a single particle that has travelled through all 4 scintillation detectors with negligible velocity change. We show the data from the IMAX flight, and from three separate Monte Carlos, one for purely accidental coincidences, and two for IMP-like events (see Section 7.4). The above $\bar{s}$-distributions have no cuts on χ^2.

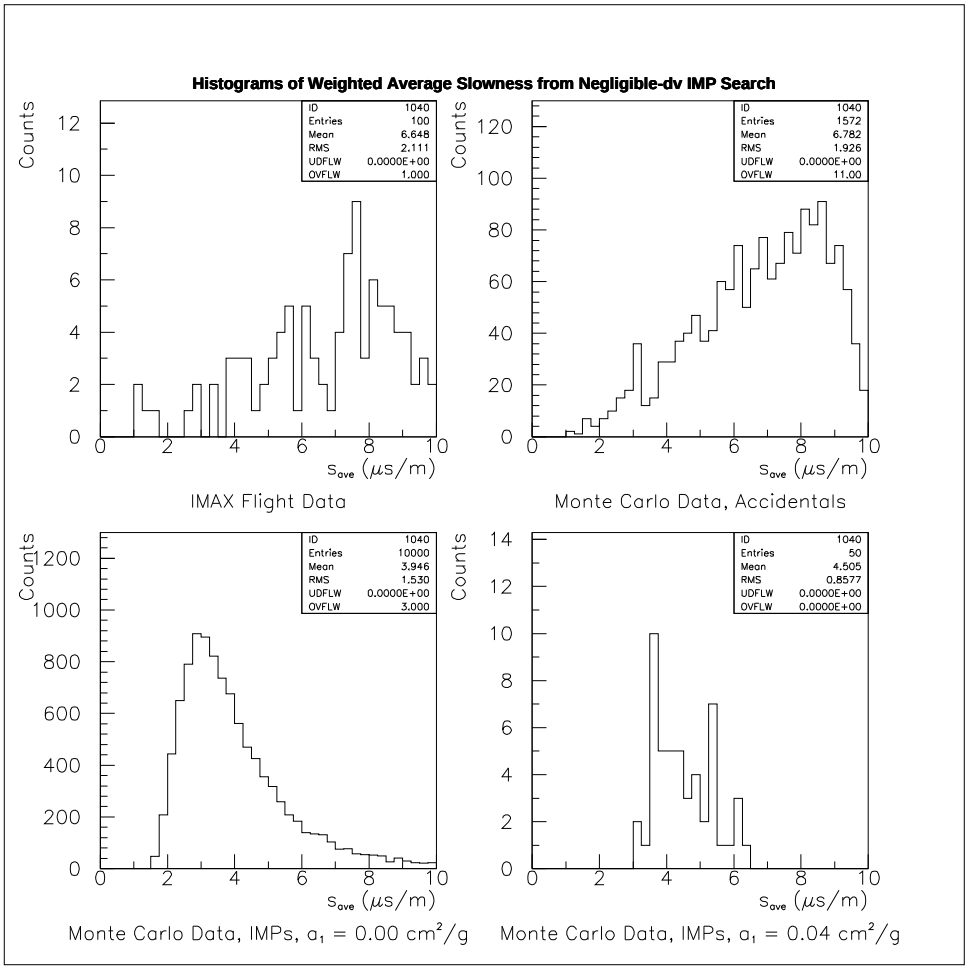

Figure 7.33: **Negligible-Δv $\bar{s}$-distributions with $\chi^2 < 60$ cut.** We show the IMAX flight and Monte Carlo $\bar{s}$-distributions for fitting each four-fold coincident event to a constant slowness. For UT $\in [10.0, 15.0]$ hours, we checked each four-fold coincidence for consistency with a single particle that has travelled through all 4 scintillation detectors with negligible velocity change. We show the data from the IMAX flight, and from three separate Monte Carlos, one for purely accidental coincidences, and two for IMP-like events (see Section 7.4). The above $\bar{s}$-distributions have a cut that requires $\chi^2 < 60$, to eliminate the events that have a very poor fit to a constant velocity IMP.

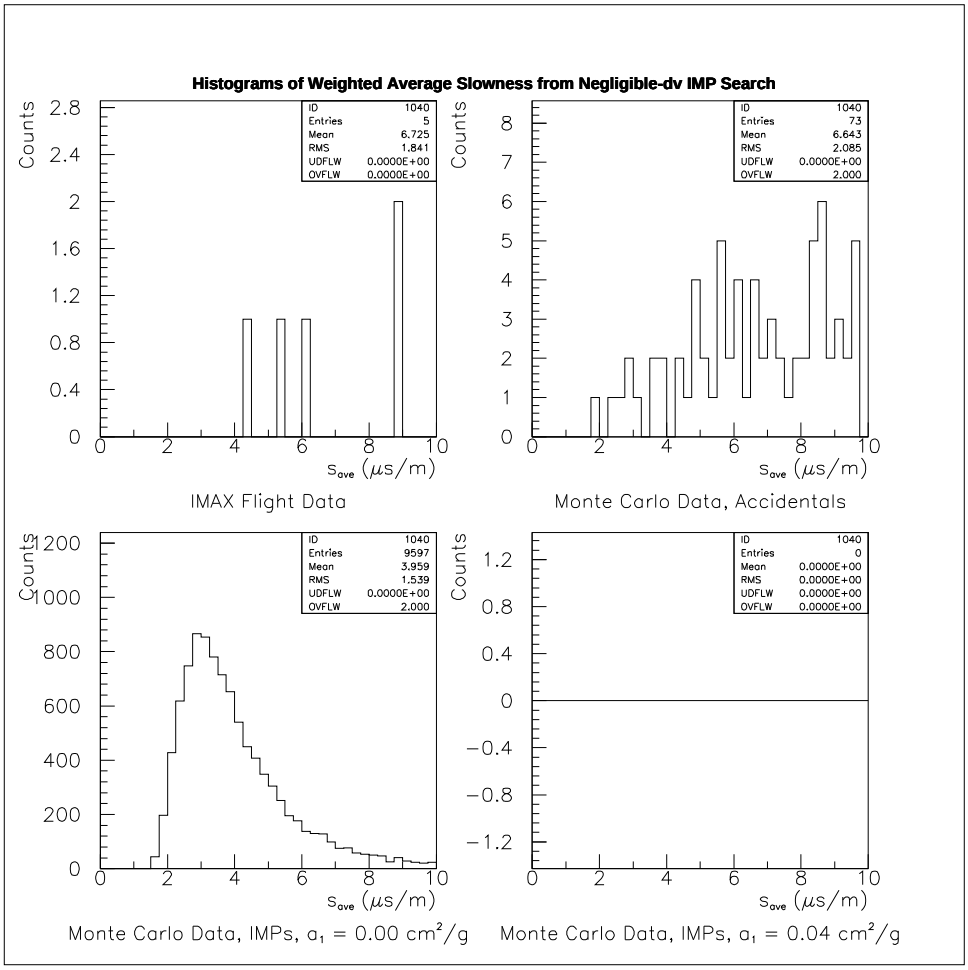

Figure 7.34: **Negligible-Δv $\bar{s}$-distributions with $\chi^2 < 2.5$ cut.** We show the IMAX flight and Monte Carlo $\bar{s}$-distributions for fitting each four-fold coincident event to a constant slowness. For UT $\in [10.0, 15.0]$ hours, we checked each four-fold coincidence for consistency with a single particle that has travelled through all 4 scintillation detectors with negligible velocity change. We show the data from the IMAX flight, and from three separate Monte Carlos, one for purely accidental coincidences, and two for IMP-like events (see Section 7.4). The above $\bar{s}$-distributions have a cut that requires $\chi^2 < 2.5$, to keep only those events that have an excellent fit to a constant velocity IMP.

7.2 Small Velocity-Decrease Search

In a similar manner, we can search for IMPs that actually slow down slightly within the IMAX telescope. We hypothesize that the energy-loss for a given amount of material is a power-law in velocity:

$$\frac{dE}{dx} = -\alpha_n v^n \quad , \tag{7.44}$$

which implies that the slowness-gain (with $\gamma \equiv 3 - n$) is:

$$\begin{aligned} \frac{ds}{dx} &= +\frac{\alpha_n}{M_x} s^{3-n} \\ &= +a_\gamma s^\gamma \end{aligned} \quad . \tag{7.45}$$

For $\gamma = 1$, the slowness as a function of the total material traversed is:

$$s_1(x) = s_0 \exp(a_1 x) \quad , \tag{7.46}$$

where s_0 is the slowness of the IMP at $x = 0$. For $\gamma \neq 1$, by solving equation 7.45, the functional form of slowness is:

$$s_{\gamma \neq 1}(x) = s_0 \left(1 - (\gamma - 1) a_\gamma s_0^{\gamma - 1} x\right)^{\frac{1}{1-\gamma}} \quad . \tag{7.47}$$

Hence, if we measure several slownesses as a function of x, for all γ, determination of s_0 and a_γ is a complicated solution to nonlinear equations[1]. However, for all γ, if $a_\gamma s_0^{\gamma-1} x << 1$, then:

$$s_\gamma(x) \approx s_0 + a_\gamma s_0^\gamma x \quad , \tag{7.48}$$

which is a much easier linear fitting problem, and permits a simple solution.

With a sequence of detectors (with thicknesses x_i and distances to the succeeding detector $d_{i,i+1}$), the observed slowness between detectors j and k will be a weighted sum of the slownesses between each pair of successive detectors between detectors j and k:

$$s_{jk} = \frac{\sum_{i=j}^{k-1} d_{i,i+1} s_{i,\gamma}(y)}{d_{j,k}} \quad , \tag{7.49}$$

[1] especially when there are unused detectors of significant grammage interspersed between the active detectors

where the slowness after the ith detector is a function of the total amount of material traversed, y:

$$s_{i,\gamma}(y) \quad = \quad s_\gamma \left(\sum_{n=1}^{i} x_n \right) \quad . \tag{7.50}$$

For small-slowness gains, when $a_\gamma s_0^{\gamma-1} x << 1$, then with equations 7.48 and 7.49, we can use the three measured slownesses to estimate the best-fit parameters s_0 and $a_\gamma s_0^\gamma$ for each event. Since only 1 degree of freedom remains with this 2-parameter fit, we should compile distributions of $(\chi^2)^{1/2}$ to search for events clustered above a slowly-varying background near $\chi^2 = 0$, as in Figure 7.35.

The histograms in Figure 7.35 show the results of this search. For IMPs, we expect a gaussian peak at $(\chi^2)^{1/2} = 0$ with a standard deviation ~ 1 (see the IMP Monte Carlos in Figure 7.35). From the Monte Carlo of accidental coincidences (Figure 7.35), we expect a background peaked at $(\chi^2)^{1/2} = 0$, but with an $1/e$-width ~ 20. The IMAX flight data closely resembles the accidental coincidence Monte Carlo, and does not have a sharp peak at zero, as would be expected from the IMP Monte Carlos.

In a similar manner as used in the $\Delta v \approx 0$ search, we estimate an upper limit on the number of slightly-slowing IMPs by taking the number of counts in the first bin as the signal (5 events), and comparing this to the background found by averaging the number of counts in the first 8 bins (7.5 ± 1 counts/bin). By applying the standard technique of estimating an upper limit for a signal above a Poisson background[127], we arrive at an upper limit on the number of IMP events during the 5 hour flight data set of 6.9 events, where we have taken care to count the signal events that would reside outside the first $\sqrt{\chi^2}$ bin (by multiplying the first bin result by 1.3).

We show the effect of different cuts of $\sqrt{\chi^2}$ on the $a_\gamma s_0^\gamma$ vs. s_0 two-dimensional distributions in Figures 7.36-7.38. We would expect an IMP signal to be more prominent in the $\sqrt{\chi^2} < 1$ histogram than in the histograms which do not have as strict a fitting requirement on $\sqrt{\chi^2} < 1$. Yet, in any case, from the IMP Monte Carlo for $a_1 = 0.04$ cm^2/g, we would expect that for the $\sqrt{\chi^2} < 1$ histogram to have a short line

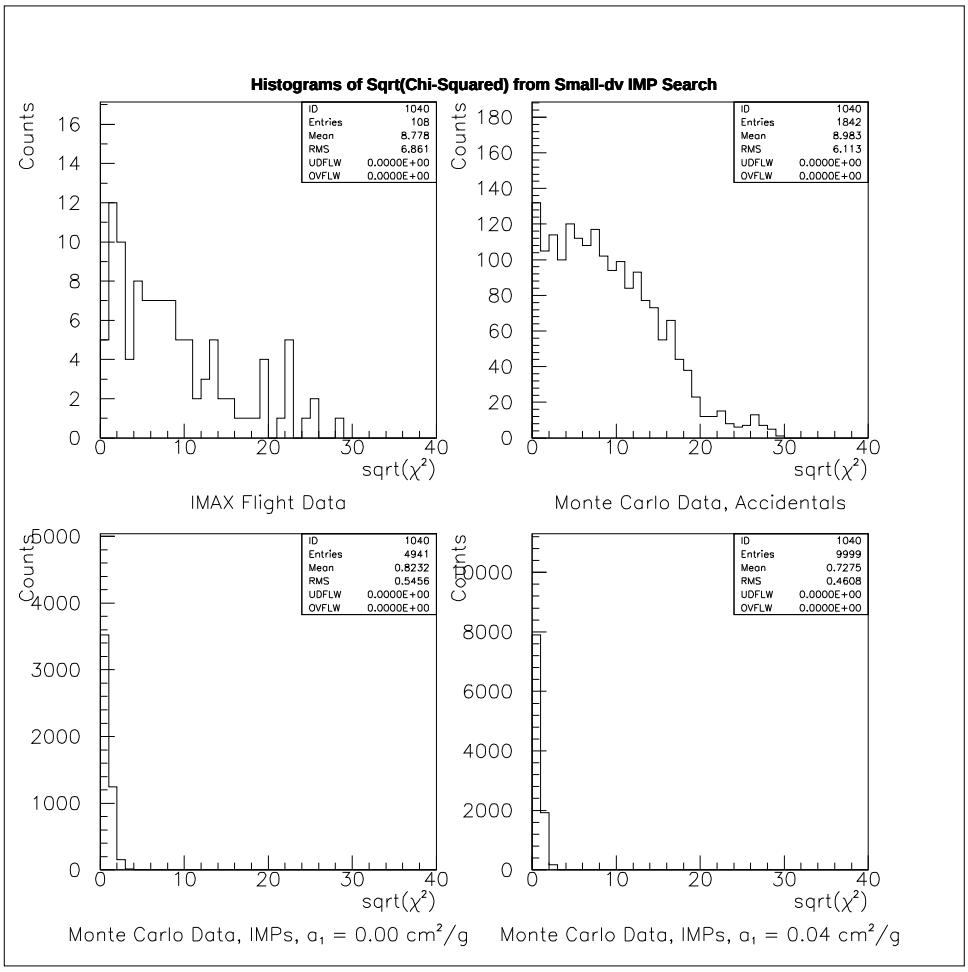

Figure 7.35: IMAX flight and Monte Carlo $\sqrt{\chi^2}$-distributions for fitting each four-fold coincident event to a slightly-slowing IMP. For UT $\in [10.0, 15.0]$ hours, we checked each four-fold coincidence for consistency with a single particle that has travelled through all 4 scintillation detectors and slowed down slightly. We show the data from the IMAX flight, and from three separate Monte Carlos, one for purely accidental coincidences, and two for IMP-like events (see Section 7.4).

segment with slope equal to one with an enhanced number of events. This is not evident in the flight data.

7.3 Large Velocity-Decrease Search

For large $a_\gamma s_0^{\gamma-1} x$, equation 7.48 breaks down, so that for large velocity-decreases, our previous two searches will be invalid. Another complication to a large velocity-change IMP search, is that the IMAX experiment had a significant amount of material between the scintillation detectors that we used (see Figure 4.8, and Tables 6.1 and 6.2)). This additional material will cause the IMP velocity to decrease while the IMP is travelling through the inert material between the two detectors. Thus the measured velocity will be the weighted average of the instantaneous velocities between the different absorbers that lie between the two detectors.

As an example, for $n = 2$, the slowness increases exponentially with the amount of material (Eq. 7.46), so that the measured slowness will be:

$$s_k = s_0 \sum_{i=k'}^{k-1} f_{i,i+1} \exp\left(a_1 \sum_{j=1}^{i} x_j \right), \tag{7.51}$$

where $f_{i,i+1} \equiv d_{i,i+1}/d_{1,i+1}$ is the fractional separation of neighboring 'absorbers', and x_i is the thickness (in g/cm^2) of each absorber (see Table 6.1), and s_0 is the slowness of the IMP just prior to entering detector 1. The index k' represents the first detector in the pair of detectors used to measure the slowness; and the index k represents the second detector of this pair (i.e., for IMAX, the 3 (k',k) detector pairs are: (1,7), (7,11), and (11,12)). We define the s_k determined in Equation 7.51 as:

$$s_k \equiv s_0 \exp(a_1 \Delta), \tag{7.52}$$

where Δ is to be determined for each detector and absorber configuration. As long as

$$\mid a_1 \left(\sum_{j=1}^{i} x_j - \Delta \right) \mid \ll 1, \text{ for all } i \in [1, k], \tag{7.53}$$

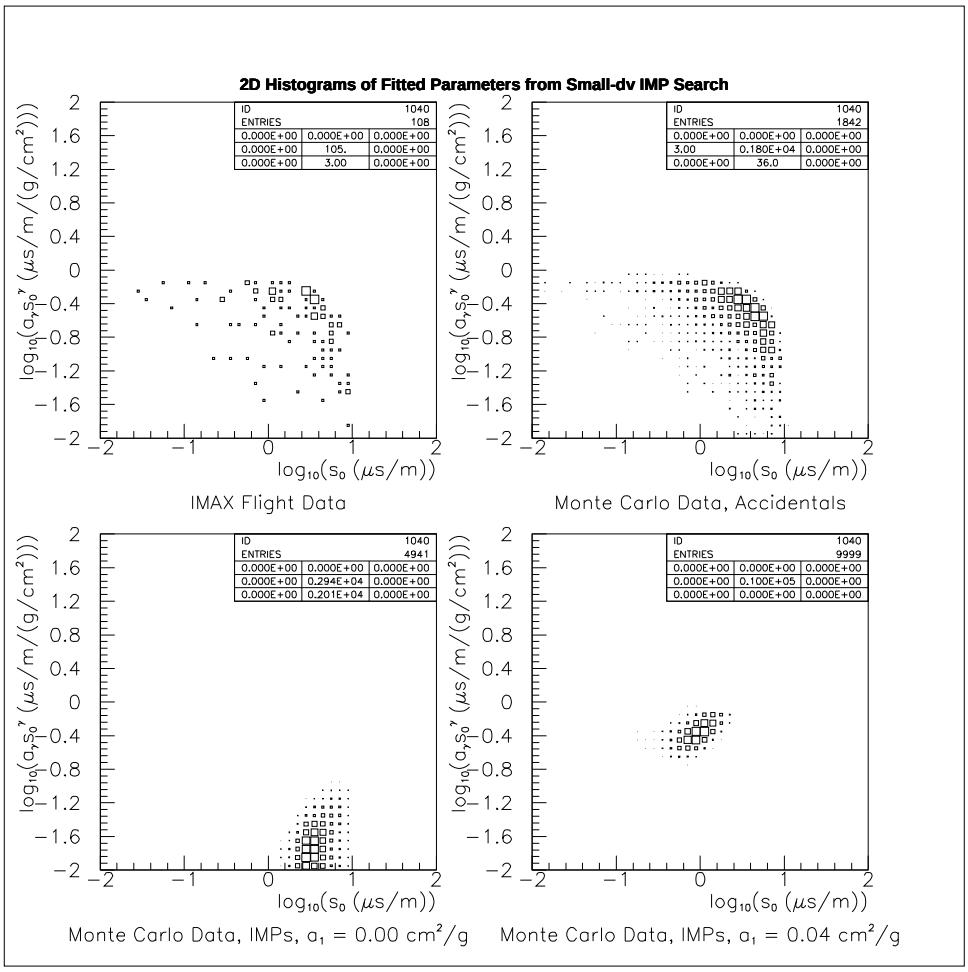

Figure 7.36: **Small-Δv search parameter distributions without $\sqrt{\chi^2}$ cut.** We show the IMAX flight and Monte Carlo two dimensional $(\log_{10}(a_\gamma s_0^\gamma), \log_{10}(s_0))$-histograms for fitting each four-fold coincident event to a slightly-slowing IMP. For UT $\in [10.0, 15.0]$ hours, we checked each four-fold coincidence for consistency with a single particle that has travelled through all 4 scintillation detectors and slowed down at a small rate. We show the data from the IMAX flight, and from three separate Monte Carlos, one for purely accidental coincidences, and two for IMP-like events (see Section 7.4). The above histograms have no cuts on $\sqrt{\chi^2}$.

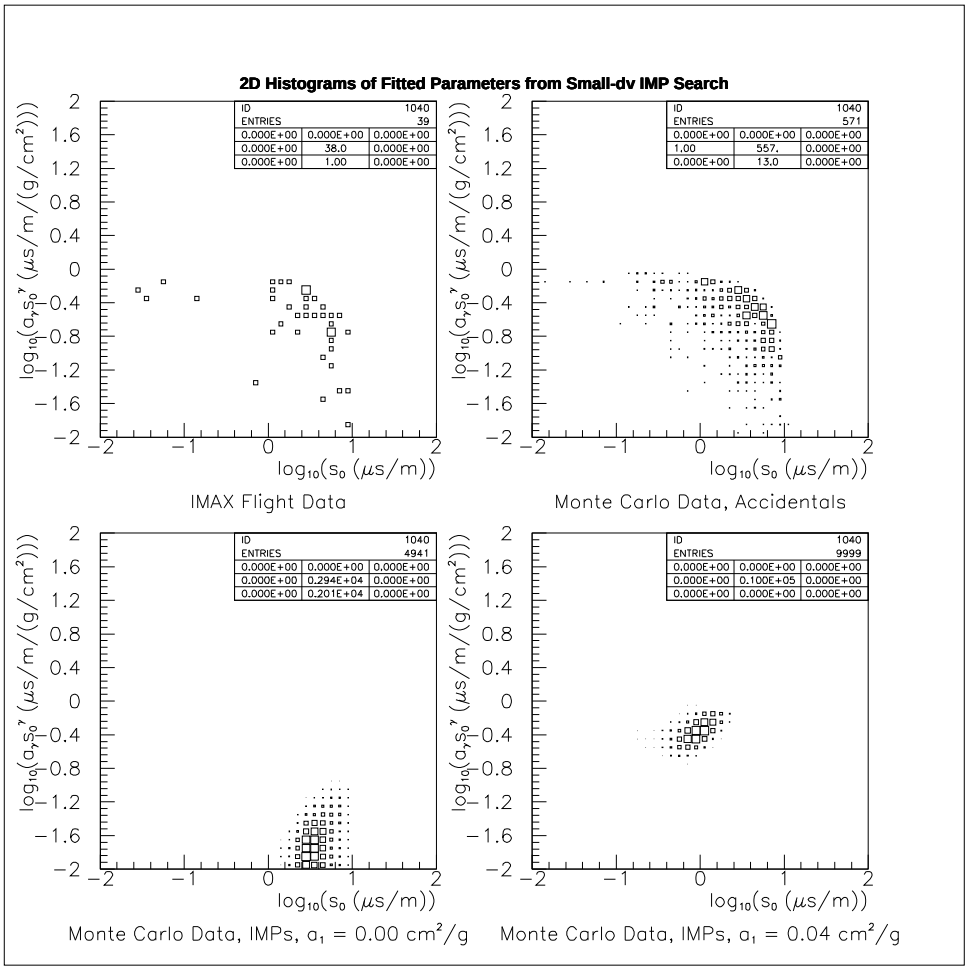

Figure 7.37: **Small-Δv search parameter distributions with $\sqrt{\chi^2} < 5$ cut.** We show the IMAX flight and Monte Carlo two dimensional $(\log_{10}(a_\gamma s_0^\gamma), \log_{10}(s_0))$-histograms for fitting each four-fold coincident event to a constant slowness. For UT $\in [10.0, 15.0]$ hours, we checked each four-fold coincidence for consistency with a single particle that has travelled through all 4 scintillation detectors and slowed down at a small rate. We show the data from the IMAX flight, and from three separate Monte Carlos, one for purely accidental coincidences, and two for IMP-like events (see Section 7.4). The above histograms have a cut that requires $\sqrt{\chi^2} < 5$, to eliminate the events that have a poor fit to a slightly-slowing IMP.

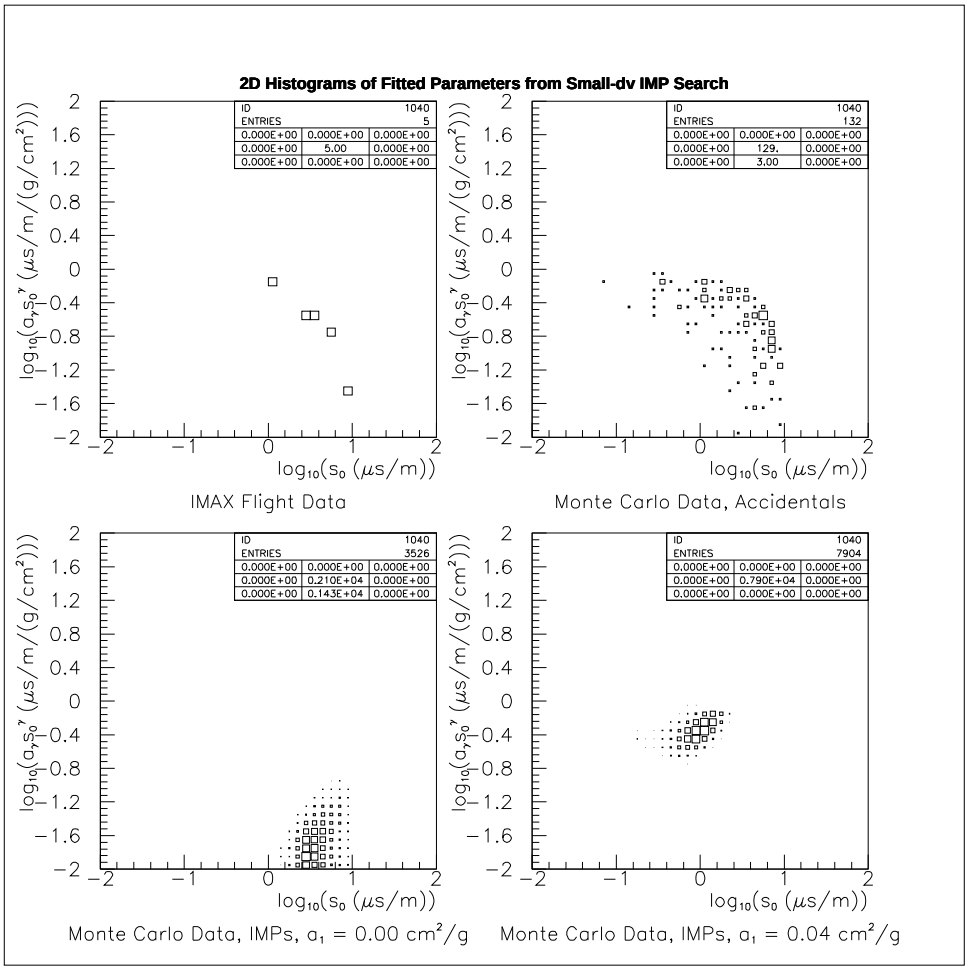

Figure 7.38: **Small-Δv search parameter distributions with $\sqrt{\chi^2} < 1$ cut.** We show the IMAX flight and Monte Carlo two dimensional $(\log_{10}(a_\gamma s_0^\gamma), \log_{10}(s_0))$-histograms for fitting each four-fold coincident event to a constant slowness. For UT $\in [10.0, 15.0]$ hours, we checked each four-fold coincidence for consistency with a single particle that has travelled through all 4 scintillation detectors and slowed down at a small rate. We show the data from the IMAX flight, and from three separate Monte Carlos, one for purely accidental coincidences, and two for IMP-like events (see Section 7.4). The above histograms have a cut that requires $\sqrt{\chi^2} < 1$, to retain only those events that have an excellent fit to a slightly-slowing IMP.

then we can easily determine Δ:

$$\Delta(k) \approx \frac{1}{k} \sum_{i=1}^{k} \sum_{j=1}^{i} x_j. \tag{7.54}$$

Since we measure the value of the slowness between IMAX detectors S1 and S2 (detectors 7 and 11 respectively) with the greatest precision, we choose to redefine s_k in terms of the slowness s_7^0 for an IMP just prior to entering detector 7 (IMAX detector S1) ($s_k \equiv s_7^0 \exp(a_1 \Delta(k))$, where s_k is the average slowness determined from Eq. 7.51 (or measured) and s_7^0 is the instantaneous slowness determined from Eq. 7.46). With this definition, $\Delta(7)$ will be the negative of the weighted sum (eq. 7.51) of the absorber and detector thicknesses prior to detector S1 (e.g. T1, C1a, C1b, C3a, C3b, C3c), and $\Delta(11)$ will be the weighted sum of the absorber and detector thicknesses of S1, C2a, C2b, and C2c, and $\Delta(12)$ will be the unweighted sum of the material in S1, C2a, C2b, C2c, and S2. We use Table 6.1 to determine $\Delta(n)$ for each of the 3 successive slowness measurements, and these values are summarized in Table 7.9.

Slowness	n	$\Delta(n)$ **(g/cm^2)**
s_7	7	-3.747 ± 0.173
s_{11}	11	1.878 ± 0.107
s_{12}	12	5.20 ± 0.18

Table 7.9: The values of $\Delta(n)$ for the detector and absorber geometry used in the IMAX experiment.

With the values of $\Delta(n)$ tabulated above, we take the logarithm of both sides of Equation 7.52 and perform a *linear* regression on the 3 equations (one equation for each slowness measurement (s_7, s_{11} and s_{12})) to determine the best fit values of s_7^0 and a_1:

$$\ln(s_n) = a_1 \Delta(n) + \ln(s_7^0). \tag{7.55}$$

We still have only one degree-of-freedom per event, so we compile the $(\chi^2)^{1/2}$ for this large-Δv search in Figure 7.40.

We show the large-Δv $(\chi^2)^{1/2}$-distribution from the IMAX flight and from Monte Carlos in Figures 7.39 and 7.40. By eliminating those events with $a_1 < 0$ in the accidental

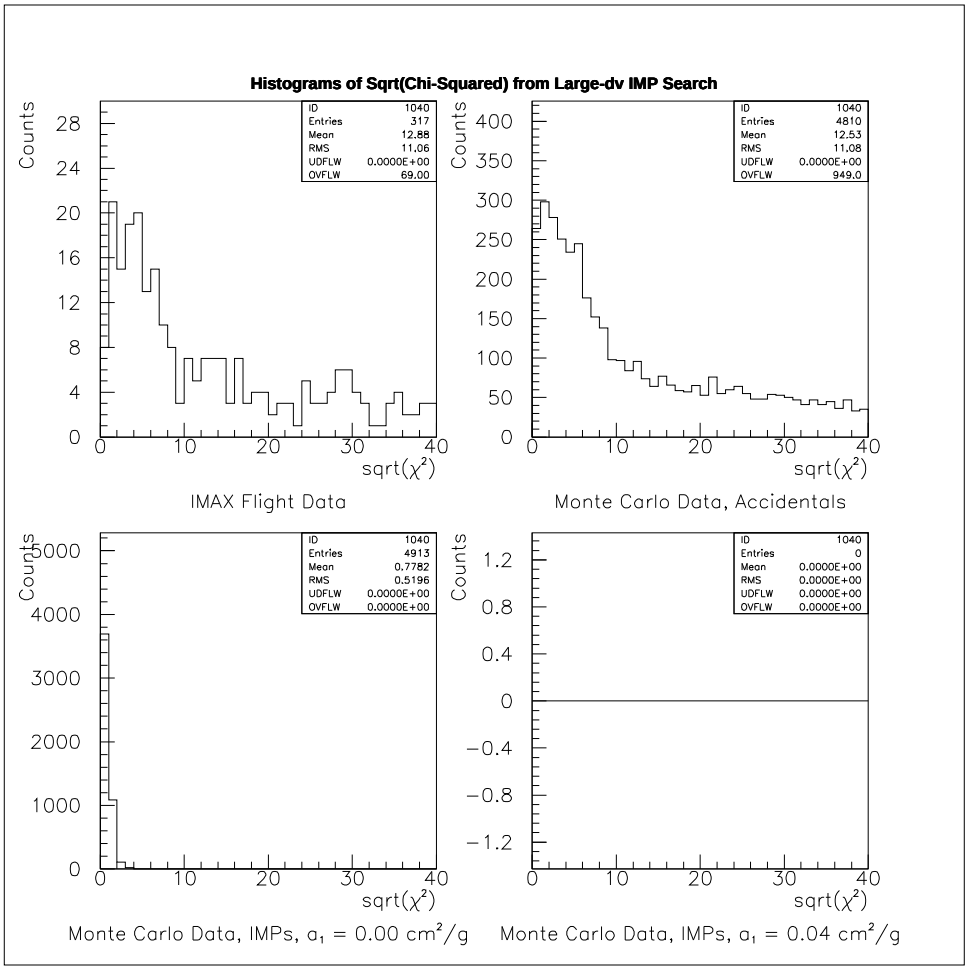

Figure 7.39: We show the IMAX flight and Monte Carlo $\sqrt{\chi^2}$-distributions for fitting each four-fold coincident event to a large-Δv IMP; for the unphysical region, $a_1 < 0$. For UT $\in [10.0, 15.0]$ hours, we checked each four-fold coincidence for consistency with a single particle that has travelled through all 4 scintillation detectors and slowed down at a large rate. We show the data from the IMAX flight, and from three separate Monte Carlos, one for purely accidental coincidences, and two for IMP-like events (see Section 7.4).

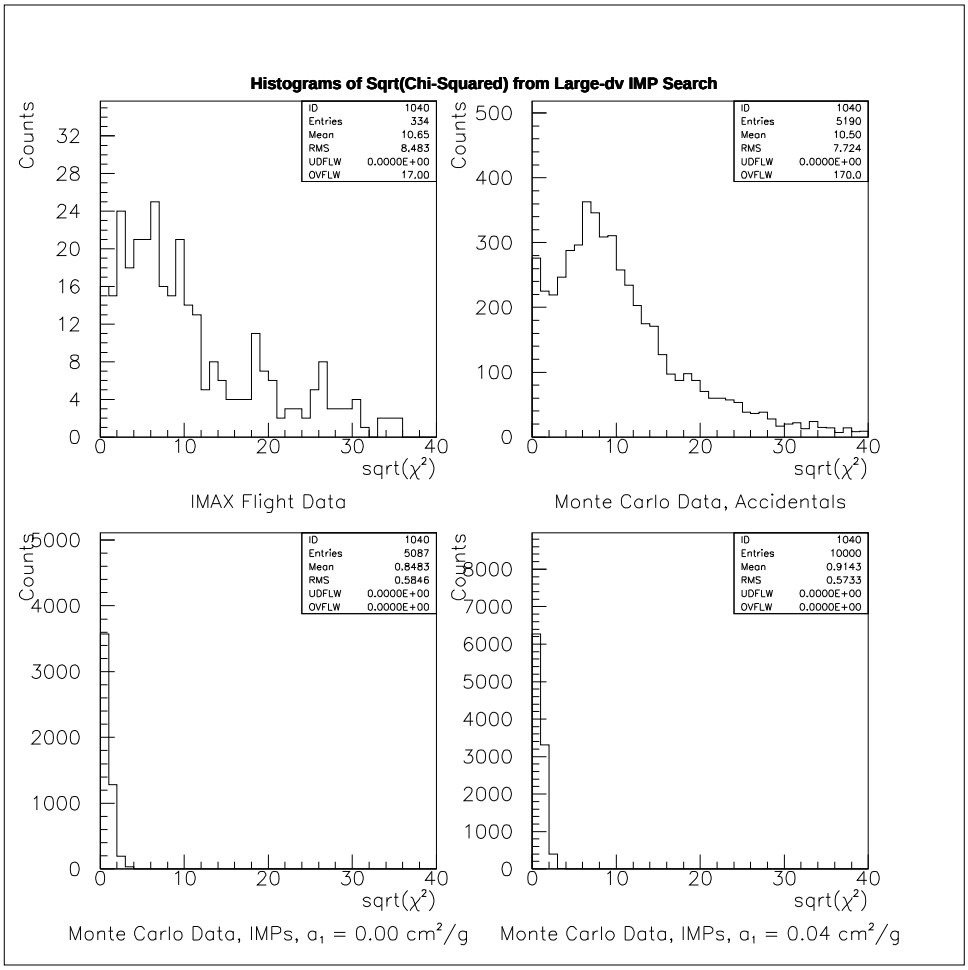

Figure 7.40: We show the IMAX flight and Monte Carlo $\sqrt{\chi^2}$-distributions for fitting each four-fold coincident event to a large-Δv IMP; for the physical region, $a_1 > 0$. For UT $\in [10.0, 15.0]$ hours, we checked each four-fold coincidence for consistency with a single particle that has travelled through all 4 scintillation detectors and slowed down at a large rate. We show the data from the IMAX flight, and from three separate Monte Carlos, one for purely accidental coincidences, and two for IMP-like events (see Section 7.4).

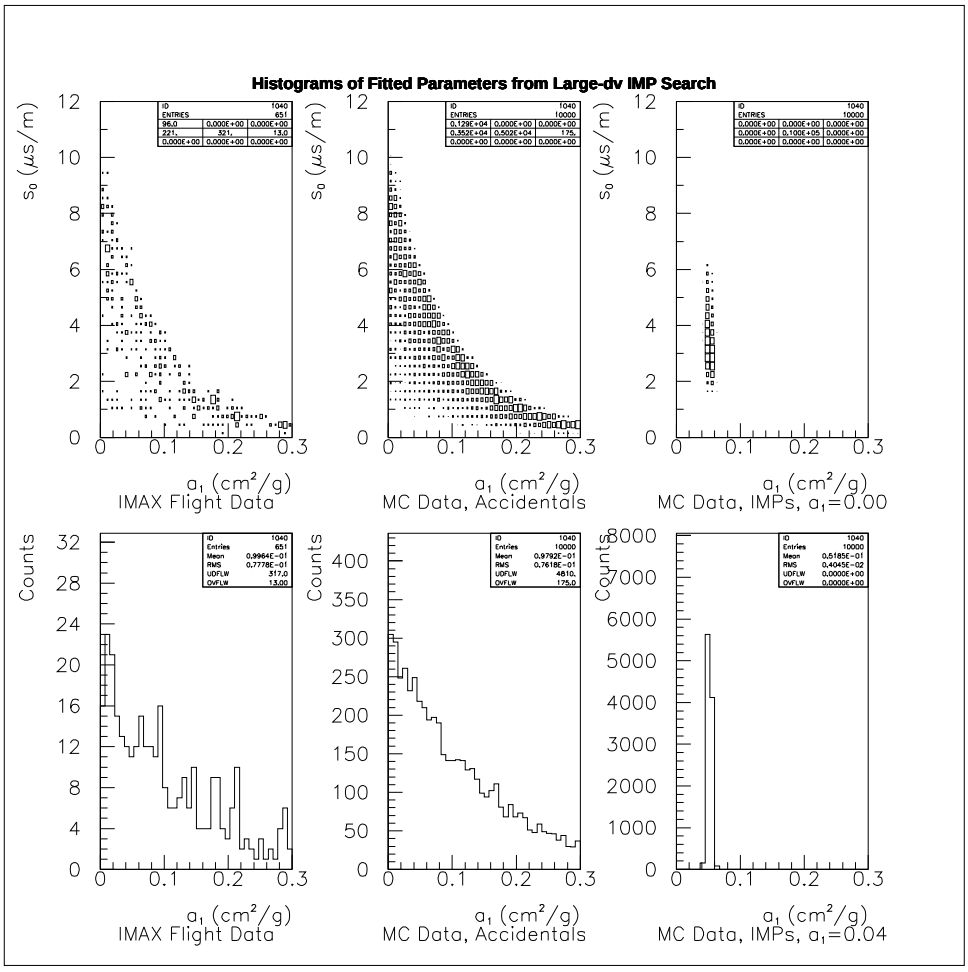

Figure 7.41: **Large-Δv search parameter distributions without the $\sqrt{\chi^2}$ cut.** We show the IMAX flight and Monte Carlo two dimensional (s_0, a_1)-histograms and one dimensional a_1-histograms for fitting each four-fold coincident event to a large-Δv IMP. For UT $\in [10.0, 15.0]$ hours, we checked each four-fold coincidence for consistency with a single particle that has travelled through all 4 scintillation detectors and slowed down at a large rate. We show the data from the IMAX flight, and from two separate Monte Carlos, one for purely accidental coincidences, and one for IMP-like events (see Section 7.4). The above histograms have no cuts on $\sqrt{\chi^2}$.

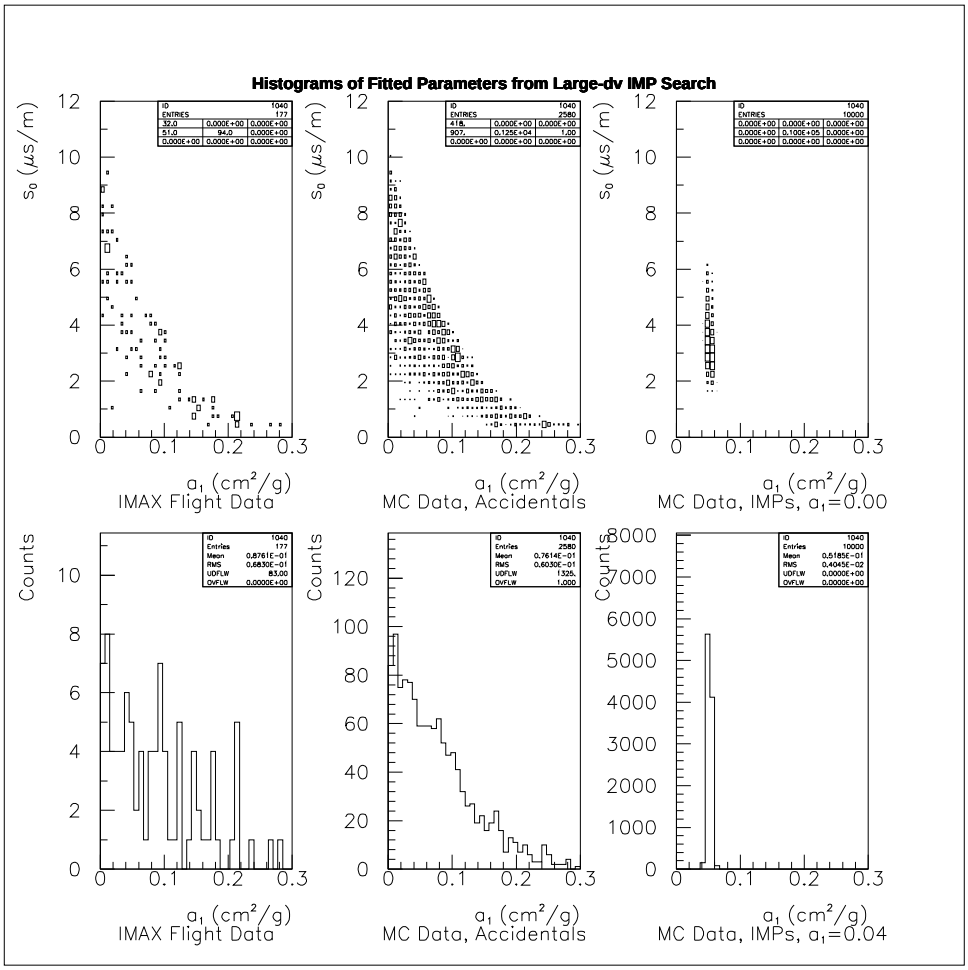

Figure 7.42: **Large-Δv search parameter distributions with $\sqrt{\chi^2} < 5$ cut.** We show the IMAX flight and Monte Carlo two dimensional (s_0, a_1)-histograms and one dimensional a_1-histograms for fitting each four-fold coincident event to a large-Δv IMP. For UT $\in [10.0, 15.0]$ hours, we checked each four-fold coincidence for consistency with a single particle that has travelled through all 4 scintillation detectors and slowed down at a large rate. We show the data from the IMAX flight, and from two separate Monte Carlos, one for purely accidental coincidences, and one for IMP-like events (see Section 7.4). The above histograms have a cut that requires $\sqrt{\chi^2} < 5$, to eliminate the events that have a poor fit to an IMP with large-Δv.

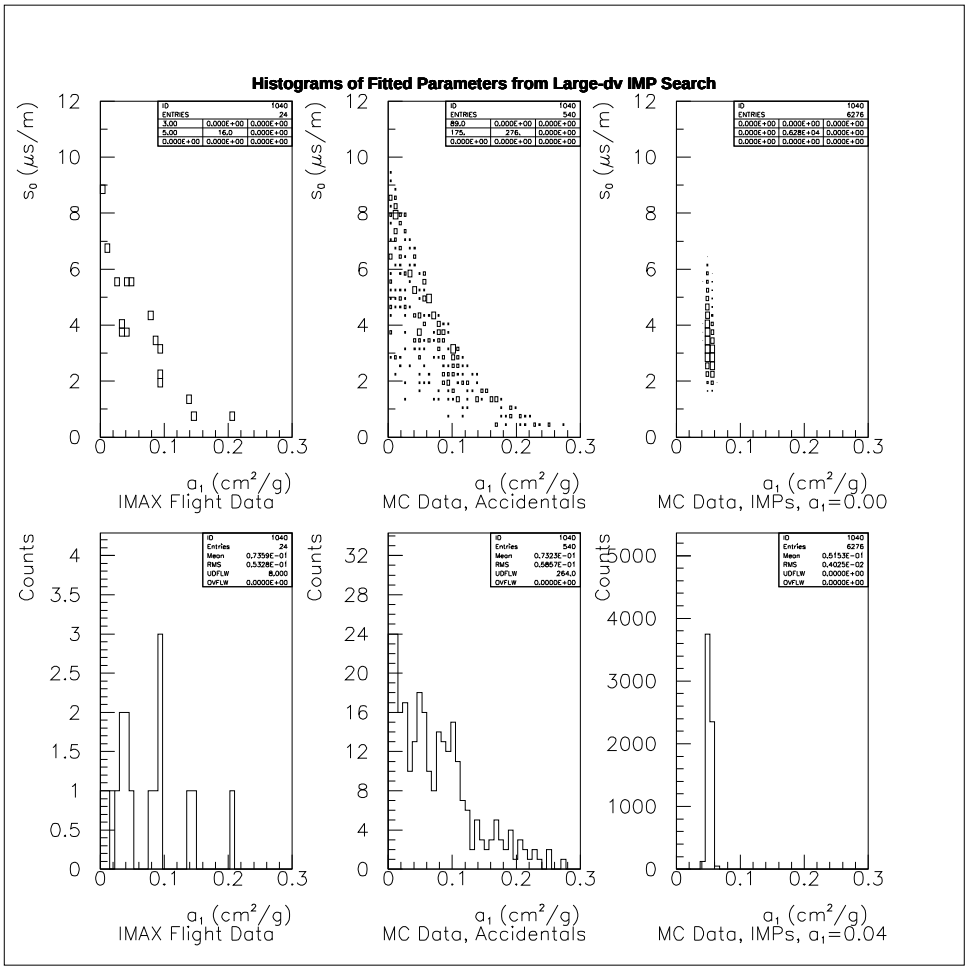

Figure 7.43: **Large-Δv search parameter distributions with $\sqrt{\chi^2} < 1$ cut.** We show the IMAX flight and Monte Carlo two dimensional (s_0, a_1)-histograms and one dimensional a_1-histograms for fitting each four-fold coincident event to a large-Δv IMP. For UT $\in [10.0, 15.0]$ hours, we checked each four-fold coincidence for consistency with a single particle that has travelled through all 4 scintillation detectors and slowed down at a large rate. We show the data from the IMAX flight, and from two separate Monte Carlos, one for purely accidental coincidences, and one for IMP-like events (see Section 7.4). The above histograms have a cut that requires $\sqrt{\chi^2} < 1$, to keep only those events that have an excellent fit to an IMP with large-Δv.

coincidence Monte Carlo and possibly in the flight data in Figure 7.40, we create a wide anti-peak, or dip,[2] at $\sqrt{\chi^2} = 0$ of width ~ 4, and a small, narrow peak at $\sqrt{\chi^2} = 0$ of width ~ 1. The IMP Monte Carlos both show a gaussian distribution of width ~ 1, as expected.

In a similar manner as used in the $\Delta v \approx 0$ and the small-Δv searches, we estimate an upper limit on the number of large-Δv IMPs by taking the number of counts in the first bin as the signal (16 events), and comparing this to the (assumed to be flat) background found by averaging the number of counts in the first 4 bins (18.25 ± 2.14 counts/bin). We only averaged over the first 4 bins due to the large bump in the physically allowed ($a_1 > 0$) $\sqrt{\chi^2}$-distribution for the accidental coincidence Monte Carlo at $\sim 8 \pm 3$. We then arrive at an upper limit on the number of IMP events during the 5 hour flight data set of 11.1 events (95% C.L.), where we have taken care to count the signal events that would reside in the second $\sqrt{\chi^2}$ bin (by multiplying the first bin result by 1.3).

We have histograms of the fitted parameters a_1 and s_0 with different cuts on $\sqrt{\chi^2}$ in Figures 7.41-7.43. As in the small-Δv search, we would expect any IMP signal events to be most prominent in the $\sqrt{\chi^2} < 1$ distributions of a_1, with a narrow peak at particular values of a_1, as indicated by the IMP Monte Carlo in these figures. For $\sqrt{\chi^2} < \infty$, we find that the histogram of a_1 for the flight data has some possibly significant fluctuations from the accidental coincidence Monte Carlo background. However, when we restrict the data set to $\sqrt{\chi^2} < 5$ and then to $\sqrt{\chi^2} < 1$, we don't see any significant evidence for these fluctuations remaining, as the a_1 histograms would show under the large-Δv IMP hyptothesis. However, there may be a small hint of a signal at $a_1 = 0.09$ cm^2/g with a small narrow peak in the a_1 distribution shown in the IMAX flight data in Figure 7.43, though the statistics are too low to really see the signal. Regardless, the number of events in this small peak is five, which is consistent with being below the upper limit of 11.1 events which we set in the last paragraph.

[2] or equivalently, we create a peak at $\sqrt{\chi^2} \sim 8 \pm 3$

7.4 Monte Carlo of the 3 Different Searches

The accidental coincidence Monte Carlo is quite simple: we choose three time-delays each from a uniform distribution of a certain width (e.g. these distributions should replicate the distributions in Figure 5.16). With these time-delays, we compute the time-delay uncertainties as we did for the actual data at 14.0 hours UT (the time-delay uncertainties are time-dependent, see Chapter 6). These time-delays and uncertainties served as the input variables to the same fitting procedures described in Sections 7.1.1-7.1.3, and the resulting $(\chi^2)^{N/2}$ distributions are shown in Figures 7.31,7.35, and 7.40, and the resulting fitted parameters are shown in Figures 7.32-7.34,7.36-7.38, and 7.41-7.43. This Monte Carlo confirms that the χ^2 distribution for the negligible Δv search is nearly flat, and that the $(\chi^2)^{1/2}$ distributions for the 1 degree-of-freedom $\Delta v \neq 0$ searches do not have a strong peak at zero, as would be expected if we had just plotted histograms of χ^2 rather than histograms of $(\chi^2)^{1/2}$ (for 1 degree-of-freedom the distribution of χ^2 goes like $1/\chi^2$ for small χ^2, which has a strong peak at zero).

The Monte Carlo for IMP-like events consisted first of choosing an input IMP speed, v, from a 'cut-off' Maxwellian distribution (equation 1.3)[17][18]. The second step of the IMP-like event Monte Carlo is to determine whether or not an IMP with this velocity and a pre-determined energy loss (a_γ) will produce time-delays that fall within the histograms shown in Figure 5.16. In order to determine whether an IMP will make these cuts, we propagate the IMP through the telescope using Equations 7.46 and 7.49 (for $\gamma = 1$) or Equations 7.47 and 7.49 (for $\gamma \neq 1$). For $\gamma = 1$ and two different values of $a_1 \in \{0\%, 4\%\}/\mathrm{g/cm^2}$, we show the resulting $(\chi^2)^{N/2}$ histogram in Figures 7.31, 7.35, and 7.40, and the resulting fitted parameters are shown in Figures 7.32-7.34, 7.36-7.38, and 7.41-7.43. This Monte Carlo confirms that our $\Delta v \neq 0$ searches have gaussian peaks of standard deviation ~ 1 at $(\chi^2)^{1/2} = 0$ (see Figures 7.31, 7.35, and 7.40), and that our $\Delta v = 0$ search does not have a peak at $\chi^2 = 0$ for $a_1 = 4\%/\mathrm{g/cm^2}$ (since the IMPs are slowing down) and *does* have a peak at $\chi^2 = 0$ for $a_1 = 0\%/\mathrm{g/cm^2}$ (see Figure 7.31).

7.4.1 Determination of the Range of Acceptable a_1 for Each IMP search

With the IMP Monte Carlo, we can input different values of a_1 to determine the smallest a_1 where each of the IMP searches ($\Delta v \approx 0$, small-Δv, and large-Δv) fail. We found that for $a_1 < 0.013$ cm^2/g, all the searches perform as advertised, giving values of $\chi^2 < 2$ and positive values for the fitted a_1 and s_0. For $a_1 = 0.013$ cm^2/g, the negligible velocity change search fails for the first time, giving $\chi^2 > 8 \pm 5$, with very few events in the first bin of the χ^2-histogram, ($\chi^2 < 2.5$). When $a_1 = 0.07$ cm^2/g, the small-Δv search fails, giving unphysical, negative values for the fitted parameters a_1 and s_0, though the χ^2 values were still acceptably small ($\sqrt{\chi^2} < 2.5$). At $a_1 = 0.24$ cm^2/g, the large-Δv IMP search fails, giving $\sqrt{\chi^2} = 6 \pm 1$. However, this failure of the large-Δv search does not affect our results because the velocities of the dark matter Maxwellian distribution are too small. For $a_1 \geq 0.123$ cm^2/g, all of the IMPs (with velocities less than the galactic escape velocity of $v_{\max} = 640$ km/s) get stopped in the atmosphere or gondola shell[3] above the IMAX detectors. In Table 7.10, we show the fraction of the IMP Monte Carlo events which can traverse the atmospheric/gondola overburden and satisfy the D-module's time-delay constraints. The velocities of the IMPs above the atmosphere were chosen from a cutoff Maxwellian distribution (Equation 1.3). The velocity of the IMPs ($n = 2$) degrades exponentially with the thickness of the atmospheric overburden. Since the IMPs have initial velocities $v < 640$ km/s, a large value of a_1 will soon degrade the velocities to be below our minimum velocity of $v \sim 100$ km/s. In Table 7.10, we see that for the assumed Maxwellian velocity distribution, the time-delay gate widths and delays have been well-chosen. For no velocity degradation ($a_1 = 0.00$ cm^2/g), only 2.2% of the events are lost from this Maxwellian distribution due to the D-module timing cuts. However, when $a_1 = 0.08$ cm^2/g, the D-module does not detect 59.7% of the Maxwellian distribution since the lower velocity IMPs slow down significantly in the atmosphere and the measured time-delays will be too long for the D-module's time-delay cuts. When $a_1 \geq 0.123$ cm^2/g, none of the IMPs from the cutoff Maxwellian velocity distribution

[3]The overburden at float altitude is 5 g/cm^2 for the atmosphere and 1.08 g/cm^2 for the aluminum gondola shell.

have a large enough velocity to satisfy the D-module detector cuts after propagating through the atmosphere and gondola. This maximum value of a_1 corresponds to a maximum cross-section to mass ratio of $\sigma_1/m_x = 2.2 \times 10^{-25}$ cm^2/GeV, and will be used in Chapter 9 to place constraints on IMPs. As a point of warning, due to our uncertainty of the response of plastic scintillators to low velocity particles, we did not include the D-module's discriminator thresholds when we computed the fraction of events accepted in Table 7.10. However, if a theoretical model can be developed for the efficiency for light production by *carbon* recoils, then with the results discussed in Section 2.6, we can easily include the light yield and the discriminator thresholds in the IMP Monte Carlo.

a_1	$f_{\rm cut}$
0.00	97.8 %
0.01	97.5 %
0.02	95.5 %
0.03	92.1 %
0.04	85.4 %
0.05	77.9 %
0.06	66.8 %
0.07	55.4 %
0.08	40.3 %
0.09	22.5 %
0.10	9.6 %
0.11	2.4 %
0.12	0.2 %
0.122	0.1 %
0.123	0.0 %

Table 7.10: We tabulate the fraction, $f_{\rm cut}$, of IMP Monte Carlo events which can traverse the atmospheric/gondola overburden *and* satisfy the D-module timing cuts, as a function of the slowing-down parameter a_1. The units of a_1 are cm^2/g.

CHAPTER 8

FOLLOW-UP IMP SEARCH EXPERIMENTS AT MOUNTAIN ALTITUDE

In the months 6/93-10/93, we set up an experiment on top of Mt. Lemmon (atmospheric overburden ~ 750 g/cm^2) at the University of Arizona High Altitude Cosmic Ray Observatory, currently operated by the U. of Arizona Atmospheric Sciences Department. This experiment consists of a stack of white boxes that each contain a 1 cm thick, 0.72 m^2 square piece of plastic scintillator. The white box integrates the light from the scintillators, and the light is collected by 4 RCA4522 5-inch photomultiplier tubes. The tubes and scintillators were borrowed from GSFC, so as to simulate (as closely as possible) the operating conditions aboard the IMAX gondola.

In one run, which lasted 12 days (10/29/92), we observed < 1 IMP-like event (non-slowing or slightly slowing). We were using the D-module in coincidence with our D-module prototype (Delayed Coincidence Detector Module or DCD-module) to trigger the readout of the D-module. We found that the high electrical radiofrequency interference from the radio transmission towers on Mt. Lemmon, and the higher dark current noise from the different type of PMTs caused many more accidental delayed coincidences at low discriminator thresholds than desired (10^{-2} Hz). Such accidental rates demanded an end-to-end coincidence of each scintillation detector to lower the accidental rate to 10^{-4} Hz. The DCD-module provides this end-to-end coincidence for each counter, while the D-module does not. Our discriminator thresholds for the DCD-module are slightly higher than the D-module's discriminator thresholds during flight (~ 7.0 MeV/(g/cm^2) as compared to ~ 3.5 MeV/(g/cm^2)). The solid-angle of the detector configuration on Mt. Lemmon is ~ 835 cm^{2}sr, which is ~ 8.4 times the acceptance during flight.

In our last run, we have actually observed events on Mt. Lemmon that are similar to the anomalous events seen during the flight – with one characteristic in common – a strong peak near the beginning of the T_{23} gate. These events are not caused by new particle physics, and are caused by crosstalk between the D-module and other modules used in the experiment (see Section 6.5 for details).

CHAPTER 9

IMPLICATIONS OF IMAX IMP SEARCH

The results of the IMAX IMP search are summarized in Tables 9.11 and 9.12 and Figure 9.44, and we overlay the constraints from the IMAX large-Δv IMP search upon the previous constraints from other direct searches for IMPs in Figures 9.45 and 9.46 (see chapter 2, especially Figures 2.1 and 2.2). The boundaries of the IMAX-constrained region have simple explanations:

- The discriminator for detector S2 had the highest setting of the four discriminators, at an energy loss of $dE/dx \sim 3.5$ MeV/g/cm^2 (see Table 6.8), which corresponds to a transport cross-section of:

$$\sigma = \frac{1}{v^2}\frac{dE}{dx} \sim 6.23 \times 10^{-21} \text{ cm}^2, \tag{9.56}$$

  where $v \sim 300$ km/s.

- The D-module operated noise-free at cool temperatures at float altitude for only five hours, during which time it registered ~ 5 events that were consistent with an IMP losing less than $1 - \exp(-0.013/\text{g/cm}^2 \times 18.82 \text{ g/cm}^2) \sim 22\%$ of its velocity from the top of the atmosphere to the bottom of detector S2 (see Chapter 7).[1] This a_1 upper limit for the negligible velocity search corresponds to an upper limit on the cross-section to mass ratio of $\sigma/m_x < 2.31 \times 10^{-26}$ cm^2. With an IMAX acceptance of ~ 100 cm^{2}sr, and an active time at float of $\sim 1.4 \times 10^4$ s, this corresponds to an upper limit on the IMP flux of 6.5×10^{-6} cm^{-2}s^{-1}sr^{-1} (95 %

[1] The 18.82 g/cm^2 used here includes the atmospheric overburden and the thickness of the gondola shell, but does not include the the thickness of the last detector, TOF2, since the IMP only needs to penetrate a small fraction of this detector to be detected, see Table 6.2.

C.L.), or a maximum detectable mass of $m_x \sim 10^{11}$ GeV (assuming IMPs are all the Galactic halo dark matter).

- IMPs with $\sigma/m_x < 2.1 \times 10^{-25}$ cm^2/GeV will lose less than $1 - \exp(-0.123 \times 18.82) \sim 90.1\%$ of their velocity while traveling through the atmosphere and the IMAX telescope. Our analysis indicates that during the five hours of quality data acquisition at high altitude, we observed < 11.1 large-Δv slowing events consistent with these cross-sections (or an upper limit on the flux of 7.9×10^{-6} cm^{-2}s^{-1}sr^{-1}). Similar results hold true for the small-Δv search, where less than $1 - \exp(-0.07 \times 18.82) \sim 73\%$ change in velocity is required.

- The three-fold delayed coincidence rate was $\sim$ 4 Hz, so with the three detector acceptance of $\sim$ 135 cm^{2}sr, we have an upper limit of 3×10^{-2} cm^{-2}s^{-1}sr^{-1}, which applies to all IMPs that can traverse the material above IMAX detector S2 without slowing significantly ($\sigma/m_x < 2.1 \times 10^{-25}$ cm^2/GeV). This result is completely overshadowed by the large-Δv result.

- The TOF1 single counting rate rate was $\sim$ 4000 Hz, so with the TOF1 acceptance of $\sim$ 9120 cm^{2}sr, we have an upper limit of 0.44 cm^{-2}s^{-1}sr^{-1}, which applies to all IMPs that can traverse the air above the IMAX payload and not lose more than 90% of its velocity (6.08 g/cm^2), or $\sigma/m_x < 3.3 \times 10^{-25}$ cm^2/GeV). The discriminator for TOF1 was set lower than the other discriminators, at $dE/dx = 0.9$ MeV/g/cm^2.

The IMAX constrained regions of IMP parameter space are indeed quite useful. Even without a detailed model for the dependence of IMP-nucleus elastic scattering cross-sections upon nuclear mass and spin, we see from Figure 9.45 that we are probably exploring a region of IMP parameter space in which IMPs can still be all the halo dark matter. We are the *first* experiment to search for IMPs in the triangle of parameter space with cross-sections $\sigma \in [7 \times 10^{-21}, 10^{-18}]$ cm^2, masses $m_x > 10^7$ GeV, and slowing-rates $\sigma/m_x > 10^{-28}$ cm^2/GeV. For $m_x < 10^7$ GeV, $\sigma > 7 \times 10^{-21}$ cm^2, and $\sigma/m_x < 2.1 \times 10^{-21}$ cm^2/GeV, our experiment can constrain f_d to be five orders of magnitude lower than published experimental limits[61][47]. We achieve this high sensitivity by using

a delayed coincidence between multiple detectors to reject the cosmic ray background, which prior dark matter searches at high altitude have been unable to accomplish.

The 'non-vertical' gray-shading of the IMAX large-Δv constraints shown in Figure 9.44 are the result of Equation 2.22 – for low cross-sections, only those IMPs in the high-velocity tail of the Maxwellian distribution (Equation 1.3) can produce a significant light yield in the scintillation detectors. Therefore, the fraction of the nominal flux (Equation 1.2) that can be detected by the IMAX scintillation detectors will be a function of the cross-section, as shown by the jagged lower edge of the gray-shade right triangle in Figure 9.44.

When we actually assume a specific IMP-nucleus interaction model to parametrize the different IMP scattering cross-sections with different nuclei, we indeed find that our IMP search does place useful *new* constraints on IMP parameter space, closing the already discussed wide-open windows in parameter space ($m_x > 10^6$ GeV). The windows shown here are from the Starkman *et al.* interpretation[47], adapted from and including the results of the recent BPRS publication[116]. The BPRS collaboration was able to chip away about half of the previously larger window W_2 for the spin-dependent interactions, but they were unable to further constrain the window W_2 for coherent interactions. We effectively eliminate the small remaining window W_2 for the spin-dependent IMP-nucleus interactions, and a large fraction of the remaining window W_2 for the coherent IMP-nucleus interactions. The remaining portion of the window W_2 can be constrained by a sea level IMP search with low thresholds and a significant background rejection capability.

For our experiment, we estimate the $\mathcal{F}$ factors for IMP propagation through detector S2 by using Equation 2.12 and the atomic composition of the detectors, gondola, and air (see Chapter 6 for grammage estimates). We find that for the IMAX experiment that $\mathcal{F} \approx 170$ for spin-dependent interactions, and $\mathcal{F} \approx 1.4 \times 10^5$. The $\mathcal{F}$ factors serve to redefine the raw cross-section into a proton cross-section equivalent.

By inspection of Figures 2.5, 2.1, and 9.45, we find that our results constrain monopoles, fractionally-CHAMPs, and neutraCHAMPs with the first direct search in the mass range $m_x \in [\sim 10^6, \sim 10^9]$ GeV. Of course, these particles have been searched for indirectly before, via astrophysical reasoning (e.g., the exquisite Parker limit for monopoles[20], or cannibalization of neutron stars by CHAMP black holes[66]) or via experiment (e.g., for $m_x < 10^6$ GeV, an *invalid* but somewhat direct neutraCHAMP search by charge exchange in plastic etch detectors[17][59][60], and also for $m_x < 10^6$ GeV, a search by Adams *et al.* for the X-rays emitted by neutraCHAMPs hitting the atmosphere[63]). But a direct search, like our balloon-borne multiple plastic scintillation detector search, often has the advantage of model indepedence over the usual strong model dependence of an indirect search[2]. For example, our direct IMP search can in principle detect several wildly different types of particles (monopoles, CHAMPs, strange quark nuggets, neutraCHAMPs), while the indirect search by Adams *et al.* [63] could only detect neutraCHAMPs.

The results tabulated in Tables 9.11 and 9.12 should be in such form to facilitate re-interpretation of our results (such as more sophisticated explorations of f_d, σ, and m_x parameter space), should new data on the dark matter problem become available in the future. If one wants to place constraints on a specific particle model for IMPs (e.g., monopoles, neutraCHAMPs, strange quark nuggets), then one should take caution: the large-Δv search results only apply to those particles with dE/dx proportional to v^2 (e.g., strange quark nuggets, supermassive neutrons), while the small-Δv search applies to particles with energy loss proportional to any power of v (i.e. $dE/dx = Cv$, as in the case of neutraCHAMPs slowing in a classical r^4 nuclear dipole potential (see Appendix A), or for the Ahlen-Kinoshita monopole energy loss formalism[56]).

[2]Of course there are exceptions to this maxim.

Search	$\frac{dE}{dx}(THR)$	$\sigma_{\rm min}(\mathbf{cm}^2)$	$a_1^{\rm max}$ $(\frac{\rm cm^2}{g})$	$(\frac{\sigma}{m_x})^{\rm max}$ $(\frac{\rm cm^2}{\rm GeV})$	**A (cm^{2}sr)**
$\Delta v \approx 0$	3.5	6.2×10^{-21}	0.013	2.31×10^{-26}	100
small Δv	3.5	6.2×10^{-21}	0.07	1.2×10^{-25}	100
large Δv	3.5	6.2×10^{-21}	0.123	2.1×10^{-25}	100
Triples	3.5	6.2×10^{-21}	0.123	2.1×10^{-25}	135
Singles Rate	0.9	1.6×10^{-21}	0.38	3.3×10^{-25}	9120

Table 9.11: Summary of IMAX Results, part 1. For each IMP search, we tabulate the energy loss detection threshold ($dE/dx(THR)$(**MeV/g/cm^2**)), the corresponding threshold cross-section including the β^2-dependence of dE/dx ($\sigma_{\rm min}$), the maximum slowing down rate ($a_1^{\rm max}$), the corresponding maximum elastic cross-section to mass ratio ($(\sigma/m_x)^{\rm max}$), and the geometry factor (**A**) for the search. The incident velocity acceptance for the searches was nominally $v_0 \in [99.6, 752]$ km/s (for high slowing down rates, larger initial velocities were acceptable).

Search	**N**	**B**	$n_{s,\rm max}$	$\phi_{\rm max}(\frac{1}{\rm cm^2 s\ sr})$	$m_{\rm max}$ **(GeV)**
$\Delta v \approx 0$	5	4.0 ± 0.3	9.1	6.5×10^{-6}	1.5×10^{11}
small-Δv	5	7.5 ± 0.1	6.9	4.9×10^{-6}	2.0×10^{11}
large-Δv	16	18.3 ± 2.1	11.1	7.9×10^{-6}	1.3×10^{11}
Triples	4 Hz	0 Hz	4 Hz	3×10^{-2}	3.3×10^{7}
Singles	4000 Hz	0 Hz	4000 Hz	0.44	2.27×10^{6}

Table 9.12: Summary of IMAX Results, part 2. For each IMP search, we tabulate the number of signal (**N**) and background (**B**) events observed, the 95% C.L. Poisson upper limit ($n_{s\rm max}$) on the number of IMP events, the upper limit on the flux ($\phi_{\rm max}$), and the maximum mass detectable ($m_{\rm max}$) (assuming IMPs are all the dark matter).

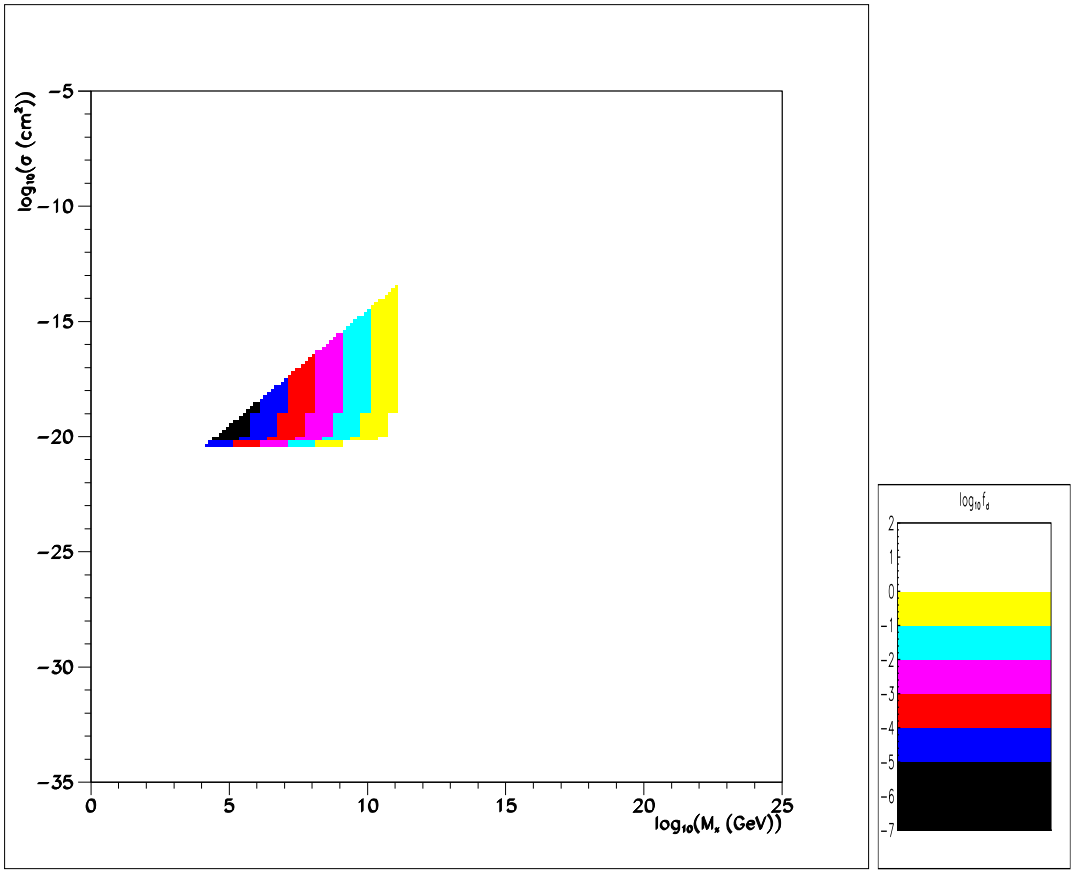

Figure 9.44: Plot of SIMP parameter space with IMAX large-Δv constraints (mass, elastic cross-section, and maximum dark matter mass fraction. The maximum SIMP halo matter fraction is shown in gray-shades as a function of SIMP mass and transport cross-section. The darkest gray regions (black) correspond to the maximum halo matter fraction being $f_d < 10^{-5}$, while the lightest gray (white) region corresonds to $f_d > 1$ (unconstrained). The gray-scales increment logarithmically (see the gray-scale chart). See Figure 2.1.

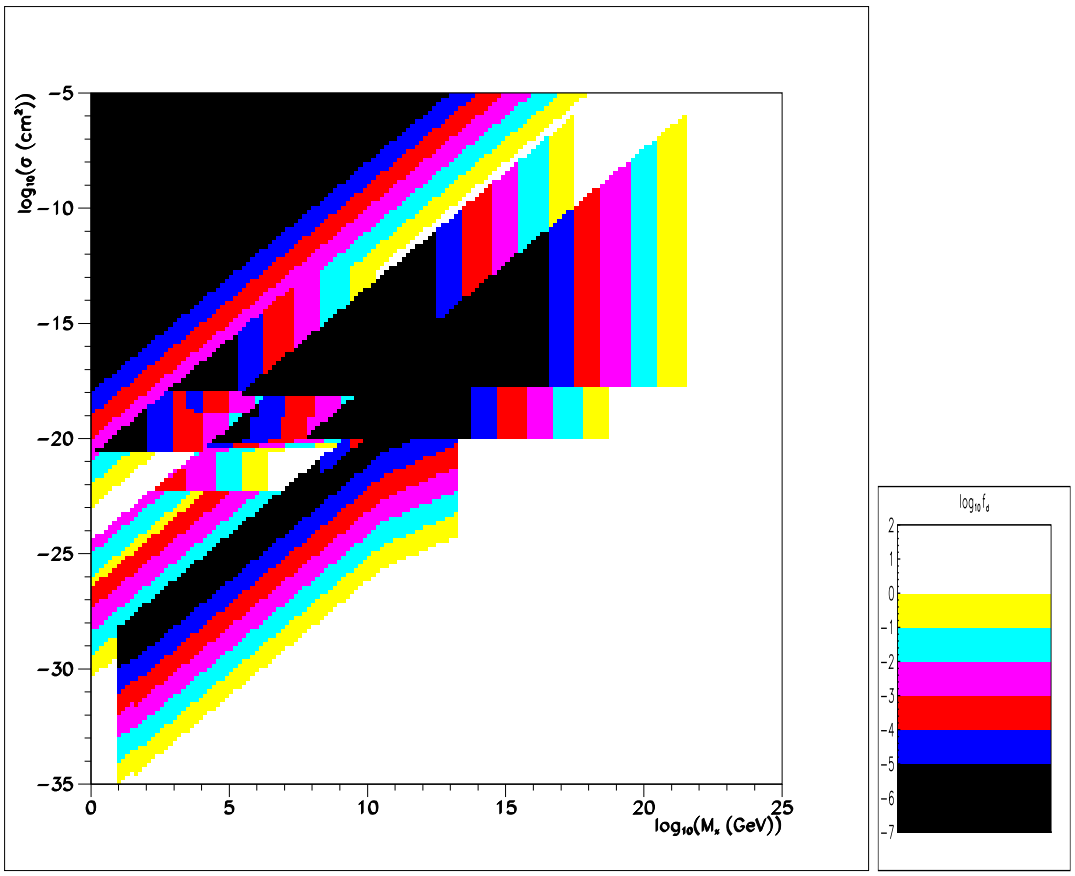

Figure 9.45: The maximum charged SIMP halo matter fraction is shown in grey-shades as a function of SIMP mass and transport cross-section. The darkest grey regions (black) correspond to the maximum halo matter fraction being $f_d < 10^{-5}$, while the lightest gray regions (white) corresonds to $f_d > 1$ (unconstrained) (see gray-scale chart). See Figures 2.2 and 9.44. The previous window at $\sim 10^7$ GeV and $\sigma \sim 10^{-20}$ cm^2 has been constrained by our IMAX results.

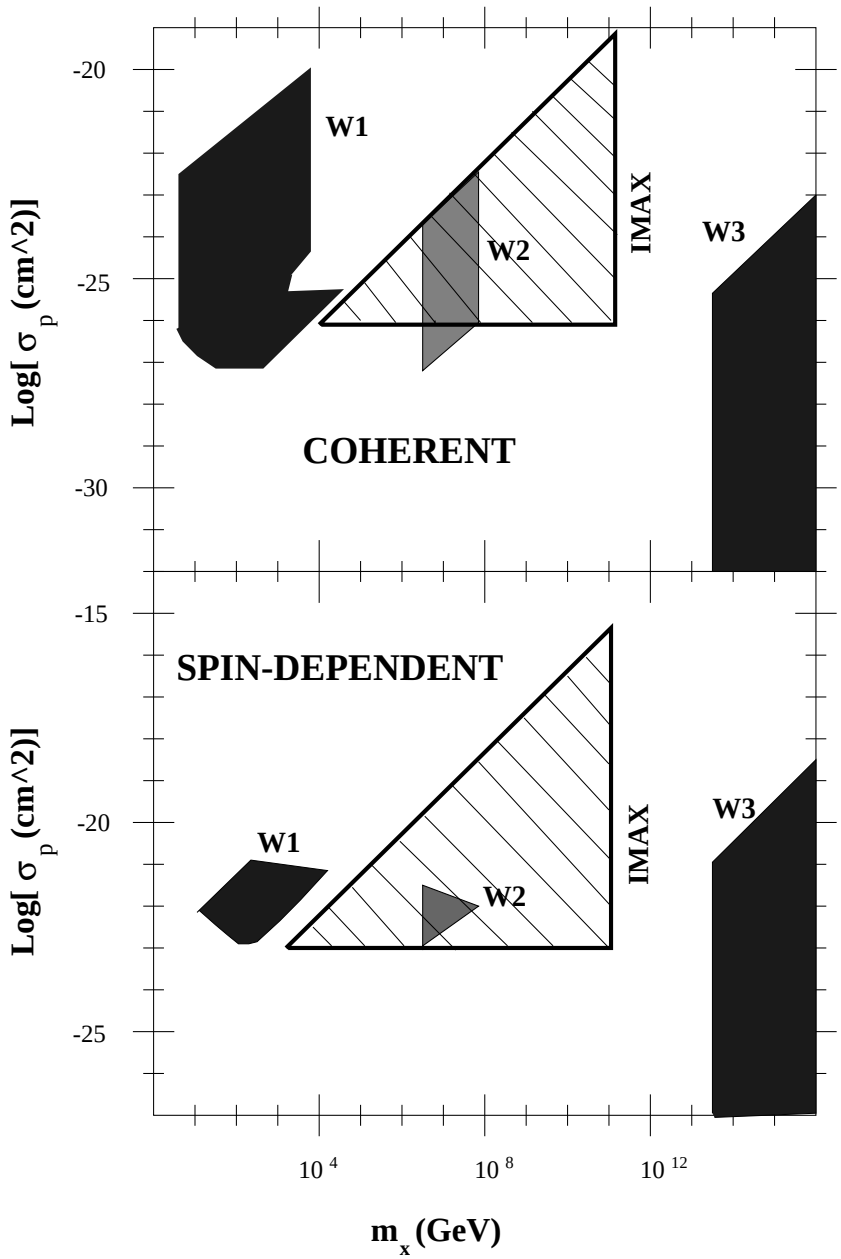

Figure 9.46: We show the IMAX constraints on the SIMP mass/cross-section parameter space for coherent interactions and for spin-dependent interactions. Without the IMAX results, there are three different non-excluded windows in each parameter space W_1, W_2, and W_3. The hatched areas are the IMAX excluded regions, assuming that SIMPs are all the galactic halo dark matter ($f_d = 1$).

APPENDIX A

CLASSICAL COMPUTATION OF NEUTRACHAMP ENERGY LOSS DUE TO POLARIZATION BY ^{14}N

De Rújula, Glashow and Sarid [42] speculate that charged massive particles, euphemistically called CHAMPs, close the universe, and comprise dark galactic haloes. CHAMPs come in two forms, $X^{\pm}$, with a possible mass range of $m_x \in [10^4, 10^6]$ GeV. CHAMPs can also be neutralized by binding to oppositely charged particles, e.g. X^+e^- and X^-p. X^-p has a tightly-bound ground state, $E_0 = 25$ keV, $r_{xp} = 28.8$ fm, and hence interacts relatively weakly with other particles and photons. Therefore, since X^-p systems interact relatively weakly and move relatively slowly (as compared to neutrinoes), they can constitute cold dark matter, and are dubbed "neutraCHAMPs."

Since the sun-earth system moves at the same speed as the velocity dispersion of the galactic neutraCHAMP ensemble, we might expect, in a satellite-based detector, to see neutraCHAMPs with speeds within the approximate interval $v \in (0, 800$ km/s], with strong sidereal modulation. Ground- and balloon-based neutraCHAMP detection experiments have been completed or are currently in progress [17][61][64][63]. Experiments in the atmosphere require a good estimate of the rate of energy loss and range of neutraCHAMPs, in order to give experimentalists a good idea of what X^-p flux and velocity distribution they can expect, given their atmospheric depth. Even in satellite experiments [62], the rate of energy loss needs to be known well, in order to optimize detector response.

Previous authors [42, 65, 82] only compute *estimates* of the upper and lower bounds of the energy loss of X^-p in the atmosphere. Estimates of upper and lower

bounds of the energy loss are of some use in speculating whether or not neutraCHAMPs can be detected as cosmic rays, but experimentalists desire a more refined calculation of the energy loss, if they hope to plan and carry out experiments in the atmosphere, giving definitive results.

A.1 Basic Equations

The energy loss of a neutraCHAMP, X^-p, traversing pure ^{14}N, as a function of velocity will be calculated, and the result will be scaled for other light elements. Since the velocity of the collision between the X^-p and a nitrogen atom is much less than the orbital velocities of the electrons in the nitrogen electron cloud ($v_e \approx Z\alpha c$), and also much less than the velocity of the neutraCHAMP proton ($v_p \approx \alpha c$), the colliding X^-p only slightly disturbs the electron cloud of nitrogen atom. Since in this adiabatic approximation, no quantum transitions can occur, we can take the *undisturbed* charge distribution of the nitrogen atom as the electric field source. The electric field due to the nitrogen atom then polarizes the X^-p when it is within the nitrogen atom [138, 139, 140]. Since the Bohr radius of the X^-p is $r_{xp} = 28.8$ fm, which is much smaller than the typical radius of a nitrogen electron, $r_n \approx 4000$ fm, we can effectively ignore the polarization of the nitrogen atom by the X^-p.

The standard quantum theory of the linear Stark effect [141] gives the polarizability of the of the ground state of the hydrogenic neutraCHAMP as:

$$\chi = -2e^2 \sum_{n>1} \frac{|< n,0,0 \mid r \mid 1,0,0 >|^2}{E_0 - E_n}. \tag{A.57}$$

Following the elegant summation method of Dalgarno and Lewis [142, 143, 144, 145], the polarizability of the X^-p ground state is:

$$\chi = 4.5 r_{xp}^3 = 4.5 \left(\frac{m_e}{m_p}\right)^3 r_{pe}^3 = 1.08 \times 10^5 \ \text{fm}^3, \tag{A.58}$$

where r_{pe} is the hydrogen Bohr radius. Notice that the neutraCHAMP polarizability is about 10^8 times the neutron polarizability, $\chi_n \approx 1.1 \times 10^{-3}$ fm^3[146], and about 10^{-9}

times the hydrogen atom polarizability, $\chi_h = 6.67 \times 10^{14}$ fm^3. Therefore, we cannot ignore the neutraCHAMP structure.

Using Jackson's result [150] for the interaction energy of an external-field induced dipole with the external field, the interaction potential is :

$$V(r) = -\frac{1}{2}\vec{p}\cdot\vec{E} = -\frac{1}{2}\chi \mid \vec{E} \mid^2 . \tag{A.59}$$

We can approximate quite well the interaction potential by ignoring electronic screening of the nucleus. Since the electric field due to the nucleus is Ze/r^2, the potential is:

$$V(r) = -\frac{1}{2}\frac{Z^2e^2\chi}{r^4} \tag{A.60}$$

Given this interaction potential, in the center of mass frame, and using classical collision theory [151], we can calculate the scattering angle as a function of impact parameter, b, and the center of mass kinetic energy, $E_c = \frac{m_n E}{m_n + m_x}$, where E is the initial kinetic energy of the neutraCHAMP in the lab frame, m_n is the mass of the nitrogen nucleus and m_x is the mass of the neutraCHAMP. The center of mass kinetic energy, E_c, for nitrogen is:

$$E_c = 7 \text{ keV } \left(\frac{v}{v_0}\right)^2 . \tag{A.61}$$

The equation for the scattering angle is [151]:

$$\theta = \pi - 2\int_{r_0}^{\infty} \frac{bdr}{r^2\left(1 - \frac{V(r)}{E_c} - \frac{b^2}{r^2}\right)^{\frac{1}{2}}}, \tag{A.62}$$

where r_0 is the largest positive root of the denominator of the above integrand.

The scattering cross-section as a function of angle is:

$$\frac{d\sigma}{d\Omega} = \frac{-b}{\sin\theta}\frac{db}{d\theta}. \tag{A.63}$$

From this result, the energy transfer cross-section is:

$$\frac{d\sigma}{dT} = \frac{4\pi}{T_m}\frac{d\sigma}{d\Omega}, \tag{A.64}$$

where T is the energy transferred to the nitrogen atom, $T = T_m \sin^2(\theta/2)$, and $T_m = 4m_x m_n E/(m_x + m_n)^2 = 28 \text{ keV}(v/v_0)^2$ is the maximum energy transferred. Then the energy loss is:

$$\frac{1}{\rho}\frac{dE}{dx} = -\frac{N_a}{A}\int_0^{T_m} T\frac{d\sigma}{dT}dT, \tag{A.65}$$

N_a is Avogadro's number, and A is the atomic weight of nitrogen [139, 152].

If the impact parameter, b, is taken as the independent variable for the integration, $d\sigma = 2\pi b db$ and $T(b) = T_m \sin^2(\theta(b)/2)$, so that the energy loss is:

$$\frac{1}{\rho}\frac{dE}{dx} = -\frac{2\pi N_a T_m}{A}\int_{b_{\min}}^{b_{\max}} \sin^2\left(\frac{\theta(b)}{2}\right) b db. \tag{A.66}$$

A.2 Scattering in a r^{-4} potential

From the above attractive form of the interaction potential, we find that the centripetal potential [151],

$$V'(r) = V(r) + \frac{E_c b^2}{r^2}, \tag{A.67}$$

will then go to $-\infty$ as r goes to zero, and to zero from the positive side as r goes to ∞. Therefore, somewhere in between 0 and ∞, the effective potential will have a maximum. If we only include the r^{-4} term of the potential, with no electronic screening, the maximum of the effective potential occurs at $r_m = \sqrt{\chi Z^2 e^2/E_c b^2}$, and has a value $V'_m = E_c^2 b^4/2\chi Z^2 e^2$. If $E_c = V'_m$, an unstable $(X^- p, {}^{14}N)$ orbit arises. Near $E_c = V'_m$, the colliding ${}^{14}N$ will loop several times around the $X^- p$ before scattering at a finite angle. If E_c is fixed, and the impact parameter, b is varied, we can observe this critical phenomenom from a different aspect, as follows. For $b \gg b_c$, the scattering angle, $\theta(b)$ (in center of mass coordinates) is negligible. If

$$b = b_c = \sqrt[4]{2\chi Z^2 e^2/E_c} = \frac{b_{c0}}{(v/v_0)^{0.5}}, \tag{A.68}$$

then $\theta(b)$ goes to $-\infty$, due to the unstable orbit, and for $b \ll b_c$, $\theta(b) \approx \pi$. For nitrogen, $b_{c0} = 216$ fm.

The $\theta(b)$ curve can be calculated analytically, if we ignore the electronic screening of the potential, and insert the r^{-4} Coulomb potential in Equation A.60 into Equation A.62, then for $b < b_c$, by Gradshteyn and Ryzhik[153], equations 3.165.2, 8.121.3, and 8.112.1:

$$\theta(b) = \pi - \frac{2b}{b_c} K\left(\frac{1}{\sqrt{2}}\sqrt{1+\sqrt{1+\frac{b^2}{b_c^2}}}\right), \tag{A.69}$$

where $K(r)$ is the complete elliptic integral of the first kind. For $b \geq b_c$, by Gradshteyn and Ryzhik, equation 3.157.2 [153]:

$$\theta(b) = \pi - 2\frac{\sqrt{2}}{\sqrt{1+\sqrt{1-\frac{b_c^4}{b^4}}}} K\left(\sqrt{\frac{1-\sqrt{1-\frac{b_c^4}{b^4}}}{1+\sqrt{1-\frac{b_c^4}{b^4}}}}\right). \tag{A.70}$$

With the $\theta(b)$ curve, we can easily calculate the energy loss:

$$\frac{1}{\rho}\frac{dE}{dx} = -2\pi\frac{N_a}{A} b_c^2 T_m \, I, \tag{A.71}$$

where $I(s_{\min}, s_{\max})$ is the dimensionless integral

$$I(s_{\min}, s_{\max)} = \int_{s_{\min}}^{s_{\max}} \sin^2(\theta(s)/2)) s ds, \tag{A.72}$$

$s = b/b_c$, $T_m \equiv 4m_n m_x E/(m_n + m_x)^2$, E is the kinetic energy of the $X^- p$ system, and N_a is Avogadro's number.

A.3 Impact Parameter Limits

We may classically calculate a differential cross-section for scattering when the de Broglie wavelength of the colliding nucleus is small compared to any significant dimension of the collision, and when the collision is well-defined in terms of the uncertainty principle [139].

The de Broglie wavelength of a particle of reduced mass $\mu = 14 m_p$, moving at a velocity, $v = \beta c$, is $\lambda = \hbar c/\mu\beta c$. At $v_0 = 10^{-3}c = 300$ km/s, $\lambda = 14$ fm. This wavelength may be compared with the smallest electronic screening distance, $r_1 = 3900$ fm [147] [148] [149], the $X^- p$ radius, $r_{xp} = 28.8$ fm, and the nitrogen nuclear radius, $r_n = 3.4$ fm.

Another limit, r_e, is set by the condition that the electric field, $\vec{E}$, due to the nucleus, must be much smaller than the internal electric field of the X^-p system, $\vec{E}_{xp}$, so that the induced X^-p dipole moment, $\vec{p}$, is linear in $\vec{E}$, and so that the X^-p is not torn apart:

$$\mid \vec{E} \mid \cong \frac{Ze}{r_e^2} \ll \mid \vec{E}_{xp} \mid \cong \frac{e}{r_{xp}^2}, \tag{A.73}$$

or:

$$r_e \gg Z^{\frac{1}{2}} r_{xp} = 76 \text{ fm}. \tag{A.74}$$

Since we have an attractive potential, proportional to r^{-4}, we can calculate the relationship between the turning point of the collision (distance of closest approach), r_0, and the impact parameter, b, for $b > b_c$:

$$r_0 = \frac{b}{\sqrt{2}} \sqrt{1 + \sqrt{1 - \left(\frac{b_c}{b^4}\right)^4}}, \tag{A.75}$$

which can be inverted to get:

$$b = r_0 \sqrt{1 + \frac{1}{4}\left(\frac{b_c}{r_0}\right)^4}. \tag{A.76}$$

The minimum impact parameter, for which $r_0 \geq r_e$, is:

$$b_{\min} = r_e \sqrt{1 + \frac{1}{4}\left(\frac{b_{c0}}{r_e}\right)^4 \left(\frac{v_0}{v}\right)^2} \tag{A.77}$$

$$= 76 \text{ fm} \sqrt{1 + 16.3\left(\frac{v_0}{v}\right)^2}. \tag{A.78}$$

For $v = v_0$, $b_{\min} = 1.46 b_c = 316$ fm. When we require that $b_{\min} > \alpha b_c$, where $\alpha \geq 1.0$, we find that the range of velocity for which our calculation applies is:

$$v \in \left[4.04 v_0(\alpha^2 - \sqrt{\alpha^4 - 1}), 4.04 v_0(\alpha^2 + \sqrt{\alpha^4 - 1})\right]. \tag{A.79}$$

In classical theory, a critical impact parameter, b_c, appears for an attractive r^{-4} scattering potential. For impact parameters, $b < b_c = \sqrt[4]{2\chi Z^2 e^2 / E_c} = (216/\sqrt{v/v_0})$ fm,

the turning point of the collision is $r_0 = 0$ fm. Therefore, for such sub-critical impact parameters, the distance of closest approach, r_0, is less than both λ and r_e, and the classical calculation of a differential scattering cross-section does not apply, and a quantum mechanical calculation including inelastic nuclear effects would be more appropriate [81, 154, 155]. Since such a calculation is outside the scope of the present paper, we require that $b_{\min} > 2.0 b_c$, so that $v \in [154, 9540]$ km/s, is the range over which the present calculation holds. (If we were to require that $b_{\min} > 1.0 b_c$, then this calculation would only be valid for $v = 4.04 v_0 = 1200$ km/s, which is too narrow of a velocity range to be useful.)

For well-defined classical collisions, the uncertainty principle warrants a lower limit on the scattering angle, $\theta > \theta_{\min} \approx \lambda / 2\pi r_1$. For a particle of reduced mass $\mu = 14 m_p$, moving at a velocity, $v = \beta c$, $\theta_{\min} = \hbar c / 2\pi\mu\beta c r_1$. With $v_0 = 10^{-3} c = 300 km/s$, and $r_1 = 3900$ fm, $\theta_{\min} = 6 \times 10^{-4}$ rads. We find that this corresponds to a maximium impact parameter, $b_{\max} \approx 5 b_c$. By using the approximate b^{-4} scaling dependence of $\mid \theta(b) \mid$, for $b > b_c$, we find:

$$b_{\max} \approx 5 b_c \left(\frac{v}{v_0} \right)^{\frac{1}{4}}. \tag{A.80}$$

Setting $b_{\max} = 10 b_c$, to estimate the minimum velocity for which this calculation applies, we find $v_{\min} \sim 6.3 \times 10^{-2} v_0 = 19$ km/s.

Therefore, in the present classical calculation, the uncertainty principle does not limit us as much as the requirement that the collision is elastic. The interval of integration should be $b \in [2 b_c, 10 b_c]$, which limits us to the velocity interval $v \in [154, 9540]$ km/s.

A.4 Results

The energy loss is proportional to velocity:

$$\frac{1}{\rho} \frac{dE}{dx} = -S_0 \left(\frac{v}{v_0} \right), \tag{A.81}$$

where $v_0 = 300$ km/s. If we neglect the above discussion on the limitations of the classical approximation, and integrate over all impact parameters, then $S_0 = 0.84$ MeV cm^2/g, for all $v \ll Z\alpha c$. However, when we only integrate over the interval discussed above, $b_{\min} = 2b_c$, and $b_{\max} = 10b_c$, then $S_0 = 8.4 \times 10^{-4}$ MeV cm^2/g. There is negligible dependence of the energy loss on the mass of the neutrachamp, in the mass and velocity ranges of interest, since $m_x >> m_n$. Since the critical impact parameter, b_c, scales with $\sqrt{Z/m_n}$, the X^-p energy loss scales with $Z/\sqrt{m_n}$.

A.5 Range-Energy Relations

From our calculation of the stopping power, we may calculate a range-energy relation for the neutraCHAMP in air (assuming $S_0 = 0.84$ MeV cm^2/g):

$$R = \frac{2\sqrt{\frac{1}{2}m_p v_0^2}}{S_0}\sqrt{\frac{m_x}{m_p}}\sqrt{E_i} = 0.053\sqrt{\frac{m_x}{m_p}}\sqrt{E_i}\ \frac{\text{g}}{\text{cm}^2}, \tag{A.82}$$

where E_i is the initial Xp kinetic energy, m_p is the proton mass, and m_x is the neutraCHAMP mass, all given in MeV. The reciprocal energy-range relation for Xp is:

$$E_i = 356\frac{m_p}{m_x}R^2 \text{ MeV}, \tag{A.83}$$

where R is given in g/cm^2.

Therefore, if we hope to see Xp of mass $m_x = 10^6 m_p$, as cosmic rays at sea level, where the atmospheric depth is $T = 1000$ g/cm^2, we require a minimum energy Xp: $E > E_{\min} \approx 356$ MeV, or $v_{\min} \approx 253$ km/s. Likewise, if we expect to see Xp of the same mass as cosmic rays on a mountain-top, where the atmospheric depth is $T = 700$ g/cm^2, we require $E > E_{\min} = 174$ MeV, or $v_{\min} \approx 177$ km/s. If we assume a Maxwellian velocity distribution, with $v_0 = 300$ km/s, this is a significant improvement. However, in a balloon-borne experiment, where $T = 10$ g/cm^2, we only require $E > E_{\min} \approx 35$ keV, or $v_{\min} \approx 2.5$ km/s, so that we can essentially sample the entire velocity range.

APPENDIX B

POSSIBLE SOURCES OF CORRELATED PULSES

B.1 Correlated Pulses from Delayed particles in Cosmic Ray Air Showers

Cosmic ray air-showers can cause correlated pulses due to different particles from the same shower hitting different detectors in the stack. The delay-time for particles in an air shower can sometimes reach $\sim$ 300 ns [128][129][130]. Most of the stragglers are likely produced by high transverse momentum (p_T) collisions high in the atmosphere, which give a particle a large angle of descent with respect to the core of the air-shower, causing time-delays by the difference in path-length travelled [130]. Delayed-particles produced by the high p_T collisions require detectors with wide lateral separation (i.e., an air-shower array), so these delayed particles would not likely cause correlated pulses in our vertical stack of detectors. Some of these stragglers are likely due to low-velocity particles produced near the detectors, causing time-delays due to the difference in travel-time between low-velocity and relativistic particles. Goodman *et al.* [129][128] have observed 3 events with a delay of $\sim$ 40 ns and relatively large pulse heights, and initially attributed them to energetic delayed supermassive hadrons, but subsequent upgrades to their simulations have shown that the supermassive hadron hypothesis was unlikely.

Regardless of whether the explanation for the delayed particles is mundane or exotic, the delayed particles in air-showers would probably not cause correlated pulses in different detectors because our gate delays are greater than $\sim$ 350 ns, which is a factor of two greater than the largest delay observed in the *ground* air-shower detectors. If the delayed particles did fluctuate above $\sim$ 350 ns, there might be some evidence of correlated pulses. If we had more than a few events due to delayed particles in air-showers, the

distribution of time-delays observed would likely follow an exponential distribution for the long time-delays (350 ns) of interest [130]. Without further information, we probably would not understand the source of these correlated pulses, but they would probably not pass our 4 detector time-of-flight requirement. Additionally, most showers occur at an atmospheric depth of ~ 100 g/cm^2, and our balloon-altitude search was at ~ 5 g/cm^2, far above most showering activity and hence above most of the delayed particles. Therefore, delayed particles in air showers might only be a significant source of correlated pulses for our mountain-altitude search. Even then, the fraction of showers with particle delays greater than 300 ns is much less than 1% [129][130], so this is an insignificant source of correlated pulses (at sea level and for low thresholds, the background is probably less than 10^{-11} cm^{-2}s^{-1}sr^{-1} [128][129]).

B.2 Correlated Pulses from Muon-decay

In Section 6.4, we found that interchannel crosstalk within the D-module caused a pulse in the amplifier for channel 3 with delay $T_{43} \approx 2.06\mu$s from a pulse in channel 4. This pulse can cause false triggers with $T_{23} \sim 2.0\mu$s and $A_3 \sim 100$ mV as detailed below, but we have no fool-proof explanation for the exponentially-distributed T_{12} which is correlated with the $T_{23} = 2.0\mu$s in the anomalous events. However, we do attempt to explain this correlation with muon-decays as detailed below.

During the IMAX flight, many relativistic particles went through all four detectors, producing discriminator pulses in each channel that were in coincidence. In particular, if detector pulses triggered discriminators 2 and 4 simultaneously, and if the pulse from detector 4 is much larger than 60 pC, then the third discriminator would fire a delayed pulse, with $T_{23} = -T_{34} \sim 2.0\mu$s. Channel 4 is not part of the D-module's delayed-coincidence trigger requirement and does not seem to participate in the anomalous events, but relativistic particles can produce time-delays $T_{23} \sim 2.0\mu$s, which are a characteristic of anomalous events.

There are two possible arguments against this scenario: first, we have an anti-coincidence for relativistic particles – if any discriminator pulses (in different channels) coincidentally fire at relative time-delays of less than $\sim 0.1\mu s$, then these discriminator pulses are not allowed to start the TDC measuring process. Therefore, relativistic particles should not be able to cause anomalous time-delays at $T_{23} = 2.0\mu s$. Second, anomalous events also consist of exponentially distributed time-delays in channel T_{12} (with time-constant $\tau \approx 0.5\mu s$), which does not seem to fit the relativistic particle scheme for causing anomalous events.

The answer to the first argument is the relativistic particle signal from detector 2 is delayed by $\sim 0.080\mu s$ from the relativistic particle signal in detector 4 (possibly caused by white-box light-collection and PMT time effects in detector 2 (IMAX detector S1)). Therefore, only $\sim 0.020\mu$s of extra time-delay between counters 2 and 4 is necessary for the anticoincidence to fail between counters 2 and 4. This 0.020μs time-delay can be achieved from light-collection time fluctuations causing a jitter in the pulse-timing in detector 2, and perhaps from afterpulsing in detector 2.

The solution to the second problem demands us to actually identify the relativistic particle(s) which cause the anomalous events. If the incident particle is a negative muon, and passes through the 1$^{\text{st}}$ scintillation detector (IMAX detector T1) and then stops in one of the Čerenkov detectors (IMAX detector C1 or C3) between scintillation detectors 1 and 2 or in a support frame or magnet dewar wall, is captured by an oxygen, fluorine, aluminum or silicon nucleus, then the apparent decay lifetime of the muon is 1.8μs, 1.45μs, 0.88μs, and 0.77μs for oxygen, fluorine, aluminum and silicon, respectively [137]. When the negative muon is in orbit around a nucleus in the target, it can either decay into an electron and a couple of neutrinos or the muon can combine with a proton in the nucleus (of charge Z) and produce a nucleus with charge $Z - 1$ (e.g., $\mu^- + {}^{14}\text{Si} \rightarrow \nu_\mu + {}^{14}\text{Al}^*$), where the aluminum nucleus is in an excited state. In the case of muon decay after capture, the resulting electron will have an energy of ~ 45 MeV, enough to often initiate a small electromagnetic cascade. In the case of the

weak nuclear absorption of the muon following capture, the excited nucleus will often emit a gamma ray to reach its ground state; the gamma ray would often have an energy of tens of MeV, also enough to start a small electromagnetic cascade. The cascade would often cause 3 three nearly-coincident pulses in detectors 2-4 with a large pulse in detector 4 (IMAX detector T2). The large pulse in detector 4 would be followed in $\sim 0.1\mu$s by a pulse in detector 2 (light collection and PMT time-delays), and would also be followed by $\sim 2.0\mu$s by a pulse in detector 3 due to the observed interchannel D-module crosstalk. This complex scenario is quite possible, though remains unproven in our follow-up Mt. Lemmon experiments.

In our Tucson lab, we did test the possibility of the D-module producing anomalous events in response to such a sequence of pulses. With the G-module, we created a pulse-sequence which had $T_{12} \approx 1.50\mu$s, $T_{24} \approx 0.50\mu$s, and a large pulse in channel 4: $A_4 \sim 200$ pC. Then we pulsed this sequence into the D-module with *no* signal entering channel 3 and found that the module strobed the Ortec ADC, despite our requirement that channel 3 be part of the D-module trigger. The ADC measured $X_3 = 105 \pm 5$ mV, which is somewhat consistent with the third observed component of the anomalous events – a small signal of $X_3 \sim 250 \pm 70$ mV was seen in all anomalous events. Perhaps the discrepancy between the X_3 pulse height observed for anomalous events during flight and during this ground test is due to a shift in the X_3 pedestal by ~ 100 mV between the time of the flight and this ground test, but this shift is unlikely.

Despite the fact that the entire anomalous-event production scenario (consisting of decaying muons) has not been tested, the observation of a small anomalous signal in channel 3 during the recent crosstalk tests which is consistent with the signal in channel 3 for the flight anomalous events does indeed suggest that the anomalous events are artificial and *not* caused by new particle physics.

B.3 Correlated Pulses from PMT noise

Photomultiplier tubes (PMTs) invariably have some amount of dark current and noise pulses[131]-[135], which consists of PMT pulses which do not occur at the same time as the passage of a cosmic ray through the scintillator plastic. Dark current and noise pulses are a background to the cosmic ray signal. Dark current occurs when the PMT is completely divorced from the scintillator plastic, and from any other external source of light.

Some of the noise pulses are due to cosmic rays which actually pass through the PMT; the remainder of the noise pulses come from 'afterpulsing', phosphorescence or fluorescence processes, radioactivity, potential differences between the glass envelope and the photocathode, and thermionic emission of electrons from the photocathode. Afterpulsing usually occurs on a time-scale of less than a few microseconds after the passing cosmic ray[131], and consists of ion bombardment of the cathode and initial dynodes[135]. The ions are created by the ionization of residual gases in the PMT during electromultiplication. Fluorescence occurs on a time-scale of a few microseconds to hundreds of microseconds after the deposition of energy by a cosmic ray, while phosphoresecence occurs on the time-scale of minutes to days[131]. Both fluorescence and phosphorescence consist of the de-excitation of molecular states in the faceplate material in the PMT. Some natural level of radioactivity will always be present in the PMT faceplate or in the surrounding detectors and structural support material. Many radioactive decays cause the emission of a single beta particle or a single alpha particle, with relatively low energy, so as to cause a single pulse in a single detector at random times. This will only add to the singles rate of an individual detector, so as to enhance the overall 4-fold accidental coincidence rate. Such radioactivity will not be a source of correlated pulses. Both fluorescence and ion afterpulsing cause correlated pulses on a time-scale of microseconds, which can be a nuisance to our search for IMPs, as detailed below.

Teich *et al.*[131] have measured the time-delays between pulses in a single photomultiplier tube. They have discovered that the time-delay distribution on the $T_{i,i} \in [0.01, 10]\mu$s time-scale, has two separate contributions: a nearly-exponential distibution with decay time of $\sim 0.5\mu$s and *additionally* a very sharp peak at $\sim 0.5\mu$s, with a full-width (at half-max) of $\sim 0.1\mu$s. The position of the sharp peak seems to be a tube dependent effect [131], and can vary from $\sim 0.1\mu$s to 0.5μs. The exponential component probably comes from the afterpulsing due to ion bombardment or from the afterpulsing due to fluorescence, as discussed earlier. The sharp peak is of unknown origin, though Teich *et al.* attribute the sharp peak to "evenly-spaced cosmic rays of unknown origin" (if this was true, then a revolutionary discovery may be at hand). We follow Barton *et al.'s*[136] belief the the sharp peak is probably due to geometric effects in the ion afterpulsing in the PMT itself, and that the sharp peak is *not* caused by evenly-spaced cosmic rays.

Since the single PMT time-delay distributions, as measured by Teich *et al.*, exhibit correlated pulses on the time-delay scale of interest to our search, we should carefully investigate whether the correlated PMT pulses will significantly affect our *a priori* flat time-delay distributions. First, we will assume that there is *no* intercounter anti-coincidence of fast particles. In this case, a fast particle going through all four detectors would cause a pulse to come from each of the four detectors' PMTs with negligible (nanosecond) delays. On the time-delay scale of 0.1μs and 10μs, the PMTs of each detector might afterpulse. Therefore, the time-delay distributions T_{12}, T_{23}, and T_{34}, due to PMT afterpulsing/fluorescence would have a similar shape to the distribution shown in Ref. [131]. However, we only measure the time-delays within a certain window (e.g., $T_{12} \in [0.6, 7.6]\mu$s, $T_{23} \in [1.3, 15.0]\mu$s, $T_{34} \in [0.5, 4.5]\mu$s), so the measured distributions will be cut-off, as compared to the distribution in Ref. [131], which was measured over a wider time-scale.

However, in our experiment we had an anti-coincidence (of width 100 ns) for fast particles that go through more than one detector. Therefore, the initial pulse caused by

the cosmic ray will not be registered in any of the four detectors. If a noise afterpulse occurs in detector 1, followed successively by afterpulses (with the the time-delay windows) in detector 2, detector 3, and perhaps in detector 4, then a delayed coincidence will occur. Unfortunately, in this scenario, the correlated pulses from PMT afterpulsing will create time-delay histograms that are *not* flat, as would be expected from a sample of pure accidental coincidences.

B.4 New Particle Physics?

If we assume that the anomalous events are caused by some particle physics phenomenom, then we are inevitably led to the following conclusions.

- Since the time-delays between hits in detectors 2 & 3 is generally smaller than the time-delays between hits in detectors 1 & 2, this means that if these pulses result from a *single* particle, then this particle appears to be 'accelerating' at detector 2.
- Since *ac*-celeration seems unphysical, we hypothesize the stopping of an IMP in the top detector, followed by an interaction or decay into multiple IMPs sometime later. The interaction or decay time is governed by an exponential time distribution distribution with $\tau \sim 0.5$ μs, as evidenced in the T_{12} distribution for anomalous events.
- The anomalous T_{23} distribution is peaked at *one* value, and is not broadly distributed. We can therefore infer from kinematical laws that this must be a *two*-body decay, as opposed to a many body decay. One of these two secondary decay IMPs originating in detector 1 passes through detectors 2 & 3 unimpeded, at a velocity of $\sim (1.517 \text{ m}/2.0 \ \mu\text{s}) = 758 \text{ km/s} = 0.0025 \text{ c}$.
- This secondary IMP might pass though detector 4, but the predicted time-delay is

$$\begin{aligned} t_{34,\,\text{pred.}} &\sim (2.0 \ \mu\text{s}/1.517 \text{ m}) \times 0.336 \text{ m} \\ &= 0.44 \ \mu\text{s} \ , \end{aligned}$$

which is below the minimum time delay for channel t_{34}, $t_{34}^{\min} \sim 0.5$ μs, so it would remained undetected.

APPENDIX C

DIURNAL MODULATION OF IMP FLUX

IMPs have large scattering cross-sections, $\sigma > 10^{-24}$ cm^2. Therefore, only a small fraction of material in the earth's atmosphere, with grammage x (measured in g/cm^2), will be sufficient to significantly slow down (with $\sim 90\%$ velocity loss) halo dark matter IMPs impinging from above the atmosphere[47]:

$$x = \frac{1}{\mathcal{F}} \frac{m}{\sigma} 0.5 \ln 10 = 205 \text{ g/cm}^2 \left(\frac{m_x}{10^6 \text{ GeV}} \right) \left(\frac{10^{-20} \text{ cm}^2}{\sigma} \right), \qquad \text{(C.84)}$$

assuming $\mathcal{F} = 1$. For $\sigma/m_x > 10^{-26}$ cm^2/GeV, less than one-fifth of the atmospheric thickness will be sufficient to efficiently slow down and attenuate the IMP flux. For $\sigma/m_x > 10^{-36}$ cm^2/GeV, the thickness of the earth, $\sim 10^{10}$ g/cm^2, is sufficient to eliminate the IMP flux coming from the other side of the earth. Such dramatic attenuation might sound discouraging at first, since detectors with an excessive overburden of IMP-attenuating material would not be able to detect IMPs. However, the attenuation of IMPs *can* be used to our advantage. First, IMPs of $\sigma/m_x \gg 10^{-36}$ cm^2/GeV would not be detectable if they travel through the whole thickness of the earth. Additionally, the rotation of the galactic disk is carrying the Sun and the Earth towards the constellation Cygnus at a significant velocity ~ 240 km/s through the assumed rotationless dark matter halo[18][27]. Therefore, the IMP flux will be significantly larger when the earthbound IMP detector is on the side of the earth facing the constellation Cygnus, and smaller when the detector is on the 'Cygnus-night' side of the earth. Due to the rotation of the earth about its axis every 24 hours, we expect a diurnal modulation of the detectable IMP flux. We have calculated the amplitude of this effect to be about a factor of three during the IMAX flight, with the maximum flux at about 10 hours UT in mid-July 1992.

Collar and Avignone[30] have also calculated the effect of diurnal modulation for their underground WIMP search experiments, and have concluded that the diurnal modulation effect will be most effective at far southern latitudes such as Australia or Argentina. For $\sigma/m_x \gg 10^{-36}$ cm^2/GeV, the diurnal modulation effect[30] is a much better IMP signal than the annual modulation effect[28]. In the rest of this appendix, we give the details of our diurnal modulation calculations.

C.1 Calculation of Net Earth Velocity around the Galactic Center

The sun's motion can be split into two parts – the local rotational velocity around the galactic center towards the constellation Cygnus ($v_{\theta_0} = 220$ km/s, ($\alpha = 316°.6, \delta = +48°.1$)[158]) and the peculiar velocity of the sun with respect to nearby stars ($v_\theta =$ 20 km/s[159], ($\alpha = 271°.2, \delta = +33°.8$)[160]). We add these two velocities together vectorially to obtain the sun's net velocity $\vec{v}_\Theta$ with respect to the galactic center:

$$|\vec{v}_\Theta| = 236.2 \text{ km/s}, \tag{C.85}$$

with the right ascension α and declination δ of this velocity vector being:

$$(\alpha_\Theta = 313°.2, \delta_\Theta = 47°.7). \tag{C.86}$$

The velocity of the earth about the sun, v_e, is determined by Newtonian mechanics:

$$v_e^2 = GM_\odot \left(\frac{2}{r_e} - \frac{1}{a}\right), \tag{C.87}$$

where r_e is the separation between the earth and the sun, and $a = 1.496 \times 10^{13}$ cm is the astronomical unit. The angle of inclination of the earth's orbit around the sun with respect to the galactic plane is 23°.4. At 8.667 hours UT on 7/17/92, the earth was at a distance of $1.52037637 \times 10^{13}$ cm from the sun, and an ecliptic longitude of 115°.011[161]. From Equation C.87, this corresponds to $v_e = 29.30971$ km/s, with a right ascension and declination of ($\alpha_e = 23°.173, \delta_e = 9°.682$). When we vectorially add the earth's velocity to the sun's net velocity, we get the net velocity, $\vec{v}_{e,\text{tot}}$ of the earth:

$$|\vec{v}_{e,\text{tot}}| = 248.028 \text{ km/s}, \tag{C.88}$$

where the right ascension and declination at 2.6 hours UT 7/17/92 of the earth's velocity vector through the galaxy is:

$$(\alpha_{\Theta_e} = 322^\circ.3324, \delta_{\Theta_e} = 46^\circ.4053). \tag{C.89}$$

C.2 Calculation of the Zenith Angle of the IMAX Payload as a Function of Time

If we assume for simplicity that the rotational velocity of the galactic halo about the galactic center is small compared to the earth's galactocentric velocity, then the IMP flux would depend only on the galactocentric velocity of the earth $\vec{v}_e$ (Equation C.88) and cosine, $\cos(\Psi)$, of the angle between the zenith vector, pointing at α_z, δ_z, of the earthbound IMP detector and the earth's velocity vector, pointing at $\alpha_{\Theta_e}, \delta_{\Theta_e}$, (Equation C.89) and the amount of atmospheric overburden above the detector. The zenith angle only depends on the time of day, the day of the year, and the latitude and longitude of the experiment. Unlike many dark matter search experiments, the IMAX experiment launched from Lynn Lake, Manitoba, Canada, moved a great distance during the course of one day. The NSBF provided us with accurate tracking of the latitude, longitude, and altitude as a function of time during the flight. From 2.6 hours UT on 7/17/92 to 4.67 hours UT on 7/18/92, the earth latitude varied by about a degree, LAT(IMAX) $\in [55^\circ\,58', 57^\circ\,04']$, while the earth longitude increased rapid LONG(IMAX) $\in [100^\circ\,28', 117^\circ\,35']$. We show the universal time (UT), earth latitude, earth longitude, local sidereal time (LST), and $\cos(\Psi)$ in Table C.13, and a graph showing the dependence of $\cos(\Psi)$ on UT in Figure C.47. The IMAX zenith direction was aligned quite well with the direction of the Earth's motion through the galactic halo at 8.667 hours UT on 7/17/92, when the right ascension and declination of the IMAX zenith was:

$$(\alpha_z(8.667 \text{ hours (UT)}) = 322^\circ.74, \delta_z(8.667 \text{ hours (UT)}) = 56^\circ.517). \tag{C.90}$$

The IMAX zenith coordinates at this time (Equation C.90) should be compared with the Earth's apex coordinates on 7/17/92 (Equation C.89). These two vectors are misaligned

by $\sim 10^\circ$ in the declination, which is responsible for the cosine value being only 0.98 rather than 1.00. Nonetheless, at 8.667 hours UT on 7/17/92, we expect that the IMP flux will have a large maximum, compared to the minimum flux, expected at 21 hours UT, about 12 hours later..

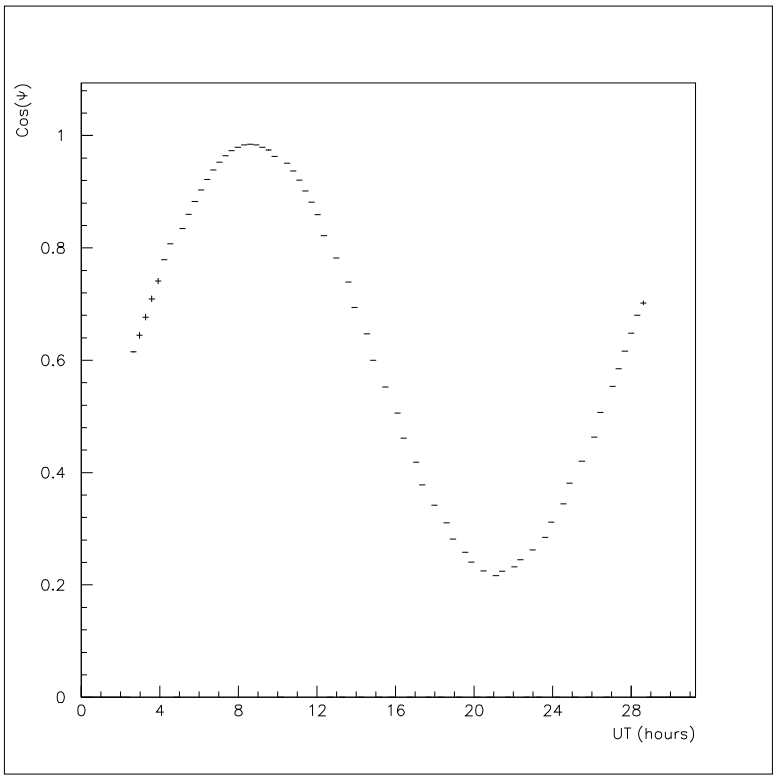

Figure C.47: We plot the cosine of the angle between IMAX zenith direction and the direction of the Earth's motion ($\cos(\Psi)$) vs. universal time (UT). The IMAX payload was launched at 2.6 hours UT, and reached float altitude at ~ 10 hours UT.

C.3 Time-dependence of counting rates during IMAX flight

In Figures C.48 and C.49, we plot two-dimensional histograms of the single detector counting rates and the multiple-detector delayed-coincidence rates versus universal time. The scaler rates are measured each second during the flight and represent the number of counts from the discriminator or coincidence unit during the previous second. At a fixed UT, there are significant fluctuations, especially for the delayed coincidence rates; these

Table C.13: For the IMAX flight (starting at 2.6 hours UT on 7/17/92), we show the universal time (UT), latitude (LAT) (or declination (δ)), longitude (LONG), local sideral time (LST), right ascension (R.A. (α)), and the cosine of the angle between the IMAX zenith direction and the direction of the earth's motion through the galactic halo ($\cos\Psi$). We also mark the positions of the minumum (at 21 hours UT) and maximum (at 8.667 hours UT) of the this cosine with an outline.

UT	LAT(δ)	LONG	LST	R.A.(α)	$\cos\Psi$
2.6	57.067	101	15.545	233.175	0.61321
2.667	56.733	101.083	15.606	234.09	0.61703
2.833	57.033	100.917	15.784	236.76	0.6365
3	56.9	100.917	15.951	239.265	0.65209
3.167	56.717	100.75	16.13	241.95	0.66852
3.333	56.667	100.683	16.301	244.515	0.68498
3.5	56.583	100.617	16.473	247.095	0.70117
3.667	56.533	100.567	16.643	249.645	0.71727
3.833	56.517	100.533	16.813	252.195	0.73319
4	56.483	100.5	16.982	254.73	0.74883
4.333	56.45	100.467	17.318	259.77	0.77917
4.667	56.567	100.583	17.645	264.675	0.80759
5	56.4	100.667	17.974	269.61	0.83428
5.333	56.533	100.75	18.302	274.53	0.85956
5.667	56.517	100.9	18.626	279.39	0.88254
6	56.533	101.083	18.948	284.22	0.90336
6.333	56.55	101.25	19.272	289.08	0.92209
6.667	56.567	101.417	19.595	293.925	0.93854
7	56.567	101.617	19.916	298.74	0.95253
7.333	56.6	101.783	20.239	303.585	0.96406
7.667	56.617	102.033	20.556	308.34	0.9729
8	56.567	102.25	20.876	313.14	0.97943
8.333	56.583	102.433	21.198	317.97	0.98316
8.667	56.517	102.683	21.516	322.74	0.98446
9	56.35	102.967	21.831	327.465	0.98345
9.333	56.483	103.217	22.149	332.235	0.97891
9.5	56.467	103.35	22.307	334.605	0.97593
9.667	56.45	103.483	22.465	336.975	0.97231
10	56.467	103.683	22.786	341.79	0.96289
10.333	56.5	103.967	23.101	346.515	0.95114
10.667	56.533	104.25	23.417	351.255	0.93705
11	56.55	104.5	23.734	356.01	0.92062

Table C.14: Continuation of Table C.13.

UT	LAT(δ)	LONG	LST	R.A.(α)	cos(Ψ)
11.333	56.567	104.6	0.062	0.93	0.9014
11.667	56.6	105.017	0.368	5.52	0.88145
12	56.617	105.283	0.685	10.275	0.85903
12.5	56.617	105.65	1.162	17.43	0.822
13	56.6	106.117	1.632	24.48	0.78215
13.5	56.567	106.55	2.105	31.575	0.73931
14	56.5	106.967	2.578	38.67	0.69408
14.5	56.467	107.35	3.054	45.81	0.64729
15	56.417	107.75	3.529	52.935	0.59974
15.5	56.383	108.167	4.002	60.03	0.55238
16	56.35	108.617	4.474	67.11	0.50593
16.5	56.35	109.067	4.945	74.175	0.46125
17	56.283	109.583	5.412	81.18	0.41833
17.5	56.283	110	5.886	88.29	0.37833
18	56.3	110.45	6.357	95.355	0.34218
18.5	56.367	110.8	6.835	102.525	0.31033
19	56.317	111.3	7.303	109.545	0.28191
19.5	56.267	111.733	7.775	116.625	0.25805
20	56.3	112.05	8.256	123.84	0.24053
20.5	56.133	112.267	8.743	131.145	0.22525
21	55.967	113.183	9.183	137.745	0.21636
21.5	56.483	112.8	9.71	145.65	0.22456
22	56.633	113.567	10.16	152.4	0.23232
22.5	56.717	114	10.633	159.495	0.24472
23	56.767	114.317	11.113	166.695	0.26236
23.5	56.783	114.7	11.589	173.835	0.28463
24	56.8	115.1	12.063	180.945	0.31179
24.5	56.85	115.417	12.544	188.16	0.34435
25	56.867	115.667	13.028	195.42	0.38084
25.5	56.85	115.95	13.511	202.665	0.42038
26	56.867	116.267	13.991	209.865	0.46305
26.5	56.783	116.583	14.471	217.065	0.50702
27	56.683	116.783	14.959	224.385	0.55336
27.333	56.667	116.967	15.281	229.215	0.58498
27.667	56.633	117.167	15.602	234.03	0.61655
28	56.617	117.317	15.927	238.905	0.6485
28.333	56.6	117.45	16.252	243.78	0.6803
28.5	56.6	117.583	16.41	246.15	0.69563
28.533	56.6	117.567	16.445	246.675	0.69895
28.667	56.6	117.55	16.579	248.685	0.71186

fluctuations are due to counting statistics. If there is a diurnal modulation of the IMP flux through the IMAX detectors, we would expect a maximum counting rate at 8.667 hours UT and a minimum counting rate at 21 hours UT. There is a significant maximum in the scaler rates at about 4.5 hours UT, which is not due to a diurnally-modulated IMP signal. This peak is due to the Pfotzer cosmic ray air shower maximum, which occurs at ~ 100 g/cm^2 atmospheric depth. Note that the triples rate levels off at around 4 Hz, the doubles rate at around 90 Hz, and the singles rates level off at different rates, between 3000 Hz and 4000 Hz. The slight non-diurnal and non-Pfotzer modulation (especially evident for TOF1) is probably due to shifting gain-levels or shifting discriminator thresholds. There is no evidence from these plots for any diurnal variation that peaks at 8.667 hours UT.

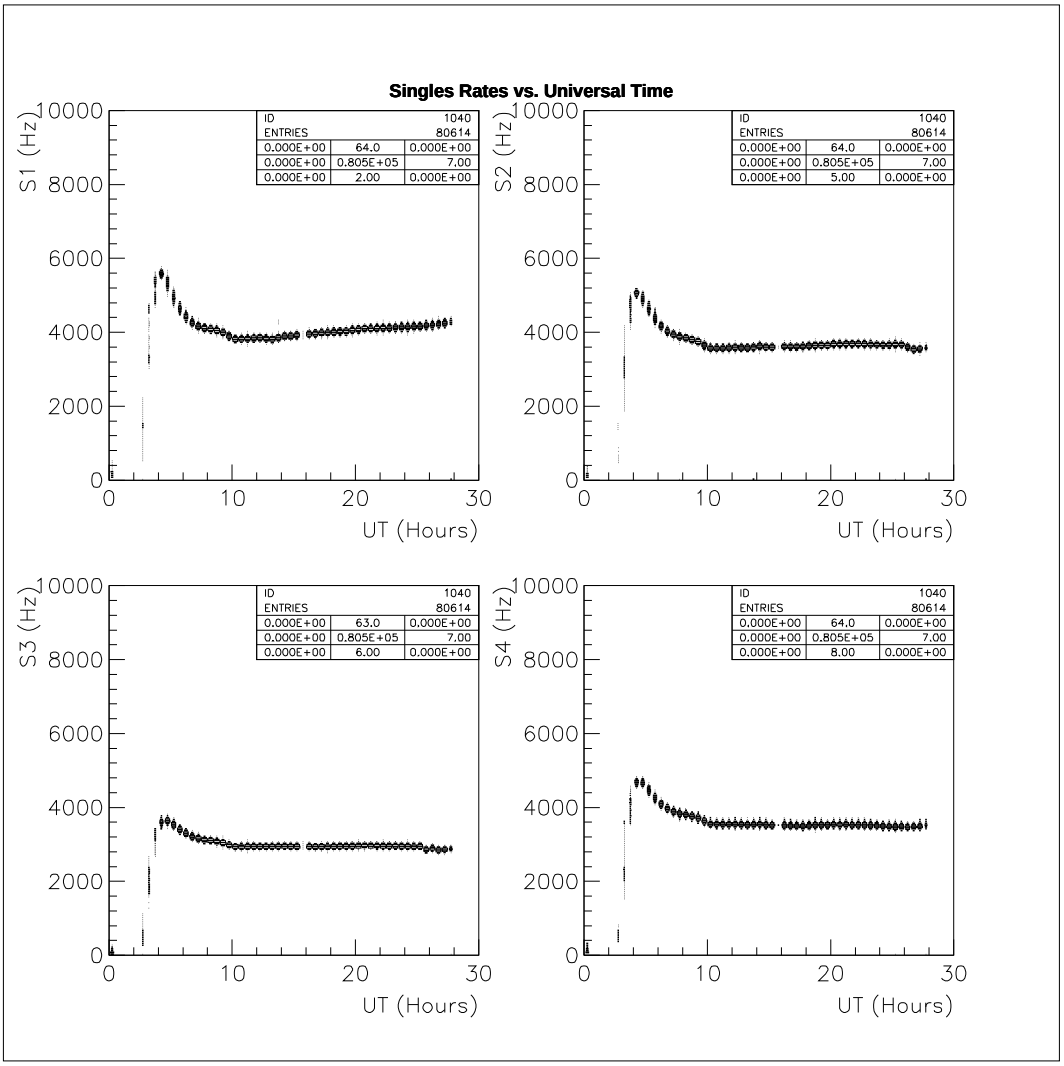

Figure C.48: We plot the single detector counting rates during the IMAX flight versus universal time. The top time of flight detector is labelled S1, the S1 detector is labelled S2, the S2 detector is labelled S3, and the bottom time-of-flight detector is labelled S4. The maximum at $\sim$ 4.5 hours UT is due to the Pfotzer cosmic ray maximum at an atmospheric overburden of $\sim$ 100 g/cm^2. The IMAX payload reached float altitude (5 g/cm^2) at 10 hours UT, where the single counting rates level off.

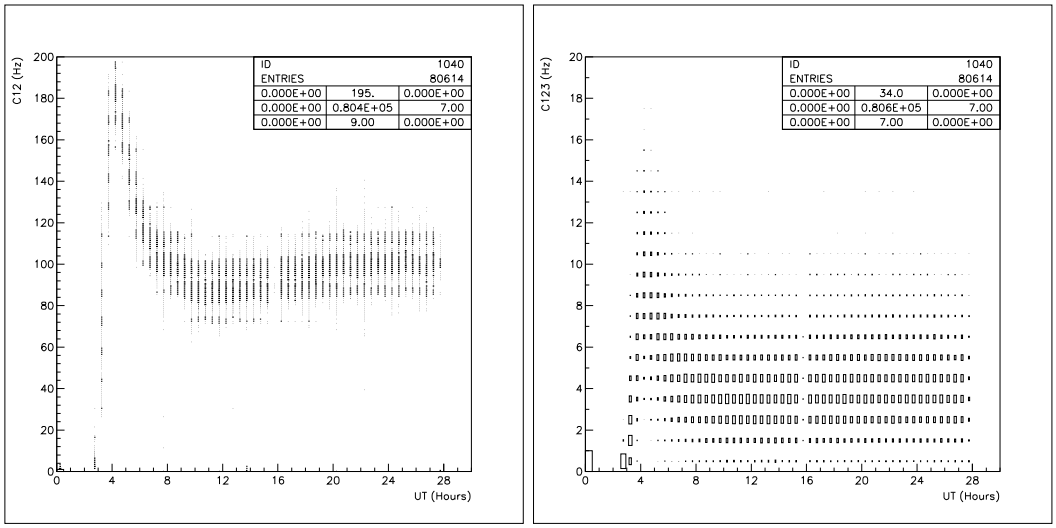

Figure C.49: We plot the multiple detector delayed coincidence counting rates during the IMAX flight versus universal time. The doubles rate, C12, is a delayed coincidence between detectors TOF1 and S1. The triples rate, C123, is a delayed coincidence between detectors TOF1, S1 and S2. The maximum at $\sim$ 4.5 hours UT is due to the Pfotzer cosmic ray maximum at an atmospheric overburden of $\sim$ 100 g/cm^2. The IMAX payload reached float altitude (5 g/cm^2) at 10 hours UT, where the single counting rates level off.

REFERENCES

[1] Vera C. Rubin, W. Kent Ford Jr., and Norbert Thonnard, "Rotational Properties of 21 Sc Galaxies with a Large Range of Luminosities and Radii, From NGC 4605 ($R = 4$ kpc) to UGC 2885 ($R = 122$ kpc)", *Astrophys. J.* **238**, 471 (1980); Rubin, Ford, Thonnard and David Burstein, "Rotational Properties of 23 Sb Galaxies", *Astrophys. J.* **261**, 439 (1982); Rubin, Burstein, Ford, and Thonnard, "Rotation Velocities of 16 Sa Galaxies and a Comparison of Sa, Sb, and Sc Rotation Properties", *Astrophys. J.* **289**, 81 (1985).

[2] Massimo Persic and Paolo Salucci, "The Universal Galaxy Rotation Curve", *Astrophys. J.* **368**, 60 (1991).

[3] Rubin, Ford, and Thonnard, "Extended Rotation Curves of High-Luminosity Spiral Galaxies. IV. Systematic Dynamical Properties, Sa→Sc", *Astrophys. J.* **L225**, 107 (1978).

[4] Burstein, Rubin, Thonnard, and Ford, "The Distribution of Mass in Sc Galaxies", *Astrophys. J.* **253**, 70 (1982).

[5] R.H. Sanders, "Finite Length-scale Anti-gravity and Observations of Mass Discrepencies in Galaxies", *Astron. Astrophys.* **154**, 135 (1986).

[6] Mordehai Milgrom and Erez Braun, "The Rotation Curve of DDO 154: a Particularly Acute Test of the Modifies Dynamics", *Astrophys. J.* **334**, 130 (1988).

[7] T.S. van Albada, J.N. Bahcall, K. Begeman, and R. Sancisi, "Distribution of Dark Matter in the Spiral Galaxy NGC 3198", *Astrophys. J.* **295**, 305 (1985).

[8] George R. Blumenthal, S.M. Faber, Ricardo Flores, and Joel R. Primack, "Contraction of Dark Matter Galactic Halos due to Baryonic Infall", *Astrophys. J.* **301**, 27

(1986).

[9] K.C. Freeman, "Parameters for Dark Halos", in **Dark Matter in the Universe**, eds. J. Kormendy and G.R. Knapp (D. Reidel, Dordrecht), p. 119 (1987).

[10] Claude Carignan and Kenneth C. Freeman, "DDO 154: a 'Dark' Galaxy?", *Astrophys. J.* **L332**, 33 (1988).

[11] Persic and Salucci, "Dark Matter in Spiral Galaxies", *Astrophys. J.* **355**, 44 (1990).

[12] Daniel Puche and Claude Carignan, "H I Studies of the Sculptor Group Galaxies. VII. Implications on the Distribution and Nature of Dark Matter in Groups", *Astrophys. J.* **378**, 487 (1991).

[13] Salucci, Keith M. Ashman, and Persic, "The Dark Matter Content of Spiral Galaxies", *Astrophys. J.* **379**, 89 (1991).

[14] Vladimir Garrido Ortega and J.A. de Freitas Pacheco, "Dark Matter in Sc Galaxies" *Astron. J.* **106**, 899 (1993).

[15] M. Schmidt, In *The Milky Way Galaxy* (IAU Symposium 106), eds. H. van Woerden *et al.*, (Reidel, Dordrecht), p. 75 (1985).

[16] F.Reif, *Fundamentals of Statistical and Thermal Physics* (McGraw-Hill, New York), pp.269-273 (1965).

[17] S.W. Barwick, P.B. Price, and D.P. Snowden-Ifft, "Search for Charged Massive Particles in Cosmic Rays", *Phys. Rev.* **L64**, 2859 (1990).

[18] J.R. Primack, D. Seckel and B. Sadoulet, "Detection of Cosmic Dark Matter", *Ann. Rev. Nucl. Part. Sci.* **38**, 751 (1988).

[19] R.A. Flores, "Dynamical Estimates of the Local Density of Dark Matter", *Phys. Lett.* **B215** 73 (1987).

[20] M.S. Turner, E.N. Parker, and T.J. Bogdan, "Magnetic Monopoles and the Survival of the Galactic Magnetic Field", *Phys. Rev.* **D26**, 1296 (1982).

[21] G. Steigman, C.L. Sarazin, H. Quintana, and J. Faulkner, "Dynamical Interactions and Astrophysical Effects of Stable Heavy Neutrinos", *Astrophys. J.* **83**, 1050 (1978).

[22] S. Dimopoulos, S.L. Glashow, E.M. Purcell, and F. Wilczek, "Is there a Local Source of Magnetic Monopoles?", *Nature* **298**, 824 (1982).

[23] John D. Anderson, Eunice L. Lau, Amthony H. Taylor, Duane A. Dicus, Doris C. Teplitz, Vigdor L. Teplitz, "Bounds on Dark Matter in Solar Orbit", *Astrophys. J.* **342**, 539 (1989).

[24] A. Gould, *Astrophys. J.* **328**, 919 (1988).

[25] Kim Griest, "Effect of the Sun's Gravity on the Distribution and Detection of Dark Matter Near the Earth", *Phys. Rev.* **D37**, 2703 (1988).

[26] P.F. Smith and J.D. Lewin, "Dark Matter Detection", *Phys. Reports* **5**, 203-280 (1990).

[27] James Binney, Andrew May, and Jeremiah P. Ostriker, "On the Flattening of Dark Haloes", *Mon. Not. R. Astron. Soc.* **226**, 149 (1987).

[28] Katherine Freese, Joshua Frieman and Andrew Gould, "Signal Modulation in Cold-Dark Matter Detection", *Phys. Rev.* **D37**, 3388 (1988).

[29] A. Gabutti and K. Schmiemann, "Detection Rate of Weakly Interacting Massive Particles", *Univ. Bern Preprint BUHE-93-1* (1993).

[30] J.I. Collar and F.T. Avignone III, "Diurnal Modulation Effects in Cold Dark Matter Experiments", *Phys. Lett.* **B275**, 181 (1992); J.I. Collar and F.T. Avignone III, "Effect of Elastic Scattering in the Earth on Cold Dark Matter Experiments", *Phys. Rev.* **D47**, 5238 (1993); D.E. Di Gregorio, A.O. Gattone, H. Huck, A.O. Machiavelli, S. Gil, J. Collar, and F.T. Avignone III, "Effects of Diurnal Modulation in Direct Cold Dark Matter Searches. The Experiment in Sierra Grande", *Laboratorio Tandar Preprint*, Comisión Nacional de Energía Atómica, Buenos Aires, Argentina (1993); Juan Collar, *Ph.D. dissertation*, University of South Carolina (1991).

[31] C. Alcock, C.W. Akelof, R.A. Allsman, T.S. Axelrod, D.P. Bennett, S. Chan, K.H. Cook, K.C. Freeman, K. Griest, S.L. Marshall, H-S. Park, S. Perlmutter, B.A. Peterson, M.R. PRatt, P.J. Quinn, A.W. Rodgers, C.W. Stubbs, and W. Sutherland (MACHO Collaboration), "Possible Gravitational Microlensing of a Star in the Large Magellenic Cloud", *Nature* **365**, 621 (1993).

[32] E. Aubourg, P. Bareyre, S. Bréhin, M. Gros, M. Lachièze-Rey, B. Laurent, E. Lesquoy, C. Magneville, A. Milsztajn, L. Moscoso, F. Queinnec, J. Rich, M. Spiro, L. Vigroux, S. Zylberajch, R. Ansari, F. Cavalier, M. Moniez, J.P. Beaulieu, R. Felet, Ph. Grison, A. Vidal-Madjar, J. Guibert, O. Moreau, F. Tajahmady, E. Maurice, L. Prévöt, and C. Gry, (EROS Collaboration), "Evidence for Gravitational Microlensing by Dark Objects in the Galactic Halo," *Nature* **365**, 623 (1993).

[33] D. Pfenniger, F. Combes and L. Martinet, "Is Dark Matter in Spiral Galaxies Cold Gas? I. Observational Constraints and Dynamical Clues about Galaxy Evolution"; D. Pfenniger and F. Combes, "II. Fractal Models and Star Non-formation", *OBSGE Preprints DM I & II* (1993).

[34] R.N. Henriksen and L.M. Widrow, "Hydrogen Clouds and the MACHO/EROS Events", *Queen's University Preprint* (1994).

[35] V.N. Gavrin, "SAGE: the Soviet-American Gallium Solar Neutrino Experiment", *Nucl.Phys.* **B28A** *(Proc. Suppl.)*, 75 (1992).

[36] A. Dar and S. Nussinov, "Implications of Solar Neutrino Experiments", *Nucl.Phys.* **B28A** *(Proc. Suppl.)*, 121 (1992).

[37] D.O. Caldwell, "Review of Dark Matter Experiments", *Nucl.Phys.* **B28A** *(Proc. Suppl.)*, 273 (1992).

[38] D.N. Schramm, "Dark Matter and Cosmology", *Nucl. Phys.* **B28A** *(Proc. Suppl.)*, 243 (1992).

[39] B.W. Lee and S. Weinberg, "Cosmological Lower Bound on Heavy-Neutrino Masses", *Phys. Rev. Lett* **39**, 165 (1977).

[40] G.B. Gelmini, L.J. Hall, and M.J. Lin, *Nucl. Phys.* **B281**, 726 (1987); G. Steigman, C.L. Sarazin, H. Quintana, J. Faulkner, "Dynamical Interactions and Astrophysical Effects of Stable Heavy Neutrinos", *Astrophys. J.* **83**, 1050 (1978); D.N. Spergel and W.H. Press, "Effect of Hypothetical, Weakly Interacting, Massive Particles on Energy Transport in the Solar Interior", *Astrophys. J.* **294**, 663 (1985).

[41] J. Preskill, *Ann. Rev. Nucl. Part. Sci* **34**, 461 (1984); B. Cabrera, *Phys. Rev. Lett.* **48**, 1378 (1982); M.S. Turner, E.N. Parker, and T.J. Bogdan, *Phys. Rev.* **D26**, 1296 (1982).

[42] A. De Rujula, S.L. Glashow, and U. Sarid, "Charged Dark Matter," *Nucl. Phys.* **B333**, 173 (1990).

[43] Stephen Wolfram, "Abundances of New Stable Particles Produced in the Early Universe", *Phys. Lett.* **B82**, 65 (1979).

[44] J. Bagger, S. Dimopoulos, E. Masso and J. Reno, *Phys. Rev. Lett.* **54**, 56 (1986).

[45] Mark W. Goodman and Edward Witten, "Detectability of Certain Dark-Matter Candidates", *Phys. Rev.* **D31**, 3059 (1985).

[46] H. Goldberg and L.J. Hall, "A New Candidate for Dark Matter", *Phys. Lett.* **B174**, 151 (1988).

[47] G.D. Starkman, A. Gould, R. Esmailzadeh, S. Dimopoulos, "Opening the Window on Strongly Interacting Dark Matter", *Phys. Rev.* **D41**, 3594 (1990).

[48] A. DeRujula and S.L. Glashow, "Nuclearites — a Novel form of Cosmic Radiation", *Nature* **312**, 734 (1984).

[49] L.E. Ibanez, *Phys. Lett* **B137**, 160 (1984); J.S. Hagelin, G.L. Kane, and S. Raby, *Nucl. Phys.* **B241**, 638 (1984); N. Cabibbo, G. Farrar, and L. Maiani, *Phys. Lett.* **B105**, 155 (1981); J. Silk and M. Srednicki, *Phys. Rev. Lett.* **53**, 624 (1984).

[50] R.D. Peccei and H.R. Quinn, "Constraints Imposed by *CP* Conservation in the Presence of PseudoParticles", *Phys. Rev. Lett.* **3B**,1440 (1977); J.E. Kim, "Light

Pseudoscalers, Particle Physics and Cosmology", *Phys. Rep.* **150**,1 (1987); M.S. Turner, "Windows on the Axion", *Phys. Rep.* **197**, 67 (1990); P. Sikivie, *Phys. Rev. Lett.* **51**,1415 (1983).

[51] D.O. Caldwell, R.M. Eisberg, D.M. Grumm, M.S. Witherell, B. Sadoulet, F.S. Goulding, and A.R. Smith, "Laboratory Limits on Galactic Cold Dark Matter", *Phys. Rev. Lett.* **61**, 510 (1988).

[52] A.M. Polyakov, *JETP Lett.* **20**, 194 (1974).

[53] G. 't Hooft, *Nucl. Phys.* **B79**, 276 (1974).

[54] V. Rubakov, *JETP Lett.* **33**, 644 (1981); Rubakov, *Nucl. Phys.* **B203**, 311 (1982); C. Callan, *Phys. Rev.* **D25**, 2141 (1982); Callan, *Phys. Rev.* **D26**, 2058 (1982).

[55] Erick J. Weinberg, "Monopoles and Grand Unification", *Monopole '83*, ed. James L. Stone, Ann Arbor, Michigan, p. 1 (1983).

[56] S.P. Ahlen and K. Kinoshita, "Calculation of the Stopping Power of Very-Low-Velocity Magnetic Monopoles", *Phys. Rev.* **D26**, 2347 (1982).

[57] J. Kim, *Phys. Rev.* **D23**, 2706 (1981).

[58] E. Witten, *Phys. Rev.* **D30**, 272 (1984).

[59] Snowden-Ifft and Price, "The Low-Velocity Response of the Solid-State Nuclear Track Detector CR-39", *Phys. Lett.* **B288**, 250 (1992).

[60] Daniel Parth Snowden-Ifft, *Ph.D. Thesis*, Dept. Physics, University of California at Berkeley, unpublished (1991).

[61] J. Rich, R. Rocchia, and M. Spiro, "A Search for Strongly Interacting Dark Matter", *Phys. Lett.* **B194**, 173 (1987).

[62] Snowden-Ifft, Barwick, and Price, "A Search for Charged Massive Particles in *IMP 8* Data", *Astrophys. J.* **L364**, 25 (1990).

[63] J.H. Adams, R.L. Kinzer, W.N. Johnson, and J.D. Kurfess, "Experimental Constraints on Charged Dark Matter from Atmospheric X-Rays", *Naval Research Laboratory Preprint* (1989).

[64] J.L. Basdevant, R. Mochkovitch, J. Rich, M. Spiro, and A. Vidal-Madjar, "Is There Room for Charged Dark Matter?" *Phys. Lett.* **B234**, 395 (1990).

[65] S. Dimopoulos, D. Eichler, R.Esmailzadeh, and G.D. Starkman, "Getting a Charge out of Dark Matter," *Phys. Rev.* **D41**, 2388 (1990).

[66] A. Gould, B.T. Draine, R.W. Romani, and S. Nussinov, "Neutron Stars: Graveyard for Charged Dark Matter", *Phys. Lett.* **B238**, 337 (1990).

[67] R.S. Chivukula, A.G. Cohen, S. Dimopoulos, and T.P. Walker, "Bounds on Halo-Particle Interactions from Interstellar Calorimetry", *Phys. Rev.* **L65**, 957 (1990).

[68] I. Goldman and S. Nussinov, "Weakly Interacting Massive Particles and Neutron Stars", *Phys. Rev.* **D40**, 3221 (1989).

[69] Kim Griest and Marc Kamionkowski, "Unitarity Limits on the Mass and Radius of Dark-Matter Particles", *Phys. Rev. Lett.* **64**, 615 (1990).

[70] J.A. Holtzman and J.R. Primack, *Astrophys. J.* **429** (1993).

[71] P.J. Kernan and L.M. Krauss, "Refined Big Bang Nucleosynthesis Constraints On Ω_{Baryon} and N_ν", *Preprint CWRU-P2-94* (1994).

[72] B. Paczynski, "Gravitational Microlensing by the Galactic Halo", *Astrophys. J.* **304**, 1 (1986).

[73] M.S. Turner, "The Meaning of Eros/Macho", *UChicago/FNAL preprint* (1993).

[74] N.W. Evans, K. Griest, and J. Jijina, "Microlensing by the Milky Way Halo", *MIT/UCSD preprint* (1994).

[75] C. Cowan, D. Ryan, and G. Buckwalter, "Muon Decays from Neutral Primaries", *Proc. 9th Internl. Cosmic Ray Conf.,* p. 1041, London (1965).

[76] C. Cowan, "The Catholic University Neutrino-Detection System", *Proc. Intern. Conf. on Instrumentation for High Energy Physics*, p. 204, Berkeley (Interscience, 1990).

[77] D.F. Ryan, V. Acosta, G.L. Buckwalter, W.M. Carey Jr., C.L. Cowan, and D.J. Curtin, "Evidence for a Sidereal-Time Dependent Cosmic Ray Signal", *Phys. Lett.* **21**, 475 (1966).

[78] G.L. Buckwalter, C.L. Cowan, and D.F. Ryan, "Confirmatory Evidence for a Sidereal-Time Dependent Neutral Component in the Cosmic Rays", *Phys. Lett.* **21**, 478 (1966).

[79] A. Subramanian and S.D. Verma, "A Cosmic Ray Experiment to Detect Neutral Particles", *Proc. 18th International Cosmic Ray Conference (ICRC)*, Vol.5, p.93, Bangalore, India (1983)

[80] T.L. Jenkins and F. Reines, "A Large Liquid Scintillator for the Detection of Antineutrino Reactions", *IEEE Trans. Nucl. Sci.* **NS-11**, No. 3, 1 (1964).

[81] J. Rafelski, M. Sawicki, M. Gadja and D. Harley, "Nuclear Reactions Catalyzed by a Massive Negatively Charged Particle", *Bull. Am. Phys. Soc.* **35**, 980 (1990).

[82] M. Sawicki and J. Rafelski, "Attenuation of the Flux of NeutraCHAMPs in the Earth's Atmosphere. A Parametric Study", *J. Phys. G: Nucl. Part. Phys.* **L16**, 197 (1990).

[83] J. Rafelski, M. Sawicki, M. Gadja, and D. Harley, "Reactions of CHAMPS in a Deuterium Environment", *University of Arizona Preprint* (1991).

[84] S.E. Jones, E.P. Palmer, J.B. Csirr, D.L. Decker, G.L. Jenson, J.M. Thorne, S.F. Taylor, and J. Rafelski. "Observation of Cold Nuclear Fusion in Condensed Matter," *Nature* **338**, 737 (1989).

[85] Patrick McGuire and Theodore Bowen, "Time-of-Flight Technique to Search for Non-Weakly-Interacting Massive Particles", *Proc. 23rd International Cosmic Ray*

Conference (ICRC), Vol.4, p.726, Calgary (1993).

[86] J.W. Mitchell, L.M. Barbier, E.R. Christian, R.L. Golden, M. Hof, A.W. Labrador, W. Menn, R.A. Mewaldt, J.F. Ormes, I.L. Rasmussen, O. Reimer, S.M. Schindler, M. Simon, S.J. Stochaj, R.E. Streitmatter, and W.R. Webber, "IMAX (Isotope Matter-Antimatter Experiment)", *Proc. 23rd ICRC*, Vol.1, p.519, Calgary (1993).

[87] McGuire, Bowen, L.M. Barbier, E.R. Christian, A.W. Labrador, R.A. Mewaldt, J.W. Mitchell, J.F. Ormes, S.M. Schindler, S.J. Stochaj, R.E. Streitmatter, and W.R. Webber (The IMAX Collaboration), "High-Altitude Time-of-Flight Search for Non-Weakly-Interacting Dark Matter in Cosmic Rays", *Proc. 23rd ICRC*, Vol.4, p.621, Calgary (1993).

[88] J.H. Taylor and R.N. Manchester, *Astrophys. J.*, **215**, 885 (1977); W.H.G. Lewin and P.C. Joss, in *Accretion Driven Stellar X-Ray Sources*, edited by W.H.G. Lewin and E.P.J. van den Heuvel (Cambridge University Press, Cambridge, England, 1983); P.C. Joss and S.A. Rappaport, *Ann. Rev. Astron. Astrophys.* **22**, 537 (1984).

[89] M. Aglietta, P. Antonioli, G. Badino *et al.*, "Search for Fractionally charged particles in the Mont Blanc LSD Detector", Proc. 23rd ICRC, Vol.4, p.609, Calgary (1993).

[90] B. Barish, G. Liu, and C. Lane, "Search for Grand Unification Monopoles and other Ionizing Heavy Particles Using a Scintillation Detector at the Earth's Surface", *Phys. Rev.* **D36**, 2641 (1987).

[91] F. Kajino, T. Kitamura, K. Mitsui, Y. Ohashi, A. Okada, Y.K. Yuan, T. Aoki, S. Matsuno, "A Search for Slowly Moving Magnetic Monopoles", *Proc. 18th International Cosmic Ray Conference (ICRC)*, Vol.5, p.56, Bangalore, India (1983); F. Kajino, S. Matsuno, Y.K. Yuan, and T. Kitamura, "First Results from a Search for Magnetic Monopoles by a Detector Utilizing the Drell Mechanism and the Penning Effect", *Phys. Rev. Lett.* **52**, 1373 (1984).

[92] T. Tsukamoto, K. Nagano, K. Anraku, M. Imori, K. Kawagoe, S. Nakamura, M. Nozaki, S. Orito, K. Yamamoto, and T. Yoshida, "Limits on the Flux of Supermassive Relics", *Europhys. Lett.* **3**, 39 (1987).

[93] J.A. Simpson, T.S. Bastian, D.L. Chenette, R.B. McKibben, and K.R. Pyle, "The Trapped Radiations of Saturn and Their Absorption by Satellites and Rings", *J. Geophys. Res.* **85**, 5731 (1980); J.A. Simpson, G.A. Lentz, R.B. McKibben, J.J. O'Gallagher, W. Schroeder, and A.J. Tuzzolino, "Preliminary Documentation for the University of Chicago Charged Particle Instrument from the Pionerr 10/11 Spacecraft, *NSSDC Tech. Ref. File B21970*, Goddard Space Flight Center, Greenbelt, Maryland (1974).

[94] E.K. Shirk and P.B. Price, "Charge and Energy Spectra of Cosmic Rays with $Z > 60$: the *SKYLAB* Experiment", *Astrophys. J.* **220**, 719 (1978).

[95] E.N. Alexeyev, M.M. Boliev, A.E. Chudakov, B.A. Makoev, S.P. Mikheyev, and Yu.V. Sten'kin, "Search for Superheavy Magnetic Monopoles at the Baksan Underground Telescope", *Lett. Nuovo Cimento* **35**, 413 (1982).

[96] K. Kawagoe *et al.*, *Phys. Lett.* **128B**, 327 (1983).

[97] R. Mewaldt, private communication, possible forthcoming publication.

[98] P.F. Smith, J.R.J. Bennett, G.J. Homer, J.D. Lewin, H.E. Walford, and W.A. Smith, "A Search for Anomalous Hydrogen in Enriched D_2O Using a Time-of-Flight Spectrometer", *Nucl. Phys.* **B206**, 333 (1982).

[99] B. Pichard, J. Rich, M. Spiro, F. Biraben, G. Grynberg, P. Verkerk, M.E. Goldberg, and P. Fayet, "On the Possibility of Detecting Superheavy Hydrogen Through Centrifugation and Atomic Spectroscopy", *Phys. Lett.* **B193**, 383 (1987).

[100] P. Verkerk, G. Grynberg, B. Pichard, M. Spiro, S. Zylberajch, M.E. Goldberg, and P. Feyet, "Search for Superheavy Hydrogen in Sea Water", *Phys. Rev. Lett.* **68**, 1116 (1992).

[101] C. Alcock, E. Farhi, and A. Olinto, "Strange Stars", *Astrophys. J.* **310**, 261 (1986).

[102] C.B. Dover, T.K. Gaisser, and Gary Steigman, "Cosmological Constraints on New Stable Hadrons", *Phys. Rev. Lett.* **42**, 1117 (1979).

[103] P.H. Frampton and S.L. Glashow, "Unstable Heavy Particles", *Phys. Rev. Lett.* **44**, 1481 (1980).

[104] Robert N. Cahn and Sheldon L. Glashow, "Chemical Signatures for Superheavy Elementary Particles", *Science* **213**, 607 (1981).

[105] M. Jura and D.G. York, "Search for Interstellar Superheavy Hydrogen", *Science* **216**, 54 (1982).

[106] Anthony Turkevich, K. Wielgoz and T.E. Economou, "Searching for Supermassive Cahn-Glashow particles", *Phys. Rev.* **D30**, 1876 (1984).

[107] C.K. Au, "On the Possible Catalytic Role of Stable Relic Heavy Charged Leptons in the P-P I Chain", *Phys. Lett.* **B120**, 31 (1983).

[108] Eric B. Norman, Stuart B. Gazes, and Dianne A. Bennett, "Searches for Supermassive X^- Particles in Iron", *Phys. Rev. Lett.* **58**, 1403 (1987); Norman, Robert B. Chadwick, K.T. Lesko, Ruth-Mary Larimer, and Darleane C. Hoffman, "Search for Supermassive Cahn-Glashow Particles in Lead", *Phys. Rev.* **D39**, 2499 (1989).

[109] J. Lindhard, M. Scharff, H.E. Schiøtt, *Mat. Fys. Dan. Vid. Selsk.* **33**, No. 14 (1963); L. Lindhard and M. Scharff, *Phys. Rev.* **124**, 128 (1961).

[110] C. Greiner, P. Koch, H. Stöcker, "Separation of Strangeness from Antistrangeness in the Phase Transition from Quark to Hadron Matter: Possible Formation of Strange Quark Matter in Heavy-ion Collisions", *Phys. Rev. Lett.* **58** 1825 (1987); C. Greiner, D. Rishke, H. Stöcker, P. Koch, "Emission of Droplets of Strange Matter in RHIC", *Z. Phys. C. – Particles and Fields* **38**, 283 (1988).

[111] R.L. Jaffe, *Phys. Lett.* **38**, 195 (1977).

[112] G. Liu and B. Barish, "Nuclearite Flux Limit from Gravitational-Wave Detectors", *Phys. Rev. Lett.* **61**, 271 (1988); T. Saito, Y. Hatano, Y. Fukada, H. Oda, "Is There Strange-Quark Matter in Galactic Cosmic Rays?", *Phys. Rev. Lett.* **65**, 2094 (1990); S. Ahlen *et al.*, "Search for Nuclearites Using the MACRO Detector", *Phys. Rev. Lett.* **69**, 1860 (1992).

[113] John Bagnasco, Michael Dine, and Scott Thomas, "Detecting Technibaryon Dark Matter", *Santa Cruz Preprint SCIPP 93/33* (1993).

[114] David E. Brahm and Lawrence J. Hall, "$U(1)'$ Dark Matter", *Phys. Rev.* **D41**, 1067 (1990).

[115] S. Orito, H. Ichinose, S. Nakamura, K. Kuwahara, T. Doke, K. Ogura, H. Tawara, M. Imori, K. Yamamoto, H. Yamakawa, T. Suzuki, K Anraku, M. Nozaki, M. Sasaki, and T. Yoshida, "Search for Supermassive Relics with a 2000 m^2 Array of Plastic Track Detectors", *Phys. Rev.* **L66**, 1951 (1991).

[116] C. Bacci, P. Belli, R. Bernabei, Dai Changjiang, Ding Linkai, W. Di Nicolantonio, E. Gaillard, G. Gerbier, Kuang Haohuai, A. Incicchitti, J. Mallet, L. Mosca, D. Prosperi, C. Tao (Beijing-Paris-Roma-Saclay (BPRS) Collaboration), "A Search for Strongly Interacting Massive Particles in the Galactic Haol (with NaI Scintillators)", *LNGS-93/80, DAPNIA/SPP-93-16 Preprint* (1993), to appear in Astroparticle Physics (1994).

[117] S. Ahlen, F.T. Avignone, R.L. Brodzinski, A.K. Drukier, G. Gelmini, and D. Spergel, *Phys. Lett.* **B195** 603 (1987).

[118] D.J. Ficenec, S.P. Ahlen, A.A. Marin, J.A. Musser, G. Tarlé, "Observation of Electronic Excitation by Extremely Slow Protons with Applications to the Detection of Supermassive Charged Particles", *Phys. Rev.* **D36**, 311 (1987).

[119] J.A. Harvey and N.W. Hill, "Scintillation Detectors for Neutron Physics Research", *Nucl. Instr. Meth.* **162**, 507 (1979).

[120] Ahlen and Tarlé, "Can Grand Unification Monopoles be Detected with Plastic Scintillators?", *Phys. Rev.* **D27**, 688 (1983).

[121] S.P. Ahlen, T.M. Liss, C. Lane and G. Liu, "Scintillation from Slow Protons: A Probe of Monopole Detection Capabilities", *Phys. Rev. Lett.* **55**, 181 (1985).

[122] D.L. Smith, R.G. Polk and T.G. Miller, "Measurement of the Response of Several Organic Scintillators to Electrons, Protons and Deuterons", *Nucl. Instr. Meth.* **64**, 157 (1968).

[123] Chuck Hurlbut, Bicron Corporation, private communication (1994).

[124] *Bicron Catalog*, Newbury, Ohio, p. B12 (1991).

[125] *Cadillac Plastic Catalog*, Tucson, Arizona, p. 50 (1989).

[126] H.J.Komori, *J.Phys.Soc.Japan*, **17**, 620 (1962).

[127] Particle Data Group, *Particle Properties Data Booklet* (North-Holland, Berkeley), p. 158 (1992).

[128] T.K. Gaisser and G.B. Yodh, "Particle Collisions above 10 TeV as seen by Cosmic Rays", *Ann. Rev. Nucl. Part. Sci.* 500-501 (1980).

[129] J.A. Goodman, R.W. Ellsworth, A.S. Ito, J.R. MacFall, F. Siohan, R.E. Streitmatter, S.C. Tonwar, P.R. Vishwanath, G.B. Yodh, "Observation of Energetic Delayed Hadrons in Air Showers – New Massive Particles?", *Phys. Rev.* **D19**, 2572 (1979); J.A. Goodman *et al.*, "Composition of Primary Cosmic Rays above 10^{13}eV from the Study of Time Distributions of Energetic Hadrons near Air-Shower Cores", *Phys. Rev. Lett.* **42**, 854 (1979); J.A. Goodman *et al.*, "Observation of Energetic Delayed Hadrons in Extensive Air Showers – New Massive Particles?", *Cosmic Rays and Particle Physics, Bartol Conference, AIP Conf. Proc.* **49**, 207-220 (1978).

[130] C. Aguirre, R. Anda, A. Trepp, F.Kakimoto, Y. Mizumoto, K Suga, N. Izu, Y. Kamouchi, N. Inoue, S. Kawai, T. Kaneko, H. Yoshii, E. Goto, K. Nishi, H.

Nakatani, Y. Yamada, N. Tajima, P.K. Mackeown, K. Murakami (Bolivian Air Shower Joint Experiment), "Arrival-time Distributions of Muons and Electrons in Large Air Showers Observed at 5200m above Sea Level", *Cosmic Rays and Particle Physics, Bartol Conference, AIP Conf. Proc.* **49**, 13 (1978).

[131] M.C. Teich, R.A. Campos, B.E.A. Saleh, "Statistical Properties of Cosmic-Ray Showers at Ground Level Determined from Photomultiplier-Tube Background Registrations", *Phys. Rev.* **D36**, 2649 (1987).

[132] R.L. Jerde, L.E. Peterson, W. Stein, "Effects of High Energy Radiations on Noise Pulses from Photomultiplier Tubes", *Rev. Sci. Instrum.* **38**, 1387 (1967).

[133] A.T. Young, "Cosmic Ray Induced Dark Current in Photomultipliers", *Rev. Sci. Instrum.* **37**, 1472 (1966).

[134] A.G. Wright, "An Investigation of Photomultiplier Background", *J. Phys. E:Sci. Instrum.* **16**,300 (1983).

[135] A.T. Young, "Photometric Error Analysis. IX: Optimum Use of Photomultipliers", *Applied Optics* **8**, 2431 (1969).

[136] J.C. Barton, R. Riley, A.G. Wright, "Effect of Photomultiplier Afterpulses in Coincidence Systems", *Proc. 15th International Cosmic Ray Conference (ICRC)*, Vol.9, p.25, Plovdiv, Bulgaria (1977).

[137] T. Suzuki, D.F. Measday, J.P. Roalsvig, "Total Nuclear Capture Rates for Negative Muons", *Phys. Rev.* **C35**, 2212 (1987).

[138] R.G.Gordon and Y.S.Kim, "Theory for the Forces between Closed-Shell Atoms and Molecules", *J.Chem.Phys.* **56**, 3122 (1972).

[139] E.Everhart, G.Stone and R.J.Carbone, "Classical Calculation of Differential Cross-Section for Scattering from a Coulomb Potential with Exponential Screening", *Phys. Rev.* **99**, 1287 (1955).

[140] W.D.Wilson and C.L. Bisson, "Inert Gases in Solids:Interatomic Potentials and their Influence on Rare-Gas Mobility", *Phys.Rev.* **B3**, 3984 (1971).

[141] C.Cohen-Tannoudji, B.Diu, F.Laloë, *Quantum Mechanics II*, (Wiley, New York), pp. 1279-1282 (1977).

[142] L.I.Schiff, *Quantum Mechanics* (McGraw-Hill, New York), Section 33 (1968).

[143] A.Dalgarno and A.L.Stewart, "On the Perturbation Theory of Small Disturbances", *Proc.Roy.Soc.* **A238**, 269 (1957).

[144] A.Dalgarno and J.T.Lewis, "The Exact Calculation of Long-Range Forces between Atoms by Perturbation Theory", *Proc. Roy.Soc.* **A233**, 70 (1955).

[145] C.Schwartz, "Calculations in Schrödinger Perturbation Theory", *Annals of Physics* **2**, 156 (1959).

[146] Particle Data Group, *Particle Properties Data Booklet* (North-Holland, Berkeley), p. 69 (1990).

[147] F.Herman and S.Skillman, *Atomic Structure Calculations* (Prentice-Hall, Englewood Cliffs, New Jersey) (1963).

[148] R.O.Jones and O.Gunnarsson, "The Density Functional Formalism, Its Applications and Prospects", *Rev.Mod.Phys.* **61**, 689 (1989).

[149] R.Parmenter, private communication.

[150] J.D.Jackson, *Classical Electrodynamics* (Wiley, New York), p.161 (1962).

[151] H.Goldstein, *Classical Mechanics, 2nd Ed.* (Addison-Wesley, Reading, Massachusetts), pp.106-127. (1980).

[152] W.D.Wilson, L.G. Haggmark and J.P Biersack, "Calculations of Nuclear Stopping, Ranges, and Straggling in the Low-Energy Region", *Phys.Rev.* **B15**, 2458 (1977).

[153] I.S.Gradshteyn and I.M.Ryzhik, *Tables of Integrals, Series, and Products, Corrected and Enlarged Edition* (Academic, San Diego) (1980).

[154] J.D.Garcia, private communication.

[155] J.Rafelski, private communication.

[156] A. Labrador, R.A. Mewaldt, S.M. Schindler, E.C. Stone, L.M. Barbier, E.R. Christian, J.W. Mitchell, R.E. Streitmatter, S.J. Stochaj, I.L. Rasmussen, "Silica Aerogel Cherenkov Counters for the Isotope Matter-Antimatter Experiment", *Proc. 23rd International Cosmic Ray Conference (ICRC)*, Vol.2, p.524, Calgary (1993); A.W. Labrador, "IMAX Aerogel Cherenkov Analysis Progress Report 8/93-11/93", Caltech/IMAX internal document, 11/5/93; A.W. Labrador, "IMAX/Caltech Memo #3", 2/3/93.

[157] R. Cahn and S.L. Glashow, *Science* **213**, 607 (1981).

[158] F.J. Kerr and D. Lynden-Bell, "Review of Galactic Constants", *Mon. Not. Roy. Astr. Soc.* **221**, 1023 (1986).

[159] M. Zeilik, S.A. Gregory and E.V.P. Smith, *Introductory Astronomy and Astrophysics*, Third Ed., Saunders College Publishing, Fort Worth, Texas, p. 285 (1992).

[160] E.V. Khrutskaya, "General Catalog of Positions and Proper Motions of 4949 Geodesic Stars from 90° to −90°", *Sov. Astron.* **29**, 353 (1985).

[161] Nautical Almanac Office, *The Astronomical Almanac for the Year 1992*, United States Naval Observatory, Washington, D.C., pp. C4-C19 (1991).

[162] A.A. Zdziarski, P.T. Zyci, R. Svensson, E. Boldt, "On Compton Reflection in the Sources of the Cosmic X-Ray Background", accepted for publication, *Astrophys. J.* (1992).

[163] Elihu Boldt, "The Cosmic X-Ray Background", *Phys. Reports.* **146**, 215 (1987).

[164] John S. Mulchaey, David S. Davis, Richard Mushotzky, and David Burstein, "Diffuse X-Ray Emission from the NGC 2300 Group of Galaxies: Implications for Dark Matter and Galaxy Evolution in Small Groups", accepted for publication in *Astrophys. J.* **L** (1992).

[165] Richard Mushotzky, "Implications of Recent Cluster Observations for Cosmology", Invited Talk presented at Texas/PASCOS Meeting: *Clusters of Galaxies*, Univ. Calif. Berkeley (1992).

[166] Atsumasa Yoshida, Toshio Murakami, Jun Nishimura, Ichiro Kondo, and Edward E. Fenimore, "A New Detection of Cyclotron Lines Seen in a Gamma-Ray Burst GB890929", *Publ. Astron. Soc. Japan* **43** (1992).

[167] Osamu Nishimura and Toshikazu Ebisuzaki, "Equivalent Width of Cyclotron Lines in Gamma-Ray Burst Spectra", *Publ. Astron. Soc. Japan* **44**, 109 (1992).

[168] Toshio Murakami, Masami Fujii, Kiyoshi Hayashida, Masayuki Itoh, Jun Nishimura, Takamasa Yamagami, Atsumasa Yoshida, Jerry P. Conner, Winifred D. Evans, Edward E. Fenimore, Ray W. Klebesadel, Kenneth M. Spencer, Hiroyuki Murakami, Nobuyuki Kawai, Ichiro Kondo, and Masahiro Katoh, "The Gamma-Ray Burst Detector System on Board Ginga", *Publ. Astron. Soc. Japan* **41**, 405 (1989).

[169] T. Murakami, M. Fujii, K. Hayashida, M. Itoh, J. Nishimura, T. Yamagami, J.P. Connor, W.D. Evans, E.E. Fenimore, R.W. Klebesadel, A. Yoshida, I. Kondo, and N. Kawai, "Evidence for Cyclotron Absorption Spectral Features in Gamma-Ray Bursts Seen with Ginga", *Nature* **335**, 234 (1988).

[170] E.E. Fenimore, J.P. Conner, R.I. Epstein, R.W. Klebesadel, J.G. Laros, A Yoshida, M. Fujii, K. Hayashida, M. Itoh, T. Murakami, J. Nishimura, T. Yamagami, I. Kondo, and N. Kawai, "Interpretations of Multiple Absorption Features in a Gamma-Ray Burst Spectrum", *Astrophys. J.* **L335**, 71 (1988).